

Doctoral Thesis

博士論文

**Geomorphological and geoenvironmental
approaches for evaluating karst terrain in Guizhou
Province, China**

(中国貴州省におけるカルスト地域の地形学・地圏環
境学的研究)

Hao CHEN

陳 昊

Department of Natural Environmental Studies,

Graduate School of Frontier Sciences,

The University of Tokyo

東京大学大学院新領域創成科学研究科

自然環境学専攻

ABSTRACT

Karst areas account for almost 20% of lands in the world and more than a quarter of the world's population depends on water from karst areas. There are several environmental problems related to karst landscape, such as soil erosion, sinkhole collapse, rocky desertification, and shortage of land resources. In order to better understand such problems based on knowledge about geomorphic systems composed of karst landforms, this paper develops a method of semi-automatic landform classification, and conducted morphometric, land-use and soil erosion analyses. The study areas are the western and central parts of Guizhou Province, China, having a typical karst landscape subject to recent desertification and soil erosion.

The semi-automatic approach was employed to classify karst landforms into sinkholes, tower karst hills and cockpit karst hills. The methodology of the landform classification is summarized as follows: 1) identification and digitization of actual sinkholes, tower karst and cockpit karst using aerial imagery, integrated with field validation; 2) sinkhole delineation from a DEM (digital elevation model); 3) exclusion of water area and distinct pseudo-sinkhole artifacts; 4) contour line extraction from the DEM; 5) delineation of hill-area polygons by defining the basal contour line for each hill; and 6) calculation of the number of contour lines and classification of cockpit karst (frequency > 1) and tower karst (frequency = 1). As a result, 423 sinkholes, 439 tower karst hills and 403 cockpit karst hills were identified in the central part of Guizhou province, and 38 sinkholes, 112 tower karst hills and 35 cockpit karst hills were identified in the western part. Comparisons with field observations indicate that the overall accuracy of the classification was higher than 85%.

For understanding the characteristics of karst landforms quantitatively, we analyzed the morphometric characteristics of the classified karst landforms. Fourteen morphometric parameters were measured in terms of horizontal, vertical and overall shapes. The obtained morphometric parameters were compared among different landform types, and the same landform type but in different study areas. It was found that the morphometric characteristics of sinkholes generally follow those of the field-based approach.

Based on the obtained knowledge about landforms, this thesis examined the two most important karst-related environmental issues in the study areas, land-use shortage and soil erosion. Land-use maps were generated from remote sensing data supported by

field observations. The result indicated that the study areas were highly cultivated even in the relatively steep hilly areas. The sinkhole areas are dominated by agricultural land-use with ratios of 51% to 83%, and over 50% of the tower and cockpit karst hills are also developed for agriculture. This situation has resulted in a serious problem of soil erosion and rocky desertification. We also evaluated erosion rates of a selected closed basin using the RUSLE model. The model gave a mean annual erosion rate of 30.24 Mg ha⁻¹ y⁻¹, which is consistent with the result of a previous study based on an in-situ sedimentation volume measurement in the central depression accumulated during 1980 to 2009. This situation allows us to use the RUSLE for more detailed evaluation of erosion distribution. The estimation of soil loss for different land-use types indicated that erosion from dense forest and grass land is much lower than that from other areas with stronger human impact. This suggests that human disturbance has significantly accelerated soil erosion and rocky desertification in the area.

In summary, this paper has provided important knowledge on geomorphology and geoenvironmental issues in the karst areas subject to recent desertification and erosion. To mitigate these problems, appropriate land-use arrangement and better protection on vegetation are needed to recover forest and grassland especially on the tower and cockpit karst hills where most erosion takes place.

LIST OF CONTENTS

ABSTRACT	I
LIST OF CONTENTS	IV
LIST OF FIGURES	VII
LIST OF TABLES	XVI
1. CHAPTER 1 INTRODUCTION	17
1.1. Review of studies on landforms in karst areas	18
1.2. Review of studies on soil erosion in karst areas	20
1.3. Review of studies on land-use in karst areas	21
1.4. Objectives of this thesis	22
2. CHAPTER 2 STUDY AREAS	24
2.1. Zhijing area	25
2.2. Weining area	26
3. CHAPTER 3 DATA AND METHODS	29
3.1. Geographical data including DEMs	29
3.2. Landform types at macro-scale.....	30
3.2.1. Karst sinkholes	31
3.2.2. Large karst depression	31
3.2.3. Tower karst	32
3.2.4. Cockpit karst	33
3.3. Semi-automatic method of karst landform classification	34
3.3.1. Sinkhole delineation	36
3.3.2. Discrimination of tower and cockpit karst hills	37
3.4. Morphometric properties of sinkholes, cockpit karst hills and tower karst hills.....	38
3.4.1. Horizontal measures	38
3.4.2. Vertical measures	39
3.4.3. Shape measures	40
3.5. Land-use classification	42
3.6. Evaluation of soil erosion rate.....	43
4. CHAPTER 4 KARST LANDFORM CLASSIFICATION	46
4.1. Sinkhole identification.....	46
4.2. Discrimination of tower and cockpit karst hills.....	53

4.3. Application of morphometric thresholds	59
4.4. Impact of DEM resolution on sinkhole identification	61
5. CHAPTER 5 MORPHOMETRIC ANALYSIS OF THE KARST LANDFORMS	63
5.1. Spatial distribution of sinkholes	63
5.2. Sinkhole morphometry and statistics	63
5.2.1. Area	63
5.2.2. Perimeter	65
5.2.3. Long-axis length	67
5.2.4. Ellipticity	69
5.2.5. Orientation	70
5.2.6. Depth	72
5.2.7. Volume	72
5.3. Morphometric analysis of tower and cockpit karst hills	74
5.3.1. Area	74
5.3.2. Perimeter	76
5.3.3. Long-axis length	78
5.3.4. Orientation	80
5.3.5. Relief	81
5.3.6. Relative relief	83
5.3.7. Slope	85
5.3.8. Aspect	86
5.3.9. Curvature	87
5.3.10. Circularity ratio	88
5.3.11. Area ratio	89
5.3.12. Terrain Ruggedness Index	90
5.3.13. Terrain Shape Index	92
5.3.14. Hypsometric integral	93
5.4. Morphometric differences between the tower and cockpit karst hills	94
5.5. Relationship between sinkholes and geologic structure	101
5.6. Implications from the morphometry of the tower and cockpit karst hills	104
6. CHAPTER 6 KARST LAND-USE CHARACTERISTICS	105
6.1. Land-use classification	105
6.2. Relationships between land-use and landforms	109

6.3. Development of rocky desertification	111
7. CHAPTER 7 SOIL EROSION IN KARST LANDFORMS.....	113
7.1. Soil erosion rate estimation.....	113
7.1.1. RUSLE factor values	113
7.1.2. Estimated annual soil loss	114
7.1.3. Soil loss per land-use type	116
7.1.4. Soil loss per landform type	119
7.2. Effect of factors in the RUSLE	120
7.3. Effect of grid size in the RUSLE.....	123
7.4. Comparisons with other areas	125
8. CHAPTER 8 INSIGHTS INTO ENVIRONMENTAL PROBLEMS	126
9. CHAPTER 9 CONCLUSIONS.....	128
ACKNOWLEDGEMENTS.....	131
REFERENCES	132

LIST OF FIGURES

Figure 2-1. Location of the study areas.....	24
Figure 2-2. Spatial distribution of elevation in the Zhijin area. The DEM used has a cell size of 3 m and was generated from topographic maps.	25
Figure 2-3. Geology of the Zhijin area based on the 1:200,000 geological map (GGS, 1976). The hillshades are from a 3-m DEM generated from topographic maps.	26
Figure 2-4. Spatial distribution of elevation in the Weining area. The DEM used has a cell size of 3 m and was generated from topographic maps.	27
Figure 2-5. Geology of the Weining area based on the 1:200,000 geological map (GGS, 1976). The hillshades are from a 3-m DEM generated from topographic maps.	28
Figure 3-1. Sinkhole at the central part of the Zhijin study area, Guizhou Province ..	31
Figure 3-2. Depression in the Weining study area, Guizhou Province	32
Figure 3-3. Sharply pointed conical tower karst hills at the eastern part of the Zhijin study area, Guizhou Province.	33
Figure 3-4. Cockpit karst hills in the Weining study area, Guizhou Province.	33
Figure 3-5. Flow chart of the semi-automatic approach for karst landform classification	35
Figure 4-1. Map of sinkholes in the Zhijin area, identified from the aerial photos and field surveys. The area within a white box is shown in Fig. 4-6.	46
Figure 4-2. Accuracy of sinkhole identification in the Zhijin area for the semi-automatic approach with or without the thresholds ($area = 60\text{ m}^2$, $E = 0.2$ and $TPI = 0$).	49
Figure 4-3. Map of sinkholes in the Weining area, identified from the aerial photos and field surveys. The area within a white box is shown in Fig. 4-7.	50
Figure 4-4. Comparison between landform classification results and the reference map in the Zhijin area.....	53
Figure 4-5. Comparison between landform classification results and reference of the Weining area.....	56
Figure 4-6. Results of the two different approaches to delineate sinkhole boundaries in the Zhijin area (area highlighted in Fig. 4-1).	60
Figure 4-7. Results of the two different approaches to delineate sinkhole boundaries in	

the Weining area (area highlighted in Fig. 4-3).	60
Figure 4-8. Hillshaded maps of a portion of the study area (highlighted in Fig. 4-1) showing sinkhole connections and the effects of DEM resampling on the depression identification. Sinkholes location are those determined by the semi-automatic approach with the thresholds of area = 60 m ² , $E = 0.2$ and $TPI = 0$	61
Figure 4-9. Effect of DEM resampling. ME and RSME are respectively the mean error and root mean square error of resampled DEMs (ASTER GDEM, SRTM-DEM and M-DEM) and the original M-DEM with a resolution of 1 m.	62
Figure 5-1. Frequency distribution of area of sinkholes in the Zhijin area. a) From the field-based approach. b) From the field-based approach after excluding large outliers. c) Log-transformed distribution from the field-based approach without the outliers. d) From the semi-automatic approach. e) From the semi-automatic approach after excluding large outliers. f) Log-transformed distribution from the semi-automatic approach without the outliers.	64
Figure 5-2. Frequency distribution of area of sinkholes in the Weining area. a) From the field-based approach. b) From the field-based approach after excluding large outliers. c) Log-transformed distribution from the field-based approach without the outliers. d) From the semi-automatic approach. e) From the semi-automatic approach after excluding large outliers. f) Log-transformed distribution from the semi-automatic approach without the outliers.	65
Figure 5-3. Frequency distribution of perimeter of sinkholes in the Zhijin area. a) From the field-based approach. b) From the field-based approach after excluding large outliers. c) Log-transformed distribution from the field-based approach without the outliers. d) From the semi-automatic approach. e) From the semi-automatic approach after excluding large outliers. f) Log-transformed distribution from the semi-automatic approach without the outliers.	66
Figure 5-4. Frequency distribution of perimeter of sinkholes in the Weining area. a) From the field-based approach. b) From the field-based approach after excluding large outliers. c) From the semi-automatic approach. d) From the semi-automatic approach after excluding large outliers.	67
Figure 5-5. Frequency distribution of long-axis length of sinkholes in the Zhijin area. a) From the field-based approach. b) From the field-based approach after	

excluding large outliers. c) From the semi-automatic approach. d) From the semi-automatic approach after excluding large outliers.	68
Figure 5-6. Frequency distribution of long-axis length of sinkholes in the Weining area. a) From the field-based approach. b) From the field-based approach after excluding large outliers. c) From the semi-automatic approach.	69
Figure 5-7. Frequency distribution of ellipticity of sinkholes in the Zhijin area. a) From the field-based approach. b) From the semi-automatic approach.	70
Figure 5-8. Frequency distribution of ellipticity of sinkholes in the Weining area. a) From the field-based approach. b) From the semi-automatic approach. ...	70
Figure 5-9. Frequency distribution of long-axis orientation of sinkholes in the Zhijin area. a) From the field-based approach in histogram. b) From the field-based approach in rose diagram. c) From the semi-automatic approach in histogram. c) From the semi-automatic approach in rose diagram.	71
Figure 5-10. Frequency distribution of long-axis orientation of sinkholes in the Weining area. a) From the field-based approach. b) From the semi-automatic approach.	71
Figure 5-11. The statistics related with sinkhole depth: a) Sinkhole depth frequency distribution in the Zhijin area; b) Sinkhole depth frequency distribution in the Weining area	72
Figure 5-12. Frequency distribution of volume of sinkholes in the Zhijin area. a) From the field-based approach. b) From the field-based approach after excluding large outliers. c) From the semi-automatic approach. d) From the semi-automatic approach after excluding large outliers.	73
Figure 5-13. Frequency distribution of volume of sinkholes in the Weining area. a) From the field-based approach. b) From the semi-automatic approach.	73
Figure 5-14. Distribution of sinkhole area as a function of volume in the Zhijin area with the field-based and semi-automatic approaches.	74
Figure 5-15. The distribution of hill areas in the Zhijin area. a) All tower karst hills with a skewed distribution. b) Tower karst hills except large outliers. c) Log-transformed normalized tower karst hill area. d) All cockpit karst hills with a skewed distribution. e) Cockpit karst hills except large outliers. f) Log-transformed normalized cockpit karst hills.....	75
Figure 5-16. The distribution of hill areas in the Weining area. a) All tower karst hills with a skewed distribution. b) Tower karst hills except large outliers. c)	

	Log-transformed normalized tower karst hill area. d) All cockpit karst hills with a skewed distribution. e) Cockpit karst hills except large outliers. f) Log-transformed normalized cockpit karst hills.....	76
Figure 5-17.	The distribution of hill perimeter in the Zhijin area. a) All tower karst hills with a somewhat normal distribution. b) All cockpit karst hills with a skewed distribution. c) Cockpit karst hills except large outliers. d) Log-transformed normalized cockpit karst hills.	77
Figure 5-18.	The distribution of hill perimeter in the Weining area. a) All tower karst hills with a normal distribution. b) All cockpit karst hills with a skewed distribution. c) Cockpit karst hills except large outliers.	78
Figure 5-19.	The distribution of hill long-axis length in the Zhijin area. a) All tower karst hills with a skewed distribution. b) Tower karst hills except large outliers. c) Log-transformed normalized tower karst hill area. d) All cockpit karst hills with a skewed distribution. e) Cockpit karst hills except large outliers. f) Log-transformed normalized cockpit karst hills.....	79
Figure 5-20.	The distribution of hill long-axis length in the Weining area. a) All tower karst hills with a normal distribution. b) All cockpit karst hills with a skewed distribution. c) Cockpit karst hills except large outliers. d) Log-transformed normalized cockpit karst hills.	80
Figure 5-21.	The distribution of hill orientation in the Zhijin area. a) All tower karst hills with a skewed distribution. b) All cockpit karst hills with a skewed distribution.	81
Figure 5-22.	The distribution of hill orientation in the Weining area. a) All tower karst hills with a skewed distribution. b) All cockpit karst hills with a skewed distribution.	81
Figure 5-23.	The distribution of hill relief in the Zhijin area. a) All tower karst hills with a skewed distribution. b) Tower karst hills except large outliers. c) Log-transformed normalized tower karst hill area. d) All cockpit karst hills with a skewed distribution. e) Cockpit karst hills except large outliers. f) Log-transformed normalized cockpit karst hills.....	82
Figure 5-24.	The distribution of hill relief in the Weining area. a) All tower karst hills with a skewed distribution. b) Tower karst hills except large outliers. c) All cockpit karst hills with a skewed distribution. d) Cockpit karst hills except large outliers.	83

Figure 5-25. The distribution of hill relative relief in the Zhijin area. a) All tower karst hills with a skewed distribution. b) Tower karst hills except large outliers. c) Log-transformed normalized tower karst hill area. d) All cockpit karst hills with a skewed distribution. e) Cockpit karst hills except large outliers. f) Log-transformed normalized cockpit karst hills.	84
Figure 5-26. The distribution of hill relative relief in the Weining area. a) All tower karst hills with a skewed distribution. b) Log-transformed normalized tower karst hill area. c) All cockpit karst hills with a somewhat normal distribution.	85
Figure 5-27. The distribution of hill slope in the Zhijin area. a) All tower karst hills with a somewhat normal distribution. b) All cockpit karst hills with a somewhat normal distribution.....	86
Figure 5-28. The distribution of hill slope in the Weining area. a) All tower karst hills with a somewhat normal distribution. b) All cockpit karst hills with a somewhat normal distribution.....	86
Figure 5-29. The distribution of hill aspect in the Zhijin area. a) All tower karst hills with a skewed distribution. b) All cockpit karst hills with a skewed distribution.	87
Figure 5-30. The distribution of hill aspect in the Weining area. a) All tower karst hills with a skewed distribution. b) All cockpit karst hills with a skewed distribution.	87
Figure 5-31. The distribution of hill curvature in the Zhijin area. a) All tower karst hills with a somewhat normal distribution. b) All cockpit karst hills with a somewhat normal distribution.....	88
Figure 5-32. The distribution of hill curvature in the Weining area. a) All tower karst hills with a somewhat normal distribution. b) All cockpit karst hills with a somewhat normal distribution.....	88
Figure 5-33. The distribution of hill circularity ratio in the Zhijin area. a) All tower karst hills with a somewhat normal distribution. b) All cockpit karst hills with a somewhat normal distribution.....	89
Figure 5-34. The distribution of hill circularity ratio in the Weining area. a) All tower karst hills with a somewhat normal distribution. b) All cockpit karst hills with a somewhat normal distribution.	89
Figure 5-35. The distribution of hill area ratio in the Zhijin area. a) All tower karst hills	

	with a somewhat normal distribution. b) All cockpit karst hills with a somewhat normal distribution.....	90
Figure 5-36.	The distribution of hill area ratio in the Weining area. a) All tower karst hills with a somewhat normal distribution. b) All cockpit karst hills with a somewhat normal distribution.....	90
Figure 5-37.	The distribution of hill <i>TRI</i> in the Zhijin area. a) All tower karst hills with a somewhat normal distribution. b) All cockpit karst hills with a somewhat normal distribution.....	91
Figure 5-38.	The distribution of hill <i>TRI</i> in the Weining area. a) All tower karst hills with a somewhat normal distribution. b) All cockpit karst hills with a somewhat normal distribution.....	91
Figure 5-39.	The distribution of hill <i>TSI</i> in the Zhijin area. a) All tower karst hills with a skewed distribution. b) Tower karst hills except large outliers. c) All cockpit karst hills with a skewed distribution. e) Cockpit karst hills except large outliers.....	92
Figure 5-40.	The distribution of hill <i>TSI</i> in the Weining area. a) All tower karst hills with a somewhat normal distribution. b) All cockpit karst hills with a somewhat normal distribution.....	93
Figure 5-41.	The distribution of hill <i>HI</i> in the Zhijin area. a) All tower karst hills with a skewed distribution. b) Tower karst hills except large outliers. c) All cockpit karst hills with a somewhat skewed distribution.	94
Figure 5-42.	The distribution of hill <i>HI</i> in the Weining area. a) All tower karst hills with a somewhat normal distribution. b) All cockpit karst hills with a somewhat normal distribution.....	94
Figure 5-43.	Box plots of morphometric parameters for the tower and cockpit karst hills in the Zhijin and Weining areas: a) area; b) perimeter; and c) long-axis length. The difference among the tower and cockpit karst hills is significant based on the <i>t</i> -test ($p < 0.05$). T_Z: tower karst hills in the Zhijin area; C_Z: cockpit karst hills in the Zhijin area; T_W: tower karst hills in the Weining area; C_W: cockpit karst hills in the Weining area.	95
Figure 5-44.	Box plots of morphometric parameters for the tower and cockpit karst hills in the Zhijin and Weining areas: a) relief and b) relative relief. The difference between the tower and cockpit karst hills is significant according to the <i>t</i> -test ($p < 0.05$). T_Z: tower karst hills in the Zhijin area;	

	C_Z: cockpit karst hills in the Zhijin area; T_W: tower karst hills in the Weining area; C_W: cockpit karst hills in the Weining area.	96
Figure 5-45.	Box plots of slope for the tower and cockpit karst hills in the Zhijin and Weining areas: a) mean; b) maximum; and c) <i>SD</i> . The difference among the tower and cockpit karst hills is Significant based on the <i>t</i> -test ($p < 0.05$). T_Z: tower karst hills in the Zhijin area; C_Z: cockpit karst hills in the Zhijin area; T_W: tower karst hills in the Weining area; C_W: cockpit karst hills in the Weining area.	97
Figure 5-46.	Box plots of curvature for the tower and cockpit karst hills in the Zhijin and Weining areas: a) mean; b) maximum; c) and <i>SD</i> . The difference between the tower and cockpit karst hills is significant based on the <i>t</i> -test ($p < 0.05$). T_Z: tower karst hills in the Zhijin area; C_Z: cockpit karst hills in the Zhijin area; T_W: tower karst hills in the Weining area; C_W: cockpit karst hills in the Weining area.	98
Figure 5-47.	Box plots of <i>HI</i> and <i>TSI</i> for the tower and cockpit karst hills in the Zhijin and Weining areas: a) <i>HI</i> and b) <i>TSI</i> . The difference between the tower and cockpit karst hills is significant based on the <i>t</i> -test ($p < 0.05$). T_Z: tower karst hills in the Zhijin area; C_Z: cockpit karst hills in the Zhijin area; T_W: tower karst hills in the Weining area; C_W: cockpit karst hills in the Weining area.....	98
Figure 5-48.	The complexity parameters. a) Box plots of circularity ratio for the tower and cockpit karst hills in the Zhijin and Weining areas. T_Z: tower karst hills in the Zhijin area; C_Z: cockpit karst hills in the Zhijin area; T_W: tower karst hills in the Weining area; C_W: cockpit karst hills in the Weining area. b) The correlation between the rank of the cockpit karst hills and the hill area in the Weining area ($R^2 = 0.43$).	99
Figure 5-49.	Box plots of the terrain ruggedness index and area ratio for the tower and cockpit karst hills in the Zhijin and Weining areas. a) Mean; b) Maximum; c) <i>SD</i> of <i>TRI</i> ; and d) area ratio. T_Z: tower karst hills in the Zhijin area; C_Z: cockpit karst hills in the Zhijin area; T_W: tower karst hills in the Weining area; C_W: cockpit karst hills in the Weining area.	100
Figure 5-50.	Distribution of sinkholes and faults: a) sinkhole frequency with the distance to the nearest fault in the Zhijin area. Linear correlation assigned: $R^2 =$	

0.88; b) sinkhole area percentage with the distance to the nearest fault in the Zhijin area. Linear correlation assigned: $R^2 = 0.89$; c) sinkhole frequency with the distance to the nearest fault in the Weining area. Linear correlation assigned: $R^2 = 0.35$; b) sinkhole area percentage with the distance to the nearest fault in the Weining area. Linear correlation assigned: $R^2 = 0.65$	102
Figure 5-51. Orientation frequency distribution of the sinkholes and the faults in: a) the Zhijin area; b) the Weining area.	102
Figure 6-1. Land-use map of the Zhijin area. AL: arable land; BL: bare land; CL: construction land; FL: forest land; GL: grass land; ML: mining land; OP: orchard and perennial plantation; PL: paddy land; SL: shrub land; TF: tidal flat; WA: water area.	105
Figure 6-2. Land-use map of the Weining area. Codes in the legend are the same as in Fig. 6-1.	106
Figure 6-3. Area percentage for each land-use type in the Zhijin area.....	107
Figure 6-4. Area percentage for each land-use type in the Weining area.....	107
Figure 6-5. Land-use map of the Mawo basin in 2009. AL: arable land; BL: bare land; CL: construction land; FL: forest land; GL: grass land; ML: mining land; OP: orchard and perennial plantation; SL: shrub land; WA: water area.	108
Figure 6-6. Area percentage for each land-use class in the Mawo basin.....	109
Figure 6-7. Area percentages of land-use types in the Zhijin area for different landform types: a) sinkhole; b) tower karst hill; c) cockpit karst hill; d) depression.	110
Figure 6-8. Area percentages of land-use types in the Weining area for different landform types: a) sinkhole; b) tower karst hill; c) cockpit karst hill; d) depression.....	110
Figure 6-9. The areal change of land-use type.....	111
Figure 6-10. Land-use maps for different periods: a) 1977; b) 2002; c) 2010.....	112
Figure 7-1. Spatial distribution of the calculated values of a) <i>K</i> -factor; b) <i>LS</i> -factor; c) <i>C</i> -factor; d) <i>P</i> -factor.....	114
Figure 7-2. The sedimentation records based on Xie et al. (2010): a) location and number of soil profile; b) sediment thickness from 1980.....	115
Figure 7-3. The field photographs of the Mawo basin: a) overview; b) exposed tree roots	

after soil erosion	115
Figure 7-4. Spatial distribution of the mean annual soil loss estimated by the RUSLE model.....	116
Figure 7-5. Box plots of erosion rates for the three major landform types in the Mawo basin. The difference among the landform types is significant based on the <i>t</i> -test ($p < 0.05$).	119
Figure 7-6. Relationships between the annual soil loss and each of the model factors except the <i>R</i> -factor. The average and standard deviation of values in each class are shown. a) slope; b) elevation; c) <i>C</i> -factor; d) <i>P</i> -factor; e) <i>K</i> -factor; f) <i>L</i> -factor.	122
Figure 7-7. Sensitivity graph of the RUSLE factors (except for <i>R</i> -factor) to grid size	123
Figure 7-8. Simulated values of the <i>LS</i> -factor and soil loss at different cell sizes: 1) mean <i>LS</i> -factor calculated with the methods adopted in the present study; 2) annual soil loss based on factors calculated by methods adopted in this study; and 3) mean <i>LS</i> -factor values divided by 4 calculated by the methods suggested by Moore and Burch (1986) and McCool et al. (1987, 1989).	124

LIST OF TABLES

Table 3-1 Annual precipitation data at the Weining weather station	30
Table 3-2 Remote sensing images (Landsat) used for detailed analyses in the Mawo basin within the Weining area.....	30
Table 3-3. Land-use classification scheme	42
Table 4-1. Numbers of 1) true positive (<i>TP</i>); 2) false positive (<i>FP</i>) and 3) false negative (<i>FN</i>) identifications in the Zhijin area for DEMs generated from different resources and the semi-automatic model with or without the thresholds. ...	47
Table 4-2. Numbers of the 1) true positive (<i>TP</i>); 2) false positive (<i>FP</i>) and 3) false negative (<i>FN</i>) identification of M-DEM of the Weining area by the running of semi-automatic model with/without the thresholds	50
Table 4-3. Summary statistics of sinkholes in the Zhijin area delineated using the two approaches	51
Table 4-4. Summary statistics of sinkholes in the Weining area delineated using the two approaches	52
Table 4-5. Confusion matrix of the classification results for the Zhijin area	54
Table 4-6. Classification of cockpit karst hills in the Zhijin area	54
Table 4-7. Summary of morphometric statistics of tower and cockpit karst hills in the Zhijin area	55
Table 4-8. Confusion matrix of the classification results for the Weining area	56
Table 4-9. Classification of cockpit karst hills in the Weining area	57
Table 4-10. Summary of morphometric statistics of tower and cockpit karst hills in the Weining area	58
Table 7-1. Classes of annual soil erosion rate	116
Table 7-2. RUSLE related values according to land-use type.....	118
Table 7-3. Area and soil loss amount for each land-use type	118

CHAPTER 1 INTRODUCTION

Karst is a specific type of landscape, developed on soluble carbonate rocks such as limestone, marble, and gypsum. In karst areas, dissolution of bedrock by water is the dominant geomorphic process, and therefore caves and extensive underground water systems are developed. Karst areas account for almost 20% of the continents and more than a quarter of the world's population lives there (Ford and Williams, 2007; De Waele et al., 2009). Abundant resources of fresh ground water often support people's life in karst areas.

However, there are several environmental problems related to karst landscape, such as subsurface erosion (piping); collapse of sinkholes, rocky desertification, heavy metal pollution, drought, and flooding. These environmental issues often affect human activities and subsistence. One important background of these problems is topographic characteristics of karst areas. To understand such characteristics, karst geomorphology has been developed to discuss the nature, genesis, controls and evolution of karst systems (Sweeting, 1973; Yuan et al., 1991; Gunn, 2004; De Waele et al., 2009; Huang et al., 2013). Karst geomorphological surveys have been applied to evaluate geomorphological impacts on the environment (Veni, 1999), assess land disturbance (Van Beynen and Townsend, 2005; De Waele, 2009) and analyze the risk of geological hazard (Parise et al., 2015). Modern techniques and modelling such as the application of DEMs (Digital Elevation Models) using GIS (Geographical Information Systems) have brought new insight into geomorphic processes and resulting landforms in karst areas (De Waele, 2009). This thesis aims to conduct geomorphological and geoenvironmental research to understand the environment of a typical karst area and the characteristics of environmental problems related to both natural and human factors. Previous research indicated that study of landforms supports the assessment of soil erosion and inappropriate land-use (Van Remortel et al., 2004; Saadat et al., 2008). This thesis follows the concept.

1.1. Review of studies on landforms in karst areas

Traditionally karst areas are identified based on geological maps to separate them from non-karst areas. Classic studies classified karst landforms by visual interpretation of topographic maps and aerial photographs, as well as field observations (Veni, 2002; Ford and Williams, 2007; Liang and Xu, 2014; Zhu et al., 2013). Some field-based studies have extensively investigated karst landforms to discuss their formation mechanisms (Tharp, 1999; Salvati and Sasowsky, 2002), establish terminology and landform classification (White, 1988; Gunn, 2004; Waltham et al., 2007; Gutiérrez et al., 2008), interrelate landforms with anthropogenic factors (Delle Rose et al., 2004; Gutiérrez et al., 2014), and assess hazard potential (Galve et al., 2009; Taheri et al., 2015; Van Schoor, 2002).

Geomorphological studies on karst areas often focus on the classification of landforms at various scales (Waltham and Fookes, 2003). Based on the spatial scale, Lowe and Waltham (1995) classified karst landscape into four groups (Table 1-1). Ford and Williams (1989) classified karst landscape into five classes based on morphogenetic aspects: glaciokarst, fluviokarst, doline karst, cone karst and tower karst.

Table 1-1. Simple classification of karst landforms according to scale (Lowe and Waltham, 1995)

Scale boundary	Example
Nano features (< 1 mm)	Nanokarren
Micro features (< 1 m)	Karren runnels (Bögli, 1960), subsoil rundkarren, pinnacle karst (Waltham, 1995)
Meso features (< 10 m)	Karren
Macro features (≥ 10 m)	Pojie, sinkhole, dry valleys, tower and cockpit karst

Traditionally landform classification was performed manually (Hammond, 1954; Evans, 2012), which is subjective, time-consuming, minimally reproducible, and unsuitable for studying large areas (Doctor and Young, 2013). With the advances of geospatial technologies such as GIS and increasing availability of spatial data including remotely-sensed images and

DEMs, more quantitative studies have been conducted in the field of karst geomorphology (Siart et al., 2009; Youssef et al., 2012; Elmahdy and Mostafa, 2013). Siart et al. (2009) mapped the karst features of central Crete in the Mediterranean Sea by combining DEMs, remote sensing images and GIS. The result had high accuracy and was utilized for geomorphological discussion. Huang et al. (2013) separate tower and cockpit karst areas using a semi-automatic approach applied to contour line data. Some other studies focused on the supervised classification of karst landforms using existing landform maps or aerial photographs as training samples (Hengl and Rossiter, 2003; Ballantine et al., 2005; Liang and Xu, 2006; 2014; Saadat et al., 2008). Liang and Xu (2014) discriminated the tower, cockpit and non-karst landforms in southern China using training samples at different spatial scale. In addition, DEMs facilitated morphometric analysis of karst landforms (Lyew-Ayee et al., 2007; Bruno et al., 2008; Basso et al., 2013). Earlier examples based on analogue topographic maps include La Valle (1968), Williams (1972) and Drake and Ford (1972), which showed the importance of morphometric analyses in understanding karst landscape. They also demonstrated the idea that geomorphic evolution in different landform assemblages reflects the interactions of tectonics, climate and earth surface processes.

Furthermore, hazards and environmental problems related to karst landforms have long been recognized worldwide (Ford, 1993; Williams, 1993; Parise and Pascali, 2003; De Waele et al., 2011). Sinkholes, one of the macro-scale landform types, are relevant because land collapsing to form sinkholes is a serious geological hazard in the karst environment (Yilmaz, 2007). Proper managements of karst resources and environment are still difficult (De Waele et al., 2011) because of the insufficient understanding of karst landforms. As a reflection of surface processes, different karst landforms possess distinct morphometric characteristics (Williams, 1972). Therefore, comprehensive landform classification maps facilitate the implement of proper hazards control and migration measures in karst areas.

However, several problems exist in the previous landform classification studies for karst areas including those based on geomorphometry. Firstly, landforms were mainly categorized based on lithology without considering morphometric differences among different landscape (Veni, 2002; Ford and Williams, 2007; Zhu et al., 2013; Liang and Xu, 2014). Secondly, studies based on supervised classification have limitations such as too time-consuming (Liang and Xu, 2014); limited size of the study area (MacMillan et al., 2000); low classification accuracy (Prima et al., 2006); and difficulty in obtaining a large number of accurate training samples (Hengl and Rossiter, 2003). Thirdly, previous landform classification studies tend to focus on either detailed landform elements (Drăguț and Blaschke, 2006) or rather generalized landforms (Saadat et al., 2008). The detailed landforms include segmented slopes such as head, side, and nose slopes, which may be too detailed for macro-scale land planning and generalized environmental assessment. On the other hand, the generalized landform types

such as mountains and valleys may be too coarse for meaningful geomorphological understanding and practical applications (MacMillan and Shary, 2009). In karst areas, geomorphic units of intermediate dimension such as sinkholes, poljies and karst hills (Siart et al., 2009) are important, but methodology of classification of such units has not been well established.

1.2. Review of studies on soil erosion in karst areas

Soil erosion is one of the most serious environmental problems in the world (Siart et al., 2009). According to Pimentel et al. (1995), nearly one-third of the world's arable land were affected by soil erosion at an erosion rate of more than 100 tons ha⁻¹ yr⁻¹. Because of increasing population and food needs, the conservation of arable land has become an urgent task. Therefore, accurate estimation of soil erosion and evaluation of its risk are needed (Boardman and Poesen, 2006). Many models such as USLE (Universal Soil Loss Equation) (Wischmeier and Smith, 1965), WEPP (Water Erosion Prediction Project) (Nearing et al., 1989a), EUROSEM (European Soil Erosion Model) (Morgan et al., 1998) and SEMMED (Soil Erosion Model for Mediterranean Regions) (De Jong and Riezebos, 1997) were developed to quantify soil erosion and associated sediment supply. In practice, the Revised Universal Soil Loss Equation (RUSLE) has probably been most extensively used (Renard et al., 1997). The popularity of the RUSLE owes to inherent property of parsimonious (available/accessible) data in the USLE and more reliable results (Morgan, 2009). In addition, it has compatibility with remote sensing (RS) and GIS.

However, it is difficult to apply soil erosion models such as the RUSLE and USLE to a karst area because of the heterogeneous nature of karst infiltration and subsurface drainage. Several soil erosion studies dealt with karst areas though. For example, Feng et al. (2016) used the RUSLE to estimate the annual soil erosion rates on hillslopes, and compared them with ¹³⁷Cs budget in depressions at two karst basins in northwest Guangxi, southwestern China. Runoff plots data were used to calculate the slope length factor (*L*) of the RUSLE model. The resulted *L* values were calibrated by adjusting the accumulated area threshold. The modeling results agreed well with the ¹³⁷Cs records. The study suggested that attention should be given to the *L*-factor when applying the RUSLE to karst hillslopes due to the discontinuous nature of runoff and significant underground seepage during storm events. Xu et al. (2008b) also evaluated soil loss and spatial distribution in a karst watershed of Guizhou Province, China, for conservation planning by integrating the RUSLE with GIS. A remote sensing image, digitized topographic maps, soil maps and precipitation data were used, and the results show high accuracy. These studies indicate that understanding erosion processes is

crucial for managing karst areas.

Febles-González et al. (2012) applied the Morgan Morgan Finney (MMF) empirical erosion model to La Habana Province, Cuba for soil erosion estimation, based mainly on the morphometric analysis of karst dolines. The results showed the area had suffered serious soil losses with an unsustainable condition of soil resources. They also discussed the effects of extreme rainfall events associated with climate change in recent years. Demirci and Karaburun (2012) also predicted soil erosion risk in a karst watershed in the western part of Istanbul, Turkey, using the RUSLE model and GIS, soil survey results, topographic maps and satellite images. The results indicated that half of the study area was under serious soil erosion risk.

Turnage et al. (1997) studied the soil erosional and depositional rates in three sinkholes with different land-use types of crop, grass and forest in eastern Tennessee, USA. Three methods were used: ^{137}Cs redistribution, buried surface soil horizons (Ab horizon) and the RUSLE. They discussed differences among the erosion estimation from the three methods, and revealed that land-use and landforms particularly the topography of dolines played important roles in determining both erosion and deposition rates.

1.3. Review of studies on land-use in karst areas

The land-use/cover is an important anthropogenic factor influencing earth surface processes (Lambin et al., 2003). The shortage of land-use resources and land degradation are serious environmental problems in karst areas (Wang et al., 2004), which threaten agriculture, natural environment and resources, engineering structures, and human sustainability (Rahman et al., 2009; de Vente et al., 2013; Gutiérrez et al., 2014; Witze, 2014). Therefore, studies on land-use in karst areas have been made worldwide. Guizhou Province in southern China is a typical area for such studies. Xiao and Weng (2007) examined the land-use changes in a karst area of Guizhou Province, from 1991 to 2001 based on satellite images. Land surface temperature (*LST*) and normalized difference vegetation index (*NDVI*) were computed based on land-use types. The results indicated that the change in *LST* was associated with changes in construction materials and vegetation abundance, and that reforestation helped maintain the karst ecosystem. Li et al. (2009) investigated rocky desertification in Guizhou Province in relation to land-use and rock types. The results showed that land-use types strongly affect desertification. Peng and Wang (2012) also analyze soil loss and surface runoff related to land-use types and rainfall events in a karst hill of Guizhou Province. They demonstrated that land-use and vegetation coverage affected the runoff and soil loss. Particularly soil erosion risk is high on over-grazing pastureland. Without vegetation, the soil loss of pastureland was five times as large as the annual soil tolerance.

Jiang et al. (2008) studied the impact of land-use change on the quality of groundwater in a karst watershed in Yunan Province, China, during 1982–2004. After the enlargement of the cultivated land, pH and the concentrations of NH_4^+ , SO_4^{4-} , NO_3^- , NO_2^- and Cl^- ions in ground water significantly increased, whereas Ca^{2+} and HCO_3^- decreased. Kelly et al. (2009) discussed the impacts of agricultural land-use on bacterial water quality in a karst ground water aquifer in the Appalachian Region, USA. They concluded that agriculture significantly affected the bacterial densities in the aquifer, and suggested that new management practices for protecting the karst groundwater resources were needed.

1.4. Objectives of this thesis

Based on the literature review above, this thesis aims to solve two major problems with geomorphological and geoenvironmental research in karst areas: 1) establish a method to better classify and understand karst landforms and its morphometric characteristics; and 2) connect geomorphological research with major environmental issues related to soil erosion and land-use. For these purposes, two areas in Guizhou Province, China, were selected as study areas. Guizhou Province consists of the catchments of the Yangtze River and the Pearl River, which are the longest river in Asia and the second largest river in China in terms of volume, respectively. The province is located in the center of the Southeast Asian Karst Area with diverse types of karst landforms. It is one of two representatives of cockpit karst landscape in the world, along with Jamaica (Lyew-Ayee et al., 2007). In addition, Guizhou Province has other types of karst landforms (Zhang, 1980), much more than in Jamaica. At the same time, the karst areas in Guizhou Province have been suffering from severe soil erosion and rocky desertification associated with inappropriate land-use. These problems are due to a high population pressure (219 people/km² in 2003), rainy subtropical monsoon climate with a mean annual precipitation of over 1,000 mm (Xu et al., 2008b), and mountainous topography with over-logging and steep-slope farming. According to Wan (2003), the area of land subject to soil erosion in Guizhou Province expanded from 2.5×10^4 km² in the 1950s to nearly 8.8×10^4 km² in the 2000s; the latter is about the half of the province area. The loss of soil directly leads to exposure of bedrock called rocky desertification, which covered an area of 3.5×10^4 km², over 20% of Guizhou Province (Wang et al., 2004). Therefore, the province is suitable for analyzing various karst landforms and their relationships with soil erosion and land-use problems. Indeed, as reviewed in the previous sections, a relatively large number of studies on karst landforms and environmental problems have been conducted in Guizhou Province.

This study employs a semi-automatic landform classification approach based on DEMs

from multiple sources, which had rarely been conducted in the previous studies. The morphometric characteristics of different landform types identified from the semi-automatic approach were also analyzed quantitatively. The results of the landform classification and morphometric analysis were verified in the field. Land-use maps for the study areas were constructed using remote sensing data and GIS. The relationship of the land-use with the landform types and characteristics were investigated. In addition, erosion rates for a selected closed basin were evaluated using the RUSLE (Revised Universal Soil Loss Equation) model. The results were discussed in relation to land-use and landform types.

CHAPTER 2 STUDY AREAS

The two study areas with typical karst landscape were selected from Guizhou Province, southwest China. The karst areas in Guizhou Province are located on the extensive Yunnan–Guizhou Plateau. In the province carbonate rocks covers ca. 130,000 km², which is 73.6 % of the total area of Guizhou Province. The total thickness of the carbonate rocks in the province reaches 1100 m. The ages of these carbonate rocks range from the Proterozoic to the Cenozoic. The carbonate rocks were uplifted by neotectonics to be the basement of the karst landforms. Because of differences in the intensity of tectonic uplift, the Guizhou Plateau has three general surface levels with different altitudinal ranges. The surfaces of the highest level are located between 2200–2900 m in elevation, forming high mountains. The middle level surfaces are at 1000–1500 m in elevation with hilly landscape. The lowest level surfaces are at 500–800 m with low-relief hilly landscape. In this work, Weining County and Zhijin County were selected for detailed studies, which correspond to the highest and middle surface levels of the Guizhou Plateau, respectively.

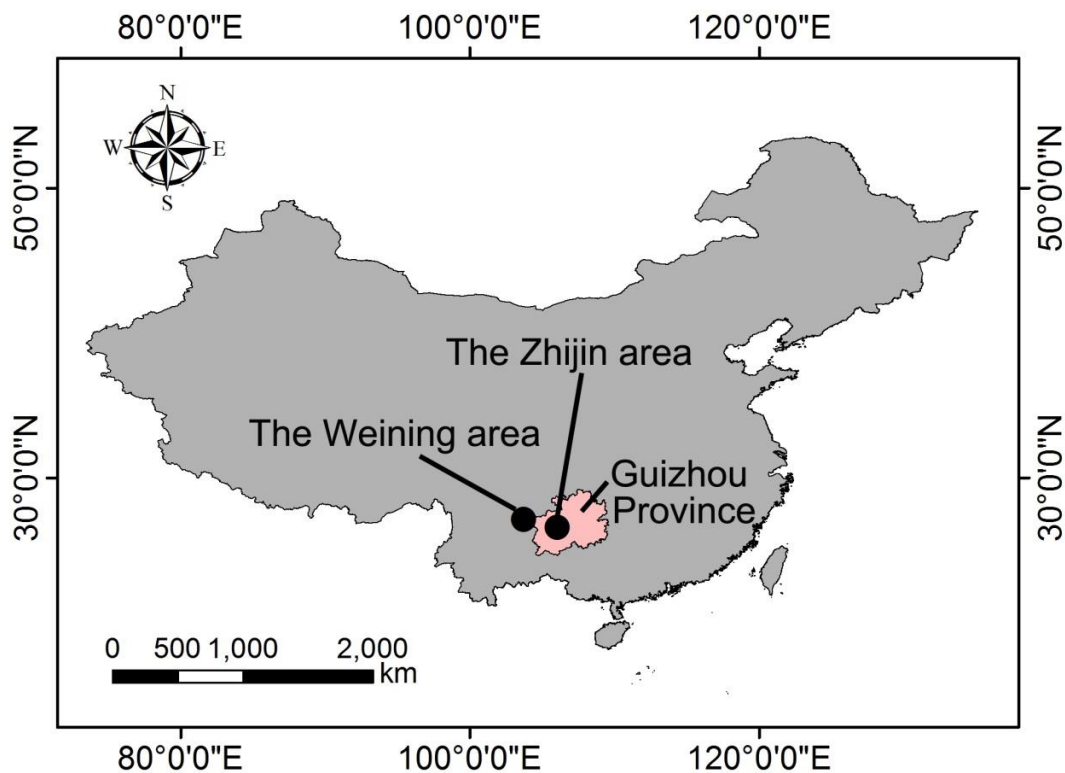


Figure 2-1. Location of the study areas

2.1. Zhijing area

The Zhijing area (E106°–106°7', N26°32'–26°40') is located the middle part of the Guizhou Plateau, southeast Zhijing County of Guizhou Province (Fig. 2-1). Zhijing County has numerous karst caves some of which are known for tourist attraction. The study area covers an area of 171.47 km², and the elevation ranges from 944 to 1715 m (Fig. 2-2). The climate is subtropical humid monsoon, with a mean annual sunshine time of 1172 h, a mean annual temperature of 14.1°C and a mean annual precipitation of 1436 mm.

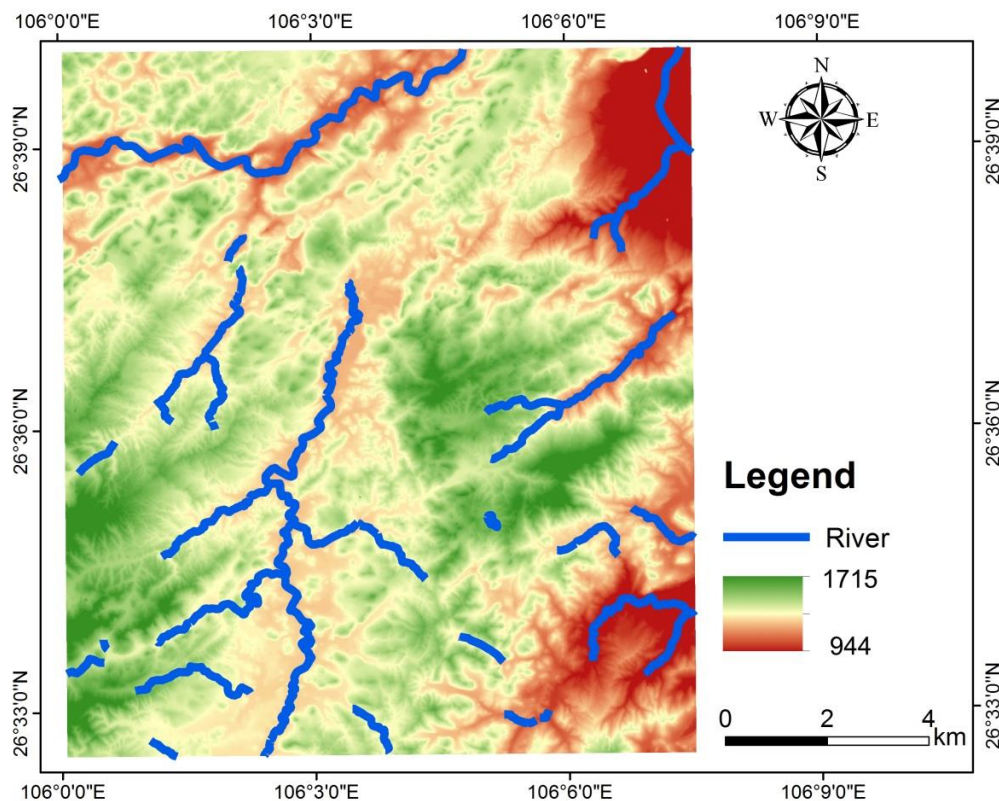


Figure 2-2. Spatial distribution of elevation in the Zhijing area. The DEM used has a cell size of 3 m and was generated from topographic maps.

The karst landforms in the Zhijing area correspond well to the area of carbonate geology, which covers 103.69 km² and 60.12% of the total area according to GIS analysis of the geology data from the Guizhou Geological Survey (GGS). The dominant rock types among the carbonate geology are limestones and dolostones of the Triassic, Permian, Carboniferous and Cambrian. The geology in non-karst areas consists of Permian basalt, shale silicalite and mudstone. Faults are well-developed with a dominant orientation of NE–SW (Fig. 2-3).

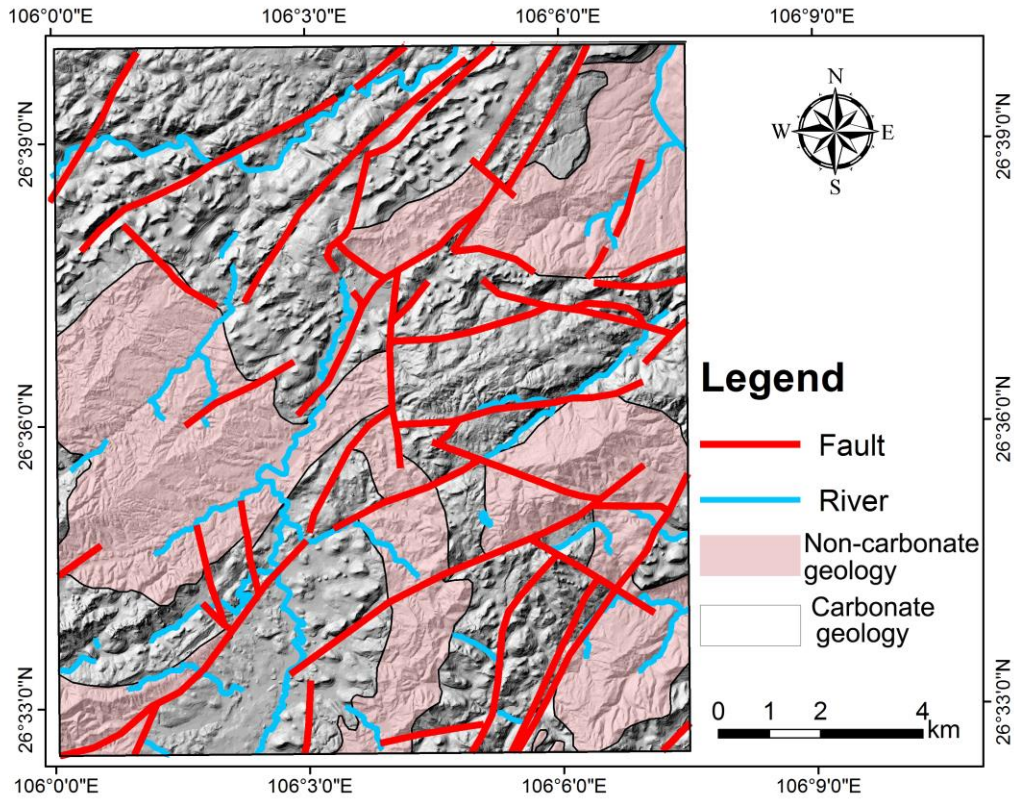


Figure 2-3. Geology of the Zhijin area based on the 1:200,000 geological map (GGS, 1976). The hillshades are from a 3-m DEM generated from topographic maps.

2.2. Weining area

The Weining area (E103°49'–103°56', N27°5'–27°12') is located in the western part of the Guizhou Plateau, northeast Weining County, Guizhou Province (Fig. 2-1). The area covers a total surface area of 171.71 km². The elevation ranges from 1800 to 2835 m (Fig. 2-4). The climate is subtropical humid monsoon, with a mean annual sunshine time of 1800 h, a mean annual temperature of 17°C and a mean annual precipitation of 850 mm.

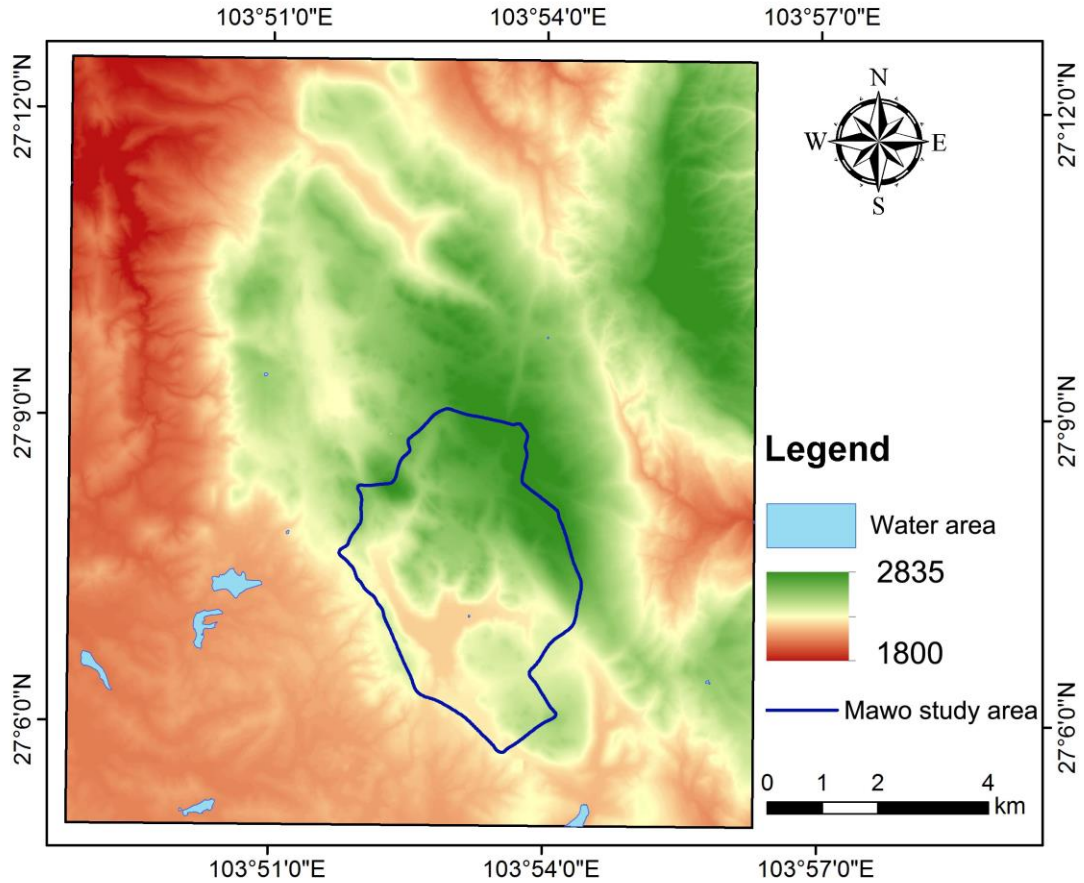


Figure 2-4. Spatial distribution of elevation in the Weining area. The DEM used has a cell size of 3 m and was generated from topographic maps.

Carbonate geology covers 154.12 km² of the Weining area, 89.75% of the total area (GGS, 1976). The dominant rocks are limestones and dolostones of the Permian, Carboniferous and Devonian. The geology in non-karst areas consists of Carboniferous loose rock of basalt, shale silicalite and mudstone. Faults are developed mainly along an NW–SE direction with a few of them along NE–SW (Fig. 2-5).

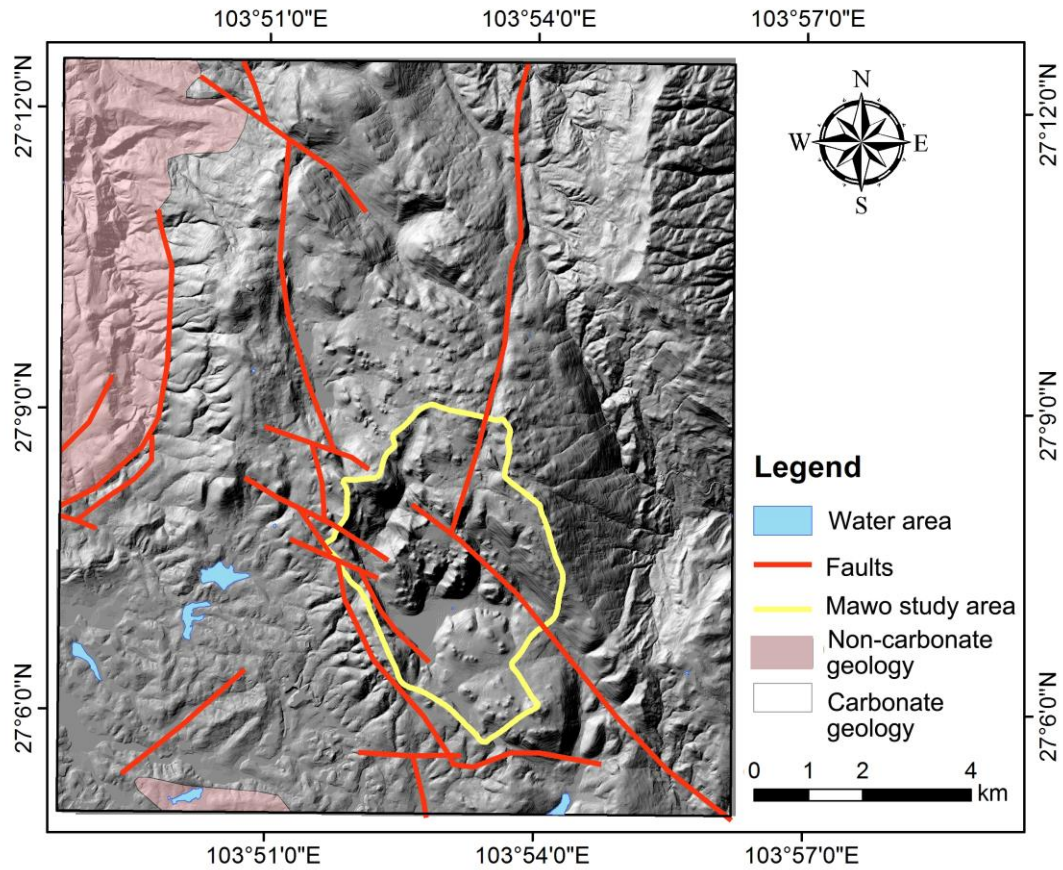


Figure 2-5. Geology of the Weining area based on the 1:200,000 geological map (GGS, 1976). The hillshades are from a 3-m DEM generated from topographic maps.

A part of the Weining area, the Mawo basin was selected for conducting detailed research on soil erosion and rocky desertification (Fig. 2-4). The basin suffers from erosion and desertification under recent agricultural development, and the closed basin is suitable for estimate soil erosion from deposited sediment.

CHAPTER 3 DATA AND METHODS

3.1. Geographical data including DEMs

Several geographical datasets were used to support landform classification, morphometric analysis, soil erosion evaluation, and land-use analysis. The data for the Zhijin area include aerial photos with 2.5 m resolution captured during the winter of 2005, 1:200,000 hydrogeological maps from the Guizhou Geological Survey, 1:10,000 topographic maps from the Guizhou Geological Survey, the ASTER GDEM with a spatial resolution of 30 m (<http://gdem.ersdac.jspacesystems.or.jp/>), SRTM-DEM (<http://srtm.csi.cgiar.org>) with spatial resolutions of 30 and 90 m, and an inventory of ground control points based on field work. The original 1 m DEM was obtained by the Guizhou Geological Survey.

To examine the effects of DEM cell size on the result of geomorphological analyses, DEMs of 3, 5, 10, 25, 30, 50, 60, 75 and 90 m grid sizes were resampled from the original 1-m DEM by reading elevation values with a certain interval, and were used in the ArcGIS environment. For the same reason, the 30-m ASTER GDEM was resampled to 3, 60 and 90 m, and the 30-m SRTM were resampled to 3 and 60 m. For producing the 60 and 90 m DEMs, simple contraction was performed by reading data with a certain interval. For producing the 3 m DEM, bilinear interpolation was applied using ArcGIS. Analyses using DEMs with different resolutions were performed only in the Zhijin area, not in the Weining area, because the former has more karst landforms with various types; for example, the number of sinkholes in the Zhijin area is much larger than that in the Weining area (see a later section for concrete numbers).

The data obtained during the extensive field work in July 2010 by the author and Professor Pan Wu, College of Resources and Environmental Engineering, Guizhou University, China, were also utilized mainly for verification of results obtained from the DEMs and remote sensing images. All data were projected to the UTM coordinate system.

The data for the Weining area include aerial photos with 2.5 m resolution captured during the winter of 2005, 1:200,000 hydrogeological maps from the Guizhou Geological Survey, and 1:10,000 topographic maps from the Guizhou Geological Survey. The aerial photos were used to produce a land-use map. A DEM with 1-m resolution is also generated from the topographic maps and then were resampled to 3-m cell size. The data obtained during the extensive field work in July 2010 by the author and Professor Pan Wu were also utilized mainly for verification of results from the DEMs and remote sensing data.

Four other datasets were used for the estimation of soil erosion rate and evaluation of rocky desertification in the Mawo basin within the Weining area: 1) meteorological data from

the Weining weather station (E104°17', N26°52') (Table 3-1), 2) land-use map of 2009 at a 1:10,000 scale, based on satellite imagery from the AVNIR-2 sensor of ALOS, 3) a soil map of 1:650,000 scale (GGS), and 4) Landsat TM images obtained during the summer from 1988 to 2010 (Path 129 and Row 41; Table 3-2). All the images were rectified and georeferenced into the UTM coordinate system using ground control points obtained from the topographic maps, and resampled into raster at 30 m resolution. The Landsat images were used for computing *NDVI*. Field data were also collected in February and May 2009, including 14 topsoil samples to measure soil properties, particle size and organic matter content. The DEM was also used to compute slope and slope length.

Table 3-1 Annual precipitation data at the Weining weather station

Record no.	Year	Annual precipitation (mm)
1	1989	850.0
2	2009	645.5
3	2010	801.5
4	2011	695.0
5	2012	1000.1

Table 3-2 Remote sensing images (Landsat) used for detailed analyses in the Mawo basin within the Weining area

Image no.	Acquisition date
1	1 May. 1988
2	24 Aug. 1992
3	10 Jul. 1996
4	23 May. 2004
5	4 Aug. 2005
6	19 May. 2006
7	31 Aug. 2009
8	13 May. 2010

3.2. Landform types at macro-scale

This study classified karst landforms into four major types as macro-scale features. Each type is explained below.

3.2.1. Karst sinkholes

Sinkholes are closed depressions common in karst terrain. These depressions are also termed as dolines by European geomorphologists (Sauro, 2003), but are generally labelled as sinkholes by engineers (Waltham and Fookes, 2003). Sinkholes in karst areas are formed when underground drainage systems develop within carbonate bedrock and reach the ground surface. Therefore, sinkholes are identified as direct conduits to underground aquifers, and are regarded as the diagnostic surface feature of karst terrains (Ford and Williams, 2013).

Sinkholes are extensively distributed in karst areas worldwide and affect engineering structures, agriculture, natural resources and environment, and human sustainability (Gutiérrez et al., 2014; Witze, 2014). As noted in Section 1.1, sinkhole collapsing is one of the most serious geological hazards in the karst environment. The sinkholes in this study are defined as the closed depressions $< 350,000 \text{ m}^2$.

In order to analyze the land-use class in sinkhole area, the sinkhole area were classified into two groups. The first group is the shallow and flat sinkhole. The land-use class of this group was identified within the sinkhole area. The second group is the deep sinkhole. It is difficult to identify the land-use type for these deep sinkholes. This group was excluded in the analysis related to the land-use (Chapters 6 and 7).



Figure 3-1. Sinkhole at the central part of the Zhijin study area, Guizhou Province

3.2.2. Large karst depression

Depressions larger than sinkholes with relatively flat floors are also found in the study area. Large karst depressions are associated with water input and output (Ford and Williams, 2007). A large karst depression is also called polje. According to Gams (1978), a polje is: 1) a plain or terraced floor in bedrock or unconsolidated sediments, 2) a closed depression with a steeply rising marginal slope, and 3) associated with karstic surface drainage.

The size difference between a sinkhole and a polje was defined differently among previous studies. Gams (1978) suggested that the plain in a polje should be wider than 400 m. However, Cvijic (1893) took 1 km as the width limit. Indeed, the area of the flat floor in a polje ranges widely up to $> 470 \text{ km}^2$, with a majority of $< 10 \text{ km}^2$ (Ford and Williams, 2007). Therefore, it is difficult to separate sinkholes from large depressions based on their dimensions.

Considering the above limitation, this paper first identify apparent sinkholes using the DEMs, and then two distinct positive (protruded) landforms, tower karst hills and cockpit karst hills, were identified. The rest of the area, which can be regarded as negative landforms other than sinkholes, was referred to as depressions, although it includes landforms other than typical depressions.



Figure 3-2. Depression in the Weining study area, Guizhou Province

3.2.3. Tower karst

Tower karst refers to isolated carbonate hills rising from alluvial plains (Zeng, 1982; Day and Tang, 2004). It is also known as “fenglin” or “peak-forest” topography. These hills display variety of shapes, such as tall sheer-sided towers, cones and hemispheres. It can be symmetrical or asymmetric in form, influenced by the dip of bedrock and erosional processes. Slope angles and individual profiles of the tower karst are usually irrelevant. The best-known tower karst is that with vertical flanks rising from the alluvial plains, but many tower hills are more truly conical in profile. Especially in China, the tower karst extends to terrains with isolated hills that have very low conical profiles (Waltham, 2008).

Normally, the tower karst is considered as an extreme karst type and restricted to wet tropical regions with significant tectonic uplift histories which have allowed long, uninterrupted development (Waltham and Fookes, 2003). A very famous region for tower karst landforms is the Yangshuo area in Guilin Province, China.



Figure 3-3. Sharply pointed conical tower karst hills at the eastern part of the Zhijin study area, Guizhou Province.

3.2.4. Cockpit karst

In contrast to tower karst, cockpit karst consists of hills in groups rising from a common base (Waltham and Fookes, 2003). It is also called as “fengcong”, “cone karst” and “peak cluster”. The cockpit karst can be defined as conical hills separated by deep closed depression. The depressions between the cockpit karst hills can be stellate dolines and poljes.

In contrast to tower karst, cockpit karst forms a continuous terrain of steep slopes and significant relief. The cockpit karst is considered as a very mature landscape which is restricted to inter-tropical regions, such as Cockpit Country in Jamaica and some areas in Guizhou Province (Waltham, 2008).



Figure 3-4. Cockpit karst hills in the Weining study area, Guizhou Province.

3.3. Semi-automatic method of karst landform classification

As a basic procedure of DEM processing for geomorphological and hydrological analysis, algorithms have been tested for reconditioning raw elevation data to obtain a sink-free (Anderson, 1988; Jenson and Domingue, 1988; Grimaldi et al., 2007). A typical method provides a DEM with closed depressions being filled up to the elevation of a surrounding lowest pixel. It raises a challenge of preserving true natural sinkholes while removing artificial depressions due to intermittent elevation sampling. This study used the most widely used algorithm proposed by Jenson and Domingue (1988), implemented in the ArcHydro Tools 2.0 (Maidment, 2002) as a part of a semi-automatic approach for macro-scale classification of karst landforms. Fig. 3-5 is the flow chart of the proposed semi-automatic approach. It is divided into two major parts. One describes the approach for identifying true sinkholes while excluding artificial sinkholes, by combining field work, visual interpretation of aerial imagery, and basic morphometric analysis (area and ellipticity) using GIS. The other illustrates the approach for discrimination of tower karst and cockpit karst hills.

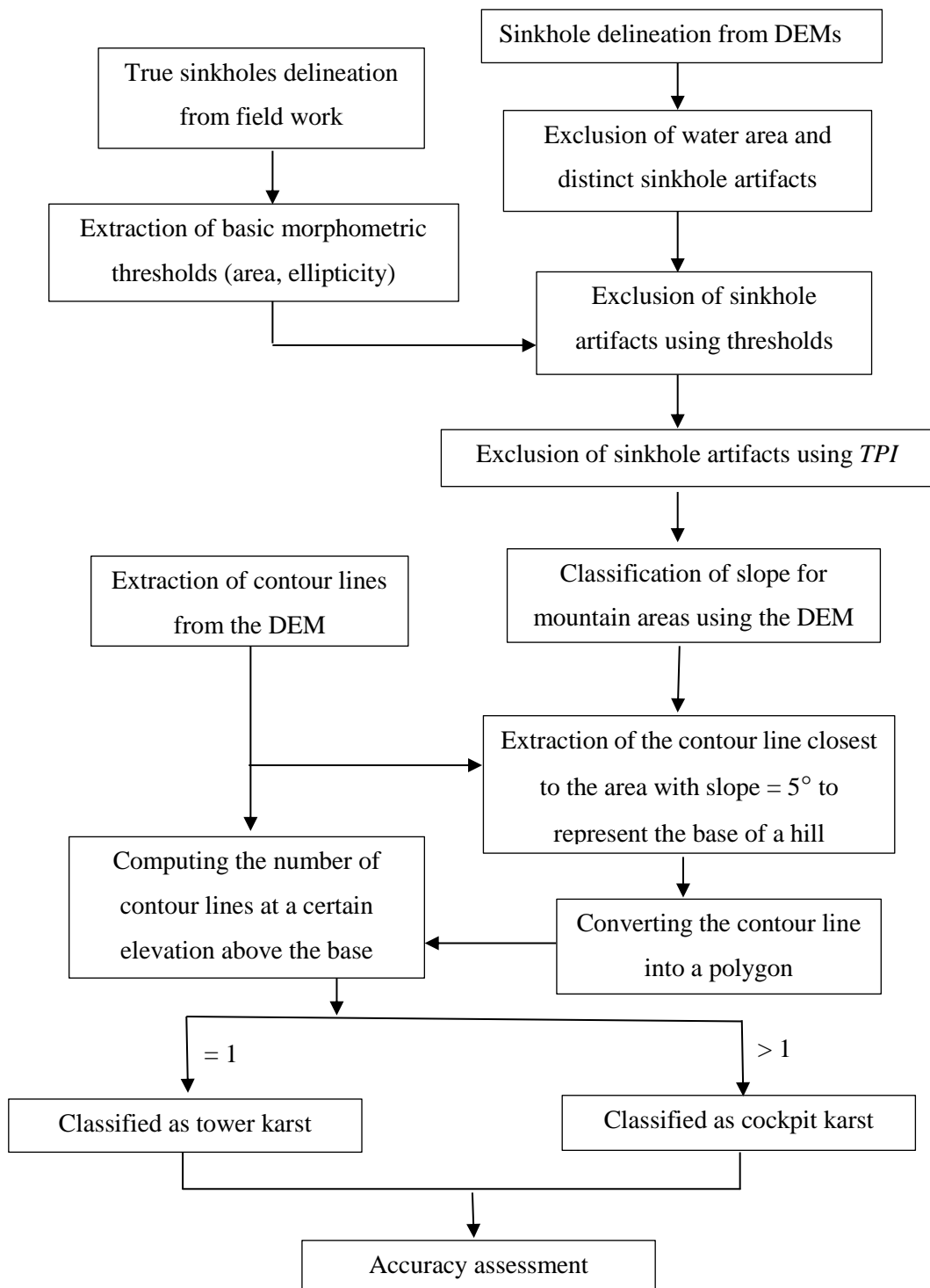


Figure 3-5. Flow chart of the semi-automatic approach for karst landform classification

3.3.1. Sinkhole delineation

As shown in the upper part of Fig. 3-5, the methodology for semi-automatic sinkhole delineation has five steps: 1) identification and digitization of true sinkholes using aerial imagery, integrated with field validation; 2) sinkhole delineation from the DEMs; 3) exclusion of water area and distinct sinkhole artifacts; 4) allocation of general threshold values of sinkhole area, ellipticity (E) and the topographic position index (TPI) for further removing artificial sinkholes; and 5) adaptation of the best DEM with the highest accuracy.

The step 4 of the above procedure is explained below. Manual inspection (step 1) indicated that the sinkholes in the study area have areas from 0.1 to 60 m². Therefore, the value of 60 m² was conservatively set as the area cutoff for true sinkholes. E is the index to evaluate the shape eccentricity of a sinkhole, calculated as:

$$E = \sqrt{1 - \frac{b^2}{a^2}} \quad (3-2)$$

where a and b are the one-half of the major and minor axis lengths of a sinkhole, respectively. The E value ranges from 0 (perfect circle) to 1. Field observation in the Zhijin karst area indicates that the sinkholes there tend to be elliptical and elongated, and that an E value of 0.2 worked as a good threshold for determining true sinkholes.

TPI introduced by Weiss (2001) depicts the difference between elevation at the central point (Z_C) and the average elevation at the surrounding points within a certain radius (r).

$$TPI = z_c - \frac{1}{n_r} \sum_{i \in r} z_i \quad (3-2)$$

where n_r is the number of the raster cells of the predetermined area, and i stands for the i -th cell. As its ability of dividing morphological classes, $TPI < 0$ representing negative topographic position was chosen to identify true sinkholes.

Furthermore, sinkholes detected within 90 m from a major river centerline are classified as artificial sinkholes. Sinkholes in karst landscape were also identified based on their underlying geology. The sinkholes recognized outside the areas of carbonate rocks were assigned as artificial and removed from the dataset.

Based on the result of the manual and automatic approaches, a large number of sinkholes were found in the study area. The accuracy of the approach was assessed by comparing the sinkholes extracted from the remote sensing images and field work with those automatically identified from the DEMs, using the spatial join function of ArcMap. For a quantitative comparison, the numbers of three classes of sinkholes were counted: 1) the number of linked records of the reference map (identified true sinkholes, true positive; T); 2) the number of non-linked records of the reference map (non-identified true sinkholes, false negative; NT); and 3) the number of non-linked records of auto-classified map (artificial sinkholes, false

positive; *AS*). Note that another commonly used class, true negative, was found to be almost null in this case. Accordingly, the accuracy statistic was calculated as:

$$\text{Accuracy} = \frac{T}{T+NT+AS} * 100\% \quad (3-3)$$

3.3.2. Discrimination of tower and cockpit karst hills

For identifying karst hills, the 3-m DEM was adopted for the discrimination of cockpit and tower karst hills, after sinkholes were identified. The methodology for this discrimination is summarized as: 1) identification of typical cockpit and tower karst hills using aerial imagery integrated with field validation; 2) extraction of contour lines from the DEM at 5 m intervals; 3) slope computation using the DEM; 4) contour line selection for delineating the base of a hill area; 5) generation of a hill area polygon using the selected basal contour lines; 6) calculation of the number closed contours lines at a certain elevation above the base of each hill; 7) classification of the cockpit karst (average contour number > 1) and tower karst (number = 1); and 8) accuracy calculation by comparing the maps obtained from steps 1 and 7 (Fig. 3-5).

Step 4 is to find the best contour line which depicts the base of a cockpit or tower karst hill. For this purpose, the slope map was overlaid on the manually produced landform classification map based on aerial photos and field work (step 1). It was found that slope $\geq 5^\circ$ is a proper threshold for separate hill areas from other gentler areas. Therefore, we extracted the contour lines with the smallest distance to the area with slope around 5° .

The objective of step 7 is to calculate the number of the summits per a hill to measure complexity of hill topography. According to the definition differences, a tower karst hill has only one summit, but a cockpit karst has several summits. More complex cockpit karst hill has more summits.

Comparing the manually produced reference landform map and the results of the DEM-based automatic approach yields nine classes that can be used for accuracy calculation: 1) identified true tower karst hills (tower true positive, *TPt*); 2) identified true cockpit karst hills (cockpit true positive, *TPc*); 3) identified true depressions (depression true positive, *TPd*); 4) tower karst hills classified as depressions (non-identified tower karst hill, false negative, *FNt*); 5) cockpit karst hills classified as depressions (non-identified cockpit karst hill, false negative, *FNc*); 6) tower karst hills classified as cockpit karst hills (false positive, *FPtc*); 7) cockpit karst hills classified as tower karst hills (false positive, *FPct*); 8) depressions classified as tower karst hills (false positive, *FPdt*); and 9) depressions classified as cockpit karst hills (false positive, *FPdc*). Note that another commonly used class, true negative, was found to be null in this case. Accordingly, the accuracy statistic was calculated as:

$$Accuracy = \frac{TPt+TPc+TPd}{TPt+TPc+TPd+FNt+FNc+FPtc+FPct+FPdt+FPdc} * 100\% \quad (3-4)$$

3.4. Morphometric properties of sinkholes, cockpit karst hills and tower karst hills

In order to understand the geomorphological characteristics of the landform types, various morphometric parameters were measured. The target landforms are sinkholes, tower karst hills and cockpit karst hills. The rest of the study area (= depression) was not considered because it includes various terrain features not clearly defined, and they cannot be delineated as a single closed unit like a sinkhole or a hill. The morphometric parameters can be grouped into three types based on the spatial direction of measurement: 1) horizontal measures (plan or horizontal direction), 2) vertical measures (vertical direction), and 3) shape measures (both horizontal and vertical directions or 3D shape).

3.4.1. Horizontal measures

1) Area

The area (A) of a sinkhole is defined as the plan area of the exposed sinkhole outline. A of a hill is defined as the area of a hill base polygon, almost corresponding to the area steeper than 5° .

2) Perimeter

The Perimeter (Pe) of a sinkhole is defined as the length of the outline of a sinkhole (Brinkmann et al., 2008). It is generally positively correlated to A , except for crenulated sinkholes, which have a long perimeter even if A is small. P of a hill is defined as the length of the outline of the hill area, i.e., the perimeter length of a hill base polygon.

3) Long-axis length

The long-axis length of a sinkhole (La) is defined as the length of the line drawn between the two most distant points along the perimeter. Like Pe , it depends upon A and plan shape. Elliptical, elongated, or composite sinkholes can have relatively long La . La of a hill is defined as the length of the line drawn between the most two most distant points along the hill base perimeter.

4) Orientation

The orientation (Or), or azimuth, is the direction of the long-axis of a sinkhole or a hill base polygon. Or in this study is record as counterclockwise from due east. Or of a sinkhole

may be correlated with geological structure especially lineaments (Upchurch and Littlefield Jr, 1988). Tibaldi et al. (1995) found that *Or* of a hill may be correlated with slope direction and the dip-direction of faults, and therefore affects landslide distribution.

5) Circularity ratio

The circularity ratio (*CI*) is define as the ratio of the plot area to the area of a perfect circle with the same perimeter (Miller, 1953):

$$CI = \frac{4\pi A}{Pe^2} \quad (3-5)$$

The value of *CI* ranges from 0 to 1. A perfect circle is represented by *CI* = 1. In contrast, an elongated form is represented by lower *CI* values. *CI* has often been applied in geomorphometric analysis not only for drainage basins (Miller, 1953) but also karst sinkholes (Carvalho Júnior et al., 2014). *CI* was computed for each sinkhole and each hill base polygon.

6) Sinkhole density

Sinkhole density (*Sd*) is defined as the number of sinkholes in a certain area. Normally its unit is numbers per km²:

$$Sd = \frac{Nd}{Area} \quad (3-6)$$

where *Nd* is the number of sinkholes, and *Area* is the area of the region considered. *Sd* is related to the distribution of the entry points of subsurface flow (Bauer, 2015).

3.4.2. Vertical measures

1) Depth

A sinkhole depth (*De*) is the difference between the highest and lowest elevation points within a sinkhole. *De* was calculated as the maximum elevation difference between the filled DEM and the original DEM.

2) Relief

The relief (*Re*) is defined for a tower or cockpit karst hill as the difference in elevation between the highest point and the hill base.

3) Relative relief

The relative relief (*rRe*) is a general parameter of a land unit such as a drainage basin, and was found to be related to drainage density (Yatsu, 1950; Schumm, 1956; Oguchi, 1997). In this study, it was computed as the ratio of relief to the hill base area for each karst hill:

$$rRe = \frac{Re}{A} * 100 \quad (3-7)$$

The unit of *rRe* is m/m².

3.4.3. Shape measures

1) Slope

Slope (*Slo*) or gradient is the ratio of maximum height change to distance. It is calculated using the elevation difference and the horizontal linear distance between two points, and converted into degrees using the arctangent function. The value of *S* ranges from 0° to 90°.

2) Volume

Volume (*V*) of a sinkhole can be calculated by assuming a cone shape depth (Plan and Decker, 2006):

$$V = \frac{1}{3} * De * A \quad (3-8)$$

This equation was used to calculate the volume of sinkholes identified from the field-based approach. The sinkhole volume for the semi-automatic approach was obtained by calculating the volumetric difference between the filled-DEM and the original DEM.

3) Aspect

Aspect (*As*) is the maximum direction of slope. In a raster surface, it can be calculated as the compass direction of the maximum slope change using a 3×3 moving window (Jenson and Domingue, 1988). The range of *As* is 0° to 360°, measured clockwise from north. It can be generally divide into ten classes: flat, North (0°–22.5°), Northeast (22.5°–67.5°), East (67.5°–112.5°), Southeast (112.5°–157.5°), South (157.5°–202.5°), Southwest (202.5°–247.5°), West (247.5°–292.5°), Northwest (292.5°–337.5°) and North (337.5°–360°). The aspect can significantly influence a microclimate and therefore is related to vegetation, agriculture and living comfort (Ali-Toudert and Mayer, 2006).

4) Curvature

Curvature (*Cu*) is the second derivative of the surface elevation. It is composed of profile (*Cpr*), plan (*Cpl*) and tangential curvature (*Ct*). It has long been used in geomorphology and hydrology (Schmidt et al., 2003).

5) Area ratio

The area ratio (*Ar*) is the ratio of the three dimensional surface area to the planimetric area and gives a more realistic estimate of land area than the commonly used plan area. It also represents topographic roughness and convolutedness (Grohmann et al., 2011). In this research, the method of Berry (2002) was used to calculate the surface area of each DEM cell:

$$Surface\ Area = \frac{Cell\ size^2}{\cos(S(\frac{\pi}{180}))} \quad (3-9)$$

where *Cell size* is the cell size. Then *Ar* is computed as

$$Ar = \frac{\text{surface area}}{\text{planimetric area}} \quad (3-10)$$

Ar is close to one in a flat area. It becomes bigger for irregular surfaces and shows a curvilinear relationship (Grohmann et al., 2011). We calculate Ar for the tower and cockpit karst hills.

6) Terrain ruggedness index

Terrain ruggedness index (TRI) is development by Sappington et al. (1999) to measure the elevation difference between adjacent cells in a DEM. The process essentially calculates the average change between the center cell and the eight surrounding cells in elevation:

$$TRI = \sqrt{\frac{\sum_{i=1}^8 (Z_0 - Z_i)^2}{8}} \quad (3-11)$$

where Z_0 is the elevation of the central cell, and Z_i is the elevation of surrounding eight cells.

7) Terrain shape index

The terrain shape index (TSI) developed by McNab (1989) is defined as the mean relative difference in elevation between the center point and the landform boundary:

$$TSI = \frac{\sum_{i=1}^N (H_i - H_0)}{N * Rad} \quad (3-12)$$

where H_0 is the elevation of the landform central point; H_i is the elevation of the landform boundary point; N is the number of the landform boundary point; Rad is the measured plot radius. The unit of TSI is in m/m. The value range of the TSI can be wide from negative to positive infinity; however, for mountainous landforms, TSI is usually negative. Lyew-Ayee et al. (2007) used TSI to represent the difference between cockpit and non-cockpit hills. Therefore it was used to depict differences in terrain shape between tower and cockpit karst hills.

8) Hypsometric integral

The hypsometric integral (HI) has been used to quantitatively describe morphological characteristics of a region (Strahler, 1952). It represents the distribution of horizontal cross-sectional area with respect to elevation in a region. HI is generally applied in a drainage basin and calculated as:

$$HI = \int_{Hmin}^{Hmax} \frac{a}{At} \times \Delta\left(\frac{h}{H}\right) \quad (3-13)$$

where $Hmax$ is the maximum elevation of a basin, $Hmin$ is the minimum elevation; At is the total area of the basin, and a is the area of the basin above a given elevation h .

HI was used to describe the differences and similarities of the cockpit and tower karst hills. The equation of the approximate HI values was adopted (Wilson, 1971):

$$HI = \frac{Hmean - Hmin}{Hmax - Hmin} \quad (3-14)$$

where $Hmean$ is the mean elevation of a cockpit or tower karst hills. HI was calculated for each karst hill.

3.5. Land-use classification

Using aerial photos and satellite images as well as a supervised classification algorithm, land-use characteristics in the two study areas were analyzed. It was also accomplished by visual interpretation of images and field work.

The land-use classification was conducted as follows: 1) Field work was carried out in March, June and July 2011, and Land-use of randomly selected 147 locations were recorded as reference data at ground control points; 2) ENVI 4.8 remote sensing software was employed to process aerial photos, and 70% of the field samples were applied for training the maximum likelihood algorithm to conduct supervised classification; 3) land-use in the two study areas was classified into five basic classes and 11 sub-classes (Table 3-3); and 4) the overall accuracy of the resulted land-use map was assessed using the rest 30% of field samples.

Table 3-3. Land-use classification scheme

Land-use class	Land-use sub-class	Description
Arable land	Paddy land (PL)	Mainly used for growing rice. Homogeneous patches with clear boundary.
	Arable land (AL)	Mainly used for growing corn and wheat with irrigation facility.
Wood land	Forest land (FL)	Patches of secondary coniferous forest.
	Shrub land (SL)	Mainly growing dense broad-leaf shrub, usually less than 3 m tall.
	Orchard and perennial plantation (OP)	Mainly orchard and tea garden.
Grass land	Grass land (GL)	Covered by grasses, usually containing lots of thorns and scattered shrubbery with crown density < 10%.
Water area	Water area (WA)	Lakes, reservoirs, and rivers.
	Tidal flat (TF)	Sand or mud areas in estuarine areas.
Construction area	Construction land (CL)	Land covered by buildings and other man-made structures.
	Mining land (ML)	Land used for mining sites and activities.
	Bare land (BL)	Land of exposed soil, sediment and rock.

For the Mawo basin of the Weining area where soil erosion research was made, a more detailed land-use map was constructed, using an image from the ALOS multi-spectral AVNIR-2 sensor acquired on the 19th March, 2009. The spatial resolution of the image is 10 m. ENVI 4.8 was used for data processing and image analysis. Geometric rectification was performed based on the 1:10,000 topographic maps to fit the image to the UTM coordinate projection system. Then supervised classification was conducted using the maximum likelihood classifier and the scheme of Table 3-3. For each land-use type, five to eight points were selected as training samples and their land-use was surveyed in the field.

3.6. Evaluation of soil erosion rate

Soil erosion characteristics in the un-gauged Mawo basin, a typical karst area of the Weining area, was analyzed with the help of the RUSLE, GIS and RS.

The RUSLE model is a modification of the original USLE model (Wischmeier and Smith, 1978) with six factors associated with climate, soil, topography, vegetation and management (Renard et al., 1997):

$$Er = R * K * L * S * C * P \quad (3-15)$$

where Er is the estimation rate of soil loss over the long term ($\text{Mg ha}^{-1} \text{y}^{-1}$); R is the rainfall-runoff erosivity factor ($\text{MJ mm ha}^{-1}\text{h}^{-1}\text{y}^{-1}$); K is the soil erodibility factor ($\text{Mg h MJ}^{-1} \text{mm}^{-1}$); L and S are the topographic factors that account for slope length and steepness, respectively; C is the cover-management factor; and P is the support practice factor. L , S , C and P is dimensionless.

R is computed using an equation related to the total storm kinetic energy and the maximum 30 minutes rainfall intensity (Renard et al., 1997). However, not only continuous rainfall intensity data at time intervals less than 30 minutes but also daily and even monthly rain fall records are limited in many parts of the world, especially in developing countries (Yu, 1998; Yu et al., 2001). The Mawo basin is located in such an area without historical precipitation data. Alternatively, in this study, R values were derived from the approach suggested by Mikhailova et al. (1997).

$$R = 7.562 Pr - 3172 \quad (3-16)$$

where Pr is the annual precipitation (mm). The resulted mean R value equals to $2865.5 \text{ MJ mm ha}^{-1}\text{h}^{-1}\text{y}^{-1}$.

The soil types in the study area are categorized into four classes: yellow brown soil, calcaric cambisols, brown calcareous soil and brown soil. For yellow brown soil and calcaric cambisols, a simple technique of the erosion-productivity impact calculator (Williams et al., 1983) was used with the analysis of the topsoil samples. Their K -values were obtained with

the following equation:

$$K = \left\{ 0.2 + 0.3 \exp[-0.0256Sa(1 - Si/100)] \right\} * \left(\frac{Si}{Cl + Si} \right)^{0.3} * \left[1.0 - \frac{0.25Co}{Co + \exp(3.72 - 2.95Co)} \right] * \left\{ 1.0 - \frac{0.7(1 - Sa/100)}{1 - Sa/100 + \exp[-5.51 + 22.9(1 - Sa/100)]} \right\} \quad (3-17)$$

where K is the soil erodibility factor in $\text{Mg acre (100 acre)}^{-1} \text{ft}^{-1} \text{Mg}^{-1} \text{in}^{-1}$, which can be converted to $\text{Mg h MJ}^{-1} \text{mm}^{-1}$ if multiplied by a constant of 0.1317; Sa , Si , Cl , and Co are the percentage of sand, silt, clay and organic carbon, respectively. The K values of brown calcareous soil were obtained from Yang et al. (2006). The K value of brown soil was acquired from the study conducted in the area adjacent to the Mawo basin (Yang, 2002). The determined K values for yellow brown soil, calcaric cambisols, brown calcareous soil and brown soil are 0.041, 0.036, 0.025 and 0.038 $\text{Mg h MJ}^{-1} \text{mm}^{-1}$.

The LS -factor was calculated using the DEM and the ArcGIS Spatial Analysis and Hydro extensions. The L -factor was generated by the formulation proposed by Wischmeier and Smith (1978):

$$L = \left(\frac{\lambda}{22.13} \right)^m \quad (3-18)$$

where λ is the slope length (m); and m is an exponent dependent on the value of the slope angle: 0.5 for slope $\geq 2.86^\circ$, 0.4 for slopes of 1.72° – 2.85° , 0.3 for slopes of 0.57° – 1.72° , and 0.2 for slopes $< 0.57^\circ$.

Slope length (λ) described as the ratio of horizontal slope length to a unit-plot slope length, in equation as follows (Moore and Burch, 1986):

$$\lambda = \text{Flow accumulation} * \text{Cellsize} \quad (3-19)$$

where *Flow accumulation* is the accumulative upslope area that drain into a given cell; and *Cellsize* is the grid size of DEM.

S was evaluated using two approaches, on slope angle less than 10° (McCool et al., 1989) and slope angle greater than 10° (Liu et al., 1994). The constituent was calculated in different scenarios:

$$S = 10.8 \sin \theta + 0.03, \quad \theta < 5^\circ \quad (3-20)$$

$$S = 16.8 \sin \theta - 0.50, \quad 5^\circ \leq \theta < 10^\circ \quad (3-21)$$

$$S = 21.91 \sin \theta - 0.96, \quad \theta \geq 10^\circ \quad (3-22)$$

where θ is the angle of slope (degs.)

Concerning the C -factor, vegetation in the Mawo basin underwent temporal changes. Therefore, the Landsat TM images for 1988–2009 were used to compute change in $NDVI$ and obtain C values for different years. The C values were calculated from the mean $NDVI$ using

the exponential scaling formula by Van der Knijff et al. (2000):

$$C = \exp\left[-\alpha \frac{NDVI}{(\beta - NDVI)}\right] \quad (3-23)$$

where α and β are unitless parameters and $\alpha = 2$ and $\beta = 1$ give reasonable results.

Small-scale terracing, stone-framed terracing and contour tillage were carried out in the farm land of the study area, and rocky desertification has occurred in the Mawo basin (Chen et al., 2012). These rocky desertification areas are marked as extensive exposure of basement rocks without vegetation and soil coverage. In relation to this the P value was assumed to be 0 for rocky area, building area and mining area; 1 for forest land, shrub land and grassland because of the absence of support practice; and 0.4 for non-irrigated arable land based on the field experiments and studies in southwestern China (Yang, 2002; Xu et al., 2008).

CHAPTER 4 KARST LANDFORM CLASSIFICATION

4.1. Sinkhole identification

In the Zhijin area, 531 sinkholes were identified in the field-based reference map (Fig. 4-1).

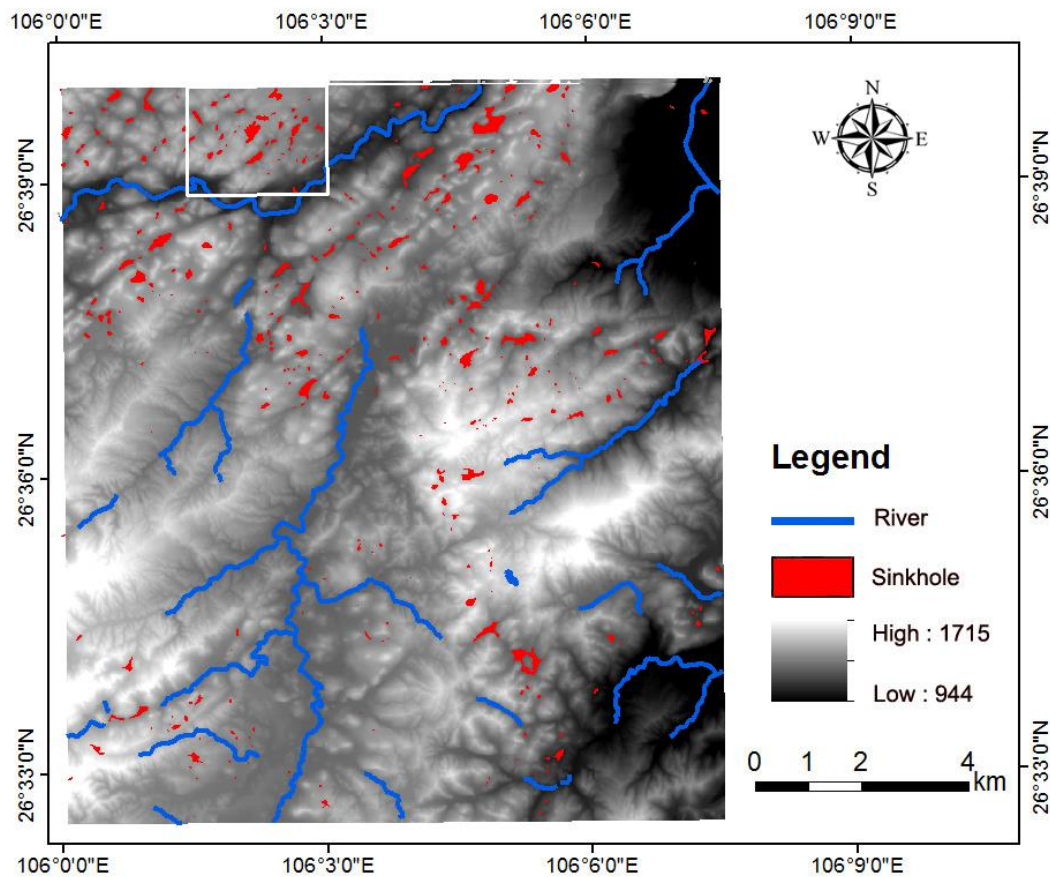


Figure 4-1. Map of sinkholes in the Zhijin area, identified from the aerial photos and field surveys. The area within a white box is shown in Fig. 4-6.

Then the results of the semi-automatic sinkhole identification were evaluated. Fig. 4-2 shows the evaluated accuracy of the semi-automatic identification model using the 3, 30, 60, 90-m DEMs from the different data sources, and Table 4-1 gives more detailed data related to the accuracy. The model accuracy with the SRTM-DEM and GDEM ranges from 7% to 55% and from 4% to 30%, respectively, and increases with the grid size. The model performance with the SRTM-DEM is better than that of the GDEM. Also for each DEM, accuracy of the model with thresholds (area = 60 m², $E = 0.2$ and $TPI = 0$) is always better than that without the thresholds, showing that the thresholds should be used. The change in the model performance with the DEMs from topographic maps (hereafter referred to as “M-DEMs”)

according to DEM resolution can be divided to two sections: grid sizes of 3–10 m and 10–90 m (Fig. 4-2). At the first section, the accuracy of the model with the thresholds decreases from 95% to 80% with increasing grid size. At the second section, the model accuracy stays in at the range of 75–80% for grid size of 10–75 m, but significantly increased to 99% at the 90-m grid size. However, since the true positive value is low for the 90-m grid size (Table 4-1), the size was not considered as a proper one for further morphometric analysis.

In general, if more sinkholes are delineated by the semi-automatic approach, the chance of identifying true sinkholes becomes higher (high *TP* value). However, the chance of detecting artificial sinkholes also increases (high *FN* value). In other words, there is a positive correlation between *TP* and *FP* (Table 4-1). For example, for the SRTM-DEM and GDEM, *TP* decreases with decrease in *FP* and with the coarsening of the grid size. Especially for the GDEM, the number of artificial sinkholes (*FN*) remains large. At the grid size of 3 m, the number of identified true sinkholes is smaller than that for any other resolutions. In this paper, the 90-m SRTM data was considered as suitable for large sinkhole identification with the proposed thresholds because of less artifacts and the acceptable amount of identified true sinkholes. In contrast, the ASTER GDEM contains abundant noise, leading to a significant number of visual artifacts with small areas that do not correspond to the field inventory. This anomaly of the ASTER GDEM makes it unsuitable for the detection of sinkholes in the Zhijin area.

Table 4-1. Numbers of 1) true positive (*TP*); 2) false positive (*FP*) and 3) false negative (*FN*) identifications in the Zhijin area for DEMs generated from different resources and the semi-automatic model with or without the thresholds.

DEM sources	Spatial resolution (m)	Thresh-olds	No. of <i>TP</i>	No. of <i>FP</i>	No. of <i>FN</i>
M-DEMs	3	N	423	108	216
		Y	415	0	27
	30	N	391	140	93
		Y	379	80	78
	60	N	262	269	68
		Y	262	0	68
90	N	187	344	51	
	Y	172	0	0	
SRTM	3	N	92	439	996

		Y	78	0	952
	30	N	138	393	455
		Y	131	0	423
	60	N	140	393	144
		Y	113	0	118
	90	N	102	431	82
		Y	102	0	82
GDEM	3	N	189	342	5179
		Y	78	0	1830
	30	N	169	262	1705
		Y	157	0	1702
	60	N	143	388	515
		Y	143	0	515
	90	N	125	406	280
		Y	125	0	280

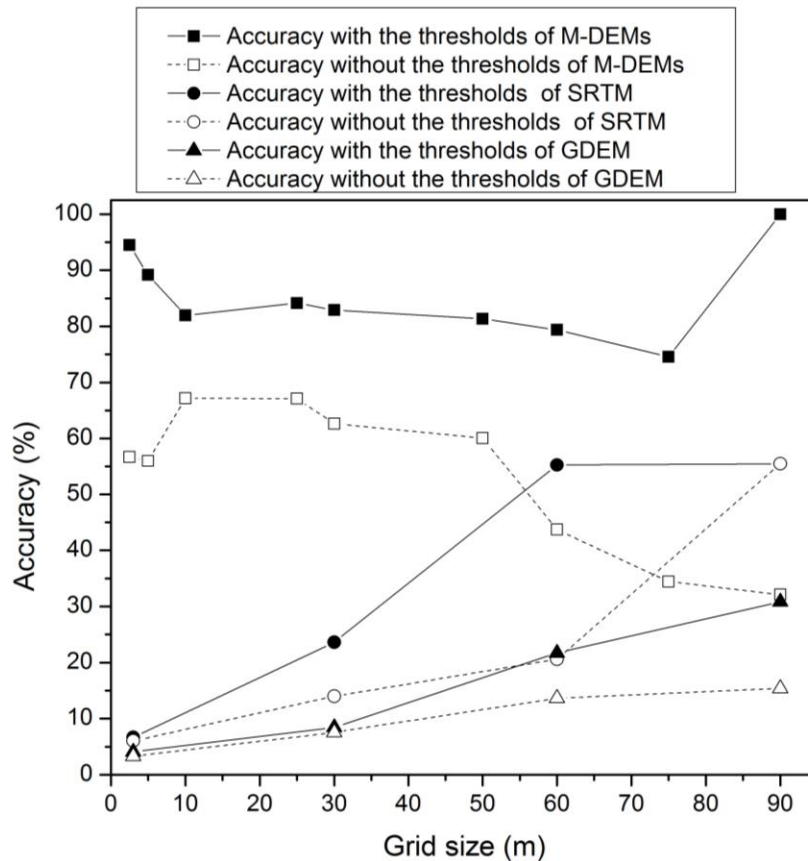


Figure 4-2. Accuracy of sinkhole identification in the Zhijin area for the semi-automatic approach with or without the thresholds (area = 60 m², $E = 0.2$ and $TPI = 0$).

According to the performance of difference data sources in the Zhijin area, the DEM generated from the topographic maps with 3-m resolution was applied in the Weining area. 57 sinkholes were identified in the reference map.

The thresholds for the semi-automatic model in the Weining area are area = 150 m², $E = 0.2$ and $TPI = 0$. The automatically delineated sinkholes were compared with those identified by the field-based approach. Table 4-2 shows the performance of the model with thresholds in the Weining area. The accuracy of the model without thresholds and with thresholds are 21.47% and 49.35%, respectively. The reason for the improvement due to the thresholds is that the thresholds filtered out a large amount of false negatives (Table 4-2).

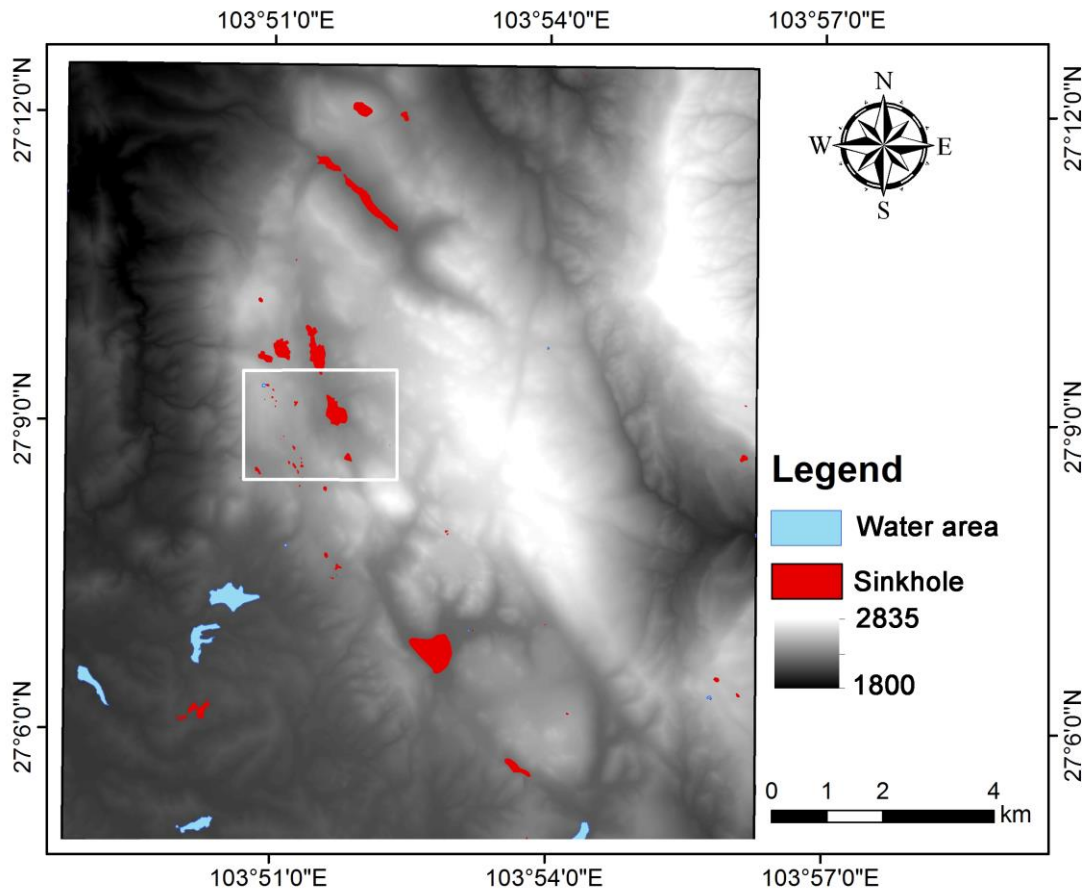


Figure 4-3. Map of sinkholes in the Weining area, identified from the aerial photos and field surveys. The area within a white box is shown in Fig. 4-7.

Table 4-2. Numbers of the 1) true positive (*TP*); 2) false positive (*FP*) and 3) false negative (*FN*) identification of M-DEM of the Weining area by the running of semi-automatic model with/without the thresholds

DEM sources	Spatial resolution (m)	Thresh-olds	No. of <i>TP</i>	No. of <i>FP</i>	No. of <i>FN</i>
M-DEM	3	N	38	120	19
		Y	38	20	19

Table 4-3. Summary statistics of sinkholes in the Zhijin area delineated using the two approaches

	Field-based approach ($n = 531$)				Semi-automatic approach ($n = 423$)			
	Min	Max	Mean	SD	Min	Max	Mean	SD
A (m ²)	60	147,985	5,423	11,761	6.25	52,100	3,342.10	4,562.25
Pe (m)	31.64	2,329.89	283.58	295.99	10	3,200	278.88	241.76
La (m)	6.15	283.60	46.68	41.69	1.61	199.72	32.51	30.65
E	0	0.99	0.78	0.15	0	0.99	0.78	0.15
Or (°)	0	179.89	82.67	48.97	1.84	178.86	17.59	50.13
De (m)	1	110	15.70	16.41	1	110	17.59	17.41
V (m ³)	125	2,663,730	60,367.96	223,139.80	2.08	303,555	20,543.83	35,901.49
Sd (km ⁻²)	—	—	5.06	—	—	—	4.03	—

Table 4-4. Summary statistics of sinkholes in the Weining area delineated using the two approaches

	Field-based approach ($n = 57$)				Semi-automatic approach ($n = 38$)			
	Min	Max	Mean	SD	Min	Max	Mean	SD
A (m ²)	148	336,143	16317.02	50801.07	192.13	10167.03	1762.95	1820.61
Pe (m)	54	3,012	440.21	609.37	66	480	190.74	98.91
La (m)	7.57	372.35	61.02	82.23	10.52	70.33	27.35	14.63
E	0.23	0.97	0.73	0.16	0.31	0.92	0.71	0.16
Or (°)	0.54	179.56	103.01	48.45	4.53	172.95	99.89	43.45
De (m)	0	11	1.27	2.06	0	3	0.33	1.04
V (m ³)	0	441,664	47,140.336	176010.34	0	6114.65	573.9	1413.31
Sd (km ²)	—	—	0.37	—	—	—	0.25	—

4.2. Discrimination of tower and cockpit karst hills

Fig. 4-4 compares the discrimination result of tower and cockpit karst hills in the Zhijin area using the automatic approach and the reference map based on aerial photos and field surveys. The cockpit karst hills cover a large area, especially in the central part of the area. The tower karst hills are more scattered over the area.

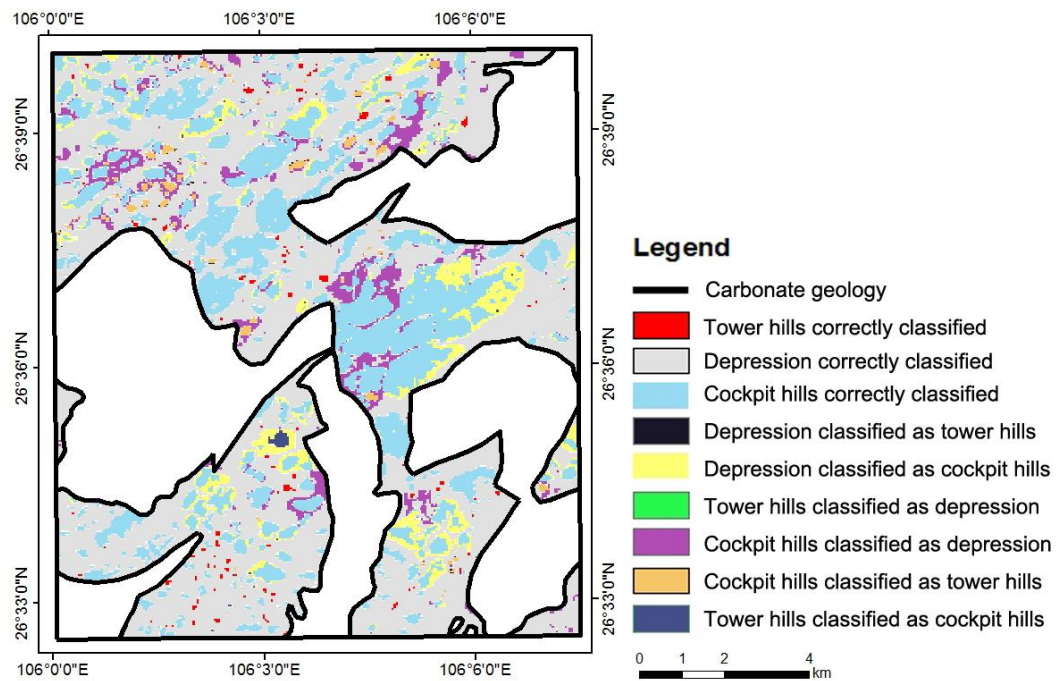


Figure 4-4. Comparison between landform classification results and the reference map in the Zhijin area.

Table 4-5 shows the confusion matrix of the classification results. According to the table, 90.19% out of 106.9 km² were correctly classified, and the overall accuracy is 85.02%. It shows that the approach successfully separated the tower and cockpit karst hills in the Zhijin area. The numbers of identified tower and cockpit karst hills are 439 and 403, respectively.

The cockpit karst hills were separated into several ranks according to the number of peaks. Table 4-6 shows the numbers of cockpit hills belonging to the different ranks. Ranks 2 and 3 are dominated amount in the Zhijin area. The summary of morphometric statistics of tower and cockpit karst hills in the Zhijin area are shown in Table 4-7.

Table 4-5. Confusion matrix of the classification results for the Zhijin area

Types of landform	Reference (km ²)			sum
	Tower karst hill	Cockpit karst hill	Depression	
Tower karst hill	0.64	1.34	0.38	2.36
Cockpit karst hill	0.18	27.94	7.27	35.39
Depression	0.29	6.44	61.61	68.34
sum	1.11	35.72	69.26	106.09

Table 4-6. Classification of cockpit karst hills in the Zhijin area

Number of cockpit karst hills according to the number of peaks in a hill (= Rank)($n = 403$)

Rank 2	Rank 3	Rank 4	Rank 5	Rank 6	Rank 7	Rank 8
336	41	16	6	2	1	1

Table 4-7. Summary of morphometric statistics of tower and cockpit karst hills in the Zhijin area

	Tower karst hills (<i>n</i> = 439)				Cockpit karst hills (<i>n</i> = 403)			
	Min	Max	Mean	<i>SD</i>	Min	Max	Mean	<i>SD</i>
<i>A</i> (m ²)	56.77	144,757.10	2,695.39	7,735.83	378.20	8,424,520.21	88,728.66	452,906.0887
<i>Pe</i> (m)	36	2166	207.68	173.67	90	47,334	1,398.77	299.41
<i>La</i> (m)	5.38	244.47	30.53	20.73	11.90	1859.64	151.57	186.68
<i>Or</i> (°)	0	180	83.85	53.82	0.27	178.51	77.40	54.37
<i>Re</i> (m)	1	77	5.79	9.42	1	1648	60.34	178.11
<i>rRe</i> (m)	0.01	2.9	0.38	0.43	0.001	43	0.43	2.31
<i>Slo</i> (°)	0.14	45.25	12.96	11.14	1.43	53.41	27.12	8.75
<i>As</i> (°)	3.73	271.66	101.31	54.12	22.86	274.11	161.64	28.92
<i>Cu</i>	0	38.19	6.93	6.44	0.24	16.79	2.72	2.79
<i>CI</i>	0.11	0.77	0.53	0.1	0.01	0.66	0.42	0.14
<i>Ar</i>	1.09	1.59	1.07	0.1	1	1.94	1.2	0.13
<i>TRI</i>	0	0.036	0.01	0.01	0	0.05	0.01	0.01
<i>TSI</i>	-1.84	0	-0.27	0.33	-12.28	-0.02	-0.52	0.74
<i>HI</i>	0.25	1	0.78	0.22	0.13	0.99	0.44	0.12

Fig. 4-5 shows the results of the discrimination of tower and cockpit karst hills in the Weining area using the semi-automatic approach and the reference map. The depression category dominates, and large area of cockpit karst hills were found at the northern part of the Weining area. The tower karst hills area distributed all over the Zhijin study area.

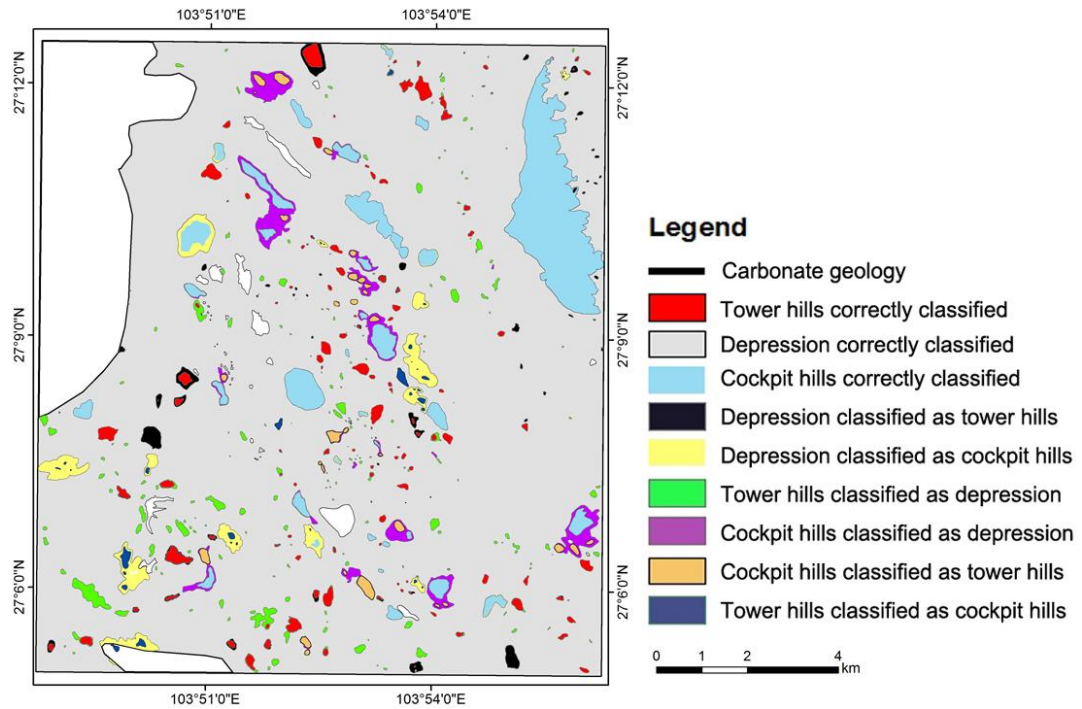


Figure 4-5. Comparison between landform classification results and reference of the Weining area

Table 4-8 shows the confusion matrix of the classification results. According to the table, 144.55 out of 152.81 km² are correctly classified, with the overall accuracy being 94.65%. It shows that the approach successfully separated the tower and cockpit karst hills in the Weining area. The numbers of identified tower and cockpit karst hills are 112 and 35, respectively.

Table 4-8. Confusion matrix of the classification results for the Weining area

Types of landform	Reference (km ²)			
	Tower karst hill	Cockpit karst hill	Depression	sum
Tower karst hill	2.07	0.69	1.04	3.80
Cockpit karst hill	0.32	9.27	2.28	11.87
Depression	1.59	2.34	133.21	137.14
sum	3.98	12.30	136.53	152.81

As show in Table 4-9, the cockpit karst hills with two peaks are dominated (24 out of 35).

In addition, there is an exceptional cockpit karst hill covering a large area with 50 peaks. Table 4-10 shows the summary of morphometric statistics of tower and cockpit karst hills in the Weining area.

Table 4-9. Classification of cockpit karst hills in the Weining area

Cockpit karst hills (n = 35)							
Rank 2	Rank 3	Rank 4	Rank 5	Rank 6	Rank 7	Rank 8	Rank 50
24	6	1	2	-	-	1	1

In addition, the individual accuracy order is depression > cockpit karst hills > tower karst hills. The individual accuracies of tower karst hills, cockpit karst hills and depression in the Zhijin area are 57.66%, 78.22% and 88.95%, respectively (Table 4-5). The individual accuracies of tower karst hills, cockpit karst hills and depression in the Weining area are 54.47%, 75.37% and 97.57%, respectively (Table 4-8). Two reasons accounts for the observation that semi-automatic approach resulted in a lower individual accuracy of the tower karst hills than that of the cockpit karst hills and depressions. Firstly, the semi-automatic approach delineates the footprints of tower and cockpit karst hills with the contour lines near slope around 5° (Section 3.3.2). However, the reference landform maps were generated based on the experiences of the expert. The footprints (outlines) of the tower and cockpit karst hills in the reference landform maps were identified using the criterion than slope > 0°. The footprints of the tower and cockpit karst hills in the semi-automatic approach were identified by slope = 5°. The lower slope threshold in the reference maps resulted in larger tower and cockpit karst hill areas than those from the semi-automatic approach. Secondly, the areas of cockpit karst hills (Tables 4-7 and 4-10) and depressions (Tables 4-5 and 4-8) are larger than those of the tower karst hills. The numbers of tower karst hills (439 in the Zhijin area and 112 in the Weining area) are larger than those of the cockpit kart hills (403 in Zhijin area and 35 in the Weining area). This large numbers and small area of the tower karst hills led large area difference between the results from the reference maps and semi-automatic approach.

Table 4-10. Summary of morphometric statistics of tower and cockpit karst hills in the Weining area

	Tower karst hills (n = 112)				Cockpit karst hills (n = 35)			
	Min	Max	Mean	SD	Min	Max	Mean	SD
<i>A</i> (m ²)	383.44	154,598.90	18,483.54	26,868.74	5,895.30	5,413,736.97	264,914.97	893,600.91
<i>Pe</i> (m)	84	2,094	573.64	416.44	384	23,490	2,338.11	3,847.82
<i>La</i> (m)	11.26	266.23	81.76	56.19	60.57	2420.81	301.86	403.03
<i>Or</i> (°)	0.31	179.12	93.15	54.38	0.42	174.49	105.43	47.43
<i>Re</i> (m)	1	66	12.63	10.34	6	192	38	41.23
<i>rRe</i> (m)	0.07	0.25	0.15	0.12	0.004	0.2	0.06	0.05
<i>Slo</i> (°)	1.79	28.67	14.69	0.66	6.76	27.52	15.93	4.92
<i>As</i> (°)	32.82	185.88	134.39	31.04	91.53	176.82	142.57	18.39
<i>Cu</i>	0.18	12.39	2.38	1.87	0.19	3.33	1.01	0.77
<i>CI</i>	0.26	0.67	0.51	0.08	0.12	0.58	0.4	0.12
<i>Ar</i>	1	1.17	1.06	0.04	1.02	1.17	1.06	0.04
<i>TRI</i>	0.1	1.27	0.68	0.26	0.33	1.25	0.74	0.2
<i>TSI</i>	-0.83	0	-0.26	0.16	-0.48	-0.06	-0.23	0.12
<i>HI</i>	0.32	0.99	0.54	0.16	0.3	0.64	0.44	0.08

4.3. Application of morphometric thresholds

The application of the thresholds has improved the accuracy of the model for all the DEMs. Fig. 4-2 and Table 4-1 evaluated accuracy and detailed performance of the model with DEMs from the different data sources in two scenarios: with or without thresholds. With the implementation of the thresholds, the model accuracy with the SRTM-DEM and GDEM improves (Fig. 4-2). As mentioned in Section 4.1, the performance of the semi-automatic approach with the M-DEMs was separated to two sections. At the 3–10 m resolution section, in contrast to the decline with the thresholds, the accuracy of the model without the threshold increases from 55% to 65% with an increasing grid interval. This may reflect the morphometric characteristics of the sinkholes in the study area that are skewed to the relatively small area class and an elongated shape; therefore, the number of the recognized true sinkholes increases with the grid size when there is no threshold. At the 10–90 m resolution section, the accuracy of the non-threshold model decreases apparently with the increasing of the grid size. However, the threshold model accuracy varies within a small range. This stable and good performance of the model and elimination of artifacts indicate that the thresholds used are appropriate. In addition, at the grid size of 90 m, the model with thresholds shows markedly high accuracy, because the false positive and false negative sinkholes were removed by the application of the thresholds (Table 4-1). As shown in Table 4-2, the numbers of the false negative sinkholes in the Weining area ranges from 120 to 20 with the application of the morphometric thresholds.

The good performance of the semi-automatic approach on the moderate-size sinkholes can be seen from the statistic characteristics in Table 4-3. For example, the mean and *SD* values of the semi-automatic sinkhole area are much smaller than those from the field-based approach. This is re-examined by the calculated sinkhole volume. The mean value of sinkhole volume by field-based approach is three times as big as that of semi-automatic approach while the statistic value of sinkhole depth by the two approaches is not significantly different with each other.

The reason for the higher efficiency of the semi-automatic approach on the moderate size sinkholes identification might be related to the detailed delineation process. As shown in Fig. 4-6, the boundaries of the sinkholes with relatively small area are similarly depicted by the two approaches. For the large sinkholes, the boundaries from the semi-automatic approach are smaller than that from the field-based approach, because the application of thresholds of area = 60 m², ellipticity = 0.2 and *TPI* = 0. On one hand, the threshold of ellipticity = 0.2 eliminated the sinkholes near circular. As shown in Fig. 4-7, the large sinkholes have shapes near circular. On the other hand, the threshold of *TPI* = 0 eliminated the pixels with positive topographic

position. The large area with any positive topographic position were excluded.

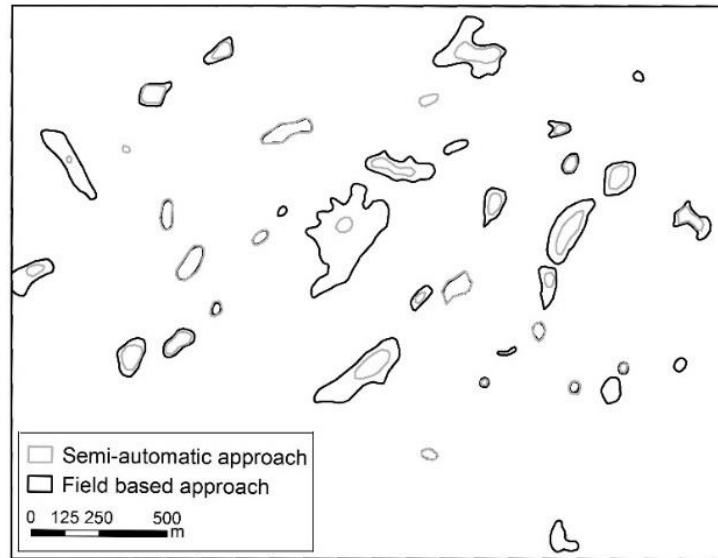


Figure 4-6. Results of the two different approaches to delineate sinkhole boundaries in the Zhijin area (area highlighted in Fig. 4-1).

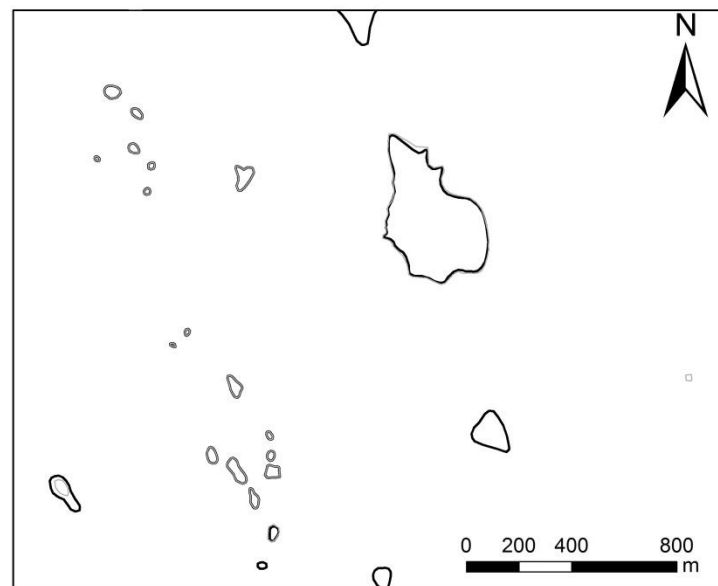


Figure 4-7. Results of the two different approaches to delineate sinkhole boundaries in the Weining area (area highlighted in Fig. 4-3).

4.4. Impact of DEM resolution on sinkhole identification

DEM resolution affects the ability to describe true sinkholes, most of which are small in the study area. It is noticed that artificial depressions (artefacts) could be generated in processing a DEM even if the DEM is highly accurate (Li et al., 2011). In the present study, the cell size of the original M-DEM is 1 m, while the smallest sinkhole in the manual dataset is 60 m² in area. Therefore, it may be unnecessary to use such a detailed DEM which might affect computing speed as well as producing many small artificial depressions due to local data noises and intermittent data sampling.

The resampling process changed the original DEMs to coarser ones and created a smoother surface by eliminating fine details (Fig. 4-8). The mean error (*ME*) and root mean square error (*RMSE*) between a resampled DEM and the original one are shown in Fig. 4-9. As expected, *ME* between the original M-DEM and its coarsened DEMs generally increases with the grid size. *RMSE* of the DEMs tends to vary except for the relatively similar values at the grid size of 60 m, which can also be seen from the similarly delineated watershed boundaries and channels in Fig. 4-8. Also *ME* and *RMSE* of the M-DEM show two patterns (Fig. 4-9): the values tend to be constant for the grid sizes < 30 m but more fluctuated at the grid sizes \geq 30 m. The absolute values of *ME* and *RMSE* for the SRTM-DEM and GDEM tend to be larger than those for the M-DEM at all the grid sizes. However, the values for the SRTM-DEM change more drastically than those for the GDEM.

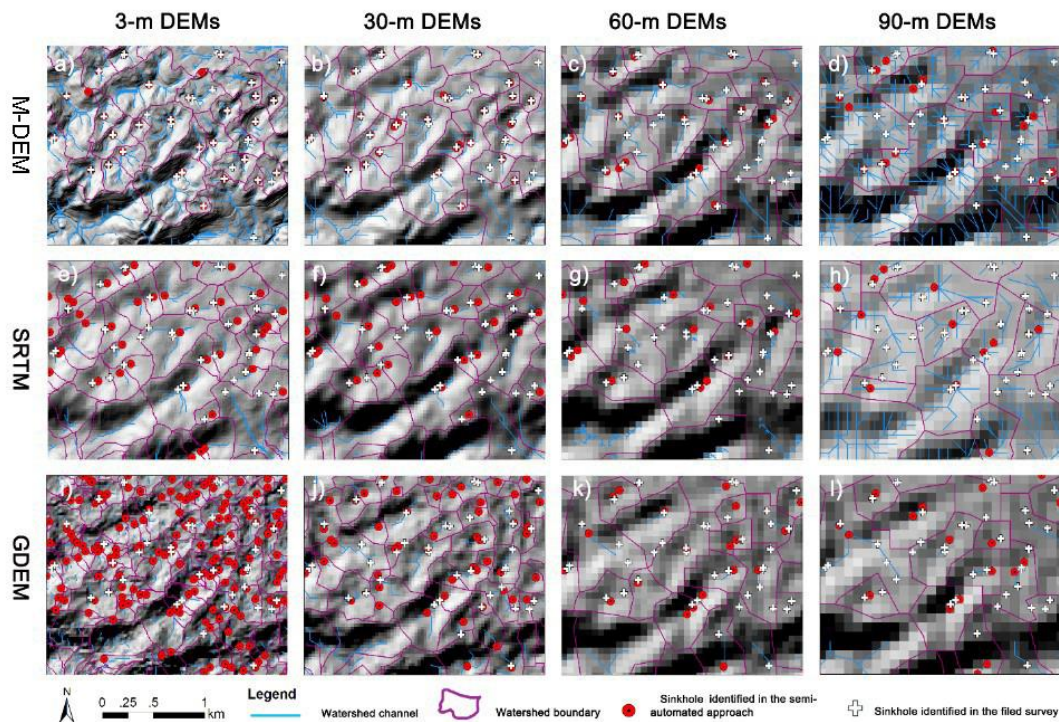


Figure 4-8. Hillshaded maps of a portion of the study area (highlighted in Fig. 4-1) showing

sinkhole connections and the effects of DEM resampling on the depression identification. Sinkholes location are those determined by the semi-automatic approach with the thresholds of area = 60 m², $E = 0.2$ and $TPI = 0$.

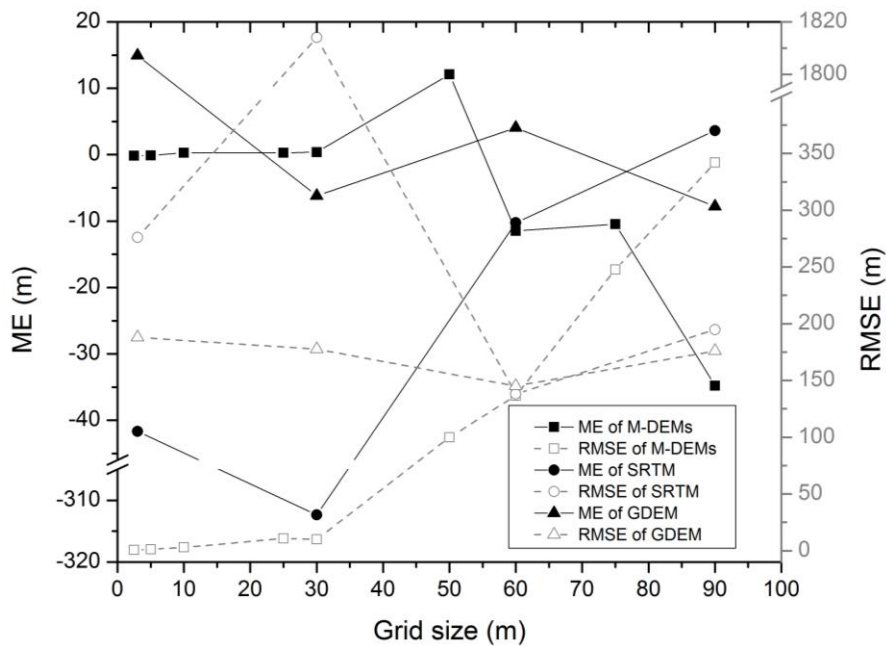


Figure 4-9. Effect of DEM resampling. *ME* and *RSME* are respectively the mean error and root mean square error of resampled DEMs (ASTER GDEM, SRTM-DEM and M-DEMs) and the original M-DEM with a resolution of 1 m.

Moreover, the resampling probably restricts the shape of sinkholes. For instance, some extremely elongated small sinkholes were likely to be excluded in the resampling process to a coarser DEM. As mentioned in Section 4.1, we can see from Fig.4-2 and Table 4-1 that the models with/without thresholds get lower accuracy at coarser grid sizes (10–90 m in resolution) in the situation of M-DEMs, since the grid cells are square in shape with clustering area characteristics. Sinkholes are more circled, so their shape may not be well represented with coarser DEMs.

CHAPTER 5 MORPHOMETRIC ANALYSIS OF THE KARST LANDFORMS

5.1. Spatial distribution of sinkholes

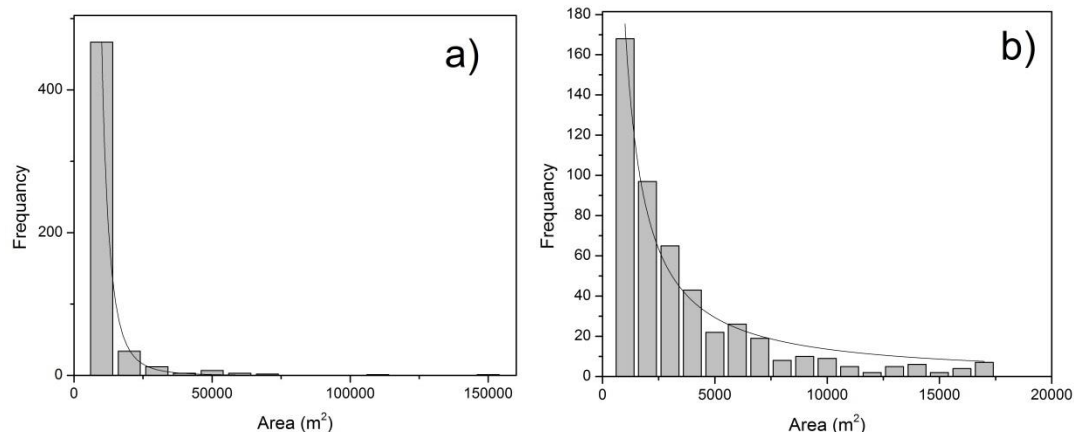
In the Zhijin area, the mean sinkhole densities from the field-based and semi-automatic approaches are 5.06 and 4.03 km⁻², respectively (Table 4-3). These values of sinkhole density are much lower than 122 km⁻² in the Hochschwab Plateau, Australia (Plan and Decker, 2006) and 91 to 146 km⁻² in the Styria basin, Austria (Bauer, 2015). However, they are comparable to those for the Suwannee River basin, Florida, USA (Denizman, 2003), where flat, broad, and shallow sinkholes develop.

In the Weining area, the mean sinkhole densities from the field-based and semi-automatic approaches are 0.37 and 0.25 km⁻², respectively (Table 4-4). Apparently sinkhole distribution is more limited there.

5.2. Sinkhole morphometry and statistics

5.2.1. Area

In the Zhijin area, the area of the sinkholes has a large range with a large standard deviation (Table 4-3). The area of the sinkholes based on the field-based approach and the semi-automatic approach skews to area < 17,000 m², with 93.79% and 97.21% of data, respectively. Small sinkholes are abundant and large sinkholes are fewer (Fig. 5-1a and d), which is the same as in temperate karst areas (Brinkmann et al., 2008; Bauer, 2015). After excluding unusually large sinkholes (Fig. 5-1b and e), a log transformation was applied to normalize the area data (Fig. 5-1c and f).



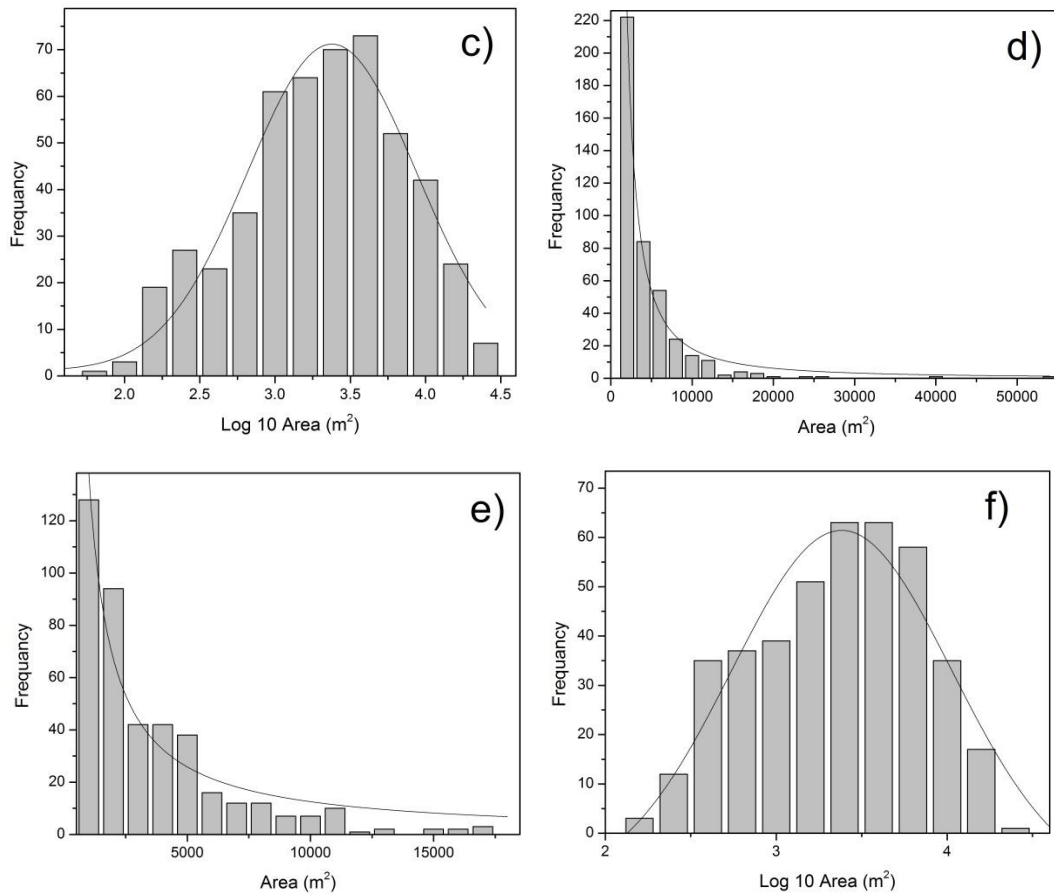


Figure 5-1. Frequency distribution of area of sinkholes in the Zhijin area. a) From the field-based approach. b) From the field-based approach after excluding large outliers. c) Log-transformed distribution from the field-based approach without the outliers. d) From the semi-automatic approach. e) From the semi-automatic approach after excluding large outliers. f) Log-transformed distribution from the semi-automatic approach without the outliers.

In the Weining area, the area of the sinkholes also varies significantly (Table 4-4). The area of the sinkholes based on the field-based approach skews to area < 17,000 m² with 91.23% of data (Fig. 5-2a). The area of the sinkholes of the semi-automatic approach skews to area < 5000 m² with 94.74% of data (Fig. 5-2d). As in the Zhijin area, small sinkholes are abundant and large sinkholes are fewer (Fig. 5-2a and d). After excluding unusually large sinkholes (Fig. 5-2b and e), a log transformation was applied to normalize the area data (Fig. 5-2c and f).

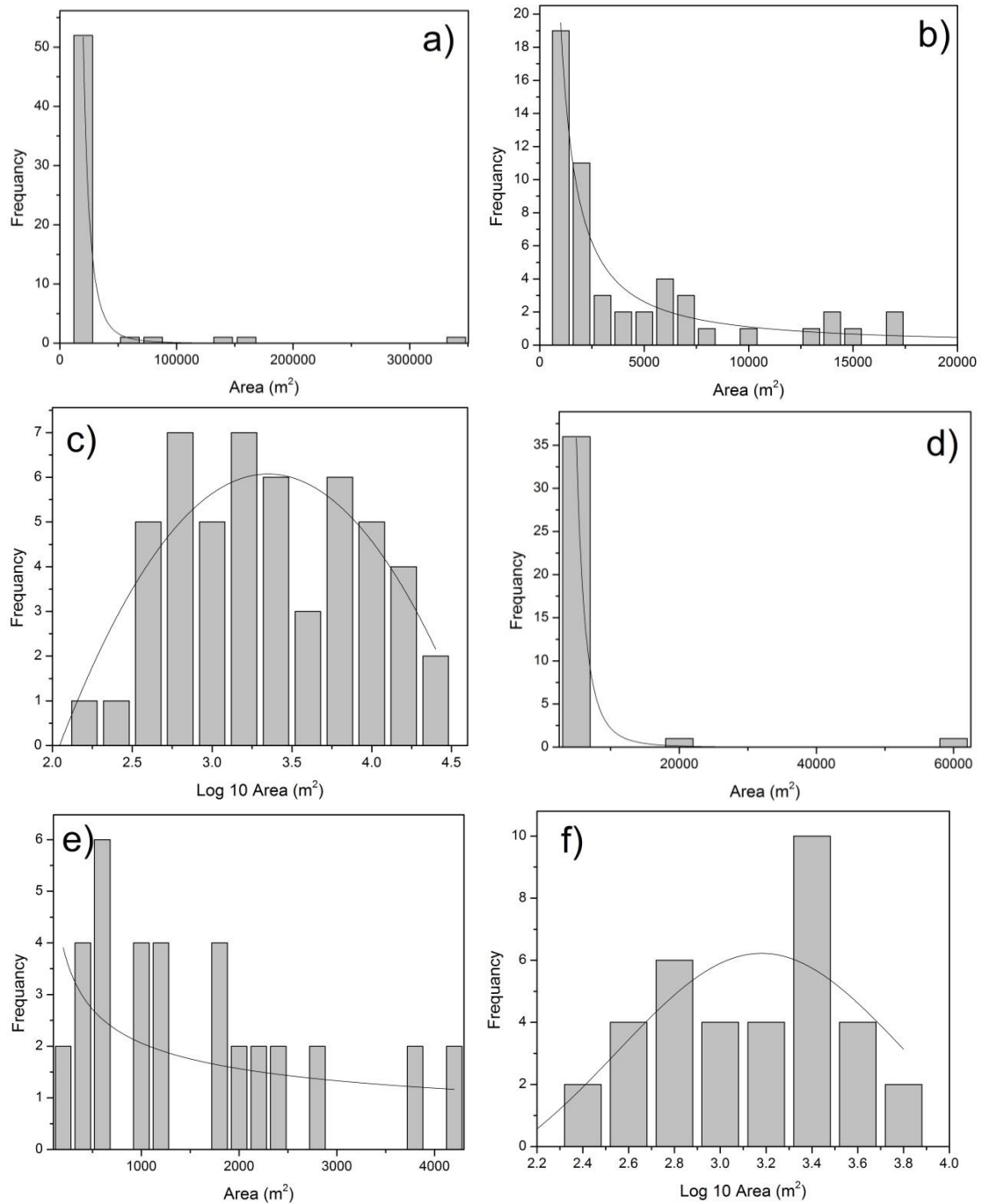


Figure 5-2. Frequency distribution of area of sinkholes in the Weining area. a) From the field-based approach. b) From the field-based approach after excluding large outliers. c) Log-transformed distribution from the field-based approach without the outliers. d) From the semi-automatic approach. e) From the semi-automatic approach after excluding large outliers. f) Log-transformed distribution from the semi-automatic approach without the outliers.

5.2.2. Perimeter

Like area, the perimeter of the sinkholes is not normally distributed and includes extremely long outliers (> 900 m) in the Zhijin area (Fig. 5-3). Like the case of area, the

normalization is made with a log transformation (Fig. 5-3b and f).

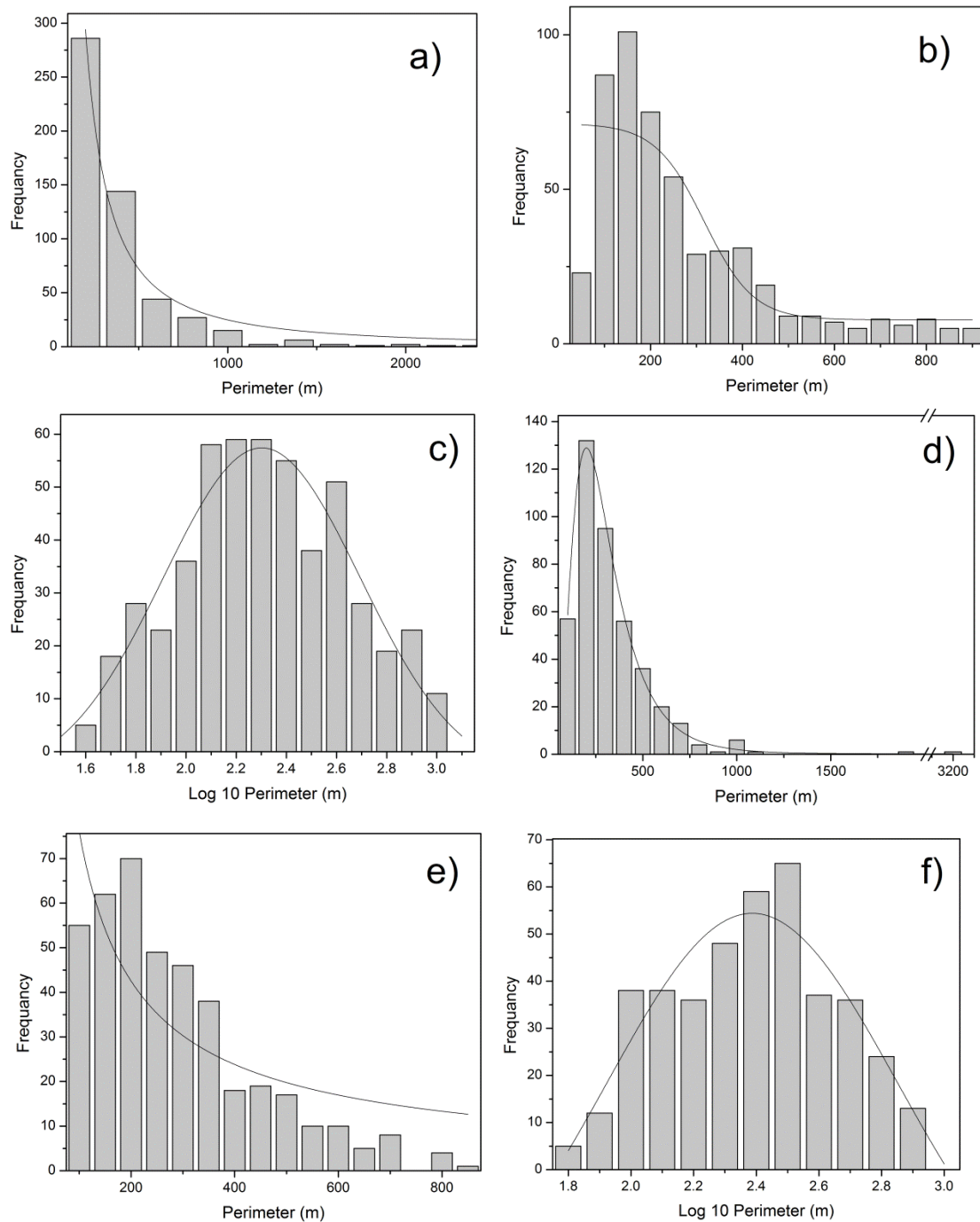


Figure 5-3. Frequency distribution of perimeter of sinkholes in the Zhijin area. a) From the field-based approach. b) From the field-based approach after excluding large outliers. c) Log-transformed distribution from the field-based approach without the outliers. d) From the semi-automatic approach. e) From the semi-automatic approach after excluding large outliers. f) Log-transformed distribution from the semi-automatic approach without the outliers.

Sinkhole perimeter values in the Wering area are more variable than those in the Zhijin area (Fig. 5-4a and c). The perimeter values derived from both approaches are skewed to length < 1,000 m with some extremely long outliers. The outliers selected are sinkholes with

perimeters > 800 m for the field-based approach and > 600 m for the semi-automatic approach. After the outliers excluded, the logarithmic perimeters of the sinkholes are normally distributed (Fig. 5-4b and d).

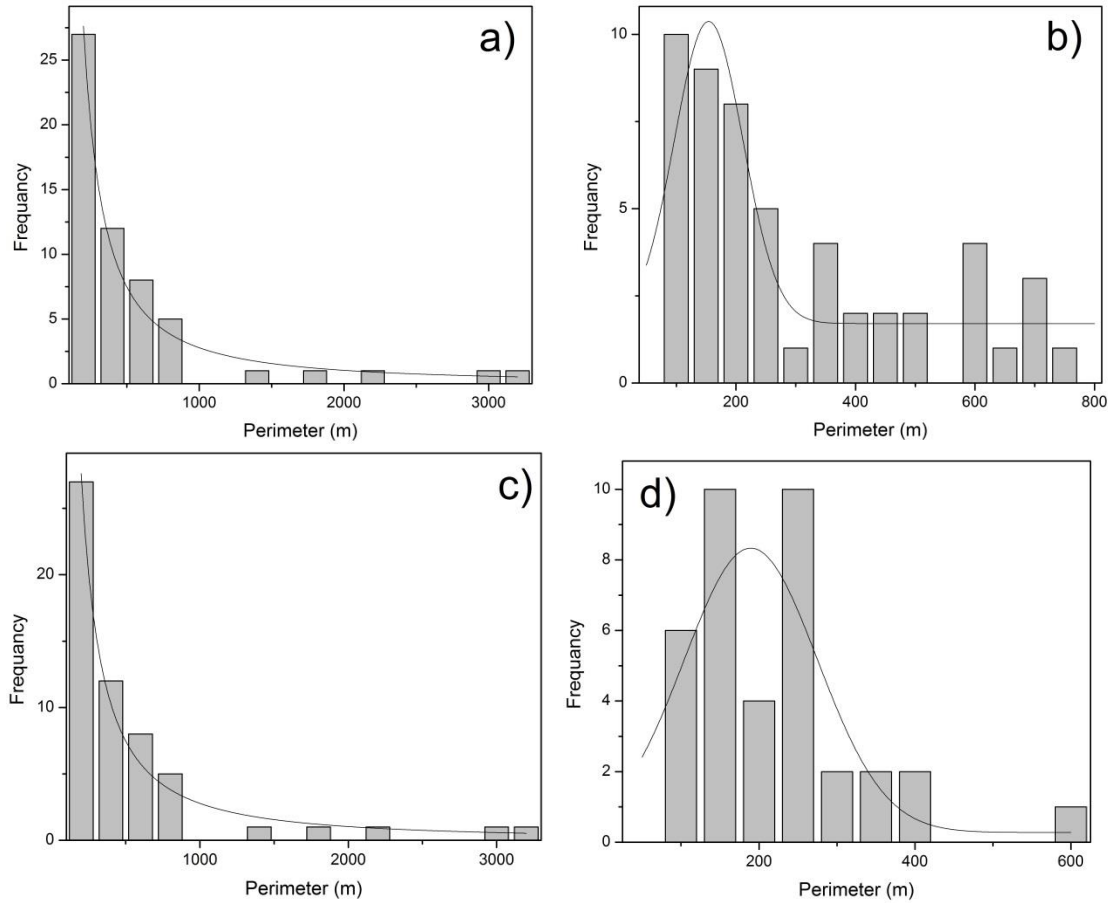


Figure 5-4. Frequency distribution of perimeter of sinkholes in the Weining area. a) From the field-based approach. b) From the field-based approach after excluding large outliers. c) From the semi-automatic approach. d) From the semi-automatic approach after excluding large outliers.

5.2.3. Long-axis length

Fig. 5-5 shows the distribution of sinkhole long-axis length in the Zhijin area skewed to < 100 m. After removing large outliers, a relatively normal frequency distribution is observed.

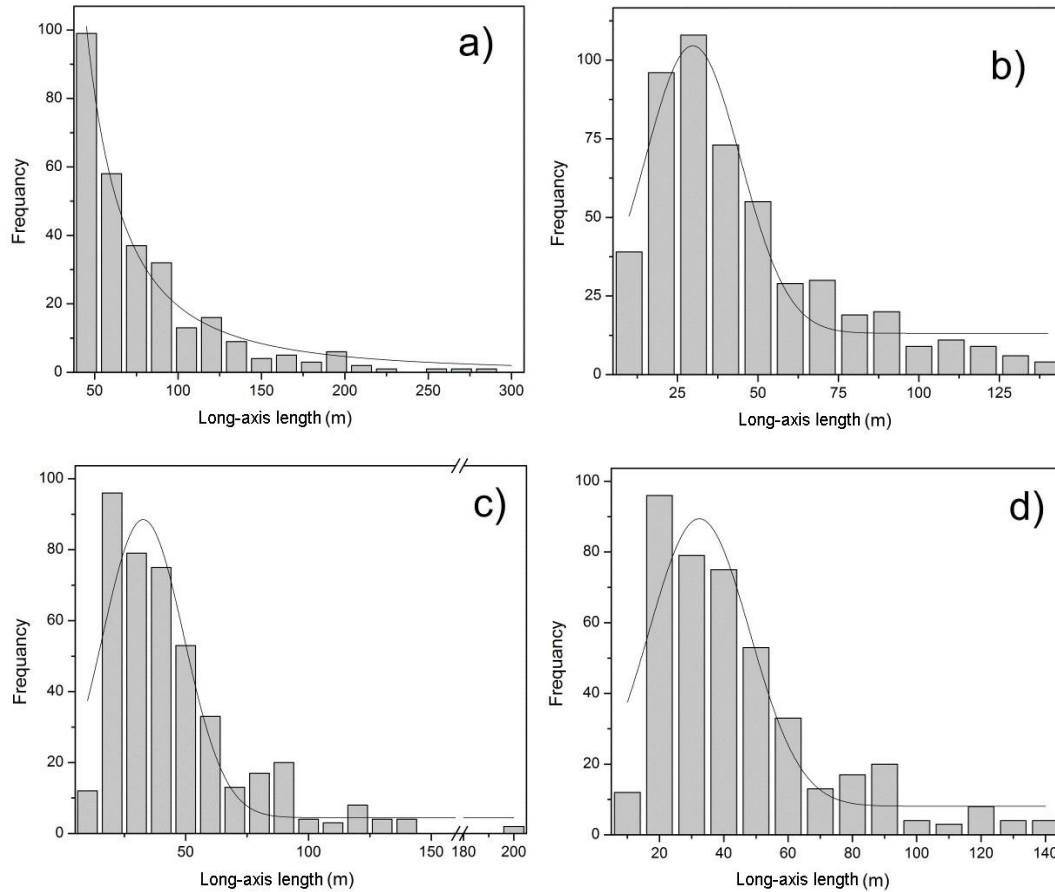


Figure 5-5. Frequency distribution of long-axis length of sinkholes in the Zhijin area. a) From the field-based approach. b) From the field-based approach after excluding large outliers. c) From the semi-automatic approach. d) From the semi-automatic approach after excluding large outliers.

The long-axis lengths of the sinkholes in the Weining area are shown in Fig. 5-6. The range in the Weining area is larger than that in the Zhijin area. The values from the field-based approach skew to < 100 m and a relatively normal distribution is found after the outliers are removed (Fig. 5-6a and b). As shown in Fig. 4-9c, the sinkhole long-axis length from the semi-automatic approach has a smaller range than that from the field-based approach. However, the values from the semi-automatic approach are also roughly normally distributed.

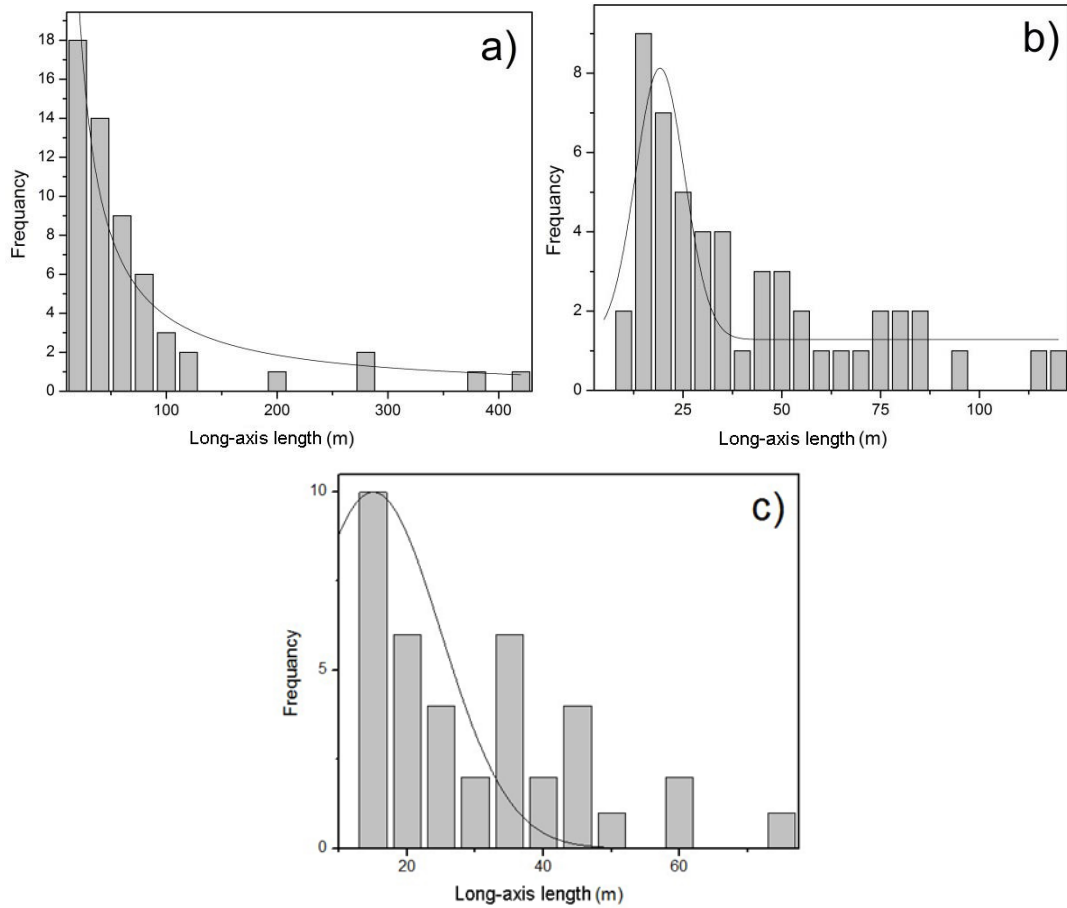


Figure 5-6. Frequency distribution of long-axis length of sinkholes in the Weining area. a) From the field-based approach. b) From the field-based approach after excluding large outliers. c) From the semi-automatic approach.

5.2.4. Ellipticity

The ellipticity value in the Zhijin area ranges from 0 to 0.99 with a mean of 0.78 and a standard deviation of 0.15 (Table 4-3). The distribution of the ellipticity is skewed to the right but roughly normally distributed (Fig. 5-7).

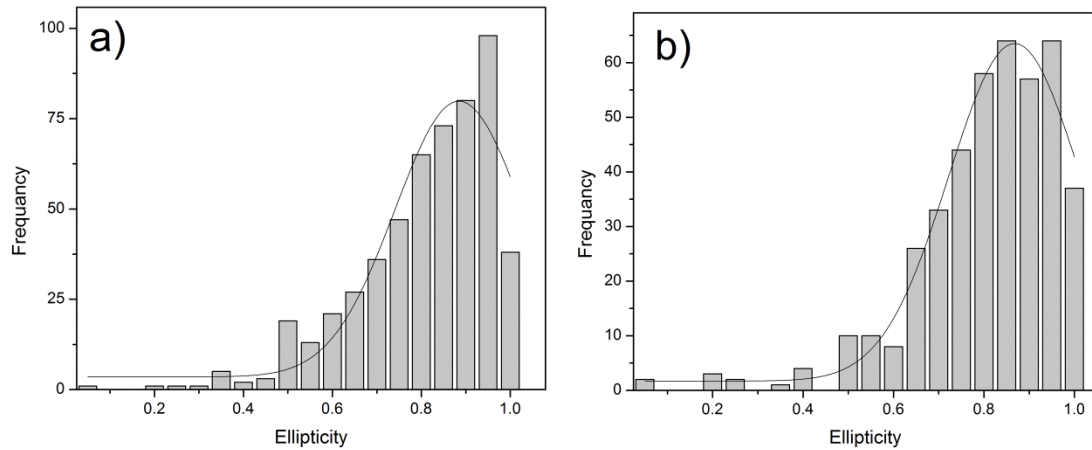


Figure 5-7. Frequency distribution of ellipticity of sinkholes in the Zhijin area. a) From the field-based approach. b) From the semi-automatic approach.

The ellipticity values in the Weining area have a smaller range than those in the Zhijin area. The ellipticity from the field-based approach ranges from 0.23 to 0.97 with a mean of 0.73 and a standard deviation of 0.16 (Table 4-4). The ellipticity from the semi-automatic approach ranges from 0.31 to 0.92 with a mean of 0.71 and a standard deviation of 0.16 (Table 4-4). The mathematical distribution of the ellipticity from the two approaches tends to be normal.

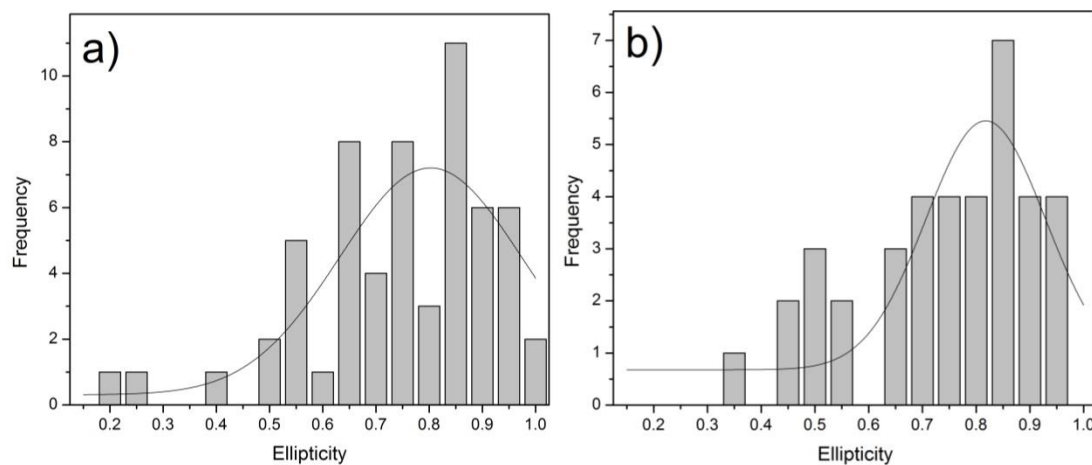


Figure 5-8. Frequency distribution of ellipticity of sinkholes in the Weining area. a) From the field-based approach. b) From the semi-automatic approach.

5.2.5. Orientation

The orientation of the sinkhole long-axis ranges from 0° to 180° (Table 4-3). For the two approaches, the orientation population in the Zhijin area is relatively evenly distributed but is slightly skewed to the value < 80° (Fig. 5-9).

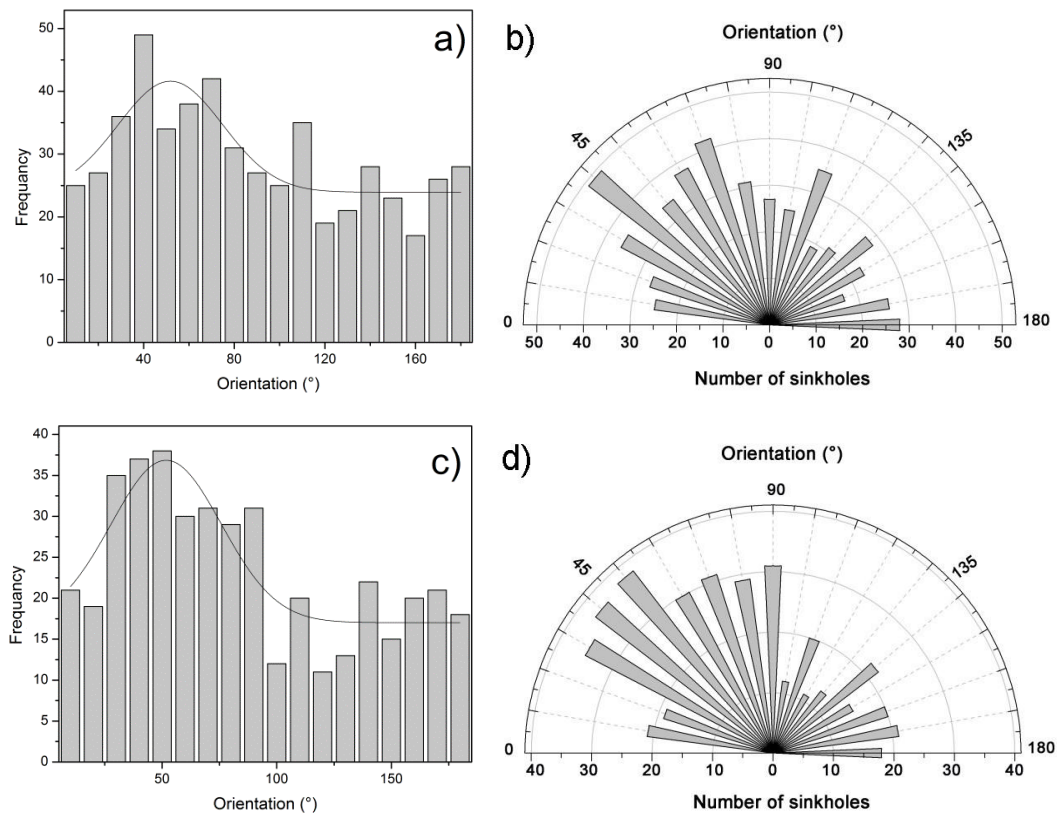


Figure 5-9. Frequency distribution of long-axis orientation of sinkholes in the Zhijin area. a) From the field-based approach in histogram. b) From the field-based approach in rose diagram. c) From the semi-automatic approach in histogram. c) From the semi-automatic approach in rose diagram.

The long-axis orientation in the Weining area has some peaks: 50°, 130° and 140° for the field-based approach and 80° and 140° for the semi-automatic approach (Fig. 5-10). The distribution is uneven.

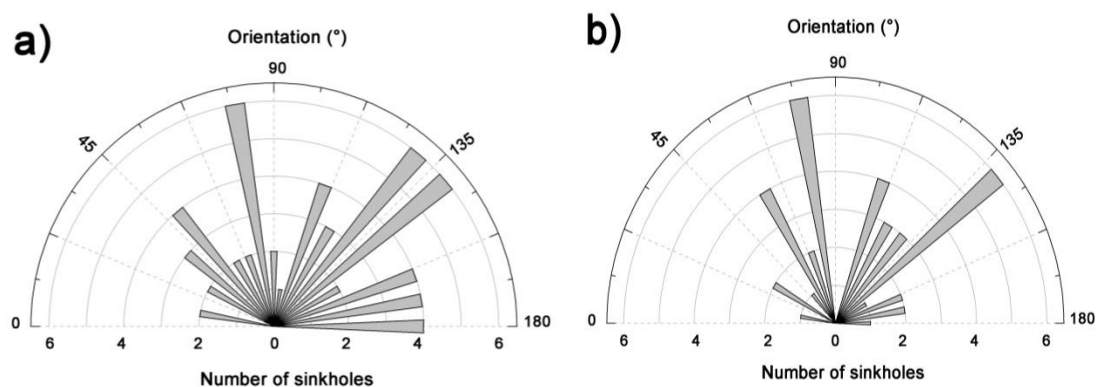


Figure 5-10. Frequency distribution of long-axis orientation of sinkholes in the Weining area. a) From the field-based approach. b) From the semi-automatic approach.

5.2.6. Depth

The sinkhole depth in the Zhijin area ranges from 1 to 110 m with mean and *SD* values of ~15 to 20 m for both approaches (Table 4-3). As shown in Fig. 5-11a, > 60% of the sinkhole depth derived from both approaches are > 20 m, demonstrating a predominance of deep sinkholes.

The sinkhole depth in the Weining area is smaller than that in the Zhijin area. The depth from the field-based approach ranges from 0 to 11 m with a mean of 1.27 and an *SD* value of 2.06 m (Table 4-4). The sinkhole depth from the semi-automatic approach is in a smaller range than that from the field-based approach. The depth ranges from 0 to 3 m with a mean of 0.33 and an *SD* value of 1.04 m (Table 4-4). As shown in Fig. 5-11b, > 90% of the sinkhole depth derived from both approaches are < 3 m, demonstrating a predominance of shallow sinkholes.

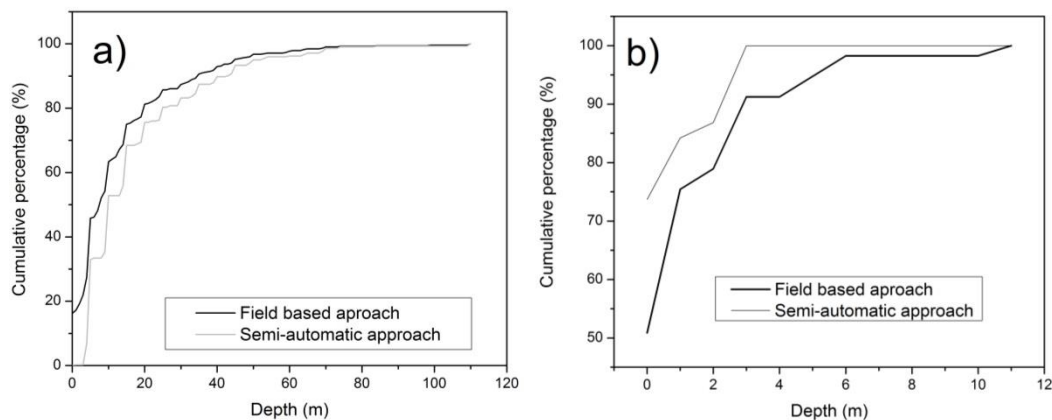


Figure 5-11. The statistics related with sinkhole depth: a) Sinkhole depth frequency distribution in the Zhijin area; b) Sinkhole depth frequency distribution in the Weining area

5.2.7. Volume

The sinkhole volume shows a large range and *SD* (Table 4-3). The population is not normally distributed but skewed strongly to smaller values, and there are extremely large outliers (Fig. 5-12a and c). After these outliers are removed and a log transformation was performed, the distribution becomes more normal (Fig. 5-12b and d).

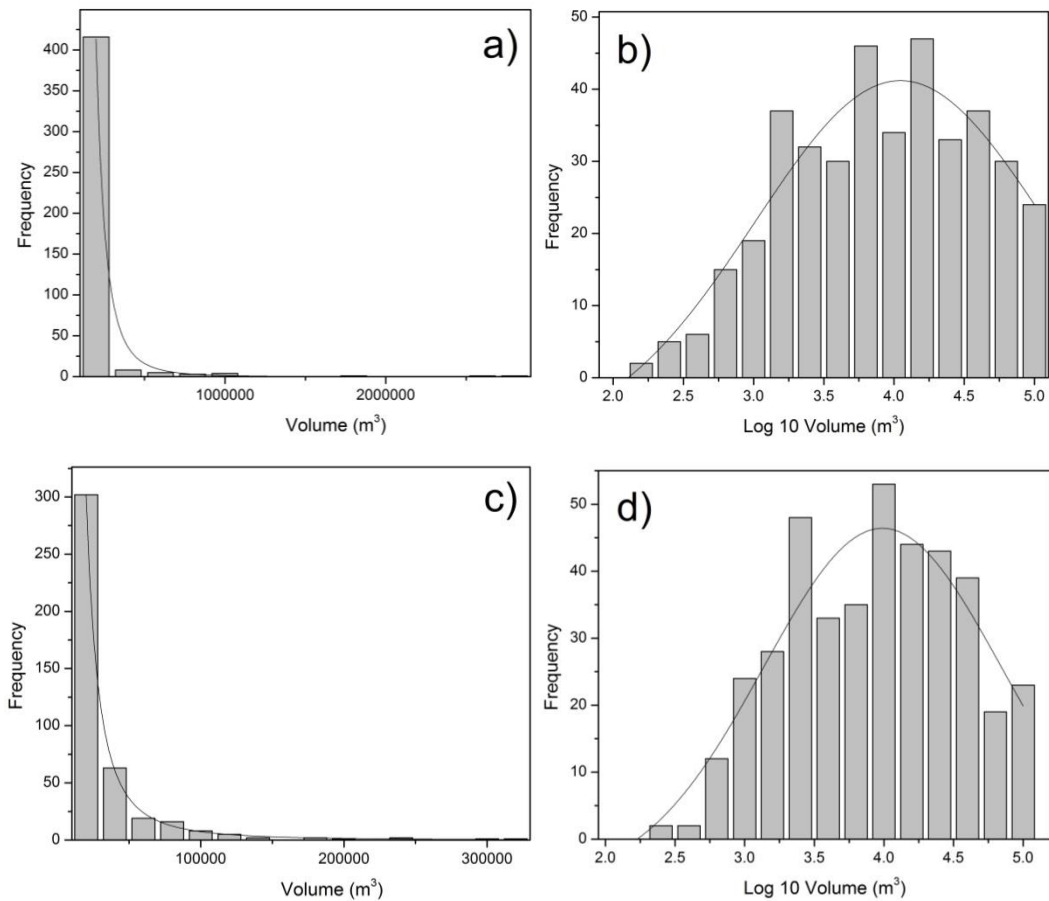


Figure 5-12. Frequency distribution of volume of sinkholes in the Zhijin area. a) From the field-based approach. b) From the field-based approach after excluding large outliers. c) From the semi-automatic approach. d) From the semi-automatic approach after excluding large outliers.

The volume population in the Weining area also clusters in small volume (Fig. 5-13). The data number is small so outlier removal and long-transformation were not performed. The sinkhole volume in the Weining area has a smaller range than in the Zhijin area.

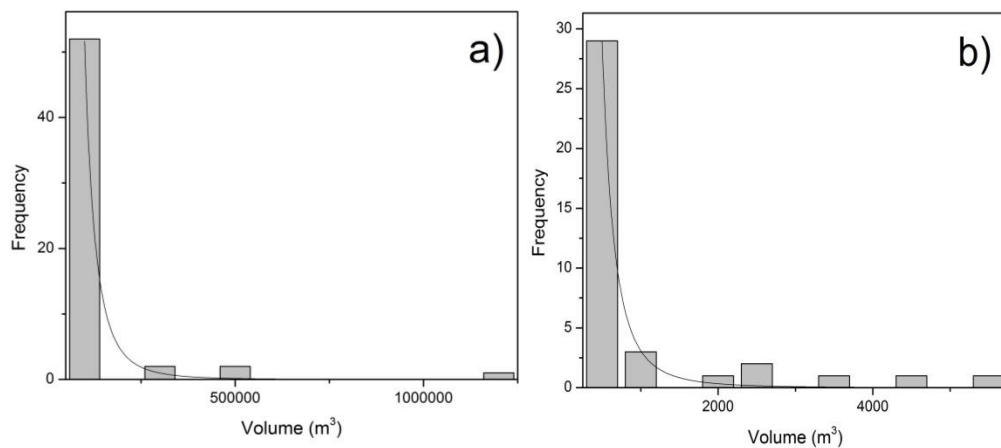


Figure 5-13. Frequency distribution of volume of sinkholes in the Weining area. a) From the

field-based approach. b) From the semi-automatic approach.

Fig. 5-14 shows the relation between sinkhole volume and area in the Zhijin area. Positive correlations are found but in the Zhijin area, their relation is linear. The pattern for the Weining area is difficult to assess because the data number is small. The field-based approach and the semi-automatic approach gave similar results in both areas.

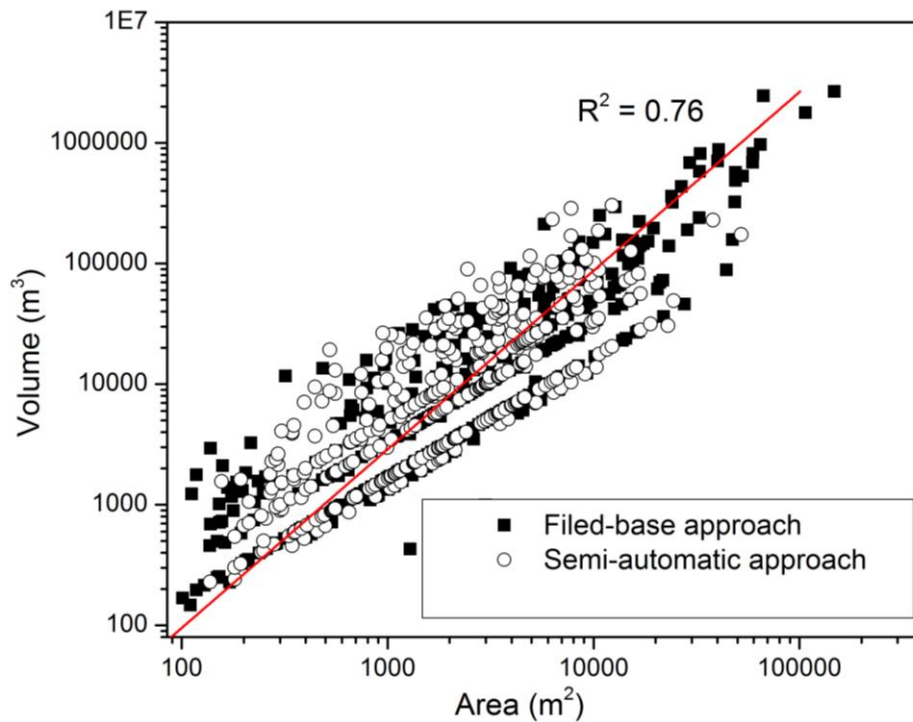


Figure 5-14. Distribution of sinkhole area as a function of volume in the Zhijin area with the field-based and semi-automatic approaches.

5.3. Morphometric analysis of tower and cockpit karst hills

5.3.1. Area

The area of the cockpit karst hill has a broader range with a larger standard deviation than that of the tower karst hill in both study areas (Tables 4-7 and 4-10). As shown in Fig. 5-15a and b, the tower karst hill area skews to area < 12,000 m² which includes 97.94% of the hills. After the exclusion of the unusual large hills (Fig. 5-15c), a log transformation was adopted to normalize the data. The cockpit karst hill area skews to the area < 20,000 m² which includes 93.03% of the hills (Fig. 5-15d and e). A log transformation was also applied to normalize the cockpit karst hill area of < 20,000 m² (Fig. 5-15f).

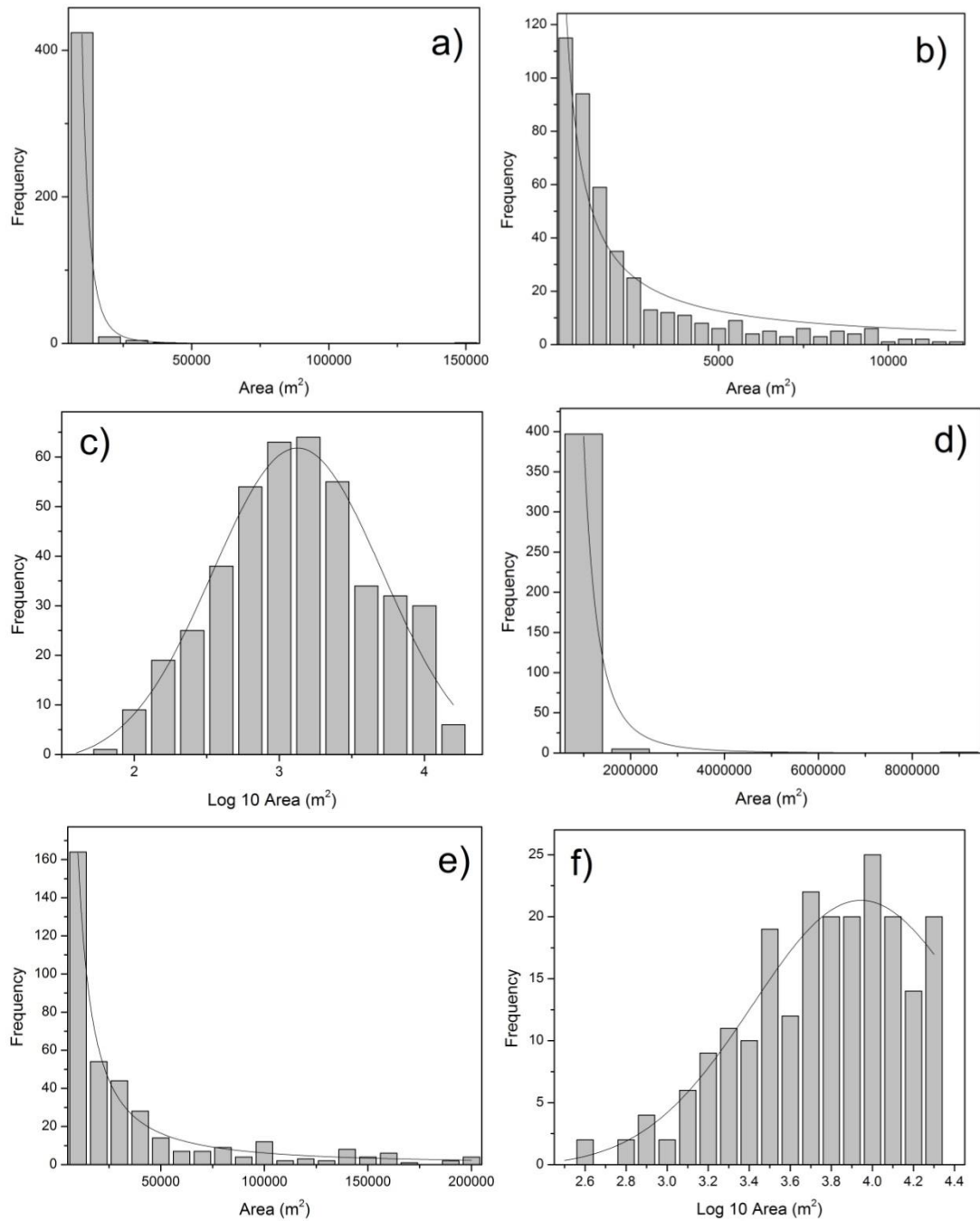


Figure 5-15. The distribution of hill areas in the Zhijin area. a) All tower karst hills with a skewed distribution. b) Tower karst hills except large outliers. c) Log-transformed normalized tower karst hill area. d) All cockpit karst hills with a skewed distribution. e) Cockpit karst hills except large outliers. f) Log-transformed normalized cockpit karst hills.

The area of the tower karst hills in the Weining area does not show a normal distribution and skewed to the area < 80,000 m² which includes 96.43% of hills (Fig. 5-16a and b). As shown in Fig. 5-16c, the area of the tower karst hills shows a normal distributed after log-transformation and exclusion of outliers. The cockpit karst hills area is skewed to the area < 200,000 m² with hills of 82.86% (Fig. 5-16d and e). As shown in Fig. 5-16f, without the outliers

(area > 200, 00 m²), the area after log transformation is normal distributed.

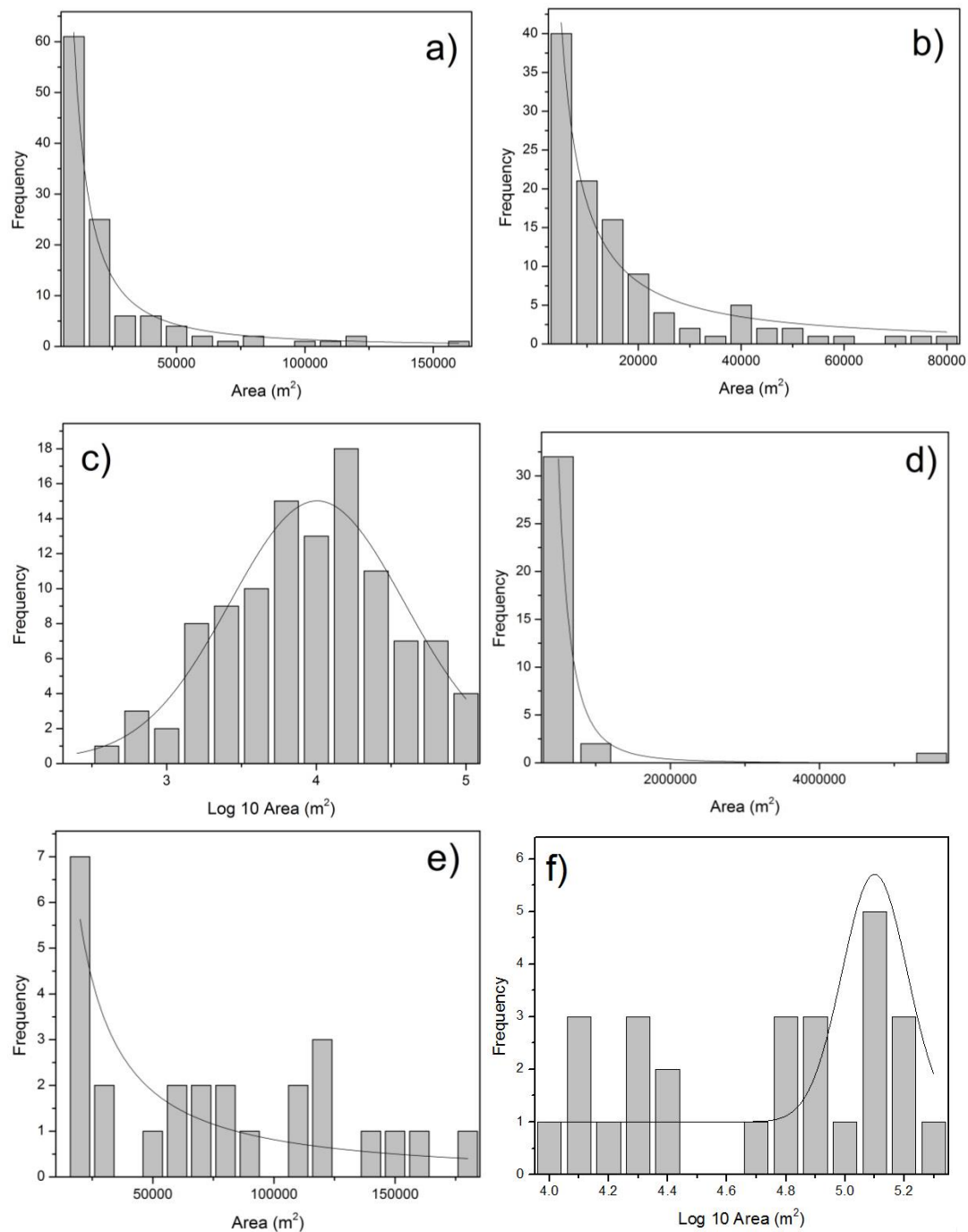


Figure 5-16. The distribution of hill areas in the Weining area. a) All tower karst hills with a skewed distribution. b) Tower karst hills except large outliers. c) Log-transformed normalized tower karst hill area. d) All cockpit karst hills with a skewed distribution. e) Cockpit karst hills except large outliers. f) Log-transformed normalized cockpit karst hills.

5.3.2. Perimeter

Perimeter data for the study areas show large ranges (Tables 4-7 and 4-10). The perimeter

of the tower karst hill is somewhat normally distributed in the Zhijin area (Fig. 5-17a), but that of the cockpit karst hill is not (Fig. 5-17b) and skewed to the perimeter < 10,000 m (Fig. 5-17c). Normalization is possible with a log transformation (Fig. 5-17d).

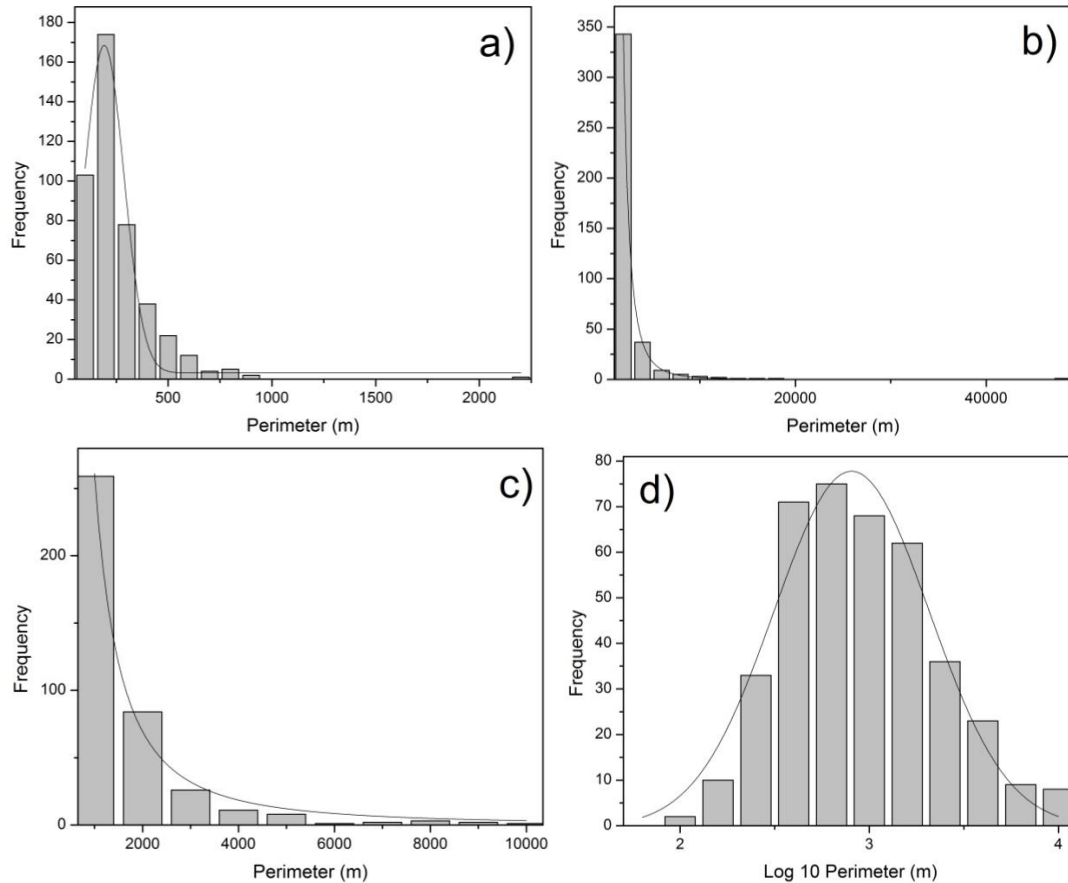


Figure 5-17. The distribution of hill perimeter in the Zhijin area. a) All tower karst hills with a somewhat normal distribution. b) All cockpit karst hills with a skewed distribution. c) Cockpit karst hills except large outliers. d) Log-transformed normalized cockpit karst hills.

The perimeter characteristics in the Weining area are similar to those in the Zhijin area. The cockpit karst hill has a larger perimeter range than that of the tower karst. Perimeter of the tower karst hill shows relatively normal distribution (Fig. 5-18a) while that of the cockpit karst hill is not (Fig. 5-18b). Without the outliers (perimeter > 3,000 m), the perimeter of the cockpit karst hill is relatively normally distributed (Fig. 5-18c).

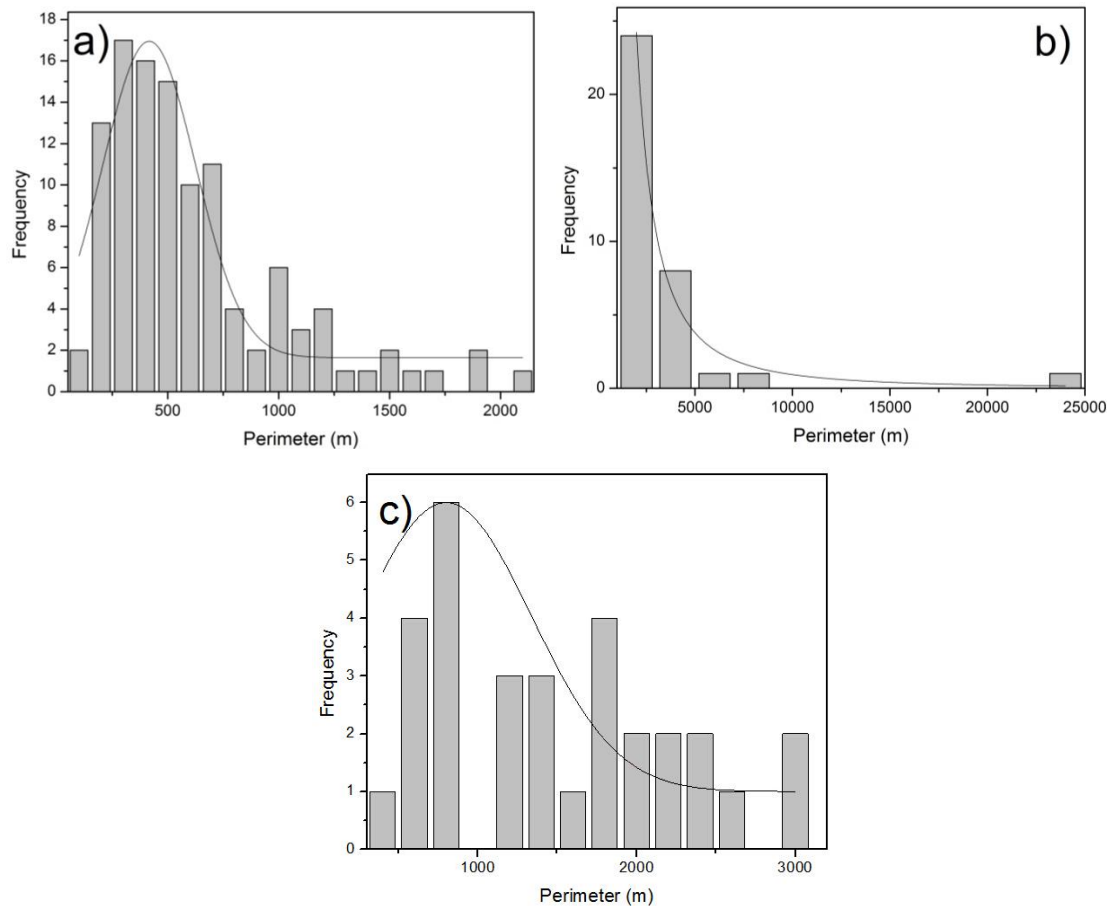


Figure 5-18. The distribution of hill perimeter in the Weining area. a) All tower karst hills with a normal distribution. b) All cockpit karst hills with a skewed distribution. c) Cockpit karst hills except large outliers.

5.3.3. Long-axis length

As shown in Table 4-7, the long-axis length of the cockpit karst hills in the Zhijin area has a larger range than that of the tower karst hills. The long-axis length of the karst hills are not normally distributed (Fig 5-19a and d); as shown in Fig. 4-24a and b, 99.54 % of the tower karst hills have long-axis length < 140 m, and for the cockpit karst hills, 97.52% are < 700 m (Fig. 5-19d and e). Their distribution can be normalized with log transformation after outliers (> 150 m) are excluded. (Fig. 5-19c and f).

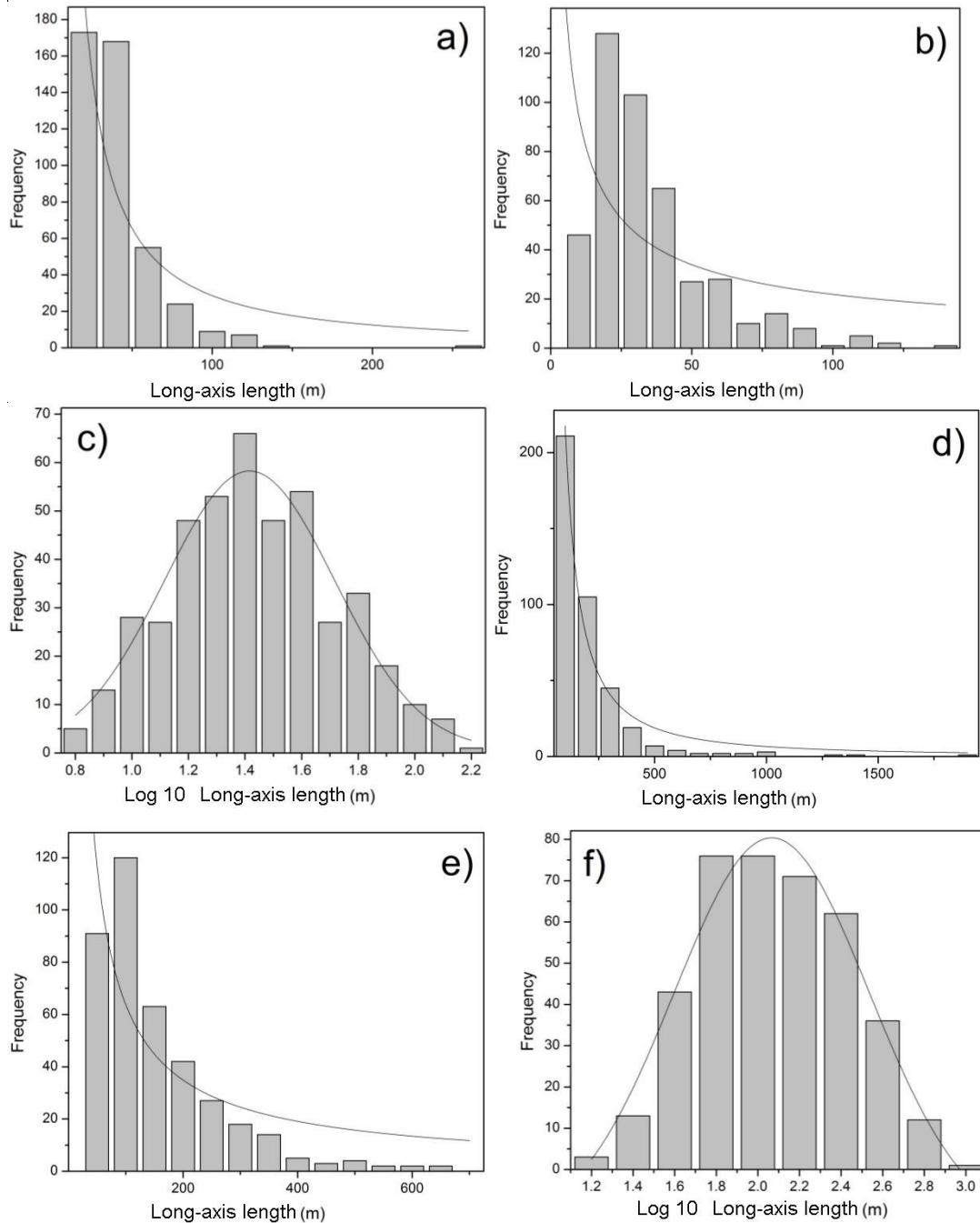


Figure 5-19. The distribution of hill long-axis length in the Zhijin area. a) All tower karst hills with a skewed distribution. b) Tower karst hills except large outliers. c) Log-transformed normalized tower karst hill area. d) All cockpit karst hills with a skewed distribution. e) Cockpit karst hills except large outliers. f) Log-transformed normalized cockpit karst hills.

The long-axis length in the Weining area has similar characteristics to that in the Zhijin area in that the cockpit karst hills show a larger value range than that the tower karst hills (Table 4-10). However, the long-axis length of all the tower karst hills are more normally distributed (Fig. 5-20a). As shown in Fig. 5-20b and c, 84.62% of the long-axis lengths of the cockpit karst hills are in the range of 0–800 m. Without the outliers (> 800 m), they are normally distributed

with after log transformation (Fig. 5-20d).

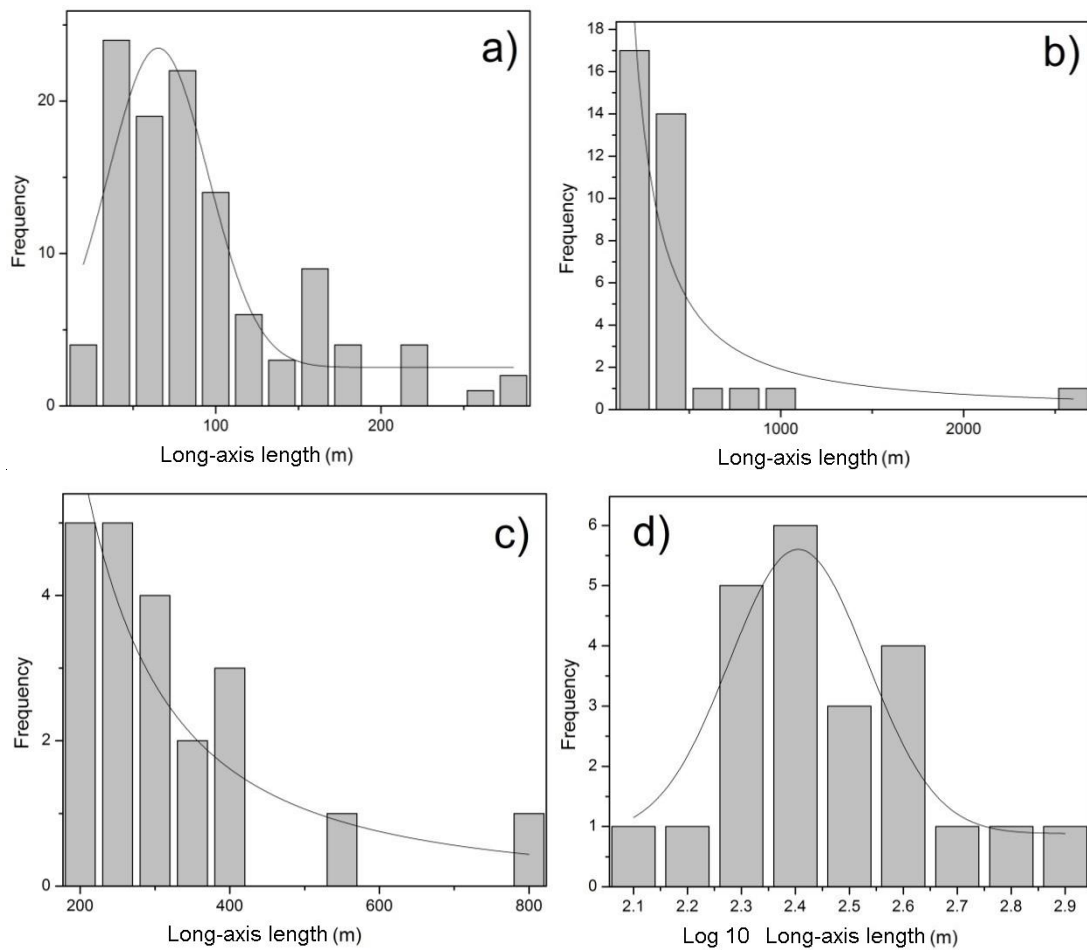


Figure 5-20. The distribution of hill long-axis length in the Weining area. a) All tower karst hills with a normal distribution. b) All cockpit karst hills with a skewed distribution. c) Cockpit karst hills except large outliers. d) Log-transformed normalized cockpit karst hills.

5.3.4. Orientation

The orientation of the tower karst hills in the Zhijin area shows the whole possible range (0° – 180°), which is wider than that of the cockpit karst hills (0.27° – 178.51°) (Table 4-7). The orientation rose diagrams with a bin of 10° are shown in Fig. 5-21. The orientation of the tower and cockpit karst hills is generally distributed in all range with slightly skewed to some peak values. The peak values of the cockpit karst hills appears in the range $< 50^{\circ}$ (30° and 50°) (Fig. 5-21b), and those of the tower karst hills are found at 10° , 40° , 70° , 90° and 140° (Fig. 5-21a).

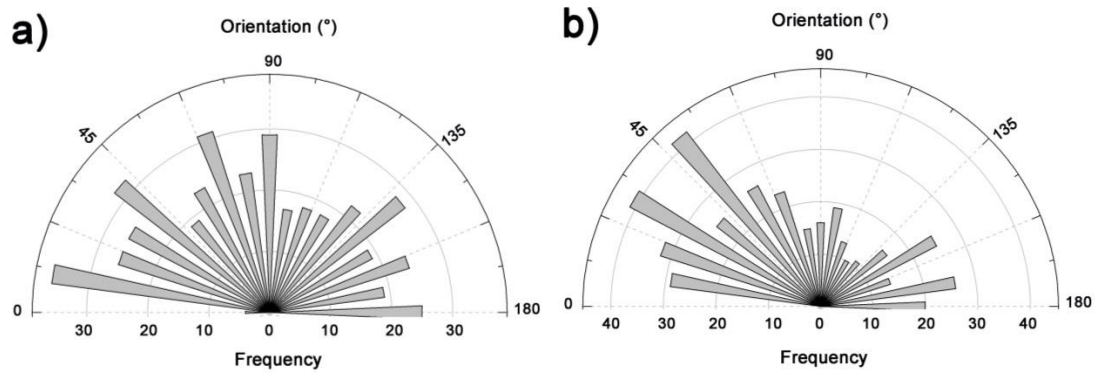


Figure 5-21. The distribution of hill orientation in the Zhijin area. a) All tower karst hills with a skewed distribution. b) All cockpit karst hills with a skewed distribution.

The orientation of hills in the Weining area is similar to that in the Zhijin area in that the values of the tower karst hills show a wider range (0.31° – 179.12°) than those of the cockpit karst hills (0.42° – 174.49°) (Table 4-10). The orientation range in the Weining area is smaller than that in the Zhijin area, reflecting smaller data sizes. The orientation distribution characteristics of the tower and cockpit karst hills have several similarities. As shown in Fig. 5-22, the orientation around 90° is less frequent while there are peaks around 45° and 135° .

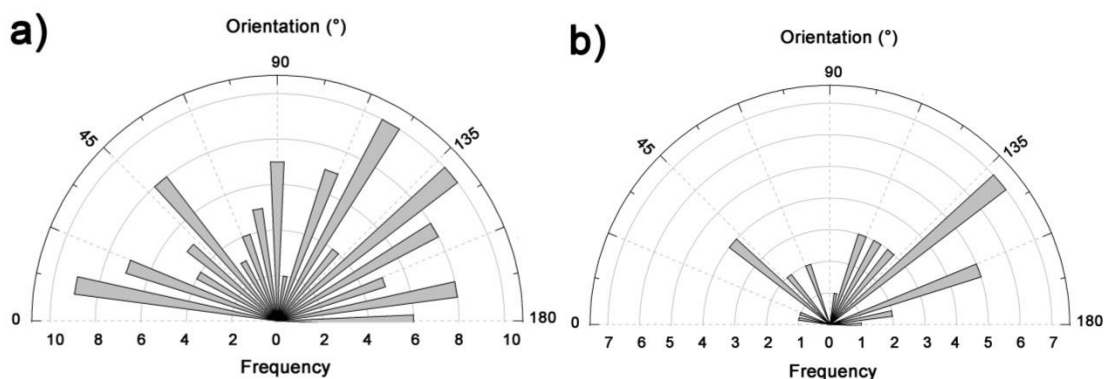


Figure 5-22. The distribution of hill orientation in the Weining area. a) All tower karst hills with a skewed distribution. b) All cockpit karst hills with a skewed distribution.

5.3.5. Relief

The relief of the cockpit karst hills in the Zhijin area is in a larger span than that of the tower karst hills (Table 4-7). The reliefs of the tower karst hills cluster in the value < 40 m (Fig. 5-23a and b). Without outliers (> 30 m), the reliefs of the tower karst hills are somewhat normally distributed with a log transformation (Fig. 5-23c). The cockpit karst hills' reliefs are skewed to the value < 150 m (Fig 5-23d and e). Without outliers, it also somewhat normally distribute with a log transformation (Fig. 5-23f).

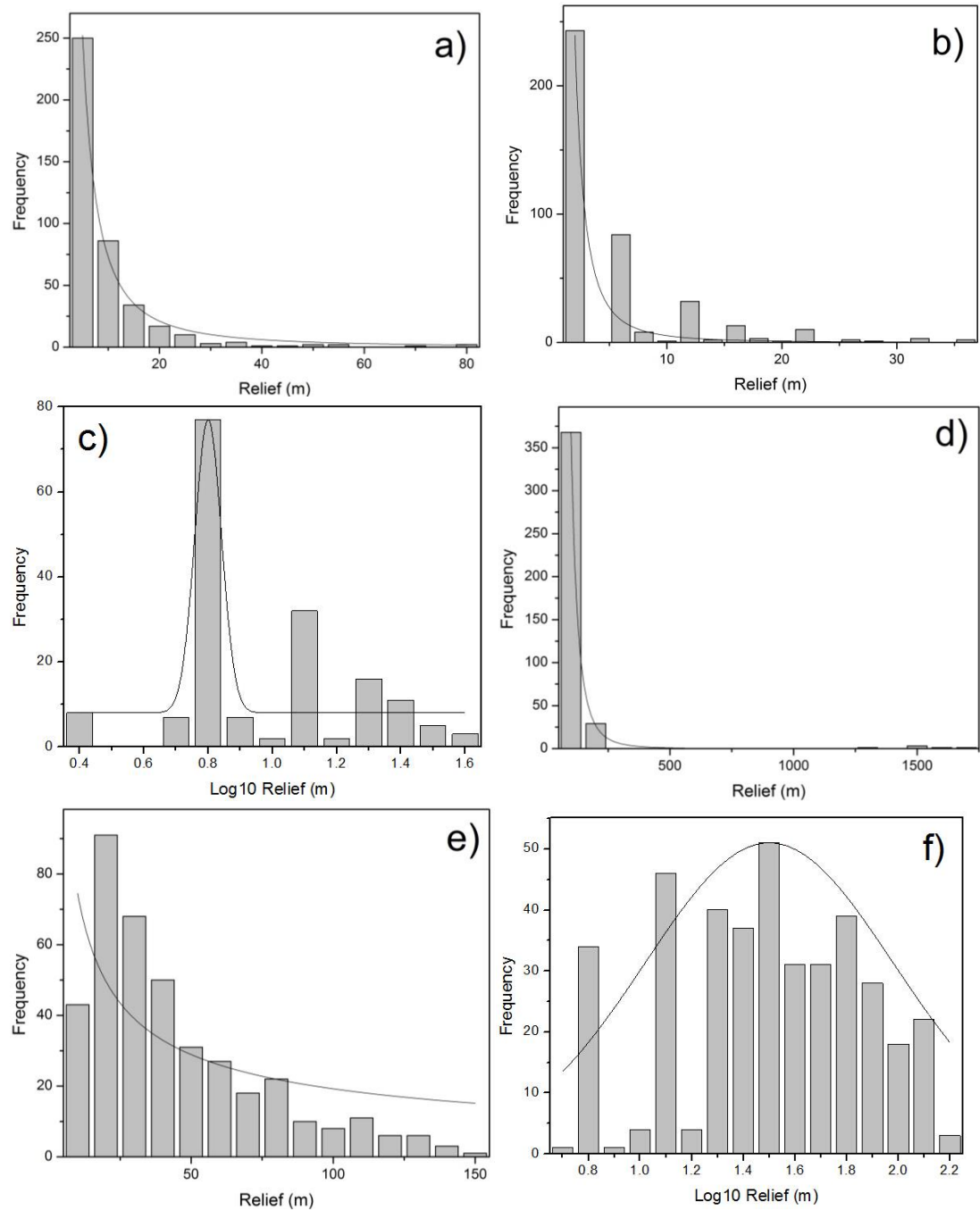


Figure 5-23. The distribution of hill relief in the Zhijin area. a) All tower karst hills with a skewed distribution. b) Tower karst hills except large outliers. c) Log-transformed normalized tower karst hill area. d) All cockpit karst hills with a skewed distribution. e) Cockpit karst hills except large outliers. f) Log-transformed normalized cockpit karst hills.

It is similar with the situation in the Zhijin area that the reliefs of the cockpit karst hills in the Weining area are also in a broader span than that of the tower karst hills (Table 4-10). The reliefs of the tower karst hills mainly distribute in the value < 30 m (Fig. 5-24a) and are somewhat normally distributed in value < 25 (Fig. 5-24b). The reliefs of the cockpit karst hills are also skewed in the range of 1 to 70 m (Fig. 5-24c). Without outliers (> 70 m), the relief

somewhat normally distribute with a log transportation (Fig. 5-24d).

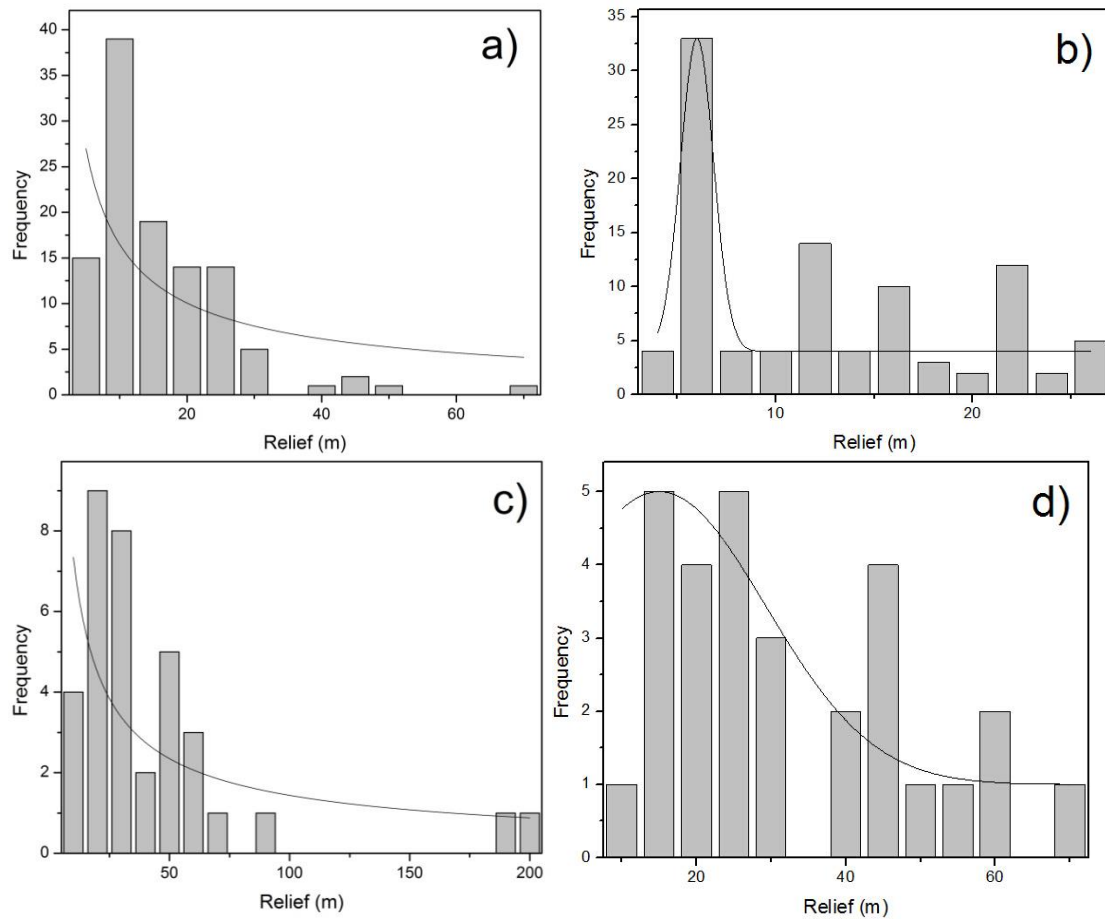


Figure 5-24. The distribution of hill relief in the Weining area. a) All tower karst hills with a skewed distribution. b) Tower karst hills except large outliers. c) All cockpit karst hills with a skewed distribution. d) Cockpit karst hills except large outliers.

5.3.6. Relative relief

Table 4-7 shows that the relative reliefs' range of the cockpit karst hills is much larger than that of the tower karst hills in the Zhijian area. The relative reliefs of the tower karst hills are in a skewed nature (Fig. 5-25a). 97.82% of the values occupy in relative relief $< 1.89 \text{ m/m}^2$ (Fig. 5-25b). Without outliers ($> 2 \text{ m/m}^2$), the normalization is completed by a log transformation (Fig. 5-25c). For the cockpit karst hills, 97.52% of relative reliefs cluster in the range of $0.02\text{--}1.17 \text{ m/m}^2$ (Fig. 5-25d). In this range, the relative relief values of the cockpit karst hills normally distribute with a log transformation (Fig. 5-25e).

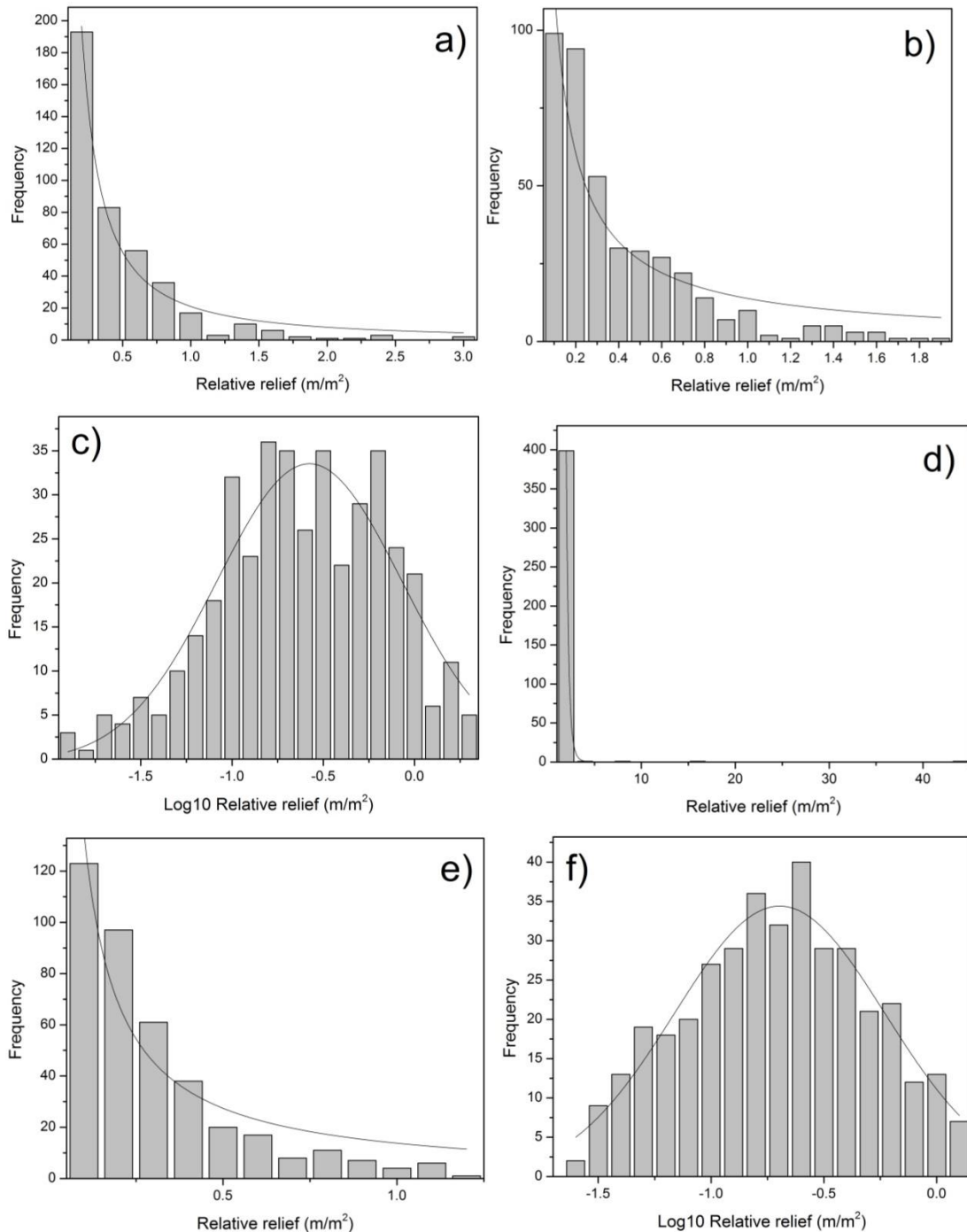


Figure 5-25. The distribution of hill relative relief in the Zhijin area. a) All tower karst hills with a skewed distribution. b) Tower karst hills except large outliers. c) Log-transformed normalized tower karst hill area. d) All cockpit karst hills with a skewed distribution. e) Cockpit karst hills except large outliers. f) Log-transformed normalized cockpit karst hills.

The relative reliefs' range of the tower karst hills is larger than that of the cockpit karst hills in the Weining area (Table 4-10). As shown in Fig. 5-26a, the relative reliefs of the tower karst hills are skewed. With a log transformation, they are somewhat normally distributing (Fig. 5-26a). And, the relative reliefs of the cockpit karst hills are in a somewhat normal distribution

(Fig. 5-26c).

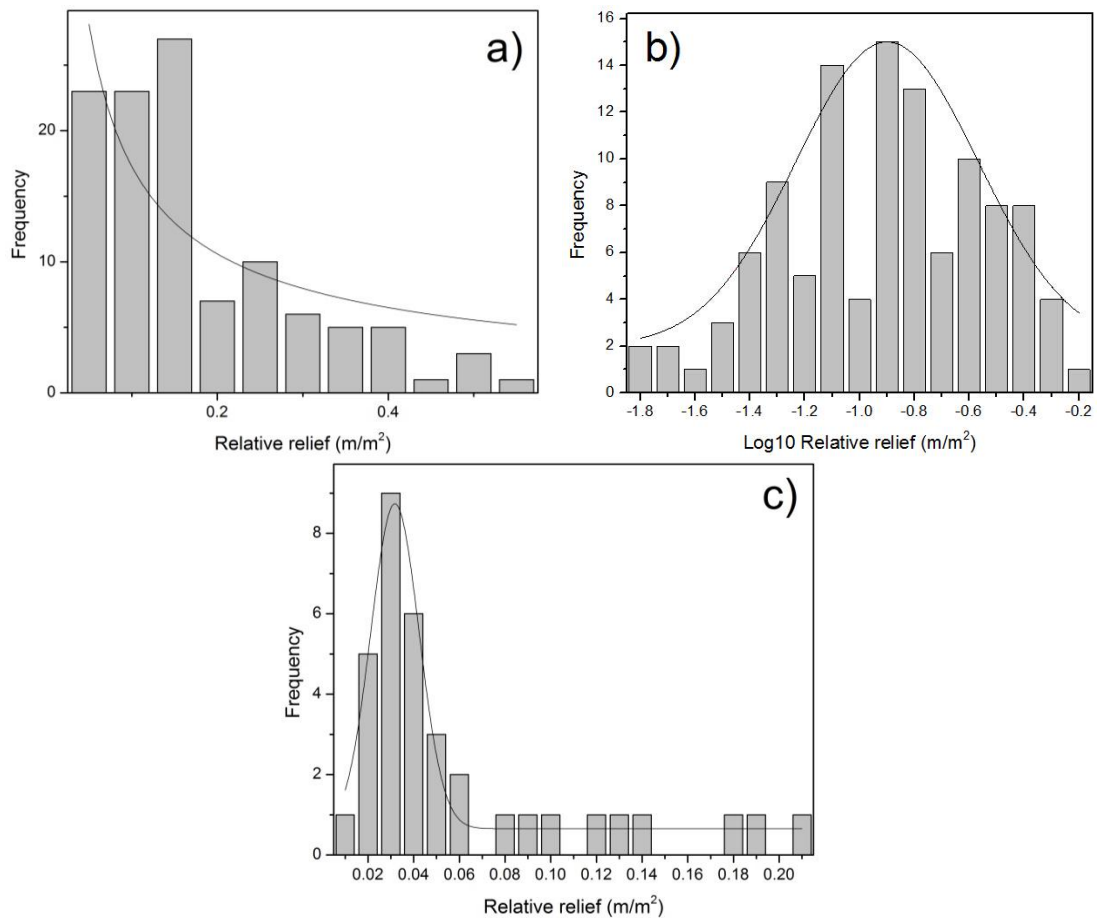


Figure 5-26. The distribution of hill relative relief in the Weining area. a) All tower karst hills with a skewed distribution. b) Log-transformed normalized tower karst hill area. c) All cockpit karst hills with a somewhat normal distribution.

5.3.7. Slope

The slopes of the cockpit karst hills cover a larger range than that of the tower karst hills in the Zhijin area (Table 4-7). As shown in Fig. 5-27, the slopes of the tower and cockpit karst hills are somewhat normally distributed. The slopes of the tower and cockpit karst hills cluster in 4°–6° and 28°–30°, respectively.

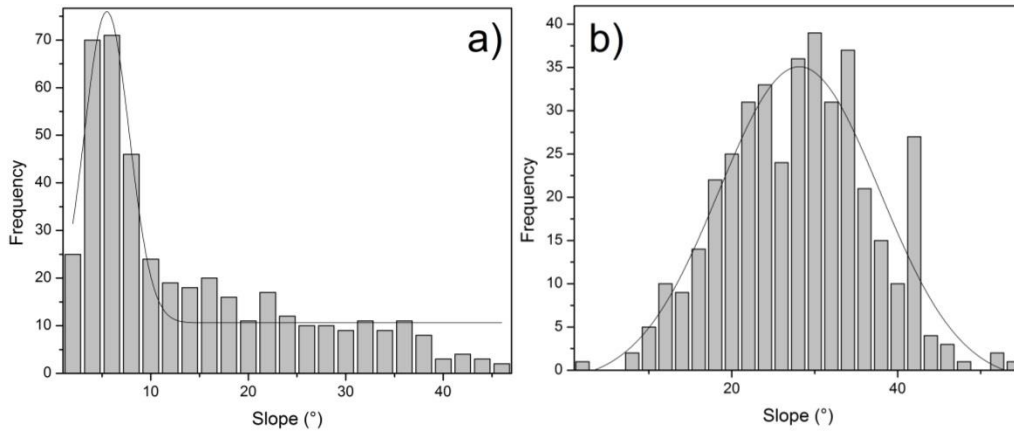


Figure 5-27. The distribution of hill slope in the Zhijin area. a) All tower karst hills with a somewhat normal distribution. b) All cockpit karst hills with a somewhat normal distribution.

The slope range of the cockpit karst hills is also larger than that of the tower karst hills in the Weining area (Table 4-10). The slopes of the tower and cockpit karst hills in the Weining area are somewhat normally distributed with similar mean values (Table 4-10).

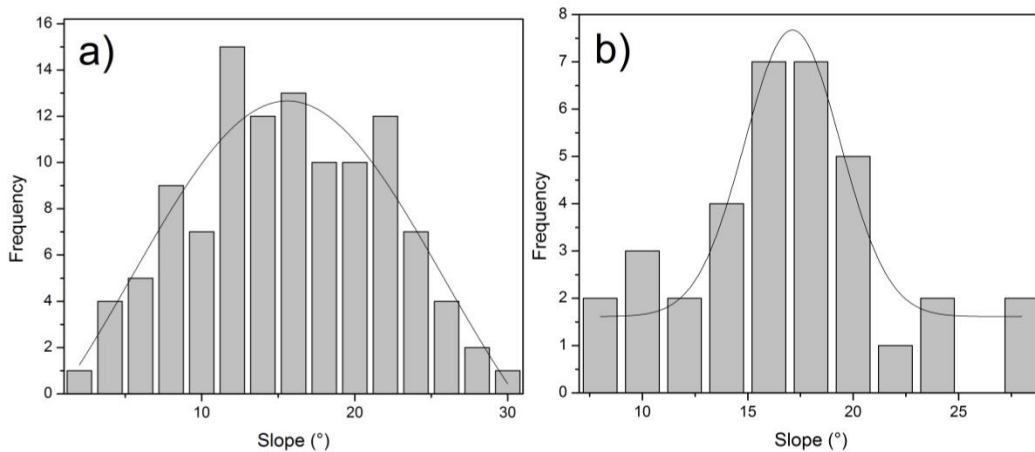


Figure 5-28. The distribution of hill slope in the Weining area. a) All tower karst hills with a somewhat normal distribution. b) All cockpit karst hills with a somewhat normal distribution.

5.3.8. Aspect

As shown in Fig. 5-29, the aspect distribution of the tower and cockpit karst hills are different in the Zhijin area. Although the aspects of the tower karst range from 3.73° to 271.66° (Table 4-7), the majority are found from Northeast to South aspect (Fig. 5-29a). The aspects of the tower karst hills cluster in 40° – 60° . For the cockpit karst hill, the value range is also from Northeast to South aspect (Table 4-7). However, the majority are in the Southeast and South aspect (Fig. 5-29b). The aspects of the cockpit karst hills cluster in 160° – 180° .

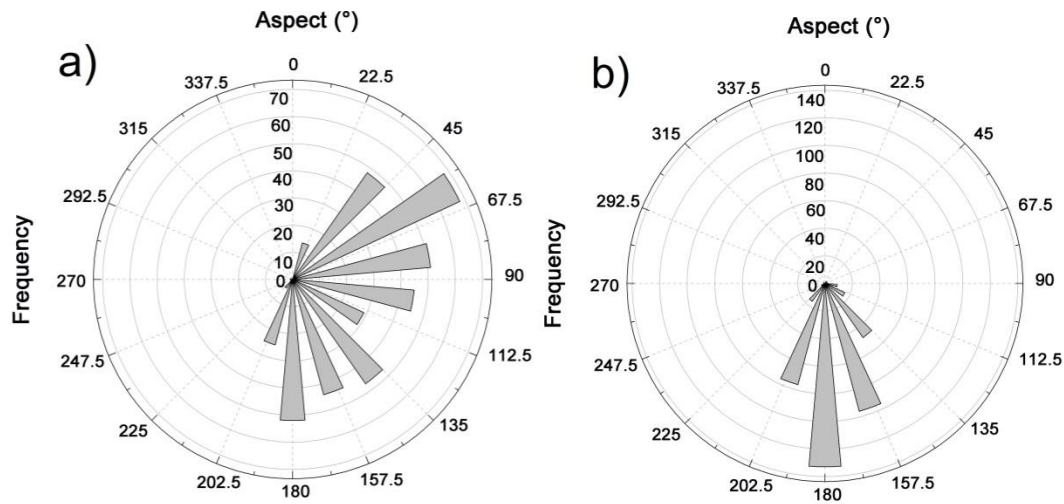


Figure 5-29. The distribution of hill aspect in the Zhijin area. a) All tower karst hills with a skewed distribution. b) All cockpit karst hills with a skewed distribution.

Different with the distribution characteristics of the Zhijin area, the aspect distributions of the tower and cockpit karst hills in the Weining area are similar (Fig. 5-30). The aspects of the tower and cockpit karst hills range in 135°–180° and cluster in 150°–160°.

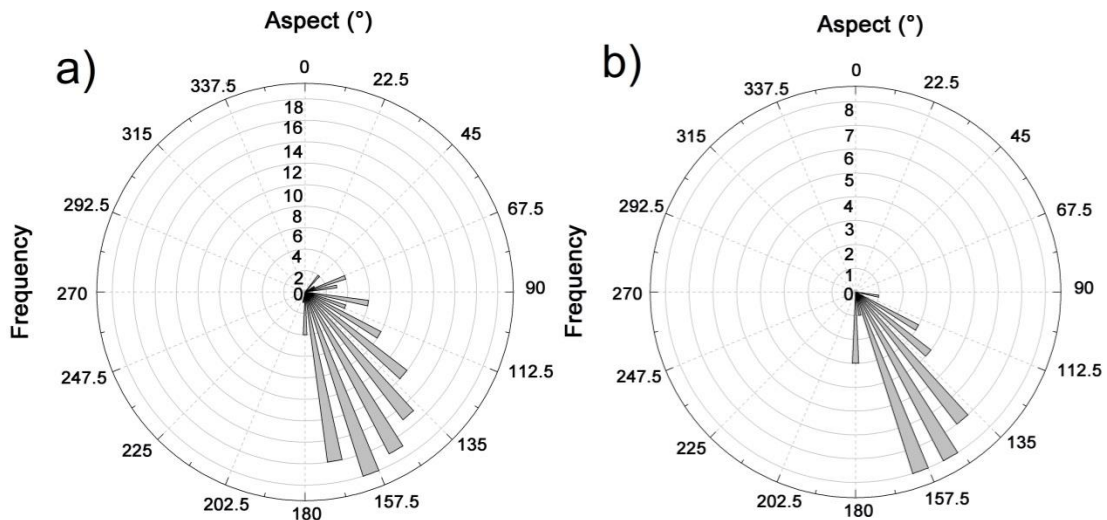


Figure 5-30. The distribution of hill aspect in the Weining area. a) All tower karst hills with a skewed distribution. b) All cockpit karst hills with a skewed distribution.

5.3.9. Curvature

The curvatures of the tower and cockpit karst hills in the Zhijin area are somewhat normally distributed as shown in Fig. 5-31. Comparing with the cockpit karst hills, the tower karst hills have a larger value range (Table 4-7). The curvatures of the tower and cockpit karst hills cluster in the range of 0–10 and 0–5, separately.

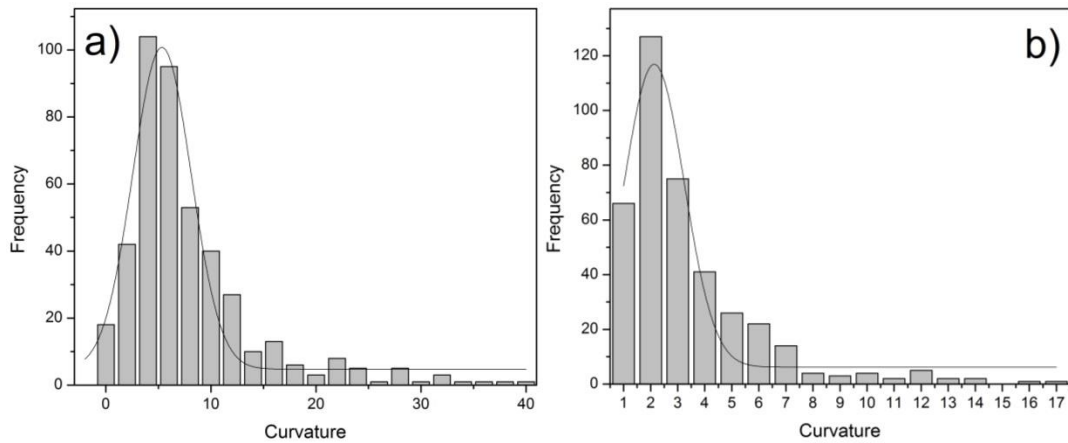


Figure 5-31. The distribution of hill curvature in the Zhijin area. a) All tower karst hills with a somewhat normal distribution. b) All cockpit karst hills with a somewhat normal distribution.

The curvatures of the tower and cockpit karst hills in the Weining area are also somewhat normally distributed as shown in Fig. 5-32. As shown in Table 4-10, the tower karst curvatures cover a larger span than that of the cockpit karst hills. The curvatures of the tower and cockpit karst hills cluster in the range of 0–3 and 0–1, separately.

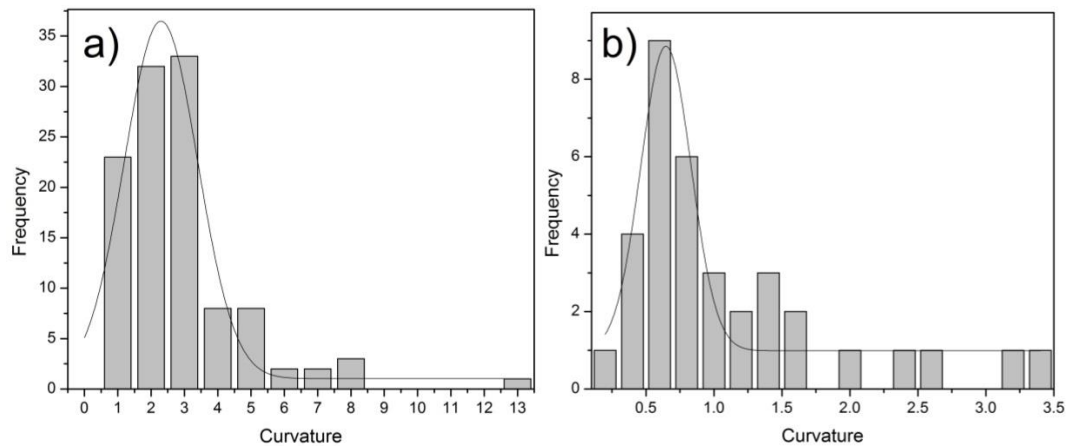


Figure 5-32. The distribution of hill curvature in the Weining area. a) All tower karst hills with a somewhat normal distribution. b) All cockpit karst hills with a somewhat normal distribution.

5.3.10. Circularity ratio

The circularity ratios of the tower and cockpit karst hills are somewhat normally distributed in the Zhijin area (Fig. 5-33). The circularity ratios of the tower karst hills range from 0.11 to 0.77 (Table 4-7). The circularity ratios of the cockpit karst hills range from 0.01 to 0.66 (Table 4-7). As shown in Fig. 4-38, the circularity ratios of the tower and cockpit karst hills cluster in the range of 0.45-0.65. The circularity ratio range of 0.45-0.65 takes 84.09% of the tower karst hills and 58.09% of the cockpit karst hills, respectively.

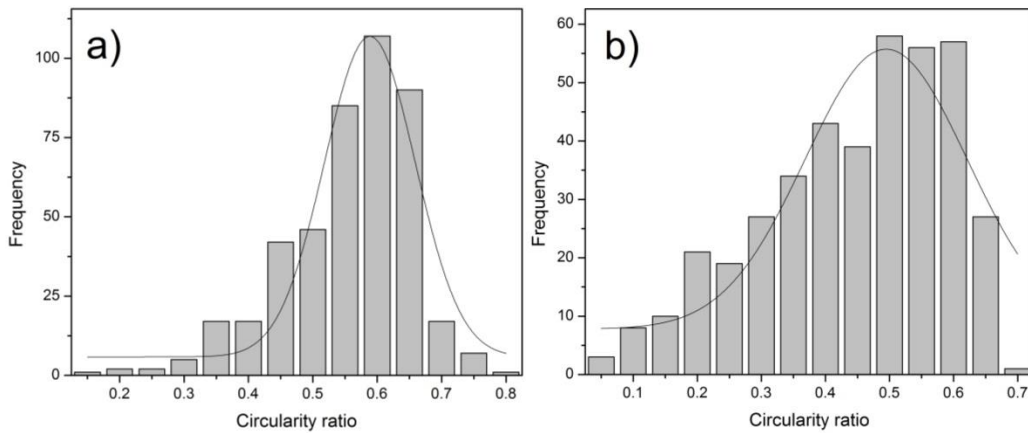


Figure 5-33. The distribution of hill circularity ratio in the Zhijian area. a) All tower karst hills with a somewhat normal distribution. b) All cockpit karst hills with a somewhat normal distribution.

The circularity ratios of the tower and cockpit karst hills are also somewhat normally distributed in the Weining area (Fig. 5-34). The circularity ratios of the tower karst hills range from 0.26 to 0.67. The circularity ratios of the cockpit karst hills range from 0.12 to 0.58 (Table 4-10). As shown in Fig. 5-34a, the circularity ratios of the tower karst hills cluster in 0.44–0.46. The circularity ratios of the cockpit karst hills cluster in 0.58–0.6.

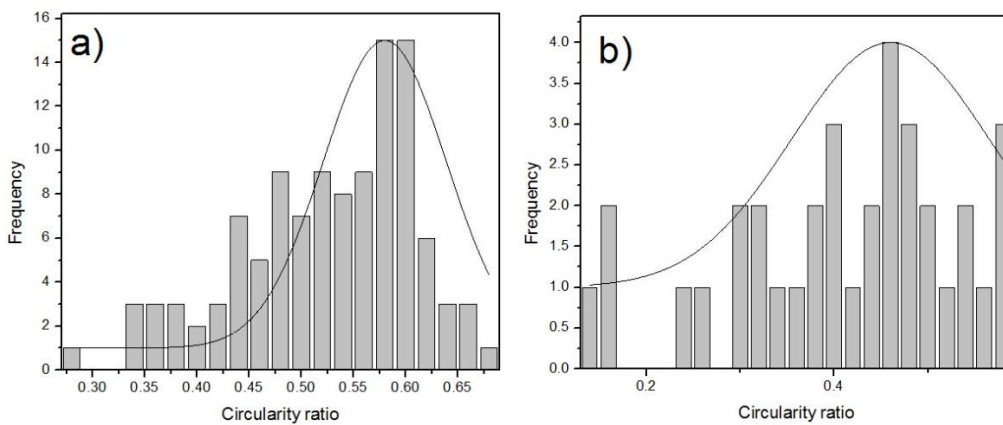


Figure 5-34. The distribution of hill circularity ratio in the Weining area. a) All tower karst hills with a somewhat normal distribution. b) All cockpit karst hills with a somewhat normal distribution.

5.3.11. Area ratio

In the Zhijian area, the area ratios of the tower and cockpit karst hills are somewhat normal distributed (Fig. 5-35). As Table 4-7, the area ratio range of the tower karst is smaller than that of the cockpit karst hills. The area ratios of the tower karst cluster in 1.0–1.05 with a percentage

of 60.59% (Fig. 5-35a). For the cockpit karst hills, 66.03% of the area ratios cluster in the range of 1.1–1.25 (Fig. 5-35b).

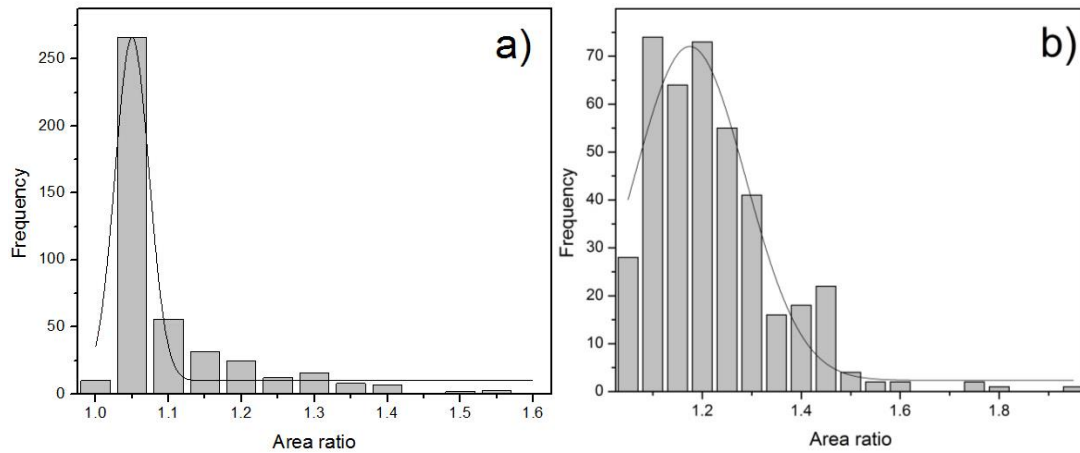


Figure 5-35. The distribution of hill area ratio in the Zhijin area. a) All tower karst hills with a somewhat normal distribution. b) All cockpit karst hills with a somewhat normal distribution.

The area ratios are also somewhat normally distributed in the Weining area. Different from the situation in the Zhijin area, the area ratios of the tower karst hills are in a larger range than that of the cockpit karst hills (Table 4-10) while the mean value and standard deviation are the same. The value distributions are shown in Fig. 4-41. The area ratios of the tower karst hills cluster in 1.02-1.08 with 60.18% (Fig. 5-36a). The area ratios of the cockpit karst hills cluster in the range of 1.04–1.05 and 1.06–1.07. The percentages are 22.86% and 25.71%, respectively.

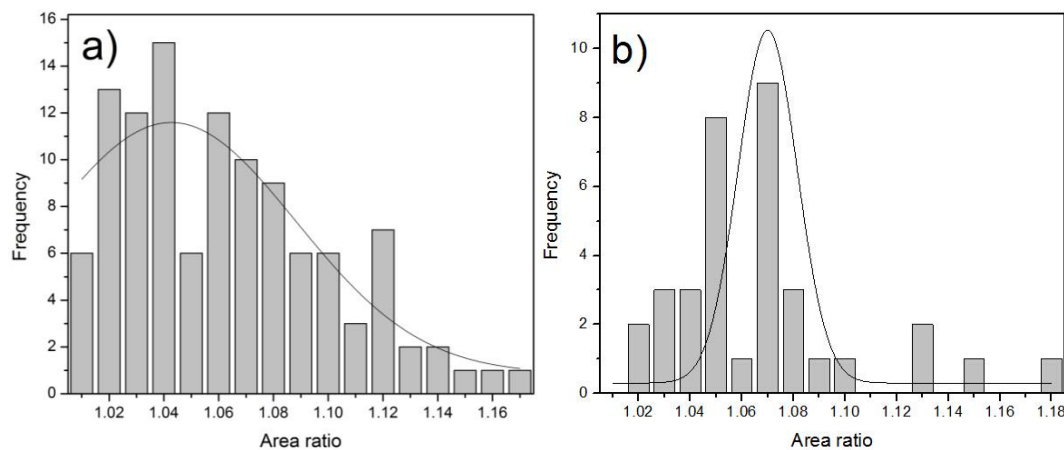


Figure 5-36. The distribution of hill area ratio in the Weining area. a) All tower karst hills with a somewhat normal distribution. b) All cockpit karst hills with a somewhat normal distribution.

5.3.12. Terrain Ruggedness Index

Table 4-7 illustrates that the cockpit karst hills are in a larger *TRI* span than that of the

tower karst hills in the Zhijin area. There are some similar features of the tower and cockpit karst hills' *TRIs*. Firstly, the mean values and the *SDs* are the same (Table 4-7). Secondly, the *TRIs* are somewhat normal distributed (Fig. 5-37). Thirdly, as shown in Fig. 5-37, the *TRIs* cluster around 0, 0.005, 0.01 and 0.15.

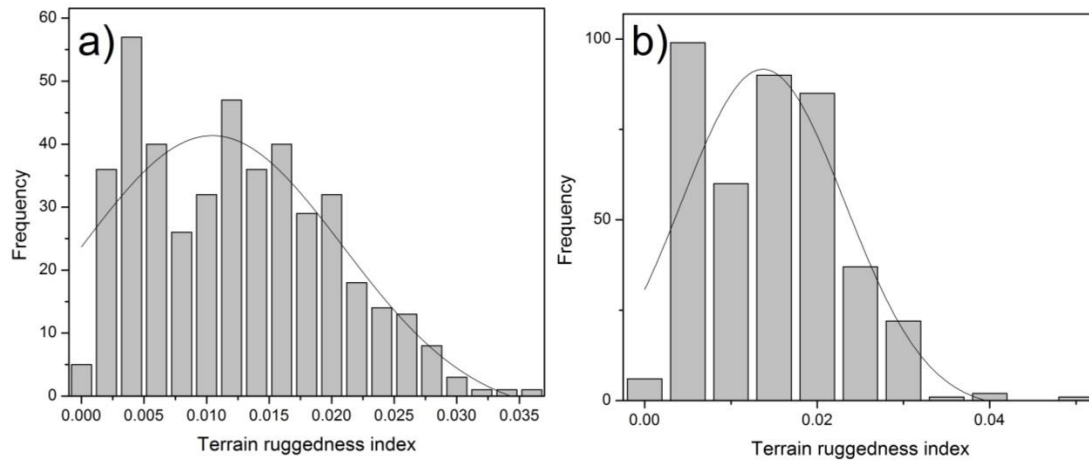


Figure 5-37. The distribution of hill *TRI* in the Zhijin area. a) All tower karst hills with a somewhat normal distribution. b) All cockpit karst hills with a somewhat normal distribution.

As shown in Table 4-10, the tower karst hills cover a larger *TRI* span than that of the cockpit karst hills in the Weining area. The mean value of the cockpit karst hills (0.74) is bigger than that of the tower karst hills (0.68). The tower and cockpit karst hills *TRIs* are also somewhat normally distributed. The tower karst hills *TRIs* cluster around 0.4, 0.6, 0.7, and 1.2 (Fig. 5-38a). The cockpit karst hills *TRIs* cluster around 0.5, 0.7, 0.8 and 1.2 (Fig. 5-38b).

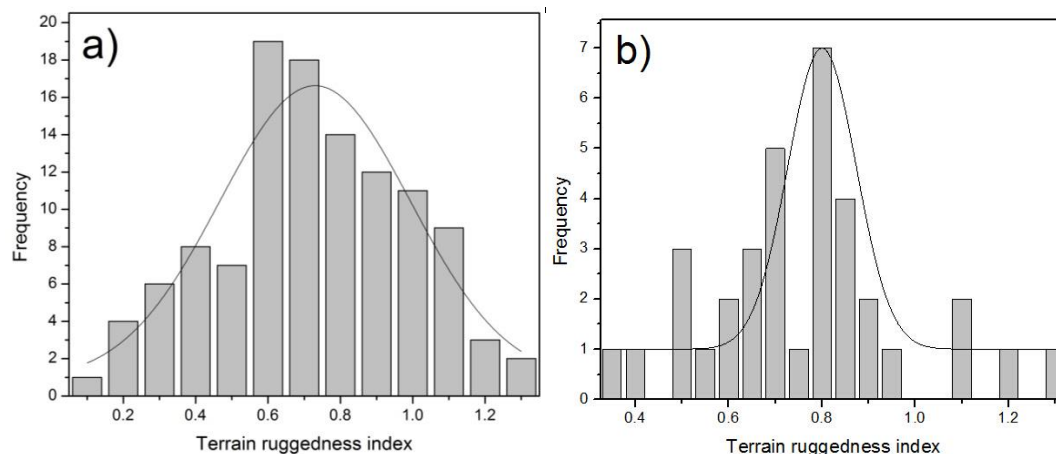


Figure 5-38. The distribution of hill *TRI* in the Weining area. a) All tower karst hills with a somewhat normal distribution. b) All cockpit karst hills with a somewhat normal distribution.

5.3.13. Terrain Shape Index

In the Zhijin area, the *TSI* range of the tower karst hills is smaller than that of the cockpit karst (Table 4-7). As shown in Fig. 5-39, The *TSIs* of the tower and cockpit karst hills are skewed distributed. 85.15% of the tower karst hills' *TSIs* are in the range of -0.5–0. And, 44.55% of the values are found in -0.1–0 (Fig. 5-39a). For the cockpit karst hills, 98.97% of the values occupy in -1–0 (Fig. 5-39c). Without outliers (< -0.5), *TSIs* of the cockpit karst hills are in normal distribution (Fig. 5-39c).

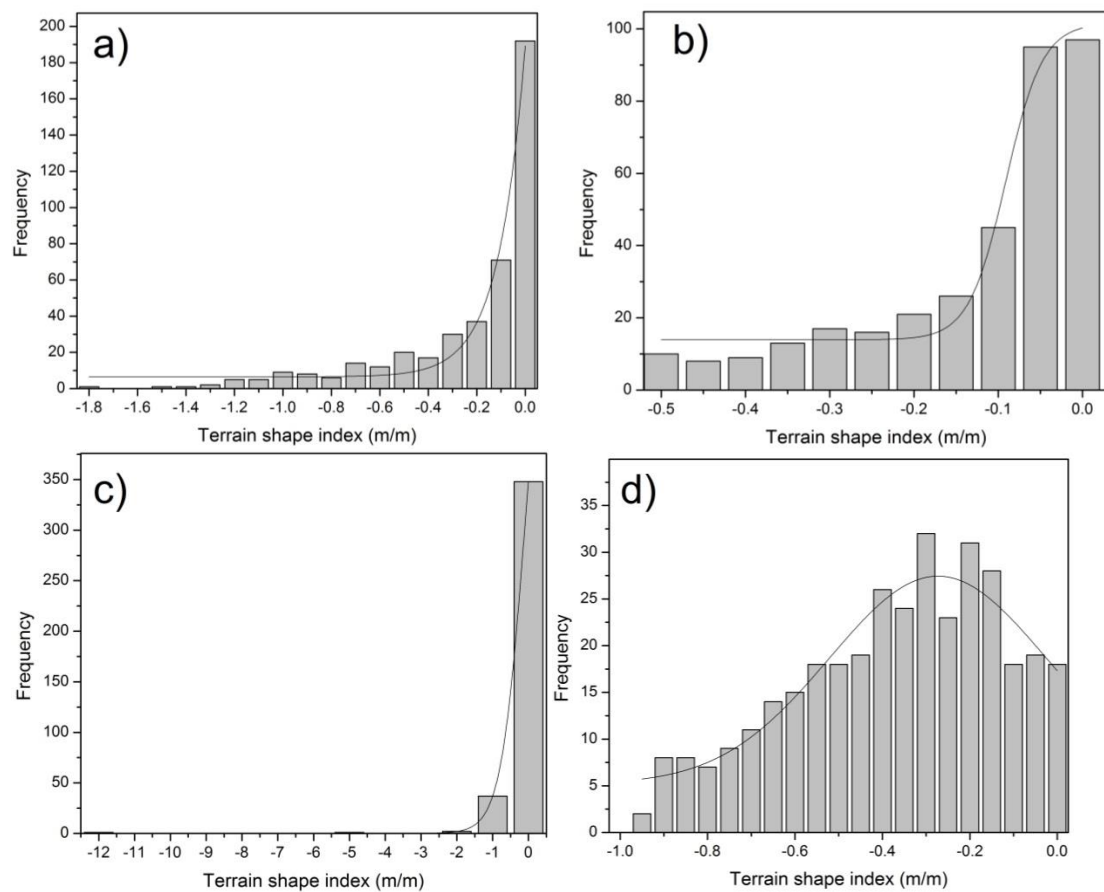


Figure 5-39. The distribution of hill *TSI* in the Zhijin area. a) All tower karst hills with a skewed distribution. b) Tower karst hills except large outliers. c) All cockpit karst hills with a skewed distribution. e) Cockpit karst hills except large outliers.

Unlike the Zhijin area, the *TSI* of the tower karst hills is in a larger range than that of the cockpit karst hills. As shown in Table 4-10, the mean values and *SDs* of the tower and cockpit karst hills are closed. The *TSIs* of the tower and cockpit karst hills are somewhat normal distributed (Fig. 5-40). In Fig. 4-45a and b, the *TRIs* of the tower and cockpit karst hills cluster in -0.2–-0.15.

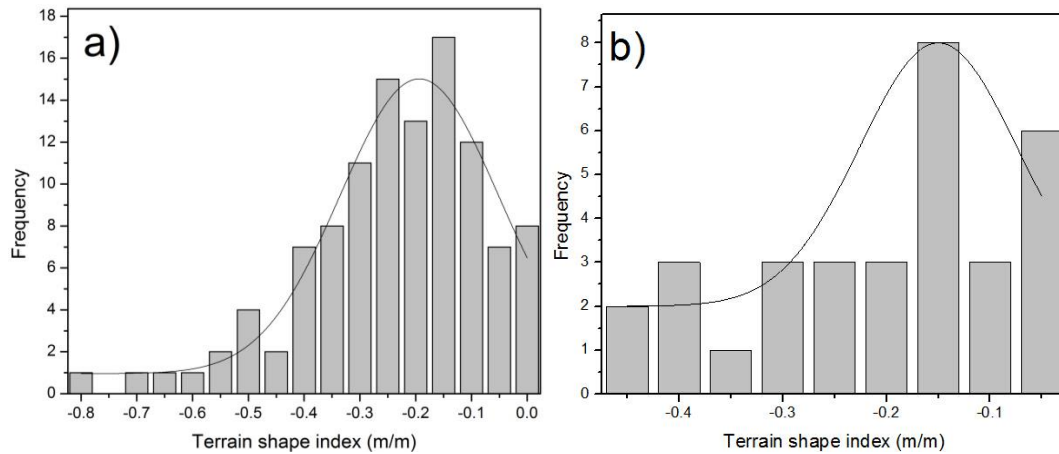
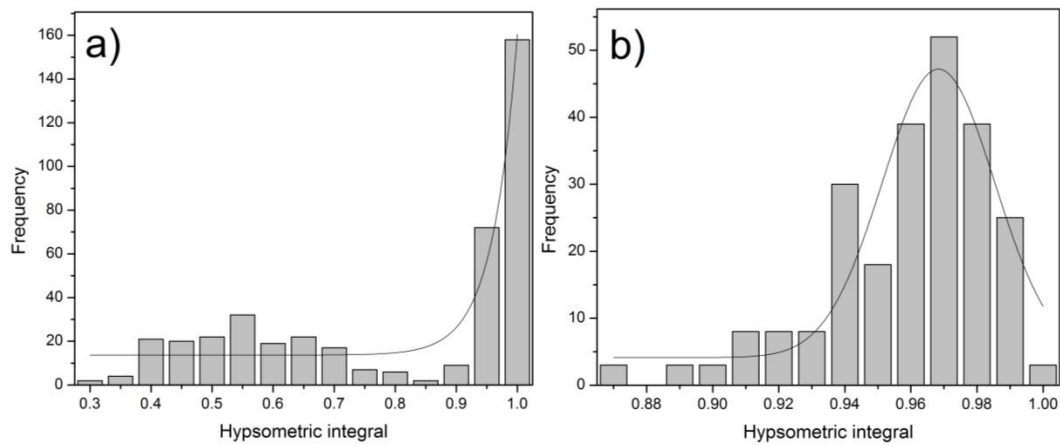


Figure 5-40. The distribution of hill *TSI* in the Weining area. a) All tower karst hills with a somewhat normal distribution. b) All cockpit karst hills with a somewhat normal distribution.

5.3.14. Hypsometric integral

As shown in Table 4-7, the *HIs* of the tower karst hills in the Zhijin area range from 0.25 to 1 with a mean value of 0.78 and a *SD* of 0.22. The values are skewed distributed as Fig. 5-41a that 54.76% of all the values are in the range of 0.9–1. In the range of 0.9–1, the *HIs* of the tower karst hills are normally distributed (Fig. 5-41b) with a cluster of 0.96-0.97. The *HIs* of the cockpit karst hills range from 0.13–0.99 with a mean value of 0.44 and a *SD* of 0.12. As shown in Fig. 5-41b, all the cockpit karst hills' *HIs* are in a somewhat normal distribution.



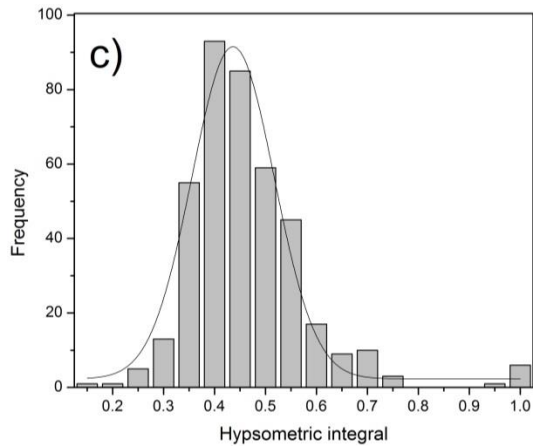


Figure 5-41. The distribution of hill *HI* in the Zhijin area. a) All tower karst hills with a skewed distribution. b) Tower karst hills except large outliers. c) All cockpit karst hills with a somewhat skewed distribution.

The *HIs* of the tower and cockpit karst hills in the Weining area are in somewhat normal distribution (Fig. 5-42). The tower karst hills *HIs* range from 0.32–0.99. 89.29% of the values cluster in 0.32–0.7 (Fig. 5-42a). As shown in Table 4-10 and Fig. 5-42b, the *HIs* of the cockpit karst hills range from 0.3–0.64 and cluster in 0.36–0.4.

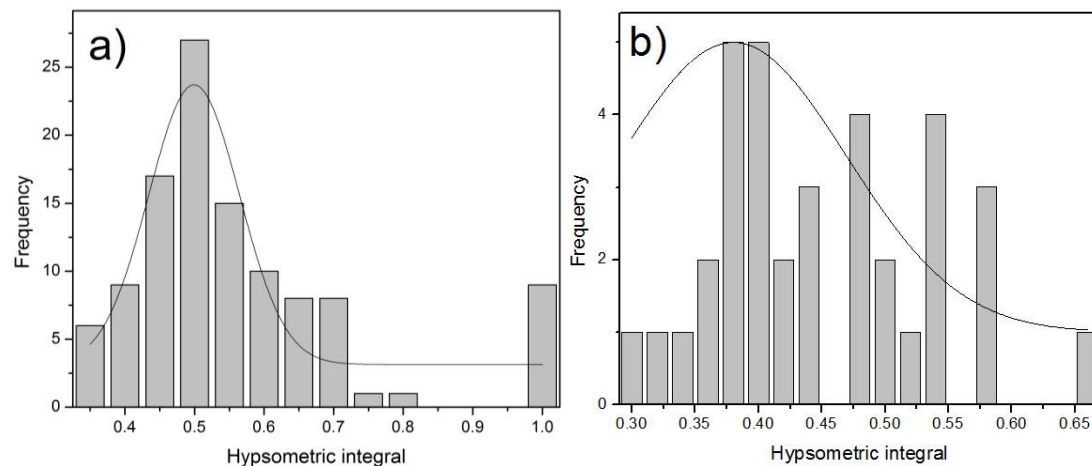


Figure 5-42. The distribution of hill *HI* in the Weining area. a) All tower karst hills with a somewhat normal distribution. b) All cockpit karst hills with a somewhat normal distribution.

5.4. Morphometric differences between the tower and cockpit karst hills

The cockpit karst hills are fewer in number but larger in area than the tower karst hills. There are 403 cockpit karst hills in the Zhijin area, occupying 7.77% of the karst area (Table 4-5). The cockpit karst hills in the Weining area are 35, occupying 33.39% of the karst area (Table 4-8). In contrast, the numbers of tower karst hills in the Zhijin and Weining areas are 112

and 439, respectively, showing that the order of abundance is switched. The tower karst hills in the Zhijin and Weining areas covers 2.25% and 2.49% of the karst area, respectively. Therefore, the area-related morphometric parameters (perimeter and long-axis length) of the cockpit karst hills are larger than those of the tower karst hills (Fig. 5-43). Fig. 5-43 provides the following results: 1) In the same study area, the difference of area, perimeter and long-axis length between the tower and cockpit karst hills is statistically significant ($p < 0.05$). For these three parameters, the cockpit karst hills show relatively large variance than tower karst hills; 2) For the these three parameters, the difference between the tower karst hills in different study areas are more apparent than that of the cockpit karst hills.

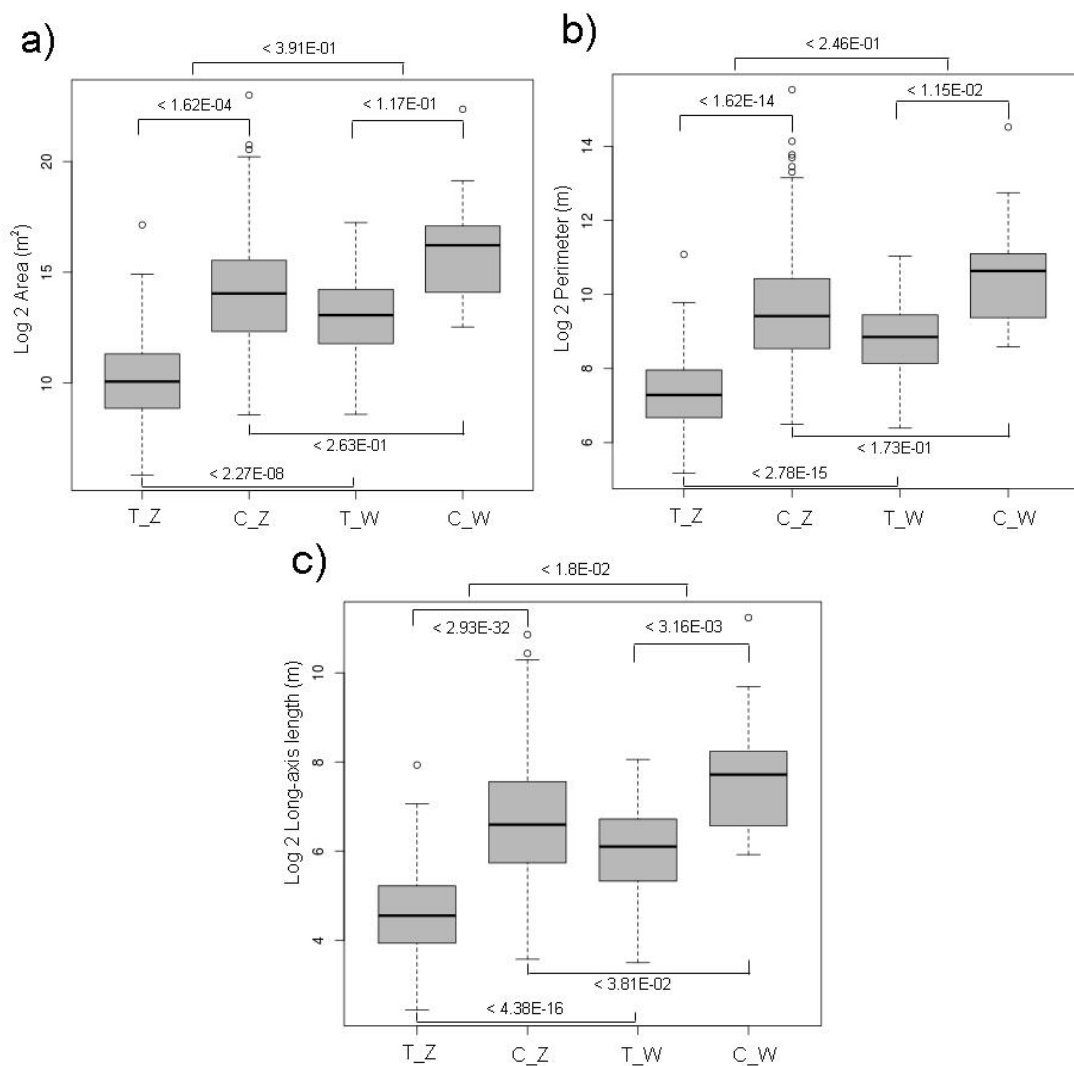


Figure 5-43. Box plots of morphometric parameters for the tower and cockpit karst hills in the Zhijin and Weining areas: a) area; b) perimeter; and c) long-axis length. The difference among the tower and cockpit karst hills is significant based on the t -test ($p < 0.05$). T_Z: tower karst hills in the Zhijin area; C_Z: cockpit karst hills in the Zhijin area; T_W: tower karst hills in the Weining area; C_W: cockpit karst hills in the Weining area.

Compared with the tower karst hills, the cockpit karst hills have higher relief but lower relative relief (Fig. 5-44, Tables 4-7 and 4-10). In Fig. 5-44a, the relief of the tower karst hills is higher than that of the cockpit karst hills in both study areas. The difference between the tower and cockpit karst hills in different study areas is significant. However, according to Fig. 5-44b, the relative relief of the cockpit karst hills is lower than that of the tower karst hills in both study areas. Especially, in the Weining area, the difference between the tower and cockpit karst hills is significant.

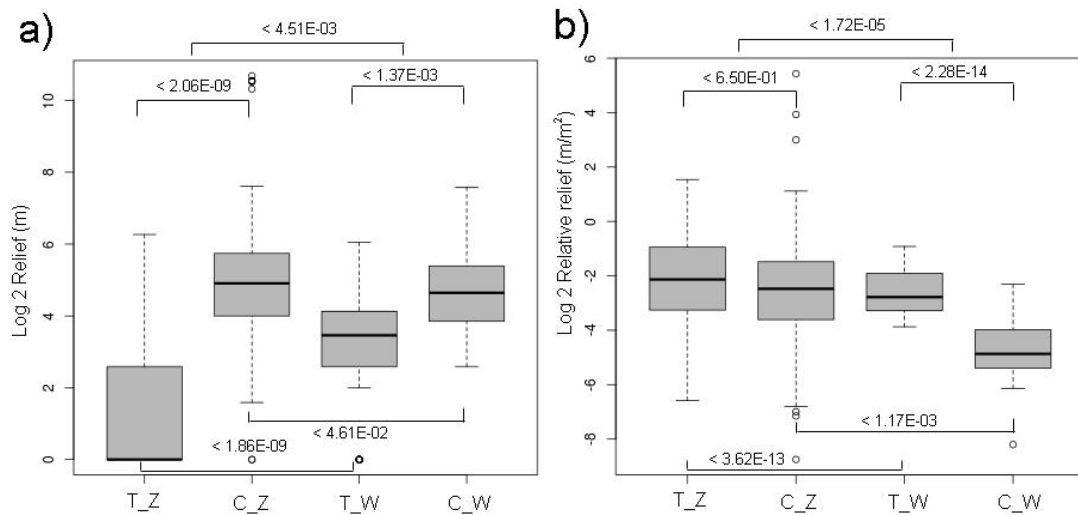


Figure 5-44. Box plots of morphometric parameters for the tower and cockpit karst hills in the Zhijin and Weining areas: a) relief and b) relative relief. The difference between the tower and cockpit karst hills is significant according to the t -test ($p < 0.05$). T_Z: tower karst hills in the Zhijin area; C_Z: cockpit karst hills in the Zhijin area; T_W: tower karst hills in the Weining area; C_W: cockpit karst hills in the Weining area.

The cockpit karst hills have steeper mean and maximum slope with higher SD values (Fig. 5-45, Tables 4-7 and 4-10) than those of the tower karst hills. In Fig. 5-45, the mean and maximum slopes and SD values of the cockpit karst hills are higher than those of the tower karst hills in both study areas. Regarding these three parameters of slope, the difference between the tower and cockpit karst hills in the Zhijin area are more apparent than those in the Weining area. Based on the t -test, the difference in the mean and maximum slopes and SD of the tower and cockpit karst hills is significant ($p < 0.05$).

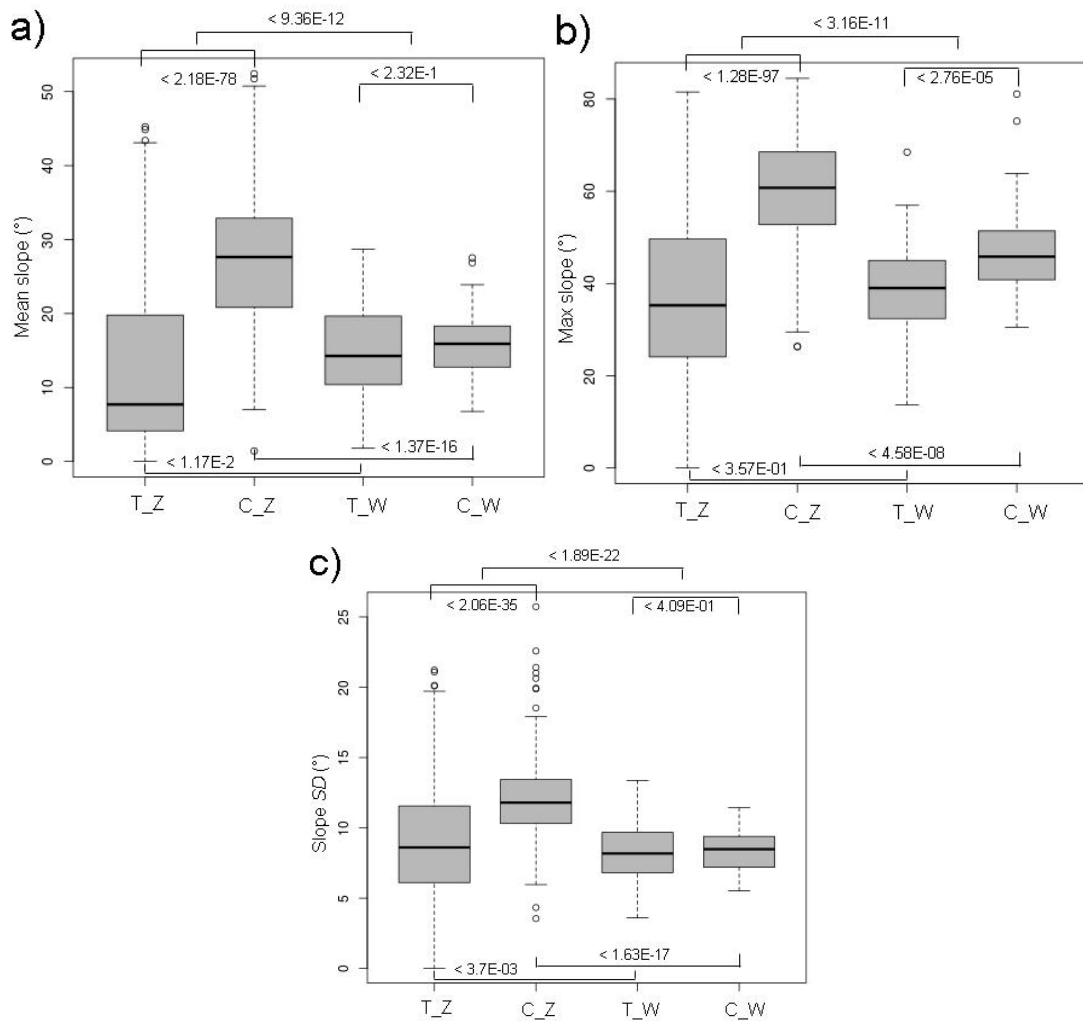


Figure 5-45. Box plots of slope for the tower and cockpit karst hills in the Zhijin and Weining areas: a) mean; b) maximum; and c) *SD*. The difference among the tower and cockpit karst hills is Significant based on the *t*-test ($p < 0.05$). T_Z: tower karst hills in the Zhijin area; C_Z: cockpit karst hills in the Zhijin area; T_W: tower karst hills in the Weining area; C_W: cockpit karst hills in the Weining area.

Concerning curvature, the cockpit karst hills have lower mean values but larger value ranges and higher *SD* values than the tower karst hills (Fig. 5-46, Tables 4-7 and 4-10). In Fig. 5-46a, the mean curvatures of the cockpit karst hills are higher than those of the tower karst hills in both study areas. The maximum curvatures and *SD* for the cockpit karst hills are higher than those for the tower karst hills. Based on the *t*-test, the difference in the mean and maximum slopes and *SD* between the tower and cockpit karst hills and those between the different study areas is significant ($p < 0.05$).

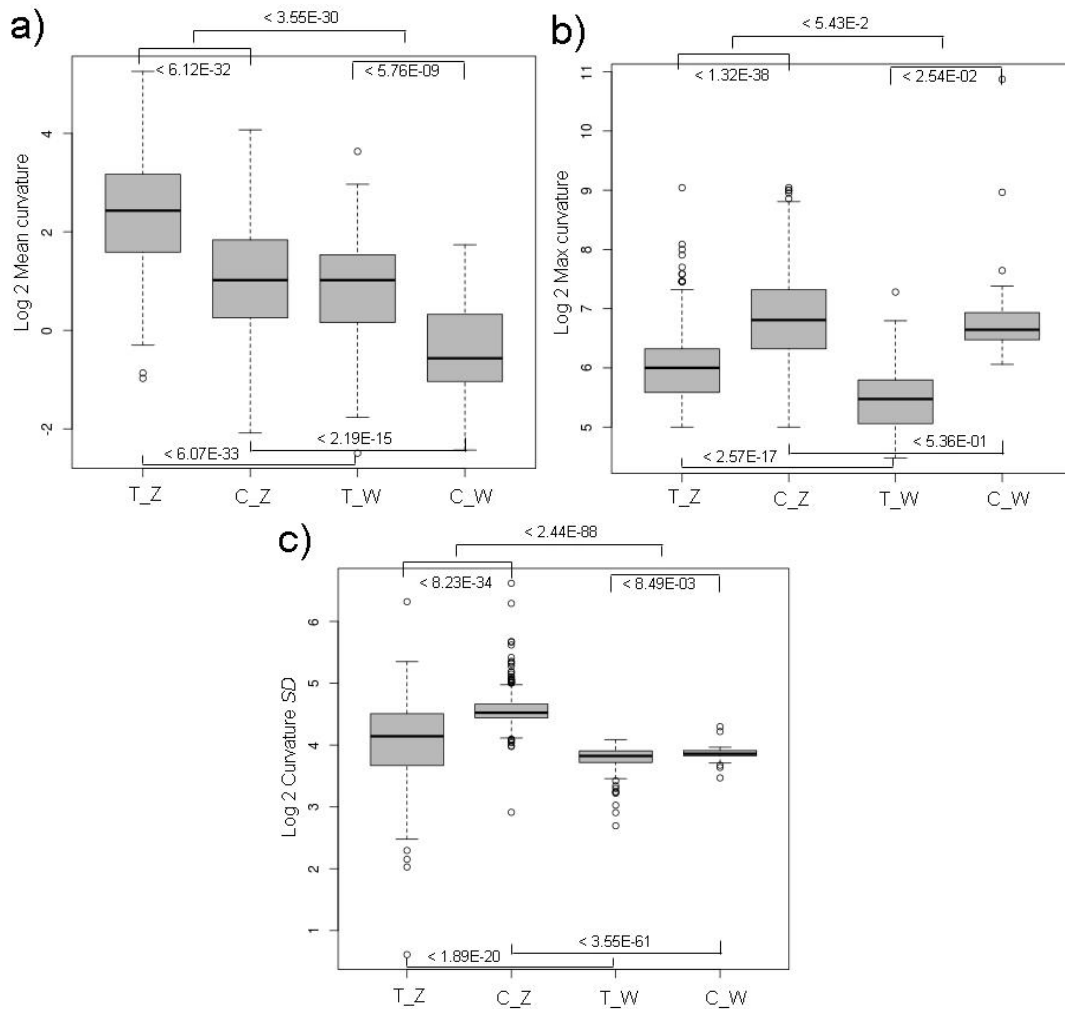


Figure 5-46. Box plots of curvature for the tower and cockpit karst hills in the Zhijin and Weining areas: a) mean; b) maximum; c) and *SD*. The difference between the tower and cockpit karst hills is significant based on the *t*-test ($p < 0.05$). T_Z: tower karst hills in the Zhijin area; C_Z: cockpit karst hills in the Zhijin area; T_W: tower karst hills in the Weining area; C_W: cockpit karst hills in the Weining area.

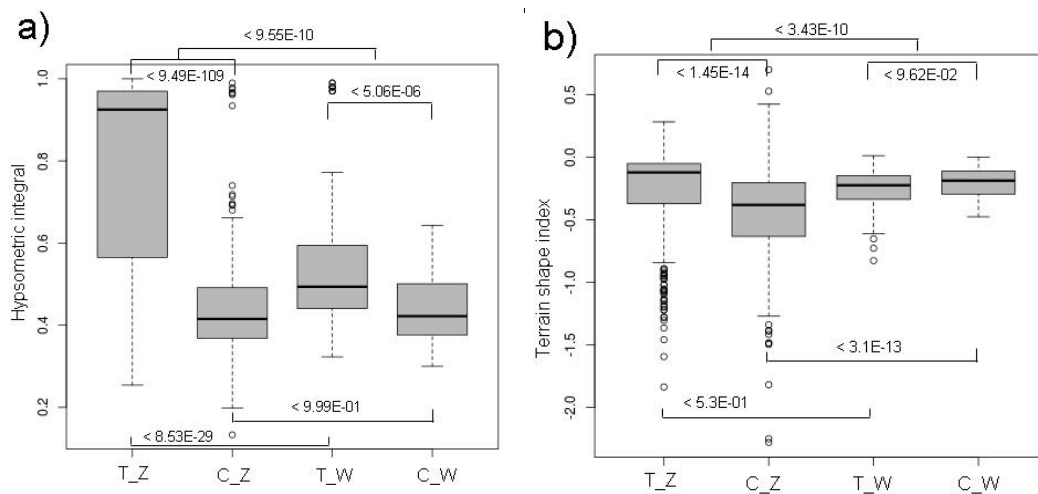


Figure 5-47. Box plots of *HI* and *TSI* for the tower and cockpit karst hills in the Zhijin and

Weining areas: a) *HI* and b) *TSI*. The difference between the tower and cockpit karst hills is significant based on the *t*-test ($p < 0.05$). T_Z: tower karst hills in the Zhijin area; C_Z: cockpit karst hills in the Zhijin area; T_W: tower karst hills in the Weining area; C_W: cockpit karst hills in the Weining area.

The *HI* values for the tower and cockpit karst hills are significant different (Fig. 5-47a). The values for the tower karst hills are higher than those of the cockpit karst hills in both study areas. The *HI* difference between the tower and cockpit karst hills is more apparent in the Zhijin area than that in the Weining area.

Fig. 5-47b shows the *TSI* difference between the tower and cockpit karst hills in the two study areas. The difference between the tower and cockpit karst hills in the Zhijin area is significant, where that in the Weining area is insignificant.

Morphology of the cockpit karst hills is more complicated than that of the tower karst hills. The higher complexity for the former is reflected in the following three observations. First, the cockpit karst hills have less circular foots than those of the tower karst hills in both study areas (Fig. 5-48a). Second, the number of peaks per hill infers the higher complexity of the cockpit karst hills (Fig. 5-48b). Lyew-Ayee et al. (2007) indicated that the hill complexity is positively correlated with the number of peaks per hill and the tower karst hills have only one peak per each. Third, the terrain ruggedness of the cockpit karst hills tends to be higher than that of the tower karst hills (Fig. 5-49a, b and c). In addition, the area ratio, an indicator of three-dimensional complexity of a hill (Lyew-Ayee et al., 2007) is higher for the cockpit karst hills in central Guizhou Province than those in western Guizhou Province (Fig. 5-49d).

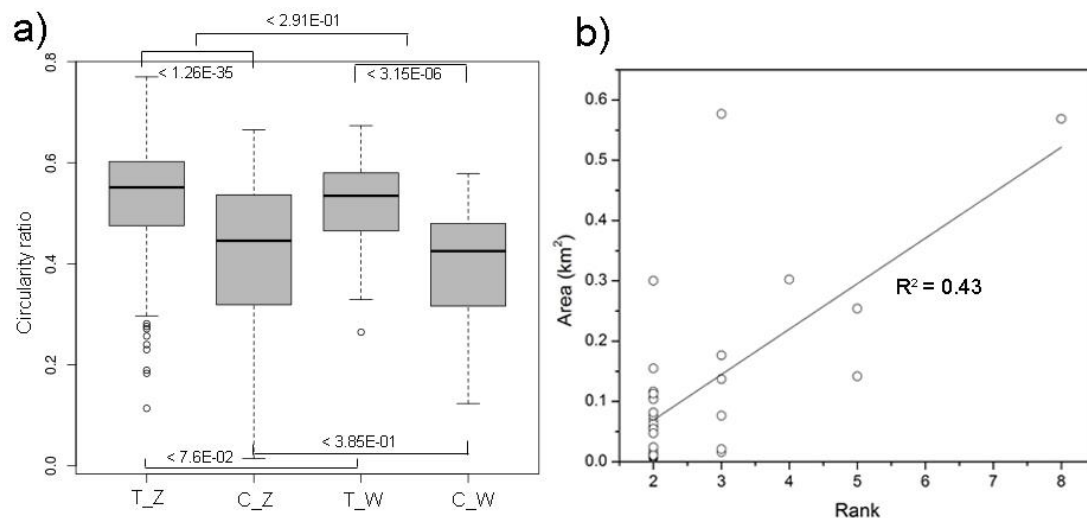


Figure 5-48. The complexity parameters. a) Box plots of circularity ratio for the tower and cockpit karst hills in the Zhijin and Weining areas. T_Z: tower karst hills in the Zhijin area; C_Z: cockpit karst hills in the Zhijin area; T_W: tower karst hills in the Weining area; C_W: cockpit karst hills in the Weining area. b) The correlation between the rank of the cockpit

karst hills and the hill area in the Weining area ($R^2 = 0.43$).

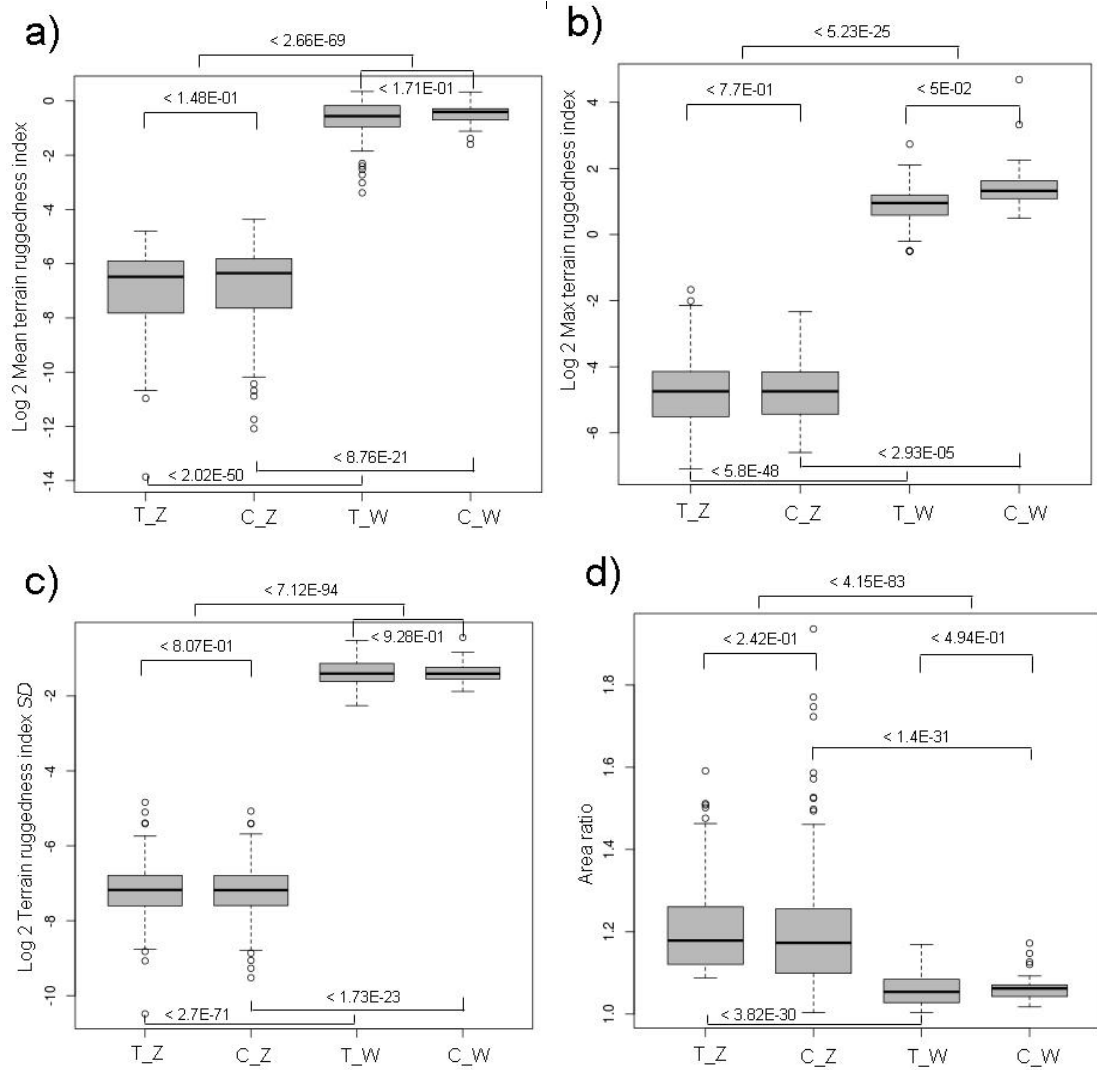


Figure 5-49. Box plots of the terrain ruggedness index and area ratio for the tower and cockpit karst hills in the Zhijin and Weining areas. a) Mean; b) Maximum; c) *SD* of *TRI*; and d) area ratio. T_Z: tower karst hills in the Zhijin area; C_Z: cockpit karst hills in the Zhijin area; T_W: tower karst hills in the Weining area; C_W: cockpit karst hills in the Weining area.

5.5. Relationship between sinkholes and geologic structure

As shown in Fig. 4-1, in the Zhijin area, large sinkholes tend to occur in the interfluves, whereas smaller sinkholes are clustered closer to the river networks. The elongation of the large sinkhole and the alignment of small sinkholes generally extend along the NE direction (Fig. 2-3). It is a striking trend similarity to that of the NE trending faults due to the effect of tectonic deformation in the study area. This performance assumed that the spatial alignment and the elongation of sinkhole long-axes are influenced by location of the faults.

To confirm this linkage between buried faults and sinkhole lines, we measured the distance between the sinkhole centroid and the nearest fault (Fig. 5-50) and the orientation between the sinkholes and faults of both study areas (Fig. 5-51). In the Zhijin area, it is noted that the number of sinkholes (Fig. 5-50a) and the area of sinkholes (Fig. 5-50b) decrease with the distance to the neighborhood fault, illustrating a potential structural control in the study area. As shown in Fig. 5-51a, the bimodal distribution of sinkholes orientation mentioned in Section 5.2 are similar with that of the fault orientation. The bimodal distribution is such that there is a separation at 80° . At the section of 0° – 80° , the high orientation frequency of sinkhole long-axis length and faults are at range of 40° – 70° . At the section of 80° – 180° , the high orientation frequency of sinkhole long-axis length and faults are at range of 40° – 70° .

The structural control in the Weining area was also found from sinkhole shape and spatial distribution. On one hand, as shown in Fig. 5-50d, the area of sinkholes decreases with the distance to the neighborhood fault. The sinkholes orientation mentioned in Section 5.2 are generally similar with that of the fault orientation (Fig. 5-51b). The sinkhole peak values correspond to those of the faults orientation at 50° , 130° and 140° . On the other hand, the faults extended along NW and NE (Fig. 2-5); therefore, the sinkholes were influenced by the structure with these two directions. The two direction impacts of the faults could be reflected in the following three aspects. Firstly, the number of sinkholes (Fig. 5-50c) generally decreases with the distance to the neighborhood fault. Secondly, there is not obvious correlation between the number of sinkholes and the distance to the neighborhood fault; however, 62.5% of the sinkholes distributed within 500 m distance of the faults (Fig. 5-50c). These sinkholes clustered among the faults and arranged along the faults extension direction (NE and NW). Thirdly, the sinkhole shape is influenced by the two direction faults. Comparing Tables 4-3 and 4-4, we can see that the mean ellipticity of the Weining area (0.73) is smaller than that of the Zhijin area (0.78). It can be inferred that the sinkhole shape tend to be less elliptic than that in the Zhijin area. This less elliptic sinkhole shape is also found in Fig. 4-6 and Fig. 4-7. In Fig. 4-6, the sinkhole shape elongates mainly along NE, especially the large sinkholes. However, in Fig. 4-7, the small sinkhole shape tends to be more circular while the large sinkholes elongate along not only NE but also NW.

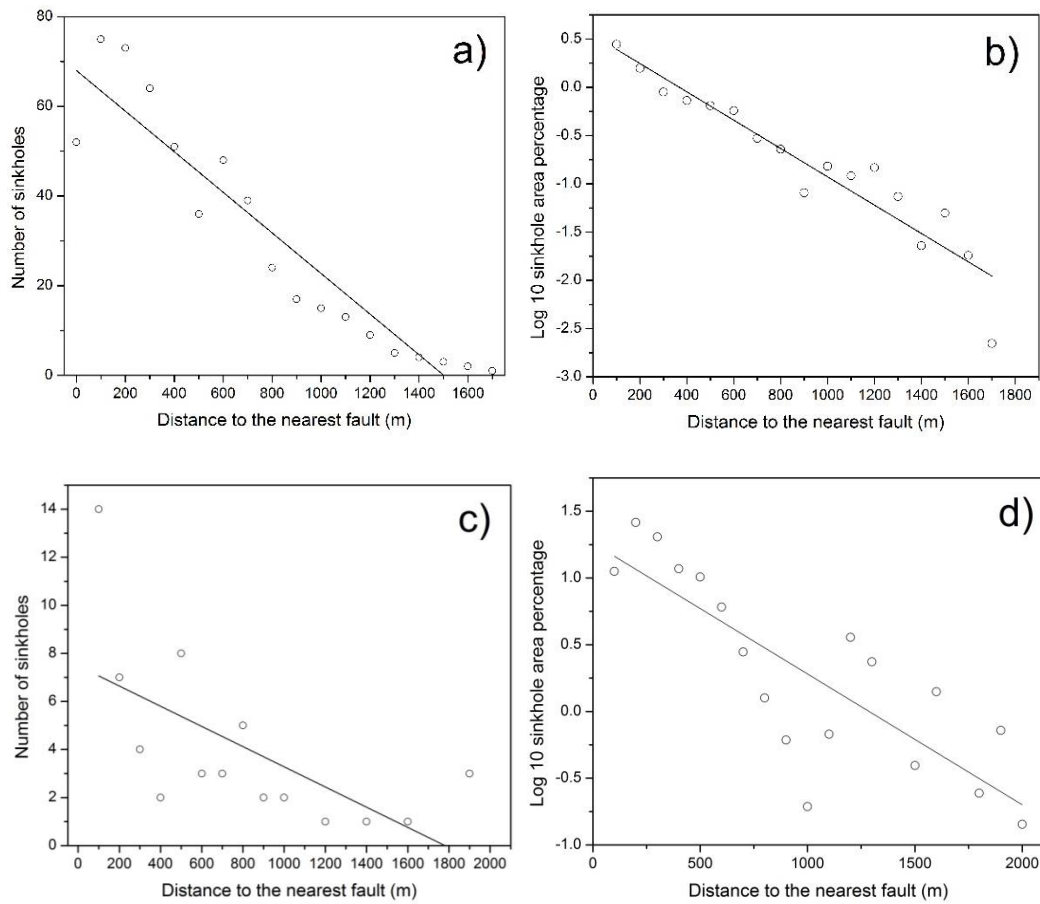


Figure 5-50. Distribution of sinkholes and faults: a) sinkhole frequency with the distance to the nearest fault in the Zhijin area. Linear correlation assigned: $R^2 = 0.88$; b) sinkhole area percentage with the distance to the nearest fault in the Zhijin area. Linear correlation assigned: $R^2 = 0.89$; c) sinkhole frequency with the distance to the nearest fault in the Weining area. Linear correlation assigned: $R^2 = 0.35$; b) sinkhole area percentage with the distance to the nearest fault in the Weining area. Linear correlation assigned: $R^2 = 0.65$.

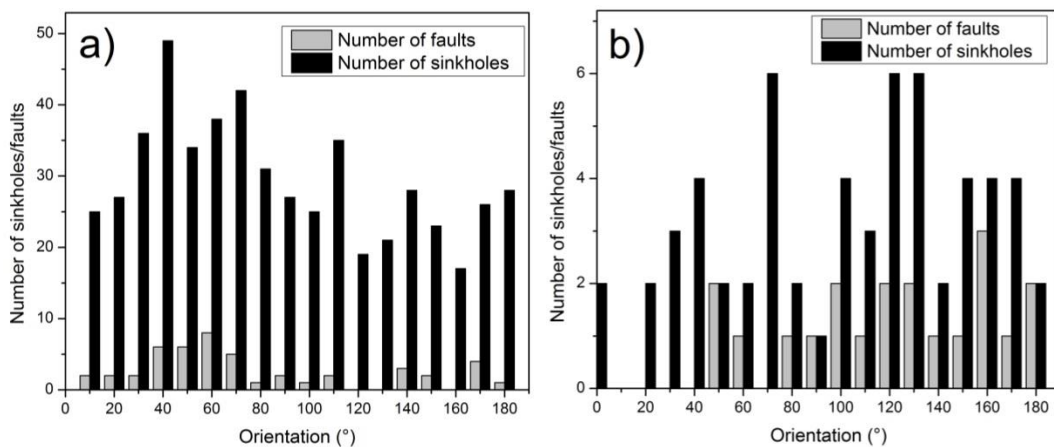


Figure 5-51. Orientation frequency distribution of the sinkholes and the faults in: a) the Zhijin area; b) the Weining area.

In addition, it is interesting that more than 1/5 of the sinkholes are in the ellipticity of 0.9–0.99 (Fig. 5-7). Intensively, in the ellipticity class of 0–0.9, there is only 34 sinkholes with the ellipticity value < 0.5 . The high sinkhole ellipticity values reflect that the study area was dominated by the irregular or non-circular sinkholes. Brinkmann et al. (2008) demonstrated that irregular or non-circular sinkholes indicates a relatively old karst landform. Therefore, the dominated irregular or non-circular sinkholes infer a relatively old karst landscape in the study area. This is not particularly surprising since the landscape is higher than 900 m elevation and was inundated in the Triassic, Permian and Carboniferous.

According to Bauer (2015), the deepening of collapsed sinkholes is associated with area-widening for sinkhole formed by solution. The linear correlation between area and volume (Fig. 5-14) demonstrates that the sinkholes in the study areas also have a solutional origin. The solution is due to the distribution of pre-Triassic carbonate rocks in the study areas (Li and Luo, 1983). The genetic process of solution sinkholes has been well-established in recent studies (Williams, 2003; Beck, 2004; Waltham et al., 2007; Gutierrez et al., 2008), including the effect of differential corrosional surface lowering (Gutiérrez et al., 2014).

5.6. Implications from the morphometry of the tower and cockpit karst hills

The tower and cockpit karst hills in both study areas show a main aspect to the east. In Section 5.3.8, we found the following aspect characteristics: 1) the tower karst aspect in the Zhijin area ranged from NE to SE; 2) cockpit karst aspect in the Zhijin area was mainly SE with few in 180° – 202.5° ; and 3) the tower and cockpit karst hills in the Weining area tend to have SE aspect. Furthermore, The mean aspect in Tables 4-7 and 4-10 for the tower and cockpit karst hills are 101.31° and 161.64° for the Zhijin area, 134.39° and 142.57° for the Weining area. There are two reasons for these characteristics. One is the fault orientations. The faults in the Zhijin area tend to extend along an NE–SW direction, while the faults in the Weining area along an NW–SE direction. The other is that the hill aspects in both areas follow the general aspect of the Yunnan–Guizhou Plateau. Zhang (1980) stated that the plateau shows stepwise elevation change toward the E.

The tower karst hills in this study have specific features. The observed structural correlation for the tower karst hills mentioned above is different from the tower karst hills in Puerto Rico (Day, 1978). The tower karst hills in Puerto Rico tend to be more asymmetric or circular with the width/length ratios between 0.91 and 1.00. The circularity values of the tower karst hills are similar in both the Zhijin and Weining areas; less than 0.8 and clusters at 0.5–0.6 (Section 5.3). This suggests erosion does not similarly affect all hillsides. In addition, Day (1978) demonstrated that the relief of the tower karst hills in Puerto Rico is < 25 m and classified them using the long-axis length/relief ratio (*LR*) based on the “head-types” proposed by Balazs (1971). The *LR* of the tower karst hills in Puerto Rico range from 1.42 to 7.5, and their head types are: Yangshuo ($LR < 1.5$), Organos ($1.5 < LR < 3.0$) and Sewu ($3.0 < LR < 8.0$). In the present study, *LR* values of the tower karst hills range from 1.07 to 61.90, including another head type, Tual ($LR > 8.0$) which are points to the difference between the study area in Puerto Rico and China.

As noted, the cockpit karst hills have higher topographic complexity, larger areas and steeper slopes than the tower karst hills in the Zhijin and Weining areas, which agrees with the result from Jamaica reported by Lyew-Ayee (2007). However, there are some differences between the study areas in China and Jamaica. In Jamaica, the cockpit karst hills have higher frequency with shape more close to a circle. The cockpit karst hills in the Chinese study areas have irregular footprints than those of the tower karst hills. This may indicate that the karst landforms in Jamaica are more matured under a tropical climate with abundant rainfall, whereas the Chinese karst landforms are still on their way to the mature stage.

CHAPTER 6 KARST LAND-USE CHARACTERISTICS

6.1. Land-use classification

The overall accuracies of the supervised land-use classification based on the aerial photos are 87.64% for the Zhijin area and 89.47% for the Weining area based on the confusion matrix. The constructed land-use maps of the Zhijin and Weining areas are shown in Fig. 6-1 and Fig. 6-2, respectively.

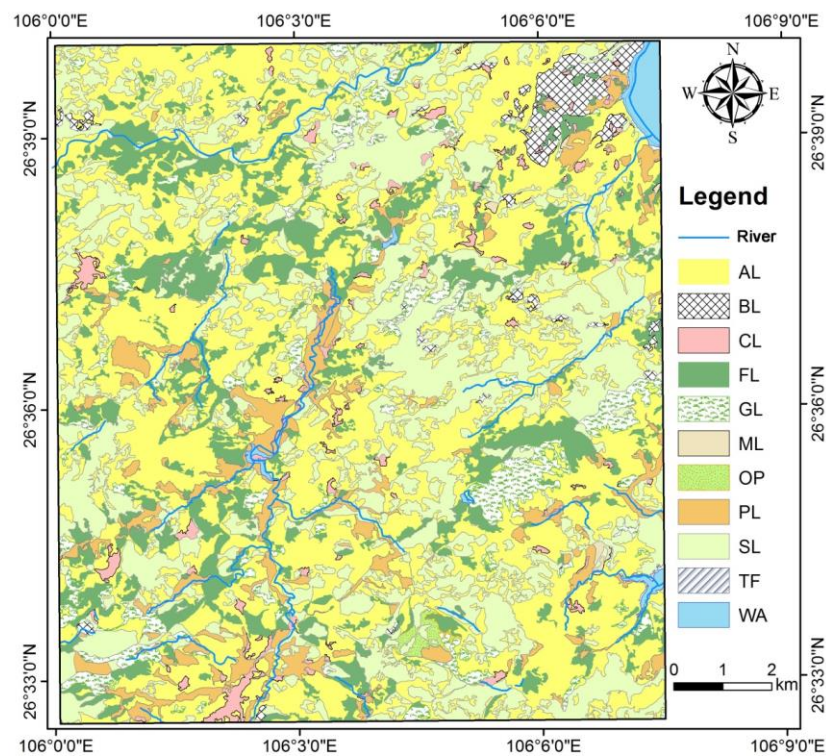


Figure 6-1. Land-use map of the Zhijin area. AL: arable land; BL: bare land; CL: construction land; FL: forest land; GL: grass land; ML: mining land; OP: orchard and perennial plantation; PL: paddy land; SL: shrub land; TF: tidal flat; WA: water area.

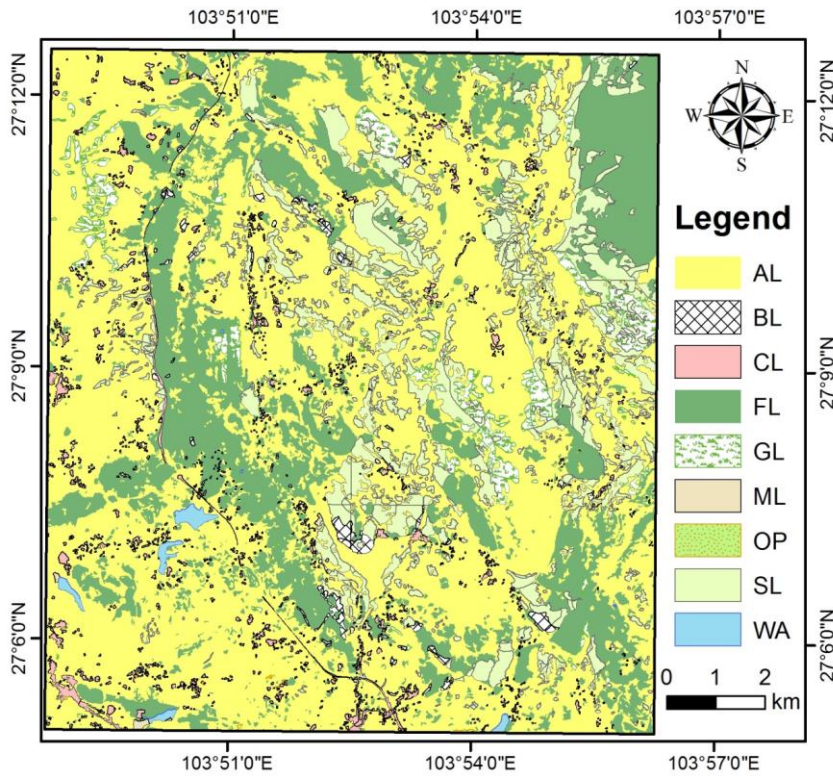


Figure 6-2. Land-use map of the Weining area. Codes in the legend are the same as in Fig. 6-1.

As shown in Fig. 6-3, the Zhijin area was highly cultivated, with dominance of farm land (arable land and paddy land) that reaches nearly 50%. Because of the complex landforms and difficulties in irrigation, arable land (dry field) was the main type of farm land. Vegetated areas (shrub land and forest land) take ~43% of the total area, and, with shrub land being 32.2% and forest land being 11.78%. The bare land covers 2.22%, indicating that rocky desertification occurred. Mining land and water area cover very small areas of 0.03% and 0.06%, respectively. Orchard and perennial plantation land takes 0.13%. Construction land and grass land cover 2.21% and 2.66%, respectively.

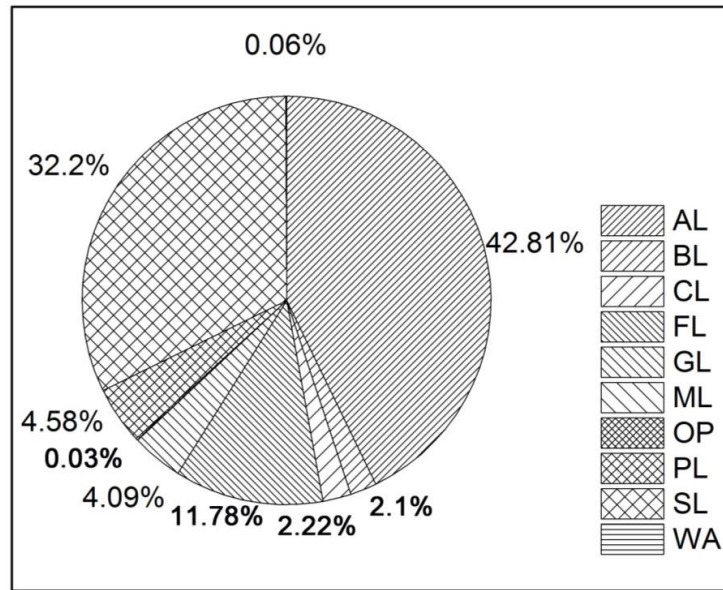


Figure 6-3. Area percentage for each land-use type in the Zhijin area

Arable land occupies ~55% of the Weining area (Fig. 6-4). There is no paddy land because of insufficient water resources. The vegetation area (forest land and shrub land) also take large area (~39%). Construction land and grass land cover 2.21% and 2.66%, respectively. Other land-use types occupy only small areas: bare land (0.99%), mining land (0.12%), orchard and perennial plantation (0.04%), water area (0.36%), Compared to the Zhijin area, the Weining area has a larger cultivated area, smaller bare land, smaller shrub land and larger forest land.

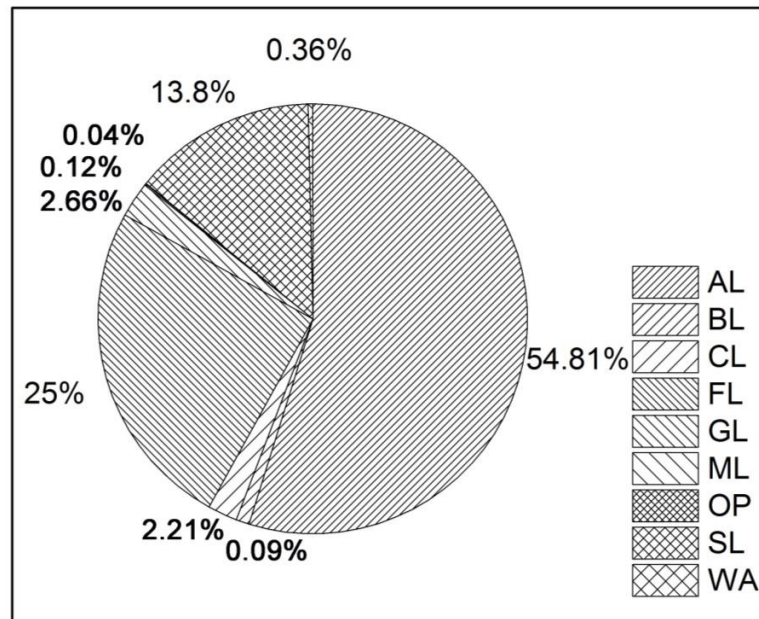


Figure 6-4. Area percentage for each land-use type in the Weining area

For the Mawo basin, the overall accuracy of the land-use map derived from the ALOS data

using the supervised classification is 89.42%. The resulted land-use map of 2009 is shown in Fig. 6-5. The area percentage for each land-use class is shown in Fig. 6-6. As a typical karst basin located in the Weining area, the Mawo basin is dominated by arable land (51.43%). The vegetation in the study area are forest land (1.14%), perennial plantation (17.16%), shrub land (24.56%) and grass land (1.37%). Field work revealed that forest land had been degraded into perennial plantation area. Bare land covers 2.76%, reflecting serious soil erosion there.

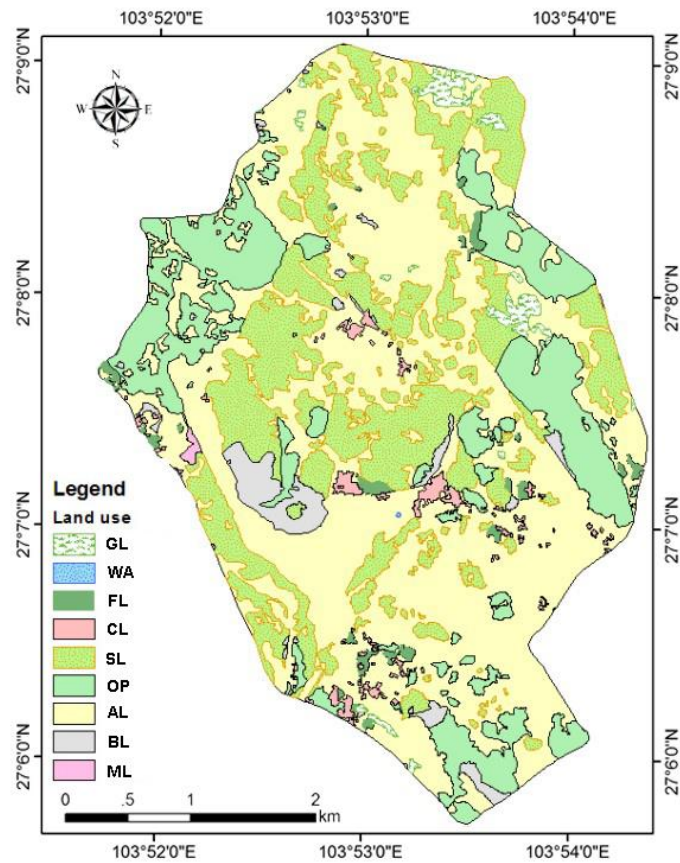


Figure 6-5. Land-use map of the Mawo basin in 2009. AL: arable land; BL: bare land; CL: construction land; FL: forest land; GL: grass land; ML: mining land; OP: orchard and perennial plantation; SL: shrub land; WA: water area.

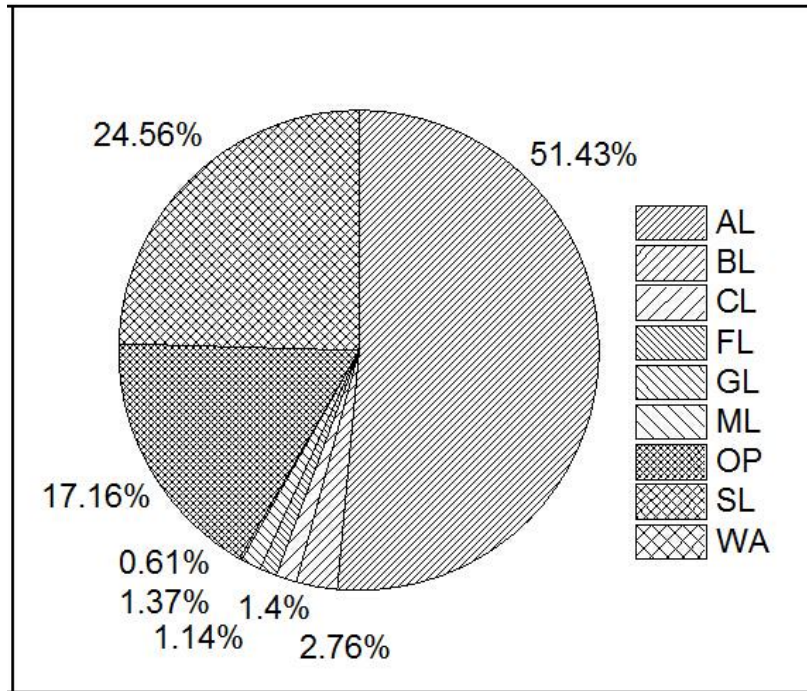
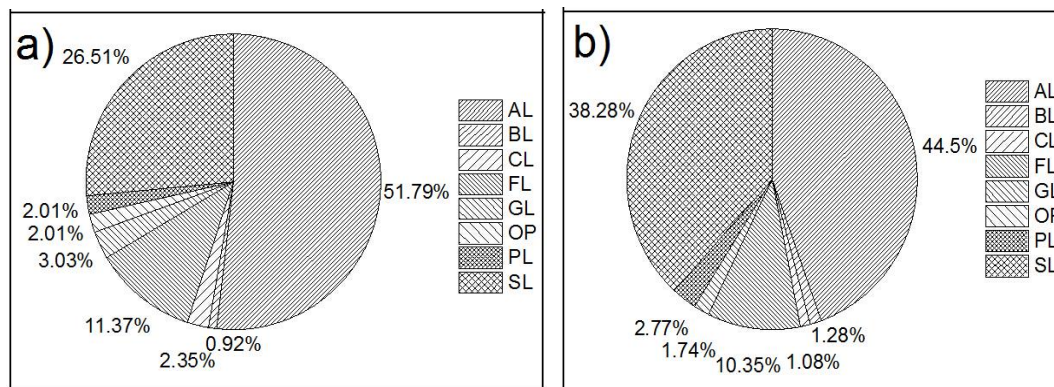


Figure 6-6. Area percentage for each land-use class in the Mawo basin

6.2. Relationships between land-use and landforms

The distribution of land-use classes in different landform types in the Zhijin and Weining areas are shown in Figs. 6-7 and 6-8, respectively. The result indicates that the study areas are highly cultivated even in the hilly areas. In the Zhijin area, agriculture in the lower areas takes higher percentages than that in the hilly areas. The sinkhole and depression areas are dominated by agricultural land-use with ratios of 51% and 45%, respectively. In the tower and cockpit karst hills, the agricultural area percentages are 44% and 38%, respectively.



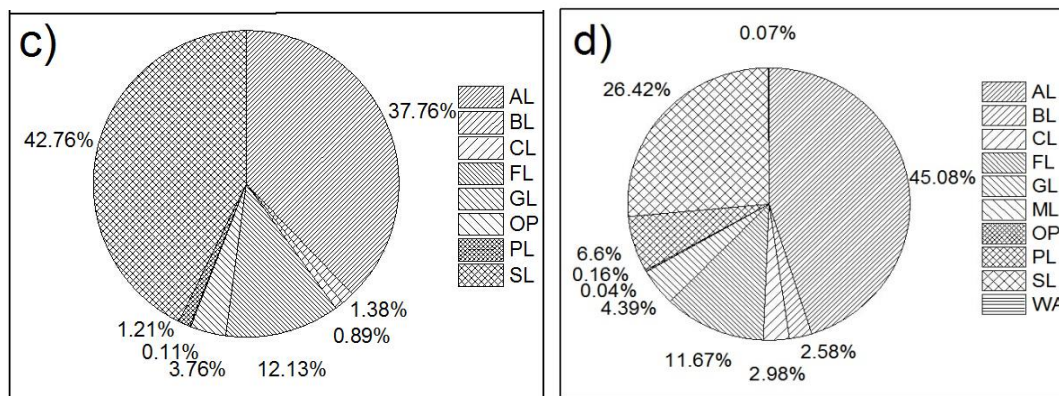


Figure 6-7. Area percentages of land-use types in the Zhijin area for different landform types: a) sinkhole; b) tower karst hill; c) cockpit karst hill; d) depression.

The agriculture area covers higher percentage in the Weining area than in the Zhijin area. As shown in Figs. 6-8, the agriculture in the sinkhole area takes a high percentage of 83%, and that in the depression area is 56%. However, not only in the lower areas but also the tower karst hills are dominated by the agriculture land with a ratio of 59%.

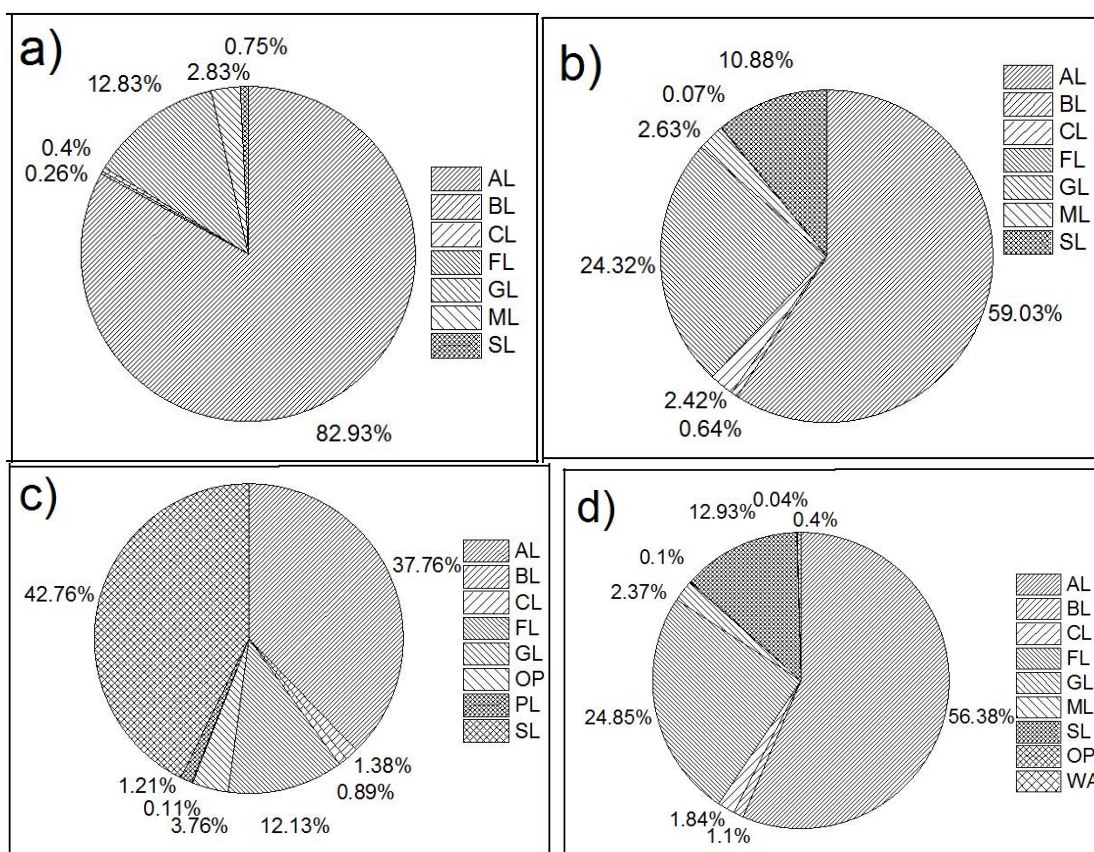


Figure 6-8. Area percentages of land-use types in the Weining area for different landform types: a) sinkhole; b) tower karst hill; c) cockpit karst hill; d) depression.

6.3. Development of rocky desertification

In order to examine the impact of human-induced landscape degradation, changes in the distribution of rocky land from 1977 to 2010 were analyzed. The rocky land is the result of rocky desertification and reflects the severe soil erosion in karst terrain. The agricultural and residential areas were significantly involved in the human activity; therefore, they can be regarded as human activity areas. Because of the low resolution of the remote sensing data in 1977, we defined the forest land and sparse forest as one class of forest. The land-use changes from 1977 to 2010 are shown in Fig. 6-9. The land-use maps for 1977, 2002 and 2010 are shown in Fig. 6-10.

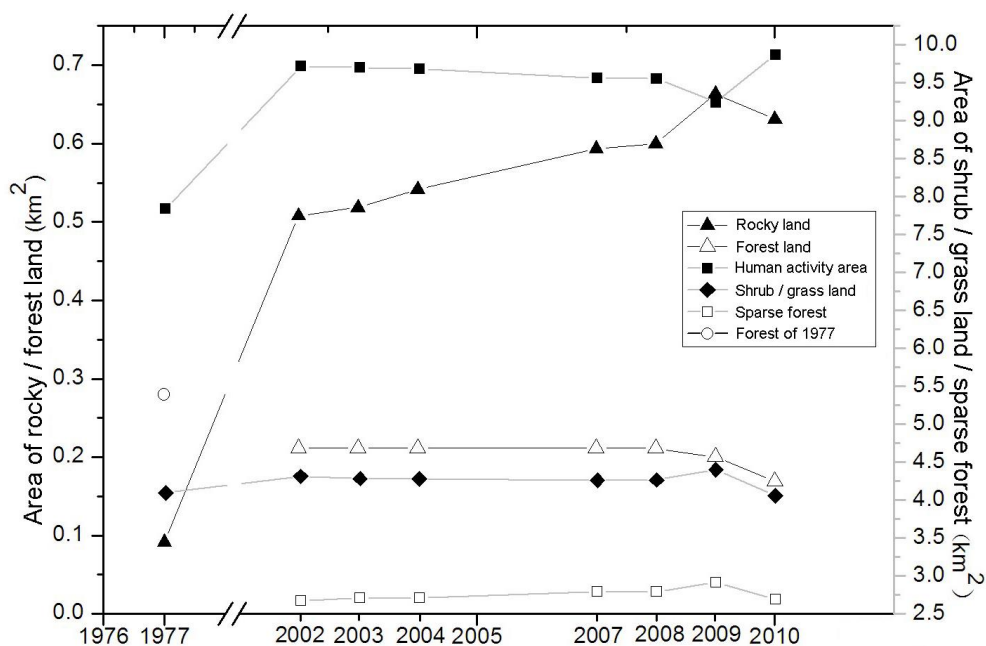


Figure 6-9. The areal change of land-use type

As shown in Fig. 6-9, the rocky land expanded dramatically from 1977 to 2002. In 2002, the sparse forest and forest land were 2.88 km², which is 2.51 km² less than those of 1977. However, the area of rocky land increased by 0.42 km², which is > 4 times more than the rocky area in 1977. During 1977–2002, the area of shrub land and the human activity area expanded by 0.22 km² and 1.87 km², respectively. Compared with the land-use distribution in 1977 (Fig. 6-10a), that in 2002 (Fig. 6-10b) was more fragile. In 2002, the rocky land occurs around the boundary of the depositional area (A to D in Fig. 6-10b) and the southern part of the study area (E in Fig. 6-10b).

Human disturbance also increased during 2002–2010. The rocky land expanded with a mean rate of 0.015 km²/year. The highest value of rocky land area is 0.66 km² in 2009 (Fig. 6-9). Fig. 6-10b and c indicates that 1) rocky land enlarged at areas with strong human

activity (C and D in Fig. 6-10b); and 2) shrub/grass land degraded to rocky land (A, B and F in Fig. 6-10c). The decrease of forest land and the increase of shrub/grass land (G in Fig. 6-10c and Fig. 6-9) also suggest that the landscape degraded with the development of rocky desertification.

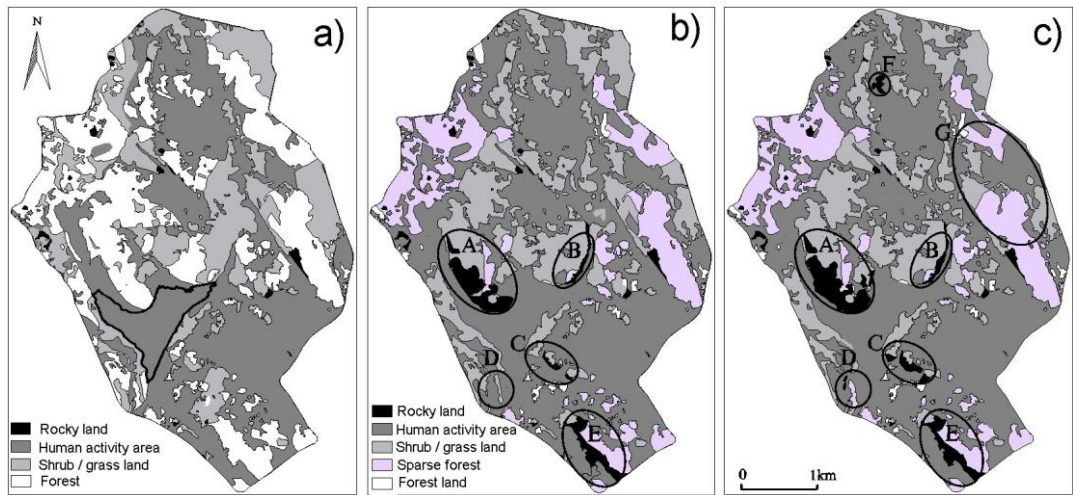


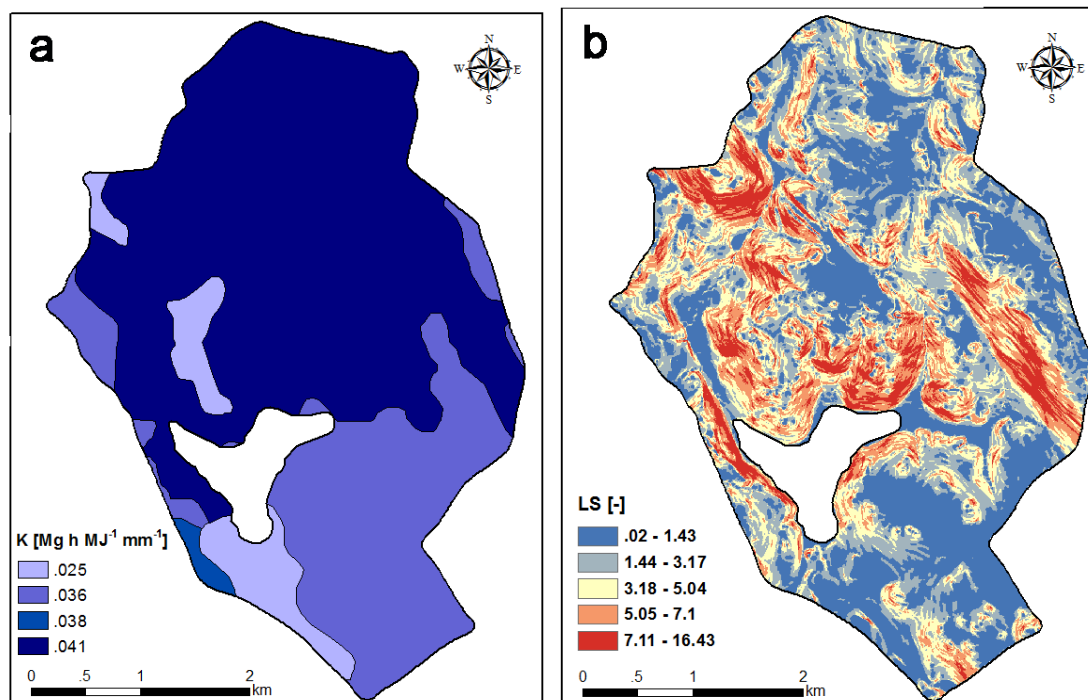
Figure 6-10. Land-use maps for different periods: a) 1977; b) 2002; c) 2010

CHAPTER 7 SOIL EROSION IN KARST LANDFROMS

7.1. Soil erosion rate estimation

7.1.1. RUSLE factor values

The distribution of values of the RUSLE factors in the Mawo basin is shown in Fig. 7-1. In Fig 7-1a, *K*-factor values are 0.025 Mg h MJ⁻¹ mm⁻¹ for brown calcareous soil, 0.038 Mg h MJ⁻¹ mm⁻¹ for brown soil. The *K*-factor value for calcaric cambisols falls in the range 0.030–0.036 with a mean of 0.036 Mg h MJ⁻¹ mm⁻¹, and that for yellow brown soil is in the range 0.036–0.045 Mg h MJ⁻¹ mm⁻¹, with a mean of 0.041 Mg h MJ⁻¹ mm⁻¹. The *LS*-factor is low in flat areas and high in steep areas, taking values between 0.02 and 16.43 (Fig. 7-1b). The *C*-factor values derived from the empirical formula range from 0.01 to 0.62 (Fig. 7-1c). *P*-factor values are explained in Section 3.6 and their distribution is shown in Fig. 7-1d. As written in Section 3.6, the *R*-factor value in the basin is 2865.5 MJ mm ha⁻¹h⁻¹y⁻¹.



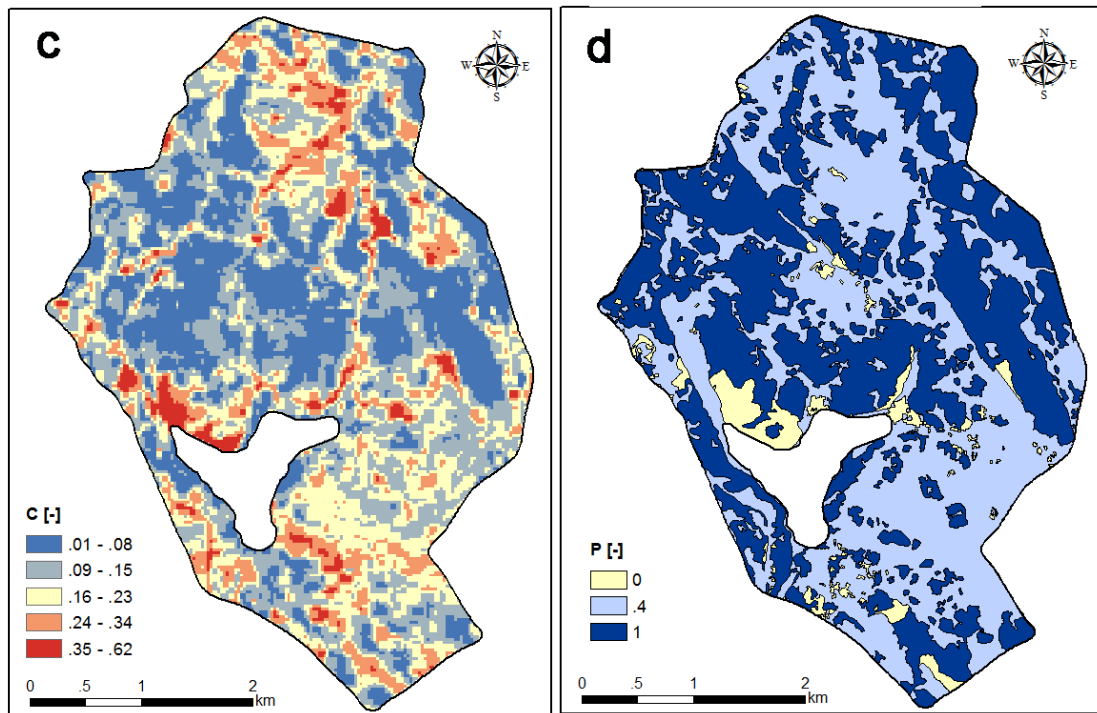


Figure 7-1. Spatial distribution of the calculated values of a) *K*-factor; b) *LS*-factor; c) *C*-factor; d) *P*-factor

7.1.2. Estimated annual soil loss

The map of soil erosion rate produced by the RUSLE model is shown in Fig. 7-4. The estimated soil erosion rate ranges from 0 to 549.17 Mg ha⁻¹ y⁻¹ with a mean of 30.24 Mg ha⁻¹ y⁻¹. In this karst basin, Xie et al. (2010) assumed the depression in the center as a perfect collector of eroded materials from surrounding hillslopes. According to their sedimentary analysis, the sedimentation there began in 1980 in response to accelerated erosion due to human activities mainly agriculture. From sediment volume in the depression, they computed the mean annual erosion rate for the period 1980–2009. The result (29.01 Mg ha⁻¹ y⁻¹) is very close to the mean annual soil loss estimated by the RUSLE (30.24 Mg ha⁻¹ y⁻¹). These values are also close to those in the literatures for the red soil region in the Jinsha River Basin of northeast Yunnan Province (Yang, 2002) and a karst catchment in middle Guizhou Province (Xu et al., 2008). The deviation of the predicted soil loss from the RUSLE falls in the range of average magnitude of error (0.2–37.6 Mg ha⁻¹ y⁻¹) obtained by Tiwari et al. (2000). Therefore, the RUSLE model and the sub-models used seem to work well for the basin.

Based on the Chinese Standard for Classification and Gradation of Soil Erosion (P.R.China, 1997), six classes of erosion rate were distinguished (Fig. 7-4 and Table 7-1: minimal (< 5 Mg ha⁻¹ y⁻¹); low (5–25 Mg ha⁻¹ y⁻¹); medium (25–50 Mg ha⁻¹ y⁻¹); high (50–80 Mg ha⁻¹ y⁻¹); very high (80–150 Mg ha⁻¹ y⁻¹) and extremely high (> 150 Mg ha⁻¹ y⁻¹). The area

and the mean soil loss rate in the studied basin for each erosion class are presented in Table 7-1. It is obvious that classes with large areas account for small quantities of soil loss, and vice versa. The erosion classes of minimal, low and medium are widely distributed (~81%) but account for only 41.74% of the total erosion. On the contrary, only ~19% of the catchment area has erosion loss $> 50 \text{ Mg ha}^{-1} \text{ y}^{-1}$, but contribute to 58.26% of the total soil loss.

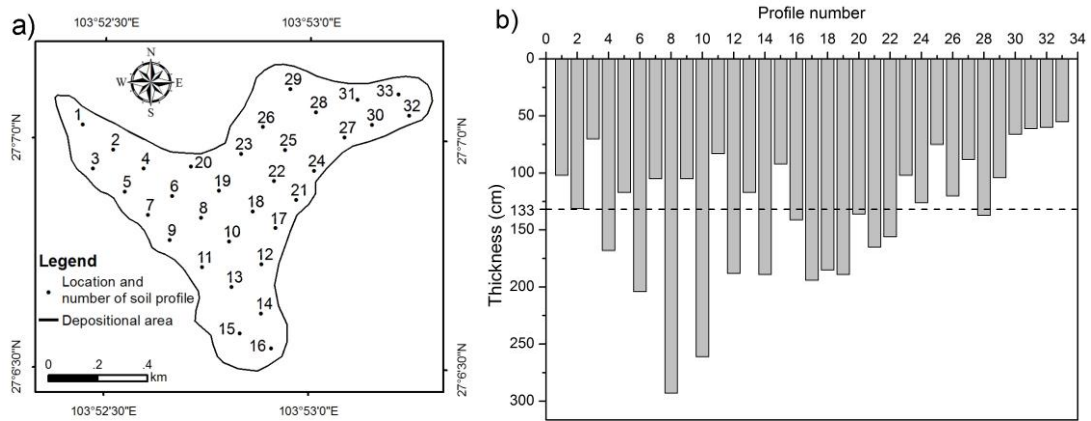


Figure 7-2. The sedimentation records based on Xie et al. (2010): a) location and number of soil profile; b) sediment thickness from 1980.

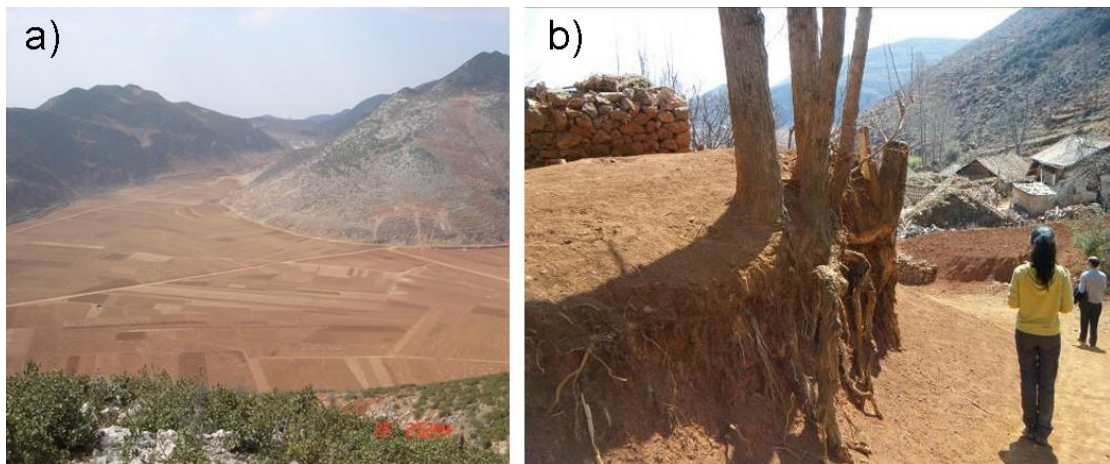


Figure 7-3. The field photographs of the Mawo basin: a) overview; b) exposed tree roots after soil erosion

Table 7-1. Classes of annual soil erosion rate

Erosion class	Class range	Area		Soil loss rate	Soil loss rate
	(Mg ha ⁻¹ y ⁻¹)	(ha)	(% of total)	(*10 ² Mg y ⁻¹)	(% of total)
Minimal	0–5	363.52	23.38	6.74	1.42
Low	5–25	599.02	38.52	81.96	17.26
Medium	25–50	303.16	19.50	109.46	23.06
High	50–80	151.18	9.72	95.62	20.14
Very high	80–150	105.86	6.81	112.25	23.64
Extremely high	> 150	32.25	2.07	68.70	14.47

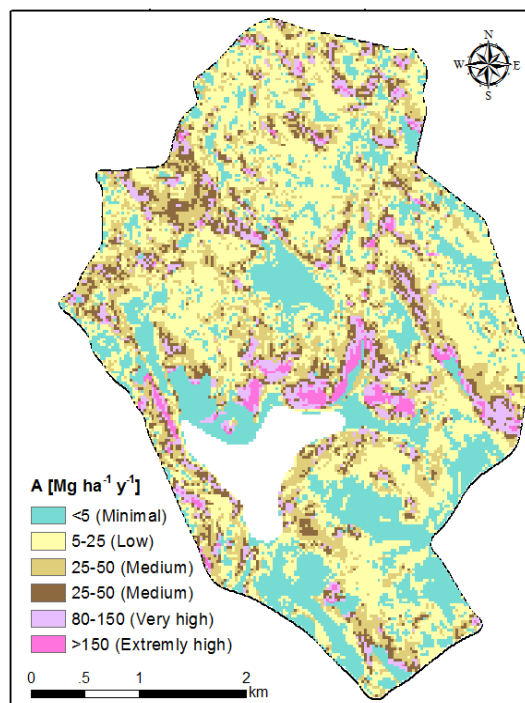


Figure 7-4. Spatial distribution of the mean annual soil loss estimated by the RUSLE model

7.1.3. Soil loss per land-use type

Soil loss estimates for different land-use types were obtained by superimposing the soil erosion maps and the land-use map (Tables 7-2 and 7-3). The results show that soil loss from the dense forest and grass land is low with 1.69% and 1.51% of the total erosion amount, respectively, because 1) their areas are small, and 2) over 30% of the dense forest and grass land areas fall on the category of the low erosion zone. Sparse forest land has an average annual soil loss rate close to that of forest land; 66.73% of sparse forest land has the minimal

to medium erosion classes, while 64.76% of the soil loss amount from sparse forest land comes from areas with the high to extremely high classes. Shrub land has the largest soil loss of approximately 50% of the gross amount of the catchment, as well as the highest annual erosion rate. Although 63.12% of shrub area falls in the zones of minimal to medium erosion, the larger erosion amount (73.41%) is from areas with the high to extremely high erosion classes. The lowest rate of average annual soil loss occurs in farm land which covers ~50% territory of the erosion area. Most of the cultivated areas do not have serious erosion that 95.19% of the area and 75.56% of the amount result from the zones of minimal to medium erosion. Based on the mean soil loss rates shown in Table 7-2, the order of mean soil erosion rates for different land-use types is: shrub land > sparse forest land > forest land > grass land > farm land. In the study area, farm land occurs in relatively flat areas, resulting in the smallest erosion. Except for this, the erosion rate is negatively correlated with vegetation density, which is high in forest and grass land but low in shrub land. The negative correlation agrees with observations in the other areas (e.g., Nearing et al. (1989); Gyssels et al. (2005)): the more plant root and canopy density, the less water flow and less erosion, because of physical and biological protection of soil.

Table 7-2. RUSLE related values according to land-use type

Land-use type	Area	Area	Mean	Mean	Mean	Mean rate	Total annual soil loss	
		percentage	<i>NDVI</i>	<i>C</i>	<i>LS</i>	<i>A</i>		
	(ha)	(%)	(-)	(-)	(-)	(Mg ha ⁻¹ y ⁻¹)	(Mg y ⁻¹)	(% of total)
Forest land	18.61	1.20	0.49	0.16	2.63	44.30	7.95	1.69
Sparse forest land	279.61	17.98	0.54	0.11	4.37	44.84	125.64	26.70
Shrub land	400.16	25.73	0.52	0.12	4.27	52.20	209.94	44.62
Grass land	22.32	1.44	0.51	0.14	2.38	32.07	7.12	1.51
Farm land	763.93	49.13	0.49	0.16	2.08	15.48	119.92	25.48
Rocky land	44.98	2.89	0.41	0.26	4.52	-	-	-
Mining land	2.58	0.17	0.32	0.40	3.07	-	-	-
Building land	22.81	1.47	0.53	0.12	1.05	-	-	-

Table 7-3. Area and soil loss amount for each land-use type

Soil loss area and amount (% of each land-use type)	Minimal		Low		Medium		High		Very high		Extremely high	
	Area	Amount	Area	Amount	Area	Amount	Area	Amount	Area	Amount	Area	Amount
Forest land	11.50	0.57	30.66	9.45	25.78	20.25	14.29	20.50	14.29	35.96	3.48	13.26
Sparse forest	7.14	0.34	28.67	9.48	30.92	25.42	18.61	26.06	12.85	29.94	1.81	8.76
Shrub land	7.07	0.27	30.89	8.80	25.16	17.52	16.77	20.32	14.00	28.31	6.11	24.78
Grass land	12.96	0.71	46.48	20.47	18.03	20.33	13.52	26.69	8.45	27.66	0.56	4.14
Farm land	32.21	4.56	49.50	41.27	13.48	29.73	3.30	12.94	1.31	8.79	0.20	2.71

7.1.4. Soil loss per landform type

In the Mawo basin, the areas of the depressions, tower and cockpit karst hills are 88.31%, 7.97% and 3.71% respectively. The mean soil erosion of the depressions ranges from 0.03 to 655.46 Mg ha⁻¹ y⁻¹ with a mean of 29.35 Mg ha⁻¹ y⁻¹. The erosion rate range of the tower karst hills is 0.41 to 382.60 Mg ha⁻¹ y⁻¹ with a mean of 34.39 Mg ha⁻¹ y⁻¹. The erosion range of the cockpit karst hills ranges from 0.03 to 315.44 Mg ha⁻¹ y⁻¹ with a mean of 35.52 Mg ha⁻¹ y⁻¹.

The *t*-test was applied to evaluate the soil erosion difference among the depressions, tower and cockpit karst hills (Fig. 7-5). These results were obtained: 1) The erosion rate difference among the landforms is statistically significant ($p < 0.05$); 2) The order of soil erosion rate is cockpit karst hills > tower karst hills > depressions; and 3). The erosion rate of the cockpit karst hills shows the most apparent difference among the three. The tower karst hills erosion rates show relatively small variance than the depression and cockpit karst hills erosion rates.

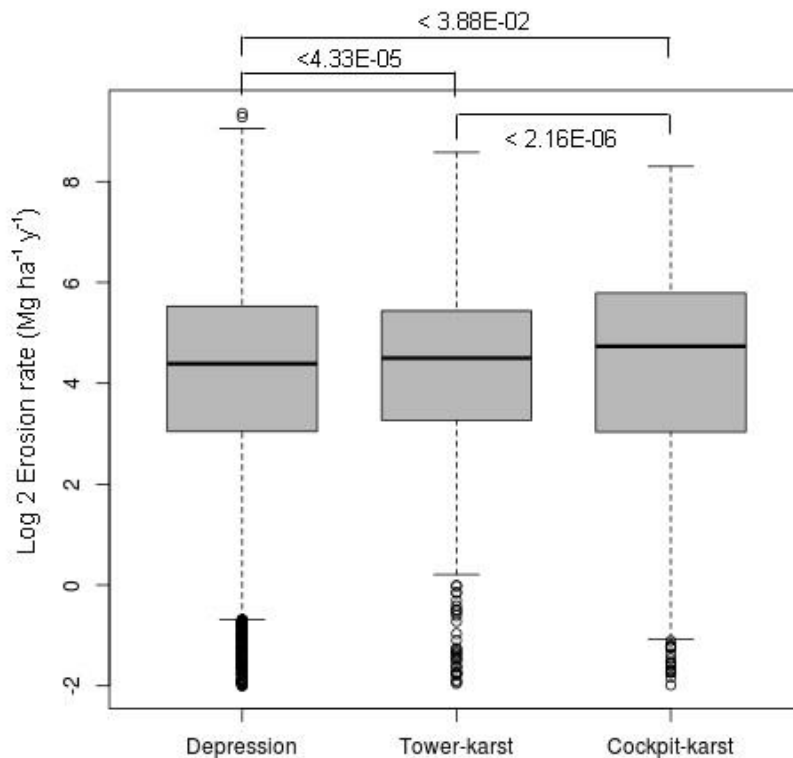


Figure 7-5. Box plots of erosion rates for the three major landform types in the Mawo basin. The difference among the landform types is significant based on the *t*-test ($p < 0.05$).

The order of soil erosion rate according to the karst landform type reflects topographic

characteristics. For example, the cockpit karst hills tend to have steeper slopes than the tower karst hills, and the depressions are gentler. The higher relief and ruggedness of cockpit karst hills than those of the tower karst hills could also contribute to the observed difference. Elsewhere in the world, soil erosion in hilly lands is also significantly affected by terrain slope, relief and ruggedness (Tamene et al., 2006; Sarangi et al., 2007; Asadi et al., 2012; Ziadat and Taimeh, 2013).

7.2. Effect of factors in the RUSLE

In order to analyze the source of the error of the RUSLE model, we specify the effect of the sub-models in the RUSLE on erosion scenario. Fig. 7-6 was created to summarize the relationship between the annual soil loss and factors in the RUSLE model except for the *R*-factor that the precipitation data for the study area were limited. Elevation was additionally taken into account to explore the relationships between soil loss and environmental factors. We divided the values of each factors into classes. The intervals of *C*-, *L*-factor, slope and elevation are 0.05, 0.2, 5° and 50 m, respectively. The *K*- and *P*-factor use the previous values based on soil and land-use type in Section 3.6. The average values and standard deviation values of annual soil loss for classes of these parameters, and the average values and standard deviation values in each classes, are also showed in the figure. The slope class with values > 45° in Fig. 7-6a, elevation classes of 2200–2250 and 2800–2850 m in Fig. 7-6b, and the *C*-classes > 0.3 in Fig. 7-6c, are excluded because they occupy only < 1.5% in a total pixel of 25118 attributed with values. In Fig. 7-6, the mean and standard deviation of soil loss tend to increase with the slope, *C*- and *P*-factors. These positive relationships between soil erosion and slope, *C*- or *P*-factor are expected. Because the vegetation and the slope steepness are positively related with the overland flow and flow velocity (Haan et al., 1994), and values for the conservation practice factor are the most uncertain but significantly influence the results (Renard et al., 1997). On the other hand, with a generally large standard deviation, the mean values of soil loss for elevation classes fluctuate slightly around the mean annual soil loss value of the catchment. Additionally, the *L*-factor shows a high concentration in the low slope length range and relatively stable *L*-value. All these results infer that: firstly, high rates of soil loss are recorded not only in the high mountains but also in low regions of the catchment; secondly, the *S*-, *C*- and *P*-factors play more important roles than *K*- and *L*-factor in the soil

erosion. This agrees with the findings by López-Vicente et al. (2009) that the *LS*-factor largely depends on slope steepness. The strong influence of the slope steepness also can be found as mentioned in Sections 5.4 and 7.1. In, Section 5.4, we demonstrated that cockpit hills have higher slope steepness than that of tower karst hills. Therefore, the cockpit karst hills have a higher erosion rate than the tower karst hills (Section 7.1).

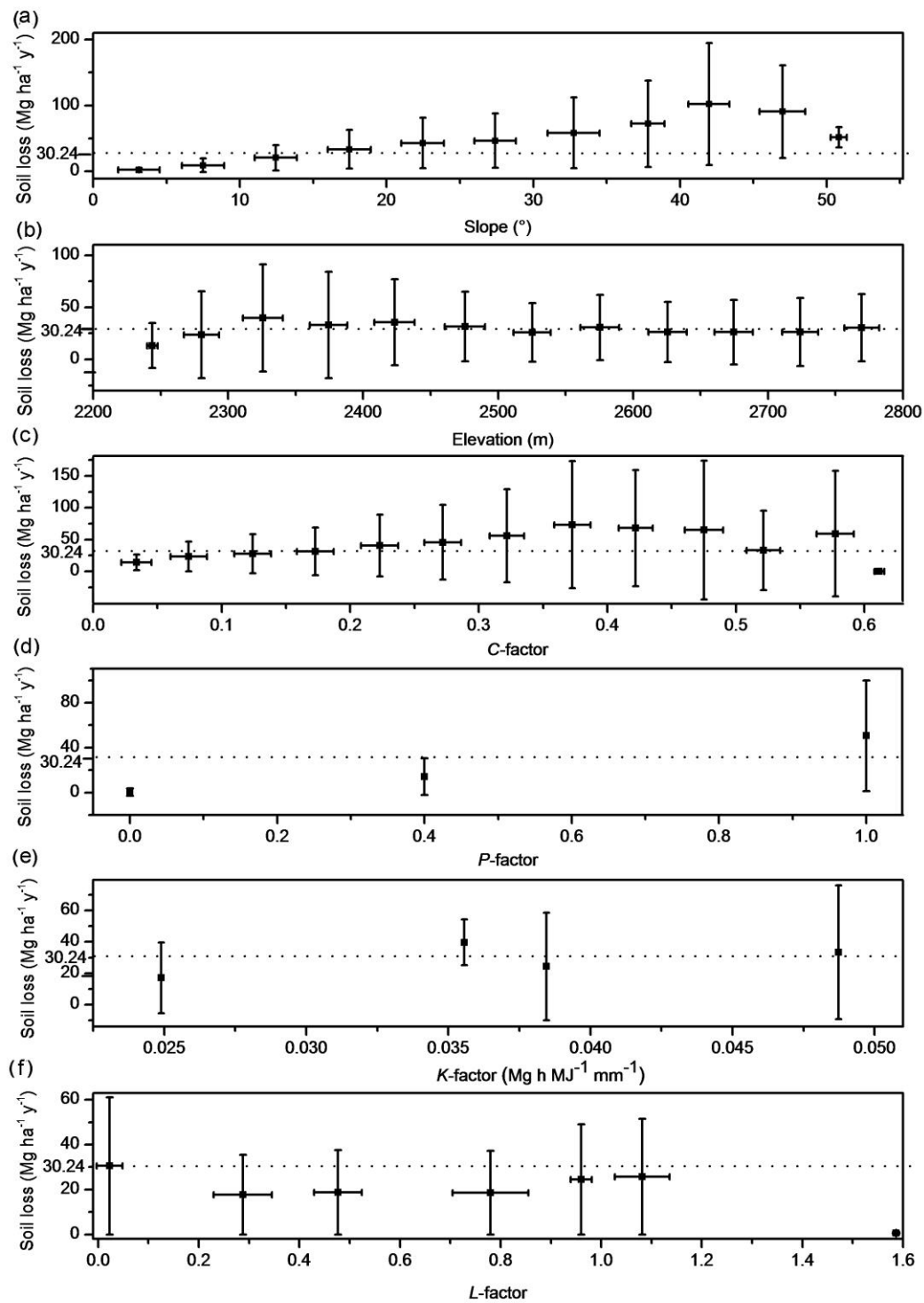


Figure 7-6. Relationships between the annual soil loss and each of the model factors except the *R*-factor. The average and standard deviation of values in each class are shown. a) slope; b) elevation; c) *C*-factor; d) *P*-factor; e) *K*-factor; f) *L*-factor.

7.3. Effect of grid size in the RUSLE

Cell dimension influences the magnitude and variability of the soil erosion reconstructed by the RUSLE. This fact also reflects that higher resolution of data does not assure better model prediction. Fig. 7-7 shows the sensitivity of the *K*-, *L*-, *S*-, *C*- and *P*-factors normalized by the maximum value at different spatial resolution in the study area. It shows that, unlike the stability of *K*- and *P*-factors, the *L*- and *S*-factors are very sensitive to the grid size. The high fluctuation of the *L*-factor curve implies that the *L*-factor is more sensitive than the *S*-factor in the study area. In particular, the *C*-factor presents slight sensitivity at grid size > 50 m.

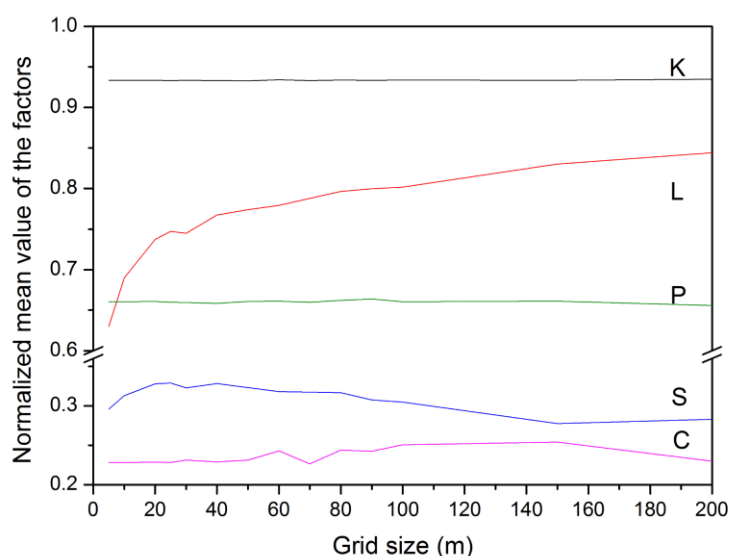


Figure 7-7. Sensitivity graph of the RUSLE factors (except for *R*-factor) to grid size

In order to analyze the significant influence of the *LS*-factor in detail, the output of the RUSLE model and sensitivity of the *LS*-factor at the spatial resolution of 5–200 m were evaluated. The methods described by Moore and Burch (1986) and McCool et al. (1987; 1989) were used to simulated the *LS*-factor. The results of the two methods are generally four times as large as those derived from the adopted methods. Fig. 7-8 shows the mean values of soil loss and *LS*-factor and the mean *LS*-values divided by 4 based on the method of Moore and Burch (1986) and McCool et al. (1987; 1989). In Fig. 7-8, it is obvious that the coarser grid sizes lead to higher average values of the *LS*-factor and mean soil loss. Likewise, the mean *LS*-values calculated by the method of Moore and Burch (1986) generally increase with increasing grid size, except for the grid size of 70 and 150 m. For

the approach of McCool et al. (1987; 1989), the change in the mean *LS*-values with grid size can be divided into two parts. One is the grid size range of 5–60 m. In the scenario of the resolution higher than 60 m, fine grid size values correspond to high values of the *LS*-factor. The other is the grid size of 60–200 m, and the curve of mean *LS* values shows fluctuations, with a maximum *LS* value in grid size of 90 m. The positive correlation of the *LS* values and grid size agrees that high resolution does not assure better model prediction (Van Rompaey et al., 1999).

However, previous studies has found that soil loss is more sensitive with slope steepness than slope length (McCool et al., 1987) and coarse resolution inputs generally lead to low *LS*-values and corresponding soil loss values (Wu et al., 2005; Lee and Lee, 2006). The difference between the present and previous studies may be due to the scale and topographic features of different study areas. In a large study area with remarkable terrain difference and large drainage area such as the Bosung basin (Lee and Lee, 2006), the sensitivity of the *S*-factor is higher than that of the *L*-factor. On the contrary, the *L*-factor computed from the grid size may be more sensitive than the *S*-factor in the study area with relatively small catchment and drainage area (though high relief). Therefore, as no rules has been clearly proposed, discretion of the *S*- and *L*-factor's sensitivity based on basin characteristics and modeling complexity is needed for quantitative estimation of soil loss, for selecting the best grid size for analysis.

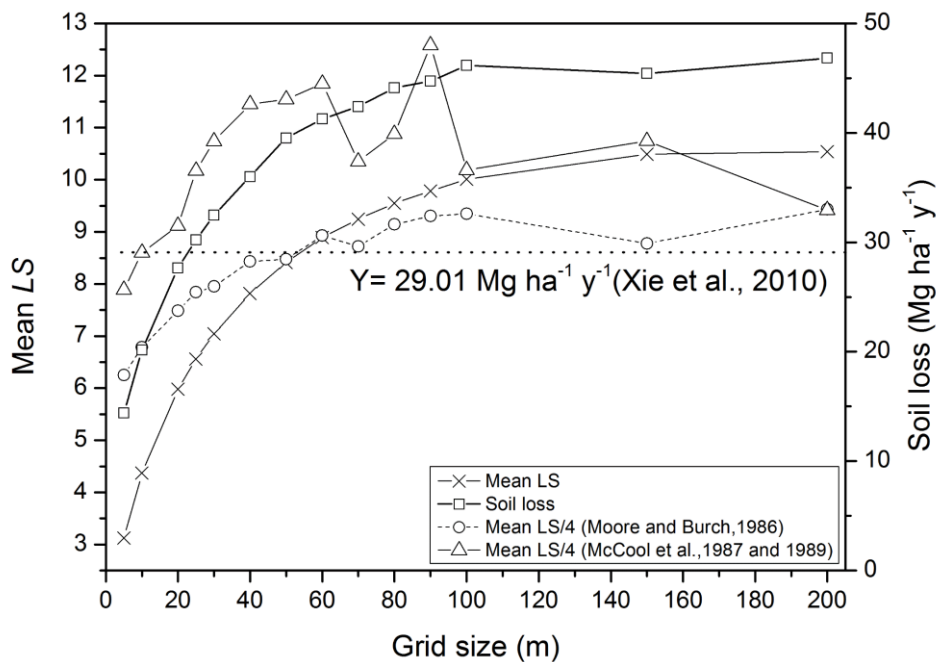


Figure 7-8. Simulated values of the *LS*-factor and soil loss at different cell sizes: 1) mean

LS-factor calculated with the methods adopted in the present study; 2) annual soil loss based on factors calculated by methods adopted in this study; and 3) mean *LS*-factor values divided by 4 calculated by the methods suggested by Moore and Burch (1986) and McCool et al. (1987, 1989).

7.4. Comparisons with other areas

The serious soil erosion in the study area is common to arable land in karst regions of southwest China (Wang et al., 2004). However, the estimated soil loss of $30.24 \text{ Mg ha}^{-1} \text{ y}^{-1}$ for the Mawo basin is lower than that in the hilly catchment of Northeastern India ($51 \text{ Mg ha}^{-1} \text{ y}^{-1}$; Dabral et al., 2008), where more abundant rainfall occurs. On the other hand, the soil erosion rates for the land-use types obtained in this study also differ from those in the Chinese Loess Plateau. In the Mawo basin, soil loss for each land-use is ranked as: shrub land > sparse forest land > forest land > grass land > farm land. In the middle and eastern Loess Plateau, Wei et al. (2007) and Feng et al. (2010) measured the soil erosion rate using the ^{137}Cs method. The results show that the soil loss rate is ranked as: farm land > grass land > forest land > shrub land. This difference is due to two factors. First, small-scale stone-framed terracing and contour tillage effectively reduce soil erosion in farm land in the Mawo basin (Yang, 2002; Xu et al., 2008a), whereas the area investigated by Wei et al. (2007) in the Loess Plateau lacks effective soil protection measures. Second, shrub land in the Mawo basin mainly occurs in areas with high SL values (Fig. 7-1b). However, in the study area of the Loess Plateau, slope is relatively low and the existence of shrub can regulate surface runoff (Xu, 2005; Wei et al., 2007).

CHAPTER 8 INSIGHTS INTO ENVIRONMENTAL PROBLEMS

The results mentioned in the previous sections indicate that the environment problems in the study areas, especially soil erosion and rocky desertification, are affected by both natural topography and human land-use (Chapters 6 and 7). This has often been demonstrated in karst areas, where new settlement and agricultural activities increase landscape fragmentation and trigger rocky desertification (Wang et al., 2004). Rocky desertification is serious not only in the study area but also the surrounding areas in Southwest China (Guo et al. (2013). Especially Guizhou Province is suffered from the most serious rocky desertification in China, and the rocky area greatly increased during the 1970s to 1990s (Guo et al., 2013). The present study has also shown that rocky areas dramatically increased from the late 1970s to the early 2000s (Section 6.3).

Some studies indicated that land-use changes in karst areas may degrade epikarst which is a significant function of karst ecosystems (Pipan and Culver, 2013) controlling water infiltration (Gutiérrez et al., 2014). Furthermore, a typical human activity in karst areas is landform modifications due mainly to quarrying of carbonate rocks (Gunn, 1993; Parise and Pascali, 2003; Delle Rose et al., 2007; Canora et al., 2008). With the increasing impact of various human activities, protection of karst environment becomes challenging (Gutiérrez et al., 2014).

Based on the analyses of landforms (Chapters 4 and 5), land-use (Chapter 6), and soil erosion (Chapter 7), the following five suggestions are made for environmental conservation and sustainable development in the study areas of Guizhou Province.

First, land-use regulations need to be applied and they should be different according to the landform types. i) Cultivation within sinkholes should be limited, although arable land widely occurs not only flat areas and hills but also in sinkholes. Knowledge about the structure of sinkholes is insufficient in the study areas. For example, some shallow sinkholes may be connected to deep sinkholes but it is unknown because of filled soils. Such filled sinkholes may cause subsidence because of reactivation or soil compaction under the lack of basal support (Gutierrez et al., 2008). Cultivation in the sinkhole area, particularly those with irrigation, can be risky. ii) Paddy land with intensive irrigation should be sufficiently away from the geologic joints and faults to avoid sinkhole hazards. Even if present or buried sinkholes do not exist, the geologic structure facilitate underground water movement if irrigation is active, leading to faster solution of carbonate

rocks and generation of sinkholes.

Second, agricultural areas in hilly areas especially the cockpit karst hills need more systematic soil conservation practice. The study areas have relatively high population density, which can be an obstacle in reducing arable land. However, high population density or more available labor force may facilitate the installation of practical conservation measures such as terracing, contouring, strip cropping and covering cultivation.

Third, human activities other than agriculture also need to be reduced or regulated. For example, construction processes such as raveling and drilling may affect hydrological systems and generate various problems including faster erosion and sinkhole generation. Deforestation for any purposes decreases vegetation coverage and hence weakens soil protection. This study has indicated that deforestation is the major reason for land-use degradation and resultant rocky desertification.

Fourth, a comprehensive geospatial database including various geographical data for different periods is required. Although this research has utilized different geospatial data such as DEMs and land-use maps from satellite images, more thematic data such as population distribution and bedrock lithology are necessary for effective environmental analyses and planning. Data for past periods are also useful. For example, if the distribution of pre-existing sinkholes before recent burial is available, it is valuable for predicting sinkhole regeneration. Detailed temporal land-use data are also essential. For example, this research has suggested that grass land is prone to rocky desertification. The spatial distribution of the grass land is a key information for the future rocky desertification. Temporal changes in the distribution of grass land and progress of deforestation are basic and important information to deal with rocky desertification.

Fifth, after the construction of the geospatial database, advanced statistical modeling should be applied to the data for mapping susceptibility of sinkhole formation, rocky desertification and soil erosion. Factors including landform types, morphometric parameter values, geological structure, lithology, vegetation, land-use, level of land management, and other human activities such as construction will be considered for the susceptible modeling. The resultant susceptibility maps will be useful for cost-effective environmental management and future development in the study areas.

CHAPTER 9 CONCLUSIONS

The results of this study suggest that the semi-automatic sinkhole identification approach using various DEMs provides an effective way to analyze sinkholes, depressions, tower karst hills and cockpit karst hills in broad and/or inaccessible areas. It reduces manual errors and processing time. The comparison of results from different datasets can be realized through the application of fast data acquisition at low cost. Although the ASTER GDEM is not suitable for research in the study area, it is not a general criticism of the data and it might perform better in other areas or for different objectives.

We resampled the DEMs and set thresholds for sinkhole identification. It is to 1) remove the artificial sinkholes caused by data characteristics; 2) match various morphometric characteristics of sinkholes with distinct landscapes; and 3) improve the efficiency of the model. Although DEM coarsening was found to be effective in reducing the effects of local data errors, excessive coarsening should be avoided because all the DEMs with grid sizes > 30 m could not capture small real sinkholes. The thresholds we set are: area = 60 m^2 , ellipticity = 0.2 and TPI = 0. With these thresholds, the best performance of the model was generated by using the DEMs derived from the topographic maps, those not from satellite remote sensing. The accuracy of the semi-automatic model ranges from 0.78 to 0.95 for the DEM resolutions of 3 to 90 m. In summary, good model performance can be achieved if DEM resampling and the setting of thresholds are appropriately combined.

The application of semi-automatic approach on the classification of tower and cockpit karst hills indicated high productivity. They could be distinguished base on DEM analysis that follows their definition. It avoids 1) the misclassification on the boundary of these two types of karst hills; 2) the error on selecting training samples of the supervised classification; and 3) time- and labor-consuming visual interpretation and field work. According to the comparison with the geomorphological maps from field work and aerial photo interpretation, the accuracy of karst hill classification ranges from 85.02% to 94.65%. The proposed semi-automatic approach for landform classification is useful for establishing a basis of environmental research because field-based approaches often have limitations in areal coverage, objectiveness, and efficiency.

This study demonstrated the sinkhole morphometry derived from different approaches. Some conclusions are made: 1) The morphometric characteristics of sinkholes derived from the semi-automatic approach agree with those from the field-based approach. The sinkhole

morphometric values (area, perimeter, long-axis length, orientation, ellipticity and volume) in the study area show large value ranges. 2) Sinkhole plan shapes are skewed with irregular or elliptical shape. This indicates that the sinkholes in the region are relatively old. 3) Sinkhole long-axis length and sinkhole alignments are generally parallel with that of the faults. Tensional faults provided the necessary conduits and structural conditions for the formation of sinkholes. 4) The area-to-volume ratio argues about solution-only origin for the sinkholes in the region.

This study also demonstrated the morphometry and morphometric differences among the tower and cockpit karst hills in central and western Guizhou Province. Fourteen morphometric parameters were measured in terms of horizontal, vertical and overall shapes. As a result, compared with the tower karst hills, the cockpit karst hills have larger areas but less circular foots, higher relief with steeper mean slope values and lower curvature values but higher complexity. These differences between the tower and cockpit karst hills are clearer in central Guizhou Province concerning the vertical and shape measures but not the horizontal parameters.

The land-use shortage and soil erosion issues were also analyzed with the landform types generated by the semi-automatic approaches. The result indicated that the study areas were highly cultivated even in the karst hill areas. Over 50% of the tower and cockpit karst hills area have been developed for agriculture, although agriculture in the flatter areas is more intensive. For the differences between the central and western regions of Guizhou Province, the cultivation area takes higher percentage in the western region and the difference of agriculture ration between sinkhole and depression is clearer in the western region.

Human disturbance including agricultural land-use has led to serious problems of soil erosion in the study areas. This study evaluated erosion rates of a selected area (Mawo basin) using the RUSLE model supported by a field sedimentary record. The RUSLE gave a mean annual erosion rate of $30.24 \text{ Mg ha}^{-1} \text{ y}^{-1}$ for the period from the 1980s to the 2000s. The mean annual erosion rate obtained using the RUSLE is consistent with the result of previous research based on the record of accumulated sediment in a closed depression during 1980 to 2009. The order of soil erosion rate, cockpit karst hills > tower karst hills > depressions, reflects differences in topographic characteristics especially slope, relief and ruggedness.

Human activity significantly affected the land-use degradation and resultant rocky desertification. Analysis of satellite images has indicated that during 1977–2010, rocky

desertification enlarged by 1.08 km². Such rocky desertification started from landscape degradation associate with shifts from dense vegetation to sparse vegetation. The enlargement of rocky desertification clustered around the boundaries of human activity areas, indicating that the rocky desertification was triggered by human disturbance. This also been inferred by the order of annual soil loss in relatively natural areas: shrub land > sparse forest land > forest land. The negative correlation between soil loss and vegetation density implies the important of controlling human activity for the migration of soil erosion and rocky desertification.

Based on the results and discussion concerning analyses on landforms, land-use and soil erosion, four suggestions have been made for environmental management and sustainable development: 1) application of land-use regulations, especially in sinkholes and areas close to geological structure; 2) application of soil conservation practice to hilly areas especially the cockpit karst hills; 3) reduction or regulation of human activities other than agriculture such as construction and deforestation; 4) construction of a comprehensive geospatial database including data for both natural and human environments at different periods; and 5) statistical modeling to construct maps showing susceptibility to sinkhole formation, rocky desertification, and soil erosion. The present research will serve as a prototype or basic information for such future advanced statistical modeling.

ACKNOWLEDGEMENTS

I would firstly express my great and sincere gratitude to my supervisor, Prof. Takashi OGUCHI for his undying patience, enthusiasm and support throughout the last four years. His guidance and support led to the improvement of my research. I would also like to thank Prof. Yuichi S. HAYAKAWA at the Center for Spatial Information Science, The University of Tokyo. He supported me with professional skills. Members of the laboratory of Dr. OGUCHI also deserve my sincerest thanks for their assistant and encouragement, which was a source of inspiration to me. I am also very graceful to Prof. Pan WU in Guizhou University, China, for his tremendous help with data collection, professional advices and encouragement.

REFERENCES

- Abrahams, A. D., 1984. Channel networks: A geomorphological perspective. *Water Resources Research* 20(2), 161-188.
- Alexakis, D.D., Hadjimitsis, D.G., Agapiou, A., 2013. Integrated use of remote sensing, GIS and precipitation data for the assessment of soil erosion rate in the catchment area of “Yialias” in Cyprus. *Atmospheric Research*, 131, 108-124.
- Ali-Toudert, F., Mayer, H., 2006. Numerical study on the effects of aspect ratio and orientation of an urban street canyon on outdoor thermal comfort in hot and dry climate. *Building and Environment*, 41(2), 94-108.
- Anderson, M.G., 1988. Modelling geomorphological systems, *Modelling geomorphological systems*. John Wiley, Chichester.
- Ansan, V., Mangold, N., 2006. New observations of Warrego Valles, Mars: evidence for precipitation and surface runoff. *Planetary and Space Science* 54, 219–242.
- Arp, C., Whitman, M., Jones, B., Kemnitz, R., Grosse, G., Urban, F., 2012. Drainage Network Structure and Hydrologic Behavior of Three Lake-Rich Watersheds on the Arctic Coastal Plain, Alaska. *Arctic, Antarctic, and Alpine Research* 44, 385-398.
- Asadi, H., Raeisvandi, A., Rabiei, B., Ghadiri, H., 2012. Effect of land use and topography on soil properties and agronomic productivity on calcareous soils of a semiarid region, Iran. *Land Degradation & Development*, 23(5), 496-504.
- Azor, A., Keller, E.A., Yeats, R.S., 2002. Geomorphic indicators of active fold growth: South Mountain-Oak Ridge anticline, Ventura Basin, southern California. *Geological Society of America Bulletin* 114, 745–753.
- Balazs, D., 1973. Relief types of tropical karst areas, *Proceedings of Symposium on Karst-morphogenesis*, International Geographical Union, European region conference, pp. 16-32.
- Bali, R., Agarwal, K.K., Ali, S.N., Rastogi, S.K., Krishna, K., 2012. Drainage morphometry of Himalayan Glacio-fluvial basin, India: hydrologic and neotectonic implications. *Environmental Earth Sciences*, 66(4), 1163-1174.
- Ballantine, J.-A.C., Okin, G.S., Prentiss, D.E., Roberts, D.A., 2005. Mapping North African landforms using continental scale unmixing of MODIS imagery. *Remote Sensing of Environment*, 97(4), 470-483.
- Barnes, J.B., Pelletier, J.D., 2006. Latitudinal variation of denudation in the evolution of the Bolivian Andes. *American Journal of Science* 306, 1-31.
- Basso, A., Bruno, E., Parise, M., Pepe, M., 2013. Morphometric analysis of sinkholes in a karst coastal area of southern Apulia (Italy). *Environmental earth sciences*, 70(6), 2545-2559.
- Bauer, C., 2015. Analysis of dolines using multiple methods applied to airborne laser scanning data. *Geomorphology*, 250, 78-88.
- Baumgartner, P., 1987. Age and genesis of Tethyan Jurassic radiolarites. *Eclogae Geologicae Helveticae* 80, 831-879.

- Beck, B., 2004. Soil piping and sinkhole failures. *Encyclopedia of caves*. Elsevier, Nueva York, 523-528.
- Berry, J., 2002. Beyond Mapping Use Surface Area for Realistic Calculations. *GEO WORLD*, 15, 20-21.
- Bishop, P., 1986. Horizontal stability of the Australian continental drainage divide in south central New South Wales during the Cainozoic. *Australian Journal of Earth Sciences* 33(3), 295-307.
- Bishop, P., Hoey, T.B., Jansen, J.D., Artza, I.L., 2005. Knickpoint recession rates and catchment area: the case of uplifted rivers in Eastern Scotland. *Earth Surface Processes and Landforms* 30, 767–778.
- Bloomfield, J., Bricker, S., Newell, A., 2011. Some relationships between lithology, basin form and hydrology: a case study from the Thames basin, UK. *Hydrological Processes* 25, 2518-2530.
- Boardman, J., Poesen, J., 2006. *Soil erosion in Europe*. Wiley Online Library.
- Bögli, A., 1960. *Kalklösung und karrenbildung*. Borntträger.
- Brinkmann, R., Parise, M., Dye, D., 2008. Sinkhole distribution in a rapidly developing urban environment: Hillsborough County, Tampa Bay area, Florida. *Engineering Geology*, 99(3), 169-184.
- Brocklehurst, S.H., Whipple, K.X., 2002. Glacial erosion and relief production in the Eastern Sierra Nevada, California. *Geomorphology* 42, 1-24.
- Brookfield, M.E., 1998. The evolution of the great river systems of southern Asia during the Cenozoic India-Asia collision: Rivers draining southward. *Geomorphology* 22, 285–312.
- Bruno, E., Calcaterra, D., Parise, M., 2008. Development and morphometry of sinkholes in coastal plains of Apulia, southern Italy. Preliminary sinkhole susceptibility assessment. *Engineering Geology*, 99(3), 198-209.
- Bull, W.B., McFadden, L.D., 1977. Tectonic geomorphology north and south of the Garlock fault, California D.O. Doehring (Ed.), *Geomorphology in Arid Regions*. Proc. 8th Annual Geomorphology Symp. State Univ. of New York at Binghamton, 115–137.
- Burbank, D.W., Anderson, W., 2001. *Tectonic Geomorphology*.
- Burbank, D.W., Leland, J., Fielding, E., Anderson, R.S., Brozovic, N., Reid, M.R., Duncan, C., 1996. Bedrock incision, rock uplift and threshold hillslopes in the northwestern Himalayas. *Nature* 379, 505-510.
- Burnett, A.W., Schumm, S.A., 1983. Alluvial river response to neotectonic deformation in Louisiana and Mississippi. *Science* 222, 49–50.
- Canora, F., Fidelibus, M.D., Sciortino, A., Spilotro, G., 2008. Variation of infiltration rate through karstic surfaces due to land use changes: A case study in Murgia (SE-Italy). *Engineering Geology*, 99(3), 210-227.
- Carvalho Júnior, O.A.d., Guimarães, R.F., Montgomery, D.R., Gillespie, A.R., Gomes, R.A.T., Martins, É.d.S., Silva, N.C., 2014. Karst depression detection using ASTER,

- ALOS/PRISM and SRTM-Derived digital elevation models in the Bambuí group, Brasil.
- Chen, A., 2005. Discuss several issues on Danxia landform. theory and practice of geotourism. The 11th Collection on Geo-Tourism. Chinese Forestry Press, Beijing, pp. 1–10 (in Chinese).
- Chen, G., 1935. Red rock series in Guangdong. Quarterly Journal of Science of National Sun Yat-sen University 6(4), 783-784.
- Chen, G., 1935. Red rock systems of Guangdong Province. The Science Quarterly of The National Sun Yat-sen University 6(4), 1–30 (in Chinese).
- Chen, H., Wu, P., LIU, P., Gu, S.Y., 2012. Landscape Patterns of Rocky Desertification in the Mawoshan Karst Basin of Northwest Guizhou Province. Research of Soil and Water Conservation, 19(004), 239-243 (in Chinese, with English Abstr.).
- Chen, Y.C., Sung, Q., Cheng, K.Y., 2003. Along strike variations in morphometric feature in the Western Foothills of Taiwan: tectonic implications based on stream-gradient and hypsometric analysis. *Geomorphology* 56, 109–137.
- Cheng, K.Y., Hung, J.H., Chang, H.C., Tsai, H., Sung, Q.C., 2012. Scale independence of basin hypsometry and steady state topography. *Geomorphology* 171, 1-11.
- Cheng, S., Cheng, Z., Hua P., 2010. Anti-pressure experimental study on rocks in level cave of Jinshiyuan of Danxiashan in Guangdong Province. *Journal of Anhui Normal University: Natural Science* 33(2), 170-174.
- Chorley, G., 1957. Climate and morphometry. *Journal of Geology* 65, 628-638.
- Chorley, R.J., Schumm, S.A., Sugdden, D.E., 1984. *Geomorphology*. Methuen, 605p.
- Ciotoli, G., Della Seta, M., Del Monte, M., Fredi, P., Lombardi, S., Lupia Palmieri, E., Pugliese, F., 2003. Morphological and geochemical evidence of neotectonics in the volcanic area of Monti Vulsini (Latium, Italy). *Quaternary International* 101–102, 103–113.
- Clark, J.M., Chapman, P.J., Adamson, J.K., 2005. Influence of drought induced acidification on the mobility of dissolved organic carbon in peat soils. *Global Change Biology* 11, 791–809.
- Clark, M.L., Clark, D.B., Roberts, D.A., 2004. Small-footprint lidar estimation of sub-canopy elevation and tree height in a tropical rain forest landscape. *Remote Sensing of Environment* 91, 68–89.
- Crosby, B.T., Whipple, K.X., 2006. Knickpoint initiation and distribution within fluvial networks: 236 waterfalls in the Waipaoa River, North Island, New Zealand. *Geomorphology* 82(1), 16-38.
- Crosta, G.B., Frattini, P., 2004. Controls on modern alluvial fan processes in the central Alps, northern Italy. *Earth Surface Processes and Landforms* 29, 267–293.
- Cvijic, J., 1893. Das Karstphanomen: *Geogr. Abhand. von A. Penck*, 5(3), 2J5-319.
- Dabral, P., Baithuri, N., Pandey, A., 2008. Soil erosion assessment in a hilly catchment of North Eastern India using USLE, GIS and remote sensing. *Water Resources Management*, 22(12), 1783-1798.

- Davis, J.C., Sampson, R.J., 2002. Statistics and data analysis in geology.
- Davis, W. M., 1899. The Geographical Cycle. *Geographical Journal* 14, 481-504.
- Day, M., 1978. Morphology and distribution of residual limestone hills (mogotes) in the karst of northern Puerto Rico. *Geological Society of America Bulletin*, 89(3), 426-432.
- Day, M., Tang, T., 2004. Tower karst. *The Encyclopedia of Caves and Karst Science*, GUNN, J.(Ed). New York: Taylor and Francis, 734-736.
- De Jong, S.M., Riezebos, H.T., 1997. SEMMED: a distributed approach to soil erosion modelling. *Remote sensing*, 96, 199-204.
- De Vente, J., Poesen, J., Verstraeten, G., Govers, G., Vanmaercke, M., Van Rompaey, A., Arabkhedri, M., Boix-Fayos, C., 2013. Predicting soil erosion and sediment yield at regional scales: Where do we stand? *Earth-Science Reviews*, 127, 16-29.
- De Waele, J., 2009. Evaluating disturbance on mediterranean karst areas: the example of Sardinia (Italy). *Environmental geology*, 58(2), 239-255.
- De Waele, J., Plan, L., Audra, P., 2009. Recent developments in surface and subsurface karst geomorphology: an introduction. *Geomorphology*, 106(1), 1-8.
- DeGraff, J.V., Romesburg, H.C., 1981. Subsidence crack closure; rate, magnitude, and sequence. *International Association of Engineering Geology Bulletin* 23.
- Delcaillau, B., Deffontaines, B., Floissac, L., Angelier, J., Deramond, J., Souquet, P., Lee, J.F., 1998. Morphotectonic evidence from lateral propagation of an active frontal fold; Pakuashan anticline, foothills of Taiwan. *Geomorphology* 24(4), 263-290.
- Delle Rose, M., Federico, A., Parise, M., 2004. Sinkhole genesis and evolution in Apulia, and their interrelations with the anthropogenic environment. *Natural Hazards and Earth System Science*, 4(5/6), 747-755.
- Delle Rose, M., Parise, M., Andriani, G., 2007. Evaluating the impact of quarrying on karst aquifers of Salento (southern Italy). *Geological Society, London, Special Publications*, 279(1), 153-171.
- Demirci, A., Karaburun, A., 2012. Estimation of soil erosion using RUSLE in a GIS framework: a case study in the Buyukcekmece Lake watershed, northwest Turkey. *Environ Earth Sci*, 66(3), 903-913.
- Denizman, C., 2003. Morphometric and spatial distribution parameters of karstic depressions, Lower Suwannee River Basin, Florida. *Journal of Cave and Karst Studies*, 65(1), 29-35.
- Doctor, D.H., Young, J.A., 2013. An evaluation of automated GIS tools for delineating karst sinkholes and closed depressions from 1-meter LiDAR-derived digital elevation data, 13th sinkhole conference, pp. 449-458.
- Drăguț, L., Blaschke, T., 2006. Automated classification of landform elements using object-based image analysis. *Geomorphology*, 81(3), 330-344.
- Drake, J.J., Ford, D.C., 1972. The analysis of growth patterns of two-generation populations: the example of karst sinkholes.

- Duvall, A., Kirby, E., Burbank, D., 2004. Tectonic and lithologic controls on bedrock channel profiles and processes in coastal California. *Journal of Geophysical Research: Earth Surface* (2003–2012), 109(F3).
- Edward, A.K., Nicholas, P., 2002. Active tectonics: earthquakes, uplift, and landscape.
- El Hamdouni, R., Irigaray, C., Fernández, T., Chacón, J., Keller, E.A., 2008. Assessment of relative active tectonics, southwest border of the Sierra Nevada (southern Spain). *Geomorphology* 96(1–2), 150–173.
- Eliet, P.P., Gawthorpe, R.L., 1995. Drainage development and sediment supply within rifts, examples from the Sperchios basin, central Greece. *Journal of the Geological Society* 152(5), 883-893.
- Eschmeyer, W.N., Ferraris, C.J., Hoang, M.D., 1998. *Catalog of fishes*. California Academy of Sciences, San Francisco.
- Esper Angillieri, M.Y., 2008. Morphometric analysis of Colangüil river basin and flash flood hazard, San Juan, Argentina. *Environmental Geology* 55, 107-111.
- Evans, I.S., 2012. Geomorphometry and landform mapping: What is a landform? *Geomorphology*, 137(1), 94-106.
- Febles-González, J., Vega-Carreño, M., Tolón-Becerra, A., Lastra-Bravo, X., 2012. Assessment of soil erosion in karst regions of Havana, Cuba. *Land Degradation & Development*, 23(5), 465-474.
- Feng, T., Chen, H., Polyakov, V.O., Wang, K., Zhang, X., Zhang, W., 2016. Soil erosion rates in two karst peak-cluster depression basins of northwest Guangxi, China: Comparison of the RUSLE model with 137 Cs measurements. *Geomorphology*, 253, 217-224.
- Feng, X., Wang, Y., Chen, L., Fu, B., Bai, G., 2010. Modeling soil erosion and its response to land-use change in hilly catchments of the Chinese Loess Plateau. *Geomorphology*, 118(3), 239-248.
- Ferraris, F., Firpo, M., Pazzaglia, F.J., 2012. DEM analyses and morphotectonic interpretation: The Plio-Quaternary evolution of the eastern Ligurian Alps, Italy. *Geomorphology* 149, 27-40.
- Finnegan, N.J., Roe, G., Montgomery, D.R., Hallet, B., 2005. Controls on the channel width of rivers: Implications for modeling fluvial incision of bedrock. *Geology* 33, 229-232.
- Flint, J.J., 1974. Stream gradient as a function of order, magnitude, and discharge. *Water Resources Research* 10, 969-973.
- Ford, D., Williams, P.D., 2013. *Karst hydrogeology and geomorphology*. John Wiley & Sons, London.
- Fried, A.W., Smith, N., 1992. Timescales and the role of inheritance in long-term landscape evolution, northern New England, Australia. *Earth Surface Processes and Landforms* 17, 375–385.
- Galve, J., Gutiérrez, F., Remondo, J., Bonachea, J., Lucha, P., Cendrero, A., 2009. Evaluating and comparing methods of sinkhole susceptibility mapping in the Ebro Valley evaporite karst (NE Spain). *Geomorphology*, 111(3), 160-172.

- Gams, I., 1978. The polje: the problem of its definition. *Zeitschrift für Geomorphologie*(22), 170-181.
- Gardiner, J., 1990. River catchment planning for land drainage, flood defence and the environment. *Water and Environment Journal* 4, 442-450.
- Giannoni, F., Roth, G., Rudari, R. 2005. A procedure for drainage network identification from geomorphology and its application to the prediction of the hydrologic response. *Advances in Water Resources* 28(6), 567-581.
- Goldrick, G., Bishop, P., 1995. Differentiating the roles of lithology and uplift in the steepening of bedrock river long profiles: An example from southeastern Australia. *Journal of Geology* 103, 227-231.
- Goldrick, G., Bishop, P., 2007. Regional analysis of bedrock stream long profiles: evaluation of Hack's SL form, and formulation and assessment of an alternative (the DS form). *Earth Surface Processes and Landforms* 32, 649-671.
- Graf, W.L., 1970. The geomorphology of the glacial valley cross section. *Arctic and Alpine Research*, 303-312.
- Gratton D.J., Howarth P.J., Marceau D.J., 1990. Combining DEM parameters with Landsat MSS and TM imagery in a GIS for mountain glacier characterization. *IEEE Transactions on Geoscience and Remote Sensing* 28, 766-769.
- Gregory, K.J., Gardiner, V., 1975. Drainage density and climate. *Zeitschrift für Geomorphologie* 19, 287-298.
- Gregory, K.J., Walling, D.E., 1973. *Drainage Basin Form and Process*. Edward Arnold, London, 456p.
- Grimaldi, S., Nardi, F., Di Benedetto, F., Istanbuluoglu, E., Bras, R.L., 2007. A physically-based method for removing pits in digital elevation models. *Advances in Water Resources*, 30(10), 2151-2158.
- Grohmann, C.H., Smith, M.J., Riccomini, C., 2011. Multiscale analysis of topographic surface roughness in the Midland Valley, Scotland. *Geoscience and Remote Sensing, IEEE Transactions on*, 49(4), 1200-1213.
- Guarnieri, P., Di Stefano, A., Carbone, S., Lentini, F., Del Ben, A., 2005. A multidisciplinary approach to the reconstruction of the Quaternary evolution of the Messina Strait (with Geological Map of the Messina Strait 1:25.000 scale) G. Pasquarè, C. Venturini (Eds.), *Mapping Geology in Italy*, APAT, Roma, 45-50.
- Gunn, J., 1993. The geomorphological impacts of limestone quarrying. *Catena Supplement*, 25, 187-187.
- Gunn, J., 2004. *Encyclopedia of caves and karst science*. Taylor & Francis, New York.
- Guo, F., Jiang, G., Yuan, D., Polk, J.S., 2013. Evolution of major environmental geological problems in karst areas of Southwestern China. *Environmental earth sciences*, 69(7), 2427-2435.
- Guo, F.S., Jiang, Y.B., Hu, Z.H., Liu, L.Q., Li, H., 2011. Evolution and Genesis System Features of Danxia Lanform in Longhushan World Geopark. *Journal of Mountain Science* 29, 195-201.

- Guo, F.S., Zhou, Z.M., Kong, Y.R., 2004. Danxia landform genesis and scenic feature on Longhu Mountain, Jiangxi Province. *Areas of outstanding natural beauty: a discussion paper*, 437-439 (In Chinese).
- Gupta, V.K., Mesa, O.J., 1988. Runoff generation and hydrologic response via channel network geomorphology—Recent progress and open problems. *Journal of Hydrology* 102, 3-28.
- Gutiérrez, F., Guerrero, J., Lucha, P., 2008. A genetic classification of sinkholes illustrated from evaporite paleokarst exposures in Spain. *Environmental Geology*, 53(5), 993-1006.
- Gutiérrez, F., Parise, M., De Waele, J., Jourde, H., 2014. A review on natural and human-induced geohazards and impacts in karst. *Earth-Science Reviews*, 138, 61-88.
- Gutierrez, F., Cooper, A.H., Johnson, K., 2008. Identification, prediction, and mitigation of sinkhole hazards in evaporite karst areas. *Environmental Geology*, 53(5), 1007-1022.
- Gutiérrez, F., Parise, M., De Waele, J., Jourde, H., 2014. A review on natural and human-induced geohazards and impacts in karst. *Earth-Science Reviews*, 138, 61-88.
- Gyssels, G., Poesen, J., Bochet, E., Li, Y., 2005. Impact of plant roots on the resistance of soils to erosion by water: a review. *Progress in physical geography*, 29(2), 189-217.
- Haan, C.T., Barfield, B.J., Hayes, J.C., 1994. *Design hydrology and sedimentology for small catchments*. Access Online via Elsevier.
- Hack, J.T., 1957. *Studies of longitudinal stream profiles in Virginia and Maryland*. U.S. Geological Survey Professional Paper 294B, 45-97.
- Hack, J.T., 1973. Stream-profile analysis and stream-gradient index. *Journal of Research of the U.S. Geological Survey* 1, 421-429.
- Hack, J.T., 1975. Dynamic equilibrium and landscape evolution. In: Melhorn, W.N., Flemal, R.C. (eds.), *Theories of Landform Development*. State University of New York Publications in Geomorphology, Binghamton, 87-102.
- Hack, J.T., 1982. *Physiographic divisions and differential uplift in the Piedmont and Blue Ridge*. US Government Printing Office.
- Hadley, R.F., Schumm, S.A., 1961. Sediment sources and drainage-basin characteristics in upper Cheyenne River basin. U.S. Geological Survey Water Supply Paper 1531, 137-196.
- Hammond, E.H., 1954. Small-scale continental landform maps. *Annals of the Association of American Geographers*, 44(1), 33-42.
- Hancock, G.R., Evans, K.G. 2006. Channel head location and characteristics using digital elevation models. *Earth Surface Processes and Landforms* 31(7), 809-824.
- Hancock, G.R., Willgoose, G.R., 2001. The use of a landscape simulator in the validation of the Siberia catchment evolution model: declining equilibrium landforms. *Water Resources Research* 37, 1981-1992.

- Hao, Y.C., Sun, G.Y., 1986. China Cretaceous. China Stratigraphy 12. Beijing: Geology Press. (in Chinese).
- Harkins, N.W., Anastasio, D.J., Pazzaglia, F.J., 2005. Tectonic geomorphology of the Red Rock fault, insights into segmentation and landscape evolution of a developing range front normal fault. *Journal of structural geology* 27(11), 1925-1939.
- Hayakawa, Y.S., Oguchi, T., 2006. DEM-based identification of fluvial knickzones and its application to Japanese mountain rivers. *Geomorphology* 78(1), 90-106.
- Hayakawa, Y.S., Oguchi, T., 2009. GIS analysis of fluvial knickzone distribution in Japanese mountain watersheds. *Geomorphology* 111(1), 27-37.
- Hengl, T., Rossiter, D.G., 2003. Supervised landform classification to enhance and replace photo-interpretation in semi-detailed soil survey. *Soil Science Society of America Journal*, 67(6), 1810-1822.
- Hooke, R.L., 1972. Geomorphic evidence for late-Wisconsin and Holocene tectonic deformation, Death Valley, California. *Geological Society of America Bulletin* 83, 2073-2098.
- Horton, R.E., 1932. Drainage basin characteristics. *Transactions American Geophysics Union* 13, 350-361.
- Horton, R.E., 1945. Erosional development of streams and their drainage basins; hydrophysical approach to quantitative morphology. *Bulletin of the Geological Society of America* 56, 275-370.
- Hovius, N., 2000. Macroscale process systems of mountain belt erosion. *Geomorphology and global tectonics*, 77-105.
- Howard, A.D., 1967. Drainage basin analysis in geologic interpretation. *American Association of Petroleum Geologists Bulletin* 51, 2246-2259.
- Howard, A.D., 1990. Role of hypsometry and planform in basin hydrologic response. *Hydrological Processes* 4, 373-385.
- Howard, A.D., 1994. A detachment limited model of drainage basin evolution. *Water Resources Research* 30, 2261-2285.
- Howard, K. A., 1971. Paleozoic metasediments in the northern Ruby Mountains, Nevada. *Geological Society of America Bulletin* 82(1), 259-264.
- Huang, J., 1982. A kind of basic mode of slope development of Danxia landform. *Tropical Geomorphology* 3(2), 107-134 (in Chinese).
- Huang, J., 1992. Research report on Danxia Landform in China. *Tropical Geomorphology (Supplement)*, 1-36 (in Chinese).
- Huang, J., 1999. Distributions of Danxia landform in China. *Economic Geography* 19 (Supplement), 31-35 (in Chinese).
- Huang, J., 2002. A preliminary study on the Danxia landforms in Taining country, Fujian province, China. *Tropical Geomorphology* 22 (Supplement), 176-198 (in Chinese).

- Huang J., 2004. Quantitative survey of several important issues concerning with the formation of the Danxia landforms. *Tropical Geography* 24(2), 123-126 (in Chinese).
- Huang, J., 2010. *Danxiashan Landform*. Beijing: Science Press 2010 (in Chinese).
- Huang, J., Chen, Z.J., 2003. The discussion on the definition and classification to Danxia landform. *Econ Geogr* 23 (Supplement), 6-11.
- Huang, J., Chen, Z.J., Huang, K.G., 1992. The definition and classification of Danxia landform. *Tropical Geomorphology* (Supplement), 37-39 (in Chinese).
- Huang, W., Deng, C., Day, M.J., 2013. Differentiating tower karst (fenglin) and cockpit karst (fengcong) using DEM contour, slope, and centroid. *Environmental Earth Sciences*, 1-10.
- Huang, J., Liu, S.R., Gao, Q.Z., 2006. Study on the fluvial terraces of the Wujiang River and quantitative dating of the Jinjiling mount, northern Guangdong province. *Economic Geography* 26, 1-7 (in Chinese).
- Huang, X., Niemann, J.D., 2006. Modelling the potential impacts of groundwater hydrology on long-term drainage basin evolution. *Earth Surface Processes and Landforms* 31(14), 1802-1823.
- Hupp, C.R., 1986. The headward extent of fluvial landforms and associated vegetation on Massanutten Mountain, Virginia. *Earth Surface Processes and Landforms* 11, 545-555.
- Hurtrez, J.E., Lucazeau, F., 1999. Lithological control on relief and hypsometry in the Hérault drainage basin, *Comptes Rendues Académie des Sciences de la terre et des planètes*. *Earth and Planetary Sciences* 328(10), 687-694 (in France).
- Istanbulluoglu, E., Bras, R.L., 2005. Vegetation-modulated landscape evolution: effects of vegetation on landscape processes, drainage density, and topography. *J. Geophys. Res.* 10, 1-19.
- Jaboyedoff, M., Couture, R., Locat, P., 2009. Structural analysis of Turtle Mountain (Alberta) using digital elevation model: toward a progressive failure. *Geomorphology* 103, 5-16.
- Jenson, S.K., Domingue, J.O., 1988. Extracting topographic structure from digital elevation data for geographic information system analysis. *Photogrammetric engineering and remote sensing* 54(11), 1593-1600.
- Jenson, S.K., Domingue, J.O., 1988. Extracting topographic structure from digital elevation data for geographic information system analysis. *Photogrammetric engineering and remote sensing*, 54(11), 1593-1600.
- Jiang, Y., Zhang, C., Yuan, D., Zhang, G., He, R., 2008. Impact of land use change on groundwater quality in a typical karst watershed of southwest China: a case study of the Xiaojiang watershed, Yunnan Province. *Hydrogeology Journal*, 16(4), 727-735.
- Jiang, Y.B., Guo, F.S., Hu, Z.H., 2009. A study on the features of Danxia land form in longhushan world geopark and comparing with others in China. *Journal of mountain science* 27(3), 353-360 (in Chinese).

- Jiang, Y.B., Guo, F.S., Hu, Z.H., Liu, L.Q., Wu, Z.C., 2010. A Study on the Features of Danxia Landform and Its Landscape Types in Xinjiang Basin. *Journal of Mountain Science* 28, 505-512.
- Jiang, F.W., Guo, F.S., Jiang Y.B., Hu, Z.H., 2011. Cause of formation and protection for landscape rockfall of Danxia landform in Longhushan. *Journal of Mountain Science* 29(2), 202-209 (in Chinese).
- Jie, O.Y., Cheng, Z., Hua, P., 2011. Experimental research on vulnerability of Danxia rocks to resistance against acid erosion in Langshan, Hunan Province. *Advances in Earth Science* 26(9), 965-970.
- Jones-Cecil, M., Askew, B.L., McGRATH, M.B., 1988. Analysis of stream-profile data and inferred tectonic activity. US Government Printing Office, Eastern Ozark Mountains region.
- Judson, S., Andrews, G.W., 1955. Pattern and form of some valleys in the Driftless Area, Wisconsin. *Journal of Geology* 63, 328-336.
- Keller, E.A., Pinter, N., 1996. *Active Tectonics*. Prentice Hall, Upper Saddle River, NJ.
- Keller, E.A., Pinter, N., 2002. *Active tectonics: Earthquakes, uplift, and landscape* (second edition). Englewood Cliffs, New Jersey, Prentice Hall, 362p.
- Keller, E.A., Rockwell, T. K., 1984. Tectonic Geomorphology, Quaternary Chronology, and Paleoseismicity. *Developments and Applications of Geomorphology*, 203-239.
- Keller, G., 1986. Stepwise mass extinctions and impact events: Late Eocene to Early Oligocene. *Marine Micropaleontology* 10(4), 267-293.
- Kelly, W., Panno, S., Hackley, K., Martinsek, A., Krapac, I., Weibel, C., Stoment, E., 2009. Bacteria contamination of groundwater in a mixed land-use karst region. *Water Quality, Exposure and Health*, 1(2), 69-78.
- Kirby, E., Whipple, K.X., Patterns of exhumation and rock uplift along the eastern margin of the Tibetan Plateau inferred from thermochronology and bedrock river incision. *Eos Trans. AGU* 81(48), Fall Meet. Suppl., Abstract T52F-03.
- Kirby, E., Whipple, K.X., Tang, W., Zhiliang, C., 2003. Distribution of active rock uplift along the eastern margin of the Tibetan Plateau: Inferences from bedrock channel longitudinal profiles. *J. Geophys. Res.* 108(B4), 2217.
- Korup, O., Schmidt, J., McSavenecy, M.J., 2005. Regional relief characteristics and denudation pattern of the western Southern Alps, New Zealand. *Geomorphology* 71, 402-423.
- Koukouvelas, I.K., 1998. The Egeion fault, earthquake-related and long-term deformation, Gulf of Corinth, Greece. *J. Geodynamics* 26(2-4), 501-513.
- Krishnamurty, J., 1996. An approach to demarcate groundwater potential zones through remote sensing and a geographic information system. *International Journal of Remote Sensing* 10, 1876-1884.
- Kühni, A., Pfiffner, O., 2001. The relief of the Swiss Alps and adjacent areas and its relation to lithology and structure: topographic analysis from a 250-m DEM. *Geomorphology* 41, 285-307.

- Kusky, T.M., Ye, M.H., Wang, J.P., Wang, L., 2010. Geological Evolution of Longhushan World Geopark in Relation to Global Tectonics. *Journal of Earth Science* 21, 1-18.
- La Valle, P., 1968. Karst depression morphology in south central Kentucky. *Geografiska Annaler. Series A. Physical Geography*, 94-108.
- Labus, M., Bochen, J., 2012. Sandstone degradation: an experimental study of accelerated weathering. *Environmental Earth Sciences* 67, 2027-2042.
- Lambin, E.F., Geist, H.J., Lepers, E., 2003. Dynamics of land-use and land-cover change in tropical regions. *Annual review of environment and resources*, 28(1), 205-241.
- Langbein, W.B., 1947. Topographic characteristics of drainage basins. U.S. Geological Survey Professional Paper 968C, 125-157.
- Lavé, J., Avouac, J.P., 2001. Fluvial incision and tectonic uplift across the Himalayas of central Nepal. *J. Geophys. Res.* 106, 26,561–26,591.
- Lee, G.-S., Lee, K.-H., 2006. Scaling effect for estimating soil loss in the RUSLE model using remotely sensed geospatial data in Korea. *Hydrology & Earth System Sciences Discussions*, 3(1).
- Leeder, M.R., Seger, M.J., Stark, C.P., 1991. Sedimentation and tectonic geomorphology adjacent to major active and inactive normal faults, southern Greece. *Journal of the Geological Society* 148(2), 331-343.
- Li, B., Luo, Y., 1983. Measurement of carbonate rocks distribution area in China. *Carsologica Sinica*, 2, 008.
- Li, S., MacMillan, R., Lobb, D.A., McConkey, B.G., Moulin, A., Fraser, W.R., 2011. Lidar DEM error analyses and topographic depression identification in a hummocky landscape in the prairie region of Canada. *Geomorphology*, 129(3), 263-275.
- Li, X., He, Q.C., Dong, Y., Cao, H.J., Wang, Z.J., Duan, X.M., 2013. An Analysis of Characteristics and Evolution of Danxia Landform in the South of Chishui County. *Guizhou Acad Geographica Sinica* 34(4), 501-508 (in Chinese).
- Li, Y.-b., Shao, J.-a., Yang, H., Bai, X.-y., 2009. The relations between land use and karst rocky desertification in a typical karst area, China. *Environmental Geology*, 57(3), 621-627.
- Li, Y.H., Dingwall, P.R., Wang, H.Y., Zhou, L.Y., 2009. The evolution of Langshan Danxia landform of Hunan Province, China and its global significance. First international symposium on Danxia landform 179-187 (in Chinese).
- Li, Z.W., Guo, F.S., Sun, L., Zhang, W.X., 2012. Relations between Danxia Landform and Taoist Culture in Longhushan Mountain. *Tropical geography* 32, 647-651
- Liang, F., Xu, B., 2014. Discrimination of tower-, cockpit-, and non-karst landforms in Guilin, Southern China, based on morphometric characteristics. *Geomorphology*, 204, 42-48.
- Lifton, N.A., Chase, C.G., 1992. Tectonic, climatic and lithologic influences on landscape fractal dimension and hypsometry: implications for landscape evolution in the San Gabriel Mountains, California. *Geomorphology* 5, 77–114.

- Lin, Z., Oguchi, T., 2004. Drainage density, slope angle, and relative basin position in Japanese bare lands from high-resolution DEMs. *Geomorphology* 63, 159–173.
- Lin, Z., Oguchi, T., 2006. DEM analysis on longitudinal and transverse profiles of steep mountainous watersheds. *Geomorphology* 78, 77–89.
- Lin, Z., Oguchi, T., 2009. Longitudinal and transverse profiles of hilly and mountainous watersheds in Japan. *Geomorphology* 111, 17–26.
- Liu, B., Nearing, M., Risse, L., 1994. Slope gradient effects on soil loss for steep slopes. *Transactions of the ASAE*, 37(6), 1835-1840.
- Liu, X.R., Liu, R.H., 2003. The discussion on idea question of Danxia landform. *Economic Geography* 23 (Supplement), 12-18.
- López-Vicente, M., Navas, A., Machín, J., 2009. Geomorphic mapping in endorheic catchments in the Spanish Pyrenees: An integrated GIS analysis of karstic features. *Geomorphology*, 111(1-2), 38-47.
- Lowe, D., Waltham, T., 1995. A dictionary of karst and caves: a brief guide to the terminology and concepts of cave and karst science. British Cave Research Association.
- Luo, B.S., 1993. The development of Danxia landform in Jinjiling District and its relationship to unloading effect. *Journal of Guangdong Institute of Technology* 10(1), 83-90.
- Luo, D.C., 1999. Study on certain problems of Danxia geomorphology. *Economic Geography* 19 (Supplement), 15-18.
- Luo, W., 1998. Hypsometric analysis with a geographic information system. *Computers & Geosciences* 24, 815-821.
- Luo, W., 2000. Quantifying groundwater-sapping landforms with a hypsometric technique. *Journal of Geophysical Research: Planets* (1991–2012) 105(E1), 1685-1694.
- Luo, W., 2002. Hypsometric analysis of Margaritifer Sinus and origin of valley networks. *J. Geophys. Res.* 107(E10), 5071.
- Luoto, M., 2007. New insights into factors controlling drainage density in subarctic landscapes. *Arct. Antarct. Alp. Res* 39(1), 117–126.
- Lv, S.W., Li, X., 2012. Danxia Landform Type and Development Mode of Jiangxi Longhu Mountain Geological Park. *Advances in Geosciences* 2, 74-80.
- Lyew-Ayee, P., Viles, H., Tucker, G., 2007. The use of GIS-based digital morphometric techniques in the study of cockpit karst. *Earth Surface Processes and Landforms*, 32(2), 165-179.
- Mackin, J. H., 1948. Concept of the graded river. *Geological Society of America Bulletin* 59(5), 463-512.
- MacMillan, R., Pettapiece, W., Nolan, S., Goddard, T., 2000. A generic procedure for automatically segmenting landforms into landform elements using DEMs, heuristic rules and fuzzy logic. *Fuzzy sets and Systems*, 113(1), 81-109.

- MacMillan, R., Shary, P., 2009. Landforms and landform elements in geomorphometry. *Developments in soil science*, 33, 227-254.
- Magesh, N.S., Chandrasekar, N., Soundranayagam, J.P., 2011. Morphometric evaluation of Papanasam and Manimuthar watersheds, parts of Western Ghats, Tirunelveli district, Tamil Nadu, India: a GIS approach. *Environmental Earth Sciences* 64(2), 373-381.
- Maidment, D.R., 2002. *Arc Hydro: GIS for water resources*, 1. ESRI, Inc.
- Maidment, D.R., 2002. *ArcHydro: GIS for Water Resources*. ESRI Press, Redlands.
- Mark, D.M., 1984. Automated detection of drainage networks from digital elevation models. *Cartographica* 21(2-3), 168-178.
- Maroukian, H., Gaki-Papanastassiou, K., Karymbalis, E., Vouvalidis, K., Pavlopoulos, K., Papanastassiou, D., Albanakis, K., 2008. Morphotectonic control on drainage network evolution in the Perachora Peninsula, Greece. *Geomorphology* 102, 81-92.
- Martz, L.W., Garbrecht, J., 1992. Numerical definition of drainage network and subcatchment areas from digital elevation models. *Computers and Geosciences* 18(6), 747-761.
- Masek, J.G., Isacks, B.L., Gubbels, T.L., Fielding, E.J., 1994. Erosion and tectonics at the margins of continental plateaus. *Journal of Geophysical Research* 99, 13941-13956.
- McAllister, M., 1999. A watershed algorithm for triangulated terrains. In *CCCG*.
- McCool, D., Brown, L., Foster, G., Mutchler, C., Meyer, L., 1987. Revised slope steepness factor for the Universal Soil Loss Equation. *Transactions of the ASAE-American Society of Agricultural Engineers*, 30.
- McCool, D., Foster, G., Mutchler, C., Meyer, L., 1989. Revised slope length factor for the Universal Soil Loss Equation. *Transactions of the ASAE*, 32.
- McCulloh, R.P., 2003. The stream net as an indicator of cryptic systematic fracturing in Louisiana. *Southeastern Geology* 42, 1-17.
- McKeown, F.A., Jones-Cecil, M., Askew, B.L., McGrath, M.B., 1988. Analysis of stream-profile data and inferred tectonic activity, Eastern Ozark Mountains Region. *United States Geological Survey Bulletin* 1807, 39p.
- McNab, W.H., 1989. Terrain shape index: quantifying effect of minor landforms on tree height. *Forest Science*, 35(1), 91-104.
- Melton, M.A., 1957. An analysis of the relations among elements of climate, surface properties, and geomorphology. Dept. Geol. Columbia Univ. Tech. Rep. 11, Proj. NR 389-042, Off. of Nav. Res., New York.
- Melton, M.A., 1958. Correlation structure of morphometric properties of drainage systems and their controlling agents. *Journal of Geology* 66, 442-460.
- Merritts, D., Ellis, M., 1994. Introduction to special section on tectonics and topography. *Journal of Geophysical Research* 99, 12135-12141.
- Merritts, D., Vincent, K.R., 1989. Geomorphic response of coastal streams to low, intermediate, and high rates of uplift, Mendocino triple junction region, northern California. *Geological Society of America Bulletin* 101, 1373-1388.

- Merritts, D., Vincent, K.R., Wohl, E.E., 1994. Long river profiles, tectonism, and eustasy: a guide to interpreting fluvial terraces. *J. Geophys Res.* 99, 14031–14050.
- Mikhailova, E.A., Bryant, R., Schwager, S., Smith, S., 1997. Predicting rainfall erosivity in Honduras. *Soil Sci Soc Am J*, 61(1), 273-279.
- Miller, V.C., 1953. A Quantitative geomorphic study of drainage basin characteristics in the Clinch Mountain area Virginia and Tennessee.
- Mino, Y., 1942. *Basis Theories of Geomorphology*. Kokon-Shoin, Tokyo, 517p (in Japanese).
- Moglen, G.E., Bras, R.L., 1995. The effect of spatial heterogeneities on geomorphic expression in a model of basin evolution. *Water Resour. Res.* 31, 2613–2624.
- Moglen G.E., Eltahir, E.A., Bras, R.L., 1998. On the sensitivity of drainage density to climate change. *Water Resources Research* 34, 855-862.
- Montgomery, D.R., Balco, G., Willet, S.D., 2001. Climate, tectonics, and the morphology of the Andes. *Geology* 29, 579–582.
- Montgomery, D.R., Dietrich, W.E., 1988. Where do channels begin? *Nature* 336, 232-234.
- Montgomery, D.R., Dietrich, W.E., 1989. Source areas, drainage density, and channel initiation. *Water Resources Research* 25, 1907–1918.
- Montgomery, D.R., Dietrich, W.E., 1992. Channel initiation and the problem of landscape scale. *Science* 255, 826– 830.
- Moore, I.D., Burch, G.J., 1986. Physical basis of the length-slope factor in the Universal Soil Loss Equation. *Soil Sci Soc Am J*, 50(5), 1294-1298.
- Morgan, R., Quinton, J., Smith, R., Govers, G., Poesen, J., Auerswald, K., Chisci, G., Torri, D., Styczen, M., 1998. The European Soil Erosion Model (EUROSEM): a dynamic approach for predicting sediment transport from fields and small catchments. *Earth Surface Processes and Landforms*, 23(6), 527-544.
- Morgan, R.P.C., 2009. *Soil erosion and conservation*. John Wiley & Sons.
- Morisawa, M.E., 1959. Relation of Morphometric Properties to Runoff in the Little Mill Creek, Ohio Drainage Basin. Columbia University, Dept. of Geol., Technical Report 17, office of Naval Research, Project NR 389-042.
- Mu, X., Zhang, L., McVicar, T.R., Chille, B., Gau, P., 2007. Analysis of the impact of conservation measures on stream flow regime in catchments of the Loess Plateau, China. *Hydrological Processes*, 21(16), 2124-2134.
- Nag, S. K., Chakraborty, S., 2003. Influence of rock types and structures in the development of drainage network in hard rock area. *Journal of the Indian Society of Remote Sensing* 31(1), 25-35.
- Nearing, M., Foster, G., Lane, L., Finkner, S., 1989. A process-based soil erosion model for USDA-Water Erosion Prediction Project technology. *Trans. ASAE*, 32(5), 1587-1593.
- O'Callaghan, J.F., Mark, D.M., 1984. The extraction of drainage networks from digital elevation data. *Computer vision, graphics, and image processing* 28(3), 323-344.

- Oguchi, T., 1997. Drainage density and relative relief in humid steep mountains with frequent slope failure. *Earth Surface Processes and Landforms*, 22(2), 107-120.
- Ohmori, H., 1993. Changes in the hypsometric curve through mountain building resulting from concurrent tectonics and denudation. *Geomorphology* 8, 263–277.
- Ouyang, J., Zhu C., Peng, H., Hu, Z.N., Yu, J.B., Wang, H.Y., LV, W., Xu, L.S., 2009. Experimental research on vulnerability of Danxia rocks to resistance against acid erosion in Langshan, Hunan Province. *Advances in earth science* 26(9), 965-970 (in Chinese).
- Ouyang, J., Zhu, C., Peng, H., Yu, J., Li, L., Zhou, R., Zhang, G., Zhu, G., Li, Z., Zhong, Y., 2009. Types and spatial combinations of Danxia landform of Fangyan in Zhejiang Province. *Journal of Geographical Sciences* 19, 631-640.
- Ouyang, J., Zhu, C., Peng, H., 2013. Exploring the Development Mechanisms of Danxia Landforms in the World Nature Heritage Sites of China Danxia. *Advances in earth science* 3, 18-21 (in Chinese).
- P.R.China, M.o.w.r.o.t., 1997. Chinese standard for classification and gradation of soil erosion SL190-96. China Water Power Press, Beijing (in Chinese).
- Parise, M., Closson, D., Gutiérrez, F., Stevanovic, Z., 2015. Facing engineering problems in the fragile karst environment, *Engineering Geology for Society and Territory-Volume 5*. Springer, pp. 479-482.
- Parise, M., Pascali, V., 2003. Surface and subsurface environmental degradation in the karst of Apulia (southern Italy). *Environmental Geology*, 44(3), 247-256.
- Peng, H., 1992. The natural geomorphology research in Danxiashan. *Tropical Geography* 12, 66-76.
- Peng, H., 2000. *Danxia Geomorphology of China and its Progress in Research Work*. Guangzhou: Sun Yat-Sen University Press (in Chinese).
- Peng, H., 2001. Danxia geomorphology of China: a review. *Chinese Science Bulletin* 46 (Supplement), 38–44.
- Peng, H., 2002. The research on classification system of danxia landform 22, 28-35.
- Peng, H., Pan, Z.X., Yan, L.B., Scott, S., 2013. A review of the research on red beds and Danxia landform. *Acat Geographica Sinica* 68(9), 1170-1181 (in Chinese).
- Peng, H., Wu Z., 2003. A preliminary study on the characteristics and the distribution of red beds. *Acta Sci Nat Univ Sunyatseni* 42, 109-113 (in Chinese).
- Peng, T., Wang, S.-j., 2012. Effects of land use, land cover and rainfall regimes on the surface runoff and soil loss on karst slopes in southwest China. *Catena*, 90, 53-62.
- Pérez-Peña, J., Azañón, J., Booth-Rea, G., Azor, A., Delgado, J., 2009. Differentiating geology and tectonics using a spatial autocorrelation technique for the hypsometric integral. *Journal of Geophysical Research: Earth Surface* (2003–2012), 114.
- Pérez-Peña, J.V., Azor, A., Azañón, J.M., Keller, E.A., 2010. Active tectonics in the Sierra Nevada (Betic Cordillera, SE Spain): Insights from geomorphic indexes and drainage pattern analysis. *Geomorphology* 119, 74-87.

- Pike, R.J., Wilson, S.E., 1971. Elevation-relief ratio, hypsometric integral and geomorphic area-altitude analysis. *Geological Society of America Bulletin* 82, 1079-1084.
- Pipan, T., Culver, D., 2013. Forty years of epikarst: what biology have we learned? *International Journal of Speleology*, 42(3), 5.
- Plan, L., Decker, K., 2006. Quantitative karst morphology of the Hochschwab plateau, Eastern Alps, Austria. *Zeitschrift für Geomorphologie Supplementband*, 147, 29.
- Press, F., Siever, P., 1998. *Understanding Earth*. W.H. Freeman and Company, New York.
- Prima, O.D.A., Echigo, A., Yokoyama, R., Yoshida, T., 2006. Supervised landform classification of Northeast Honshu from DEM-derived thematic maps. *Geomorphology*, 78(3), 373-386.
- Parise, M., Closson, D., Gutiérrez, F., Stevanovic, Z., 2015. Facing engineering problems in the fragile karst environment, *Engineering Geology for Society and Territory*-Volume 5. Springer, pp. 479-482.
- Qi, D.L., Yu, R., Zhang R.S., 2005. On the spatial pattern of Danxia Landform in China. *Acta Geographica Sinica* 60(1), 41-52.
- Rahman, M.R., Shi, Z.H., Chongfa, C., 2009. Soil erosion hazard evaluation—An integrated use of remote sensing, GIS and statistical approaches with biophysical parameters towards management strategies. *Ecological Modelling*, 220(13-14), 1724-1734.
- Ramírez-Herrera, M.T., 1998. Geomorphic assessment of active tectonics in the Acambay Graben, Mexican volcanic belt. *Earth Surface Processes and Landforms* 23, 317-332.
- Ren, F., 2009. *Formation Model of Danxia Landform in the Longhushan Geopark, China*. Beijing: China University of Geosciences Press (In Chinese).
- Renard, K.G., Foster, G.R., Weesies, G.A., McCool, D., Yoder, D., 1997. Predicting soil erosion by water: a guide to conservation planning with the revised universal soil loss equation (RUSLE). *Agriculture Handbook* (Washington)(703).
- Rice, S.P., Church, M., 2001. Longitudinal profiles in simple alluvial systems. *Water Resources Research* 37, 417-426.
- Robinson, D., Williams, R., 1976. Aspects of the geomorphology of the sandstone cliffs of the central Weald: Report of an excursion to West Hoathly and Groombridge Saturday, 5 October 1974. *Proceedings of the Geologists' Association* 87, 93-99.
- Rodríguez-Iturbe, I., Valdés, J.B., 1979. The geomorphologic structure of hydrologic response. *Water Resources Research* 15, 1409-1420.
- Roe, G.H., Montgomery, D.R., Hallet, B., 2002. Effects of orographic precipitation variations on the concavity of steady-state river profiles. *Geology* 30, 143-146.
- Saadat, H., Bonnell, R., Sharifi, F., Mehuys, G., Namdar, M., Ale-Ebrahim, S., 2008. Landform classification from a digital elevation model and satellite imagery. *Geomorphology*, 100(3), 453-464.
- Salvati, R., Sasowsky, I.D., 2002. Development of collapse sinkholes in areas of groundwater discharge. *Journal of Hydrology*, 264(1), 1-11.

- Sameena, M., Krishnamurthy, J., Jayaraman, V., Ranganna, G., 2009. Evaluation of drainage networks developed in hard rock terrain. *Geocarto International* 24, 397-420.
- Sappington, J., Longshore, K.M., Thompson, D.B., 1999. A terrain ruggedness index that quantifies topographic heterogeneity. *Intermountain Journal of Sciences*, 5, 23-27.
- Sarangi, A., Madramootoo, C., Enright, E., 2007. Development of User Interface in ArcGis for estimation of Watershed Geomorphology. CSAE/SCGR 2003 Meeting, Montréal, Québec.
- Sauro, U., 2003. Dolines and sinkholes: aspects of evolution and problems of classification. *Acta carsologica*, 32(2), 41-52.
- Schmidt, J., Evans, I.S., Brinkmann, J., 2003. Comparison of polynomial models for land surface curvature calculation. *International Journal of Geographical Information Science*, 17(8), 797-814.
- Schumm, S.A., 1956. Evolution of drainage systems and slopes in badlands at Perth Amboy, New Jersey. *Geological Society of America Bulletin* 67, 597-646.
- Schumm, S.A., 1956. Evolution of drainage systems and slopes in badlands at Perth Amboy, New Jersey. *Geological Society of America Bulletin*, 67(5), 597-646.
- Schumm, S.A., 1986. Alluvial river response to active tectonics. *Active tectonics*, 80-94.
- Seeber, L., Gornitz, V., 1983. River profiles along the Himalayan arc as indicators of active tectonics. *Tectonophysics* 92, 335-367.
- Seidl, M.A., Dietrich, W.E., 1992. The problem of channel erosion into bedrock, in Schmidt, K.H., and de Ploey, J., eds. *Functional geomorphology: Catena*, suppl. 23, 101-124.
- Seong, Y.B., Owen, L.A., Yi, C., Finkel, R.C., Schoenbohm, L., 2008. Geomorphology of anomalously high glaciated mountains at the northwestern end of Tibet: Muztag Ata and Kongur Shan. *Geomorphology* 103, 227-250.
- Sepinski, T.F., Coradetti, S., 2004. Comparing morphologies of drainage basins on Mars and Earth using integral-geometry and neural maps. *Geophysical Research Letters* 31(15).
- Sharp, M., Richards, K., Willis, I., Arnold, N., Nienow, P., Lawson, W., Tison, J.L., 1993. Geometry, bed topography and drainage system structure of the Haut Glacier d'Arolla, Switzerland. *Earth Surface Processes and Landforms* 18, 557-571.
- Shimano, Y., 1992. Characteristics of the stream network composition of the drainage basin in Japanese islands. *Environ. Geol. Water Sci.* 20(1), 5-14.
- Shu, L.S., Zhou, X.M., Deng, P., Wang, B., Jiang, S.Y., Yu, J.H., 2009. Mesozoic tectonic evolution of the Southeast China Block: New insights from basin analysis. *J Asian Earth Sci.* 34(3), 376-391.
- Siart, C., Bubenzer, O., Eitel, B., 2009. Combining digital elevation data (SRTM/ASTER), high resolution satellite imagery (Quickbird) and GIS for geomorphological mapping: A multi-component case study on Mediterranean karst in Central Crete. *Geomorphology*, 112(1), 106-121.

- Silva, J.B., Pereira, M.F., Chichorro, M., 2003. Upper Paleozoic basins development under orogen-parallel sinistral transcurrent regime in the SW Iberian Massif (Portugal). In: Proc VI Congresso Nacional de Geologia, Lisboa.
- Singh, V., Tandon, S.K., 2008. The Pinjaur dun (intermontane longitudinal valley) and associated active mountain fronts, NW Himalaya: tectonic geomorphology and morphotectonic evolution. *Geomorphology*, 102, 376–394.
- Sinha, S.K., Parker, G., 1996. Causes of concavity in longitudinal profiles of rivers. *Water Resources Research*, 32, 1417-1428.
- Sklar, L.S., Dietrich, W.E., 1998. River longitudinal profiles and bedrock incision models: stream power and the influence of sediment supply. In *Rivers Over Rock: Fluvial Processes in Bedrock Channels*. American Geophysical Union Geophysical Monograph Series 107, TinklerK, WohlEE (eds), 237–260.
- Sklar, L.S., Dietrich, W.E., 2004. A mechanistic model for river incision into bedrock by saltating bedload. *Water Resources Research* 40, W06301.
- Sklar, L.S., Dietrich, W.E., 2006. The role of sediment in controlling bedrock channel slope: implications of the saltation–abrasion incision model. *Geomorphology* 82, 58–83.
- Sklar, L.S., Dietrich, W.E., 2008. Implications of the saltation–abrasion bedrock incision model for steady-state river longitudinal profile relief and concavity. *Earth Surface Processes and Landforms* 33, 1129–1151.
- Smith, K.G., 1958. Erosional processes and landforms in Badlands National Monument, South Dakota. *Geological Society of America Bulletin* 69, 975– 1008.
- Snow, R.S., Slingerland, R.L., 1987. Mathematical modeling of graded river profiles. *Journal of Geology* 95, 15-33.
- Snyder, N.P., Whipple, K.X., Tucker, G.E., Merritts, D.J., 2000. Landscape response to tectonic forcing: Digital elevation model analysis of stream profiles in the Mendocino triple junction region, northern California. *Geological Society of America Bulletin* 112, 1250-1263.
- Snyder, N.P., Whipple, K.X., Tucker, G.E., Merritts, D.J., 2003. Channel response to tectonic forcing: Analysis of stream morphology and hydrology in the Mendocino triple junction region, northern California. *Geomorphology* 53, 97-127.
- Sorriso-Valvo, M., Antronico, L., Le Pera, E., 1998. Controls on modern fan morphology in Calabria, Southern Italy. *Geomorphology* 24, 169–187.
- Stark, C.P., 2006. A self-regulating model of bedrock river channel geometry. *Geophys. Res. Lett.* 32, L04402.
- Štěpančíková, P., Stemberk, J., Vilímek, V., Košťák, B., 2008. Neotectonic development of drainage networks in the East Sudeten Mountains and monitoring of recent fault displacements (Czech Republic). Special Issue on: Impact of Active Tectonics and Uplift on Fluvial Landscapes and River Valley Development *Geomorphology* 102, 68–80.
- Stock, J.D., Montgomery, D.R., 1999. Geologic constraints on bedrock river incision using the stream power law. *Journal of Geophysical Research* 104, 4983-4993.

- Strahler, A.N., 1964. Quantitative geomorphology of drainage basins and channel networks. In: Chow, V.T. (ed.), *Handbook of Applied Hydrology*. McGraw-Hill, New York, section 4-II.
- Strahler, A.N., 1952. Hypsometric (area-altitude) analysis of erosional topography. *Bulletin of the Geological Society of America* 63, 1117-1142.
- Strahler, A.N., 1952. Hypsometric (area-altitude) analysis of erosional topography. *Geological Society of America Bulletin*, 63(11), 1117-1142.
- Sweeting, M.M., 1973. Karst landforms.
- Taheri, K., Gutiérrez, F., Mohseni, H., Raeisi, E., Taheri, M., 2015. Sinkhole susceptibility mapping using the analytical hierarchy process (AHP) and magnitude-frequency relationships: A case study in Hamadan province, Iran. *Geomorphology*, 234, 64-67.
- Tailing, P., Sowter, M.J., 1999. Drainage density on progressively tilted surfaces with different gradients, Wheeler Ridge, California. *Earth Surface Processes and Landforms* 24, 809– 824.
- Tamene, L., Park, S., Dikau, R., Vlek, P., 2006. Analysis of factors determining sediment yield variability in the highlands of northern Ethiopia. *Geomorphology*, 76(1), 76-91.
- Tarolli, P., Dalla Fontana, G., 2009. Hillslope-to-valley transition morphology: New opportunities from high resolution DTMs. *Geomorphology* 113(1), 47-56.
- Tharp, T.M., 1999. Mechanics of upward propagation of cover-collapse sinkholes. *Engineering Geology*, 52(1), 23-33.
- Tibaldi, A., Ferrari, L., Pasquarè, G., 1995. Landslides triggered by earthquakes and their relations with faults and mountain slope geometry: an example from Ecuador. *Geomorphology*, 11(3), 215-226.
- Tiwari, A., Risse, L., Nearing, M., 2000. Evaluation of WEPP and its comparison with USLE and RUSLE. *Transactions of the ASAE*, 43(5), 1129-1135.
- Toy, T.J., Hadley, R.F., 1987. *Geomorphology and Reclamation of Disturbed Lands*. Academic Press, Orlando, 480p.
- Troiani, F., Della Seta, M., 2008. The use of the Stream Length-Gradient Index in morphotectonic analysis of small catchments: a case study from central Italy. *Geomorphology* 102, 159–168.
- Tucker, G.E., Catani, F., Rinaldo, A., Bras, R.L., 2001. Statistical analysis of drainage density from digital terrain data. *Geomorphology* 36(3), 187-202.
- Turnage, K., Lee, S., Foss, J., Kim, K., Larsen, I., 1997. Comparison of soil erosion and deposition rates using radiocesium, RUSLE, and buried soils in dolines in East Tennessee. *Environmental Geology*, 29(1-2), 1-10.
- Turowski, J.M., Lague, D., Hovius, N., 2007. The cover effect in bedrock abrasion: A new derivation and its implications for the modeling of bedrock channel morphology. *J. Geophys. Res.* 112, F04006.
- Upchurch, S.B., Littlefield Jr, J.R., 1988. Evaluation of data for sinkhole-development risk models. *Environmental Geology and Water Sciences*, 12(2), 135-140.

- Van Beynen, P., Townsend, K., 2005. A disturbance index for karst environments. *Environmental Management*, 36(1), 101-116.
- Van der Knijff, J., Jones, R., Montanarella, L., 2000. Soil erosion risk assessment in Europe. European Soil Bureau, European Commission.
- Van Remortel, R.D., Maichle, R.W., Hickey, R.J., 2004. Computing the LS factor for the Revised Universal Soil Loss Equation through array-based slope processing of digital elevation data using a C++ executable. *Computers & Geosciences*, 30(9), 1043-1053.
- Van Rompaey, A.J., Govers, G., Baudet, M., 1999. A strategy for controlling error of distributed environmental models by aggregation. *International Journal of Geographical Information Science*, 13(6), 577-590.
- Van Schoor, M., 2002. Detection of sinkholes using 2D electrical resistivity imaging. *Journal of Applied Geophysics*, 50(4), 393-399.
- VanLaningham, S., Duncan, R.A., Piasias, N.G., 2006. Erosion by rivers and transport pathways in the ocean: A provenance tool using ^{40}Ar – ^{39}Ar incremental heating on fine-grained sediment. *J. Geophys. Res.*, 111.
- Veni, G., 1999. A geomorphological strategy for conducting environmental impact assessments in karst areas. *Geomorphology*, 31(1), 151-180.
- Veni, G., 2002. Revising the karst map of the united states. *Journal of Cave and Karst Studies*, 64(1), 45-50.
- Vijith, H., Satheesh, R., 2006. GIS based morphometric analysis of two major upland sub-watersheds of Meenachil river in Kerala. *Journal of the Indian Society of Remote Sensing* 34(2), 181-185.
- Vogt, J.V., Colombo, R., Bertolo, F., 2003. Deriving drainage networks and catchment boundaries: a new methodology combining digital elevation data and environmental characteristics. *Geomorphology* 53(3), 281-298.
- Vojtko, R., Benová, A., Bóna, J., Hók, J., 2012. Neotectonic evolution of the northern Laborec drainage basin (northeastern part of Slovakia). *Geomorphology* 138, 276-294.
- Walcott, R.C., Summerfield, M.A., 2007. Scale dependence of hypsometric integrals: an analysis of southeast African basins. *Geomorphology* 96, 174-186.
- Waltham, A., 1995. The pinnacle karst of Gunung Api, Mulu, Sarawak. *Cave and Karst Science*, 22(3), 123-126.
- Waltham, A., Fookes, P., 2003. Engineering classification of karst ground conditions. *Quarterly Journal of Engineering Geology and Hydrogeology*, 36(2), 101-118.
- Waltham, T., 2008. Fengcong, fenglin, cone karst and tower karst. *Cave Karst Sci*, 35(3), 77-88.
- Waltham, T., Bell, F.G., Culshaw, M., 2007. Sinkholes and subsidence: karst and cavernous rocks in engineering and construction. Springer Science & Business Media, Chichester.

- Wan, J., 2003. Land degradation and ecological rehabilitation in karst areas of Guizhou province, South Western China. *Advance in Earth Sciences*, 18(3), 447-453.
- Wang, S.J., Liu, Q.M., Zhang, D.F., 2004. Karst rocky desertification in southwestern China: geomorphology, landuse, impact and rehabilitation. *Land Degradation & Development*, 15(2), 115-121.
- Wei, W., Chen, L., Fu, B., Huang, Z., Wu, D., Gui, L., 2007. The effect of land uses and rainfall regimes on runoff and soil erosion in the semi-arid loess hilly area, China. *Journal of Hydrology*, 335(3), 247-258.
- Weiss, A., 2001. Topographic position and landforms analysis, Poster presentation, ESRI User Conference, San Diego, CA, pp. 200.
- Weissel, J.K., Seidl, M.A., 1998. Inland propagation of erosional escarpments and river profile evolution across the southeast Australian passive continental margin: in Tinkler, K.J., and Wohl, E.E., eds., *Rivers over rock: Fluvial processes in bedrock channels*. American Geophysical Union Geophysical Monograph 107, 189-206.
- Wells, S.G., Bullard, T.F., Menges, C.M., Drake, P.G., Karas, P.A., Kelson, K.I., Ritter, J.B., Wesling, J.R., 2012. Regional variations in tectonic geomorphology along a segmented convergent plate boundary pacific coast of Costa Rica. *Geomorphology* 1, 239-265.
- Weng, L., Chen, Y., 2012. *Agriculture & Technology* 3, 23-26 (in Chinese).
- Whipple, K.X., Tucker, G.E., 1999. Dynamics of the stream-power river incision model: Implications for height limits of mountain ranges, landscape response timescales, and research needs. *Journal of Geophysical Research: Solid Earth* (1978–2012) 104(B8), 17661-17674.
- White, W.B., 1988. *Geomorphology and hydrology of karst terrains*. Oxford university press, New York.
- Whittaker, A.C., Cowie, P.A., Attal, M., Tucker, G.E., Roberts, G.P., 2007a. Bedrock channel adjustment to tectonic forcing: Implications for predicting river incision rates. *Geology* 35, 103–106.
- Willgoose, G., Hancock, G., 1998. Revisiting the hypsometric curve as an indicator of form and process in transport-limited catchment. *Earth Surf. Processes Landforms* 23, 611–623.
- Williams, J., Renard, K., Dyke, P., 1983. EPIC: A new method for assessing erosion's effect on soil productivity. *Journal of Soil and water Conservation*, 38(5), 381-383.
- Williams, P.W., 1972. Morphometric analysis of polygonal karst in New Guinea. *Geological Society of America Bulletin*, 83(3), 761-796.
- Williams, P., 2003. Dolines. *Encyclopedia of caves and karst science*. Fitzroy Dearborn, New York, 304-310.
- Willis, I.C., Fitzsimmons, C.D., Melvold, K., Andreassen, L.M., Giesen, R.H., 2012. Structure, morphology and water flux of a subglacial drainage system, Midtdalsbreen, Norway. *Hydrological Processes* 26, 3810-3829.
- Wilson, L., 1971. Drainage density, length ratios, and lithology in a glaciated area of southern Connecticut. *Geological Society of America Bulletin*, 82(10), 2955-2956.

- Wischmeier, W.H., Smith, D.D., 1965. Predicting rainfall-erosion losses from cropland east of the Rocky Mountains: Guide for selection of practices for soil and water conservation, 282. Agricultural Research Service, US Department of Agriculture.
- Wischmeier, W.H., Smith, D.D., 1978. Predicting rainfall erosion losses-A guide to conservation planning. Predicting rainfall erosion losses-A guide to conservation planning.
- Witze, A., 2014. Florida forecasts sinkhole burden. *Nature*, 504, 196-197.
- Wobus, C.W., Tucker, G.E., Anderson, R.S., 2006b. Self-formed bedrock channels. *Geophysical Research Letters* 33, L18408.
- Wobus, C.W., Kean, J.W., Tucker, G.E., Anderson, R.S., 2008. Modeling the evolution of channel shape: Balancing computational efficiency with hydraulic fidelity. *J. Geophys. Res.* 113, F02004.
- Wu, S., Li, J., Huang, G., 2005. An evaluation of grid size uncertainty in empirical soil loss modeling with digital elevation models. *Environmental Modeling & Assessment*, 10(1), 33-42.
- Wu, Z.C., Peng, H., 2005. A study on Danxia landform classification in Guangdong. *Tropical geography* 25(4), 301-306 (in Chinese).
- Xiao, H., Weng, Q., 2007. The impact of land use and land cover changes on land surface temperature in a karst area of China. *Journal of environmental management*, 85(1), 245-257.
- Xie, L.S., Wu, P., Gu, S.H., Cao, Z.X., Ge, J.J., 2010. Calculation of the soil erosion modulus of basin with the measurement method of sedimentation in Karst area. *Science of Soil and Water Conservation*, 8(2), 20-23 (in Chinese, with English Abstr.).
- Xiong, K.N., Chris, W., Peng, J., Zhou, Z.F., Chen, H., Rong, L., Xiao, S.Z., Du, F.J., 2009. Researches on the feature of Chishui Danxia and its World Natural Heritage Values. *First International Symposium on Danxia Landform*, 102-112.
- Xu, J., 2005. Precipitation-vegetation coupling and its influence on erosion on the Loess Plateau, China. *Catena*, 64(1), 103-116.
- Xu, Y., Shao, X., Kong, X., Peng, J., Cao, Y., 2008a. Adapting the RUSLE and GIS to model soil erosion risk in a mountains karst watershed, Guizhou Province, China. *Environmental monitoring and assessment*, 141(1-3), 275-286.
- Xu, Y.Q., Peng, J., Shao, X.M., 2008b. Assessment of soil erosion using RUSLE and GIS: a case study of the Maotiao River watershed, Guizhou Province, China. *Environmental Geology*, 56(8), 1643-1652.
- Yang, Z., 2002. Study on Soil Loss Equation in Jinsha River Basin of Yunnan Province. *Journal of Mountain Research*, 20(Sup.), 1-9.
- Yang, G., Li, Y., An, Y., 2006. Pixel-based assessment and spatial distribution of sensitivity of soil erosion in Guizhou. *Carsologica Sinica*, 25(1), 73-78 (in Chinese, with English Abstr.).
- Yatsu, E., 1950. On relief energy of the Chichibu Mountains, Japan. *Transactions Otsuka Geographical Association*, 6, 323-330.

- Yatsu, E., 1950. On relief energy of the Chichibu Mountains, Japan. *Transactions Otsuka Geographical Association* 6, 323– 330 (in Japanese).
- Yilmaz, I., 2007. GIS based susceptibility mapping of karst depression in gypsum: a case study from Sivas basin (Turkey). *Engineering Geology*, 90(1), 89-103.
- Yu, B., 1998. Rainfall Erosivity and It's Estimation for Australia's Tropics. *Australian Journal of Soil Research*, 36(1), 143-165.
- Yu, B., Hashim, G., Eusof, Z., 2001. Estimating the R-factor with limited rainfall data: a case study from peninsular Malaysia. *Journal of Soil and water Conservation*, 56(2), 101-105.
- Yuan, D., Zhu, D., Weng, J., Zhu, X., Han, X., Wang, X., Cai, G., Zhu, Y., Cui, G., Deng, Z., 1991. *Karst of China*. Geological Publishing House Beijing.
- Zeng, Z., 1982. Characters of the karst topography in southern China. *Carsologica Sinica*, 1, 27-31.
- Zeng, Z., Huang, S., 1978. Red bed in southeastern China. *Journal of South China Normal University (Natural Science)* 2, 43–57 (in Chinese).
- Zhang, Z.g., 1980. Karst types in China. *GeoJournal*, 4, 541-570.
- Zhu, C., Peng, H., Li, Z., Zhang, G., Li, L., Yu, J., Xu, L., 2009. Age and genesis of the Danxia landform on Jianglang Mountain, Zhejiang Province. *Journal of Geographical Sciences* 19(5), 615-630.
- Zhu, X., Zhu, D., Zhang, Y., Lynch, E., 2013. Tower karst and cone karst. *Treatise on geomorphology*. Academic Press, San Diego, 327-340.
- Ziadat, F., Taimeh, A., 2013. Effect of rainfall intensity, slope, land use and antecedent soil moisture on soil erosion in an arid environment. *Land Degradation & Development*, 24(6), 582-590.
- Zimpfer, G.L., 1982. *Hydrology and Geomorphology of an Experimental Drainage Basin*. Unpublished Ph.D dissertation, Colorado State University.
- Zuazo, V.H.D., Pleguezuelo, C.R.R., 2008. Soil-erosion and runoff prevention by plant covers. A review. *Agronomy for sustainable development*, 28(1), 65-86.
- Zuchiewicz, W., 1998. Quaternary tectonics of the Outer West Carpathians, Poland. *Tectonophysics* 297, 121–132.